



Chalcogenide Glasses for Infrared Applications: New Synthesis Routes and Rare Earth Doping

Item Type	text; Electronic Dissertation
Authors	Hubert, Mathieu
Publisher	The University of Arizona.
Rights	Copyright © is held by the author. Digital access to this material is made possible by the University Libraries, University of Arizona. Further transmission, reproduction or presentation (such as public display or performance) of protected items is prohibited except with permission of the author.
Download date	08/11/2024 19:25:28
Link to Item	http://hdl.handle.net/10150/223357

CHALCOGENIDE GLASSES FOR INFRARED
APPLICATIONS: NEW SYNTHESIS ROUTES AND RARE
EARTH DOPING

By

Mathieu Hubert

A Dissertation Submitted to the Faculty of the
DEPARTMENT OF MATERIALS SCIENCE AND
ENGINEERING

In Partial Fulfillment of the Requirements
For the Degree of

DOCTOR OF PHILOSOPHY

In the Graduate College
THE UNIVERSITY OF ARIZONA

2012

THE UNIVERSITY OF ARIZONA
GRADUATE COLLEGE

As members of the Dissertation Committee, we certify that we have read the dissertation
prepared by Mathieu Hubert

entitled Chalcogenide glasses for infrared applications: new synthesis routes and rare
earth doping

and recommend that it be accepted as fulfilling the dissertation requirement for the
Degree of Doctor of Philosophy

Pierre Lucas

Date: 03/30/2012

B.G. Potter

Date: 03/30/2012

Donald Uhlmann

Date: 03/30/2012

Laurent Calvez

Date: 03/30/2012

Bruno Bureau

Date: 03/30/2012

Final approval and acceptance of this dissertation is contingent upon the candidate's
submission of the final copies of the dissertation to the Graduate College.

I hereby certify that I have read this dissertation prepared under my direction and
recommend that it be accepted as fulfilling the dissertation requirement.

Dissertation Director: Pierre Lucas

Date: 03/30/2012

STATEMENT BY AUTHOR

This dissertation has been submitted in partial fulfillment of requirements for an advanced degree at the University of Arizona and is deposited in the University Library to be made available to borrowers under rules of the Library.

Brief quotations from this dissertation are allowable without special permission, provided that accurate acknowledgment of source is made. Requests for permission for extended quotation from or reproduction of this manuscript in whole or in part may be granted by the head of the major department or the Dean of the Graduate College when in his or her judgment the proposed use of the material is in the interests of scholarship. In all other instances, however, permission must be obtained from the author.

SIGNED: Mathieu Hubert

ACKNOWLEDGEMENTS

First, I would like to sincerely thank my advisors Pierre Lucas, Laurent Calvez and Xiang-Hua Zhang for their guidance, support, advices, and for giving me the opportunity to participate in this joint PhD program between the University of Arizona and the University of Rennes. It was a great honor for me to work under their supervision and to learn from them. I would like to thank Pr. Bruno Bureau, Pr. B.G. Potter and Dr. D.R. Uhlmann for accepting to serve on my defense committee, and for the numerous advices they gave me during this PhD work.

Thanks to Pr. Jacques Lucas, the first person to introduce me to the world of chalcogenide glasses, for his support and the many instructive conversations we had.

I want to acknowledge the people who helped me during this research work: J. Le Lannic, I. Perron and F. Gouttefangeas for imaging analyses, G. Delaizir for SPS experiments, J. Rocherullé and O. Merdrignac for their help with HUP and F. Tessier for surface area measures and XRD.

Since I spent time on both sides of the Atlantic, either at the Arizona Materials Lab in Tucson or at the “Labo Verres et Céramiques” in Rennes, there are so many people I would like to thank.

Thanks to everyone at LVC, who make this place so pleasant: Catherine (tata Kate!), Johann, Laurent(s), Virginie, Didier, Corinne, Jean-Luc, Aline... I would especially like to thank Thierry Pain, for all the amazing work he does with glass and his constant kindness and Thierry Jouan, with who I shared more than just an office. Also, thanks to all the other students with whom I shared a lot (and enjoyed doing it!) during the past few years: Mathieu R., Marie-Laure, Mélinda, Quentin, Clément, Céline, Fred, Patou, Perrine, and many more.... And good luck to Elena for her PhD!

I would also like to thank the people who helped me in Tucson. First, thanks to Zhiyong, for his help during my first days at the lab. Thanks to Ozgur, for his help, his kindness and the good times we had at work or having a beer after work! Thanks to Elsa, who takes so much care of students and helped me so much. Thanks to my fellow wildcats and classmates Tony, Vijay, Fei, Dom, Mariah, Mark, Stefan, Scott, Dustin, Adam, Melia, David... and I can't forget to mention Lance (“all PhD students are stupid”). Thank you for your help and your patience with me.

I especially want to thank Piya, my guide in Tucson, who contributed a lot in making my stay in Arizona so pleasant by helping me discover the city, the American life and many other things (Starbucks...). It was also a pleasure working with you.

I would like to thank my parents for their support. Finally, thanks to all my friends: Lolo, Mali, Mou, Fatoche (“mes poules”), David, Morsail, Nogué, Jean-Louis, Billy, Nath, Carine, Annabool, Fofy, Lucy, Ninick, Pel, Lulu, Toto, 2.16, Mary, Shouk, Manos, Popo, (You can fill in the blank).

TABLE OF CONTENTS

LIST OF FIGURES.....	13
LIST OF TABLES.....	18
ABSTRACT.....	19
 CHAPTER 1: INTRODUCTION	 21
 CHAPTER 2: THERMAL IMAGING.....	 25
2.1. Introduction.....	25
2.1.1. Development of thermal imaging	25
2.1.2. Applications.....	27
2.2. The principles of thermal imaging	30
2.2.1. The Infrared region of the electromagnetic spectrum	30
2.2.2. Thermal radiations	31
2.2.3. Laws of thermal radiation.....	32
2.2.3.1. Black bodies and Planck's law	32
2.2.3.2. Wien's displacement law	33
2.2.3.3. Stefan-Boltzmann law	35
2.2.3.4. Real bodies and emissivity.....	35
2.2.4. Atmospheric transmission	37
2.3. Thermal imagers and their component parts.....	38
2.3.1. A basic thermal imager.....	38
2.3.2. Detection systems	39
2.3.2.1. Thermal detectors.....	40
2.3.2.2. Quantum detectors	41
2.3.3. Image-forming optical systems	42
2.3.3.1. Important factors to consider	42

TABLE OF CONTENTS - Continued

2.3.3.2. Reflectivity and anti-reflection coatings	43
2.3.3.3. Variations of the refractive index with wavelength and temperature	44
2.4. Materials for thermal imager optical systems.....	46
2.4.1. The ideal material	46
2.4.2. Materials for the mid-infrared (3-5 μm band)	48
2.4.2.1. Silicon (Si)	48
2.4.2.2. Oxides and oxynitrides	48
2.4.2.3. Fluorides	49
2.4.2.4. Hot pressed ceramics (Irran).....	50
2.4.3. Materials for the far-infrared (8-12 μm band).....	51
2.4.3.1. Germanium (Ge)	51
2.4.3.2. Gallium Arsenide (GaAs)	52
2.4.3.3. Cadmium Telluride (CdTe).....	53
2.4.3.4. Zinc Sulfide (ZnS)	53
2.4.3.5. Zinc Selenide (ZnSe)	54
2.4.3.6. Halides	55
2.4.3.7. Diamond.....	56
2.4.4. Chalcogenide glasses as materials for thermal imagers	56
2.4.4.1. Selenide glasses	57
2.4.4.2. Telluride-Selenide glasses	59
2.4.4.3. Telluride glasses.....	60
2.4.5. Chalcogenide glass-ceramics.....	60
2.5. Summary	62
2.6. Objectives of this study	63

CHAPTER 3: NEW SYNTHESIS METHODS FOR CHALCOGENIDE GLASSES

3.1. Introduction	65
3.2. Chalcogenide glasses	66

TABLE OF CONTENTS - Continued

3.2.1. Introduction	66
3.2.2. Optical properties	67
3.2.2.1. Band gap	67
3.2.2.2. Multi-phonon absorption	69
3.2.2.3. Absorption bands due to impurities	70
3.2.3. Thermal properties.....	71
3.2.4. Mechanical properties.....	73
3.2.4.1. Density	73
3.2.4.2. Coefficient of thermal expansion.....	73
3.2.4.3. Hardness.....	74
3.2.4.4. Young's modulus	76
3.2.4.5. Toughness	77
3.2.5. Synthesis of chalcogenide glasses in sealed silica ampoule under vacuum	77
3.3. Synthesis in open system under argon atmosphere	80
3.3.1. Introduction	80
3.3.2. Preliminary tests in rocking furnace	81
3.3.2.1. Experimental setup.....	81
3.3.2.2. Melting of a previously synthesized bulk glass	82
3.3.2.3. Melting/casting from the pure raw elements	86
3.3.2.4. Conclusion on the preliminary tests.....	87
3.4. Synthesis in closed silica chamber with homogenization device.....	88
3.4.1. Experimental setup	88
3.4.2. Synthesis of the $\text{Ge}_{25}\text{Ga}_5\text{Se}_{70}$ glass.....	90
3.4.3. Conclusion on the synthesis in open system	93
3.5. Mechano-synthesis.....	94
3.5.1. Introduction	94
3.5.2. Amorphization by mechanical alloying.....	98
3.5.2.1. Liquid Quenching model	99

TABLE OF CONTENTS - Continued

3.5.2.2. Solid state amorphization model.....	99
3.5.3. Choice of milling balls	100
3.5.4. Mechanosynthesis of GeSe₄	102
3.5.4.1. Experimental procedure	102
3.5.4.2. Coloration of the powder	103
3.5.4.3. X-Ray Diffraction	103
3.5.4.4. Differential Scanning Calorimetry.....	104
3.5.5. Mechanosynthesis of 80GeSe₂–20Ga₂Se₃	106
3.5.5.1. Experimental procedure	106
3.5.5.2. Coloration of the powder	107
3.5.5.3. Particle size distribution.....	108
3.5.5.4. X-Ray Diffraction	109
3.5.5.5. Differential Scanning Calorimetry.....	110
3.5.5.6. Mechanism of amorphization	113
3.5.6. Conclusion on mechanosynthesis	113
3.6. Conclusion.....	114

CHAPTER 4: PRODUCTION OF BULK MATERIALS FROM POWDERS OBTAINED BY MECHANOSYNTHESIS116

4.1. Introduction	116
4.2. Sintering of glasses: Principle and Techniques	117
4.2.1. Definition.....	117
4.2.2. Hot Uniaxial Pressing.....	120
4.2.3. Spark Plasma Sintering (SPS)	121
4.3. Sintering of Chalcogenide Glass Powder by Hot Uniaxial Pressing ...	123
4.3.1. Sintering of GeSe ₄ powder.....	123
4.3.1.1. Experimental procedure	123
4.3.1.2. Results.....	124

TABLE OF CONTENTS - Continued

4.3.2. Sintering of $80\text{GeSe}_2\text{--}20\text{Ga}_2\text{Se}_3$ powder	126
4.3.2.1. Experimental procedure	126
4.3.2.2. Results	127
4.3.3. Sintering of ZnSe powder	129
4.3.3.1. Preparation of ZnSe powder by mechanosynthesis	130
4.3.3.2. Hot Uniaxial Pressing	131
4.3.4. Conclusions on sintering by Hot Uniaxial Pressing	133
4.4. Sintering of Chalcogenide Glass Powder by Spark Plasma Sintering	134
4.4.1. Experimental procedure	134
4.4.2. Sintering of GeSe_4 powder	135
4.4.3. Sintering of $80\text{GeSe}_2\text{--}20\text{Ga}_2\text{Se}_3$ powder	137
4.4.3.1. Contamination by carbon	137
4.4.3.2. Optical properties	138
4.4.3.3. Homogeneity of the samples	141
4.4.3.4. Comparison with other synthesis techniques	141
4.4.4. Conclusion on Spark Plasma Sintering	143
4.5. Melting of amorphous powder in open system under argon atmosphere	144
4.5.1. Introduction	144
4.5.2. Experimental procedure	144
4.5.3. GeSe_4 powder	146
4.5.4. $\text{Ge}_{25}\text{Ga}_5\text{Se}_{70}$ powder	148
4.5.5. Conclusion	150
4.6. Conclusion	151
 CHAPTER 5: CHALCOGENIDE GLASS-CERAMICS FOR	
INFRARED APPLICATIONS	153
5.1. Introduction	153

TABLE OF CONTENTS - Continued

5.2. General Principles of Glass-ceramics.....	154
5.2.1. Background.....	154
5.2.2. Nucleation.....	156
5.2.3. Crystal growth	158
5.2.4. Ceramization processes	159
5.3. Production of glass-ceramics by Spark Plasma sintering	159
5.3.1. Introduction	159
5.3.2. Experimental procedure.....	160
5.3.3. Optical properties	161
5.3.4. X-Ray Diffraction.....	163
5.3.5. Microstructure	165
5.3.6. Mechanical properties.....	166
5.3.7. Conclusion	167
5.4. Porous glass-ceramics	168
5.4.1. Introduction	168
5.4.2. Etching in acid solution	169
5.4.3. Surface passivation	180
5.4.4. Etching in basic solution.....	183
5.4.5. Conclusion	184
5.5. Exploration of new chalcogenide glassy domains and ceramization ..	185
5.5.1. Introduction	185
5.5.2. $\text{GeSe}_2\text{-Ga}_2\text{Se}_3\text{-In}_2\text{Se}_3$ system	186
5.5.2.1. Exploration of the glassy domain	186
5.5.2.2. Influence of indium addition on the glass properties.....	187
5.5.3. $\text{GeSe}_2\text{-Ga}_2\text{Se}_3\text{-PbSe}$ system	190
5.5.3.1. Exploration of the glassy domain	190
5.5.3.2. Influence of PbSe addition on the glass properties.....	191
5.5.4. Ceramization study	193

TABLE OF CONTENTS - Continued

5.5.5. Conclusion	197
5.6. Conclusion.....	198
 CHAPTER 6: RARE EARTH DOPED CHALCOGENIDE GLASS- CERAMICS BASED ON SELENIUM.....	 200
6.1. Introduction.....	200
6.2. Luminescence of rare earth ions.....	201
6.3. Preparation of rare earth-doped 80GeSe₂–20Ga₂Se₃ glass-ceramics..	207
6.3.1. Preparation of the doped base-glass	207
6.3.2. Raman study	208
6.3.3. Ceramization of the doped glasses	209
6.3.4. X-Ray Diffraction.....	210
6.3.5. SEM observation	212
6.3.6. Optical Properties	213
6.4. Luminescence	216
6.4.1. Er-doped glass-ceramics.....	216
6.4.2. Nd-doped glass-ceramics.....	218
6.5. Lifetime measurements.....	220
6.5.1. Er-doped glass-ceramics.....	220
6.5.2. Nd-doped glass-ceramics.....	222
6.5.3. Discussion.....	224
6.6. Conclusion.....	225
 CHAPTER 7: CONCLUSION	 227
 APPENDIX A: THERMAL, OPTICAL AND MECHANICAL PROPERTIES OF GLASSES IN THE GESE₂-GA₂SE₃-IN₂SE₃ SYSTEM.....	 231

TABLE OF CONTENTS - Continued

APPENDIX B: THERMAL, OPTICAL AND MECHANICAL PROPERTIES OF GLASSES IN THE GESE₂-GA₂SE₃-PBSE SYSTEM	232
REFERENCES	233

LIST OF FIGURES

Figure 2.1: Evolution of the sales of thermal cameras in the world ranked by applications between 2005 and 2009, and the sales forecasts up to 2011 (Datas provided by Umicore IR Glass)	27
Figure 2.2: Thermal isolation of an habitation monitored by thermal imaging.....	28
Figure 2.3: Driver's vision enhancement system on a BMW Class 5 vehicle	29
Figure 2.4: The electromagnetic spectrum.....	31
Figure 2.5: Monochromatic luminescence energy of a black body as a function of its temperature	34
Figure 2.6: Atmospheric transmission spectrum	37
Figure 2.7: Schematic of a basic thermal imager.....	39
Figure 2.8: Transmission of a chalcogenide Gasir 1® glass with and without antireflection coating [16].....	44
Figure 2.9: Transmission spectra of CaF_2 and BaF_2 [19]	50
Figure 2.10: Transmission spectrum of single-crystalline germanium.....	51
Figure 2.11: Transmission spectrum of ZnSe	54
Figure 2.12: Process of chalcogenide glass lenses molding developed by Umicore IR Glass and example of lenses produced with this technique.....	58
Figure 3.1: Band-gap	67
Figure 3.2: Optical transmissions of different families of glasses.....	70
Figure 3.3: Effect of oxygen contamination on the optical transmission of a chalcogenide glass.....	71
Figure 3.4: Typical DSC curve of a glass	73
Figure 3.5: Print obtained on a glass surface after micro-indentation tests	75
Figure 3.6: Vapor pressures of the elements commonly used to prepare chalcogenide glasses	78
Figure 3.7: Typical setup used for synthesis in sealed silica ampoules under vacuum	79
Figure 3.8: a) bulk chalcogenide glass synthesized in sealed silica ampoule; b) typical heat treatment profile used for glass synthesis	80
Figure 3.9: Rocking furnace used for preliminary tests.....	82
Figure 3.10: Casted $\text{Ge}_{25}\text{Ga}_5\text{Se}_{70}$ glass, a) top view and b) side view of the bulk sample	83
Figure 3.11: Casted $\text{Ge}_{25}\text{Ga}_5\text{Se}_{70}$ glass, a) after polishing and b) observed with a 3-5 μm thermal camera; c) bubbles and d) impurities observed on the glass surface with an optical microscope (magnification x10)	84
Figure 3.12: Optical transmission of the $\text{Ge}_{25}\text{Ga}_5\text{Se}_{70}$ glass before and after melting/casting process	85

LIST OF FIGURES - Continued

Figure 3.13: GeSe ₂ crystals observed in the fumes deposited after melting/casting process	86
Figure 3.14: a) Experimental setup used for synthesis in closed silica chamber; b) As ₂ Se ₃ bulk glass obtained by Guillevic and c) observed with a 3-5 μ m thermal camera; d) rotating helix used for experiments [11]	89
Figure 3.15: a) Bulk material obtained by synthesis in closed silica chamber of Ge ₂₅ Ga ₅ Se ₇₀ composition and b) cross section	91
Figure 3.16: a) Unmelted powder grains and b) GeSe ₂ crystals observed in the bulk material	92
Figure 3.17: ball-powder-ball collisions of powder mixture during mechanosynthesis...	95
Figure 3.18: number of publications per year reporting synthesis of materials by mechanical alloying	97
Figure 3.19: Retch PM100 planetary ball mill.....	101
Figure 3.20: Evolution of the powder coloration with milling time	103
Figure 3.21: Evolution of the XRD spectra of the GeSe ₄ powder with milling time	104
Figure 3.22: Evolution of the characteristic temperatures of the GeSe ₄ powder with milling time	105
Figure 3.23: Evolution of the glass transition temperature (T _g) of the powder with milling duration	106
Figure 3.24: Evolution of the 80GeSe ₂ -20Ga ₂ Se ₃ powder coloration with milling time	107
Figure 3.25: Evolution of the particle size distribution with milling time.....	108
Figure 3.26: Evolution of the XRD spectra of the 80GeSe ₂ -20Ga ₂ Se ₃ powder with milling time	109
Figure 3.27: Evolution of the characteristic temperatures of the 80GeSe ₂ -20Ga ₂ Se ₃ powder with milling time.....	111
Figure 3.28: Magnification of the DSC curves obtained on the powders after 3h and 5h of milling showing the glass transition temperatures.....	112
Figure 4.1: Neck growth between two particles during sintering	118
Figure 4.2: a) Illustration of closed and open porosity; b) variation in the open and closed pore fractions versus the total porosity for urania sintering at 1400°C [105].....	119
Figure 4.3: Illustration of Hot Uniaxial Pressing process.....	120
Figure 4.4: Illustration of Spark Plasma Sintering process.....	121
Figure 4.5: a) Functionally graded WC/Co materials, b) diamond grinding tools prepared by SPS. Images from Fuji Electronic Industrial Co., Ltd [112]	122
Figure 4.6: a) Experimental setup and b) mold used for sintering of GeSe ₄ powder	123
Figure 4.7: Optical transmission of the GeSe ₄ glass sintered by HUP	124

LIST OF FIGURES - Continued

Figure 4.8: Impurities on the surface of the GeSe ₄ sintered glass.....	125
Figure 4.9: Hot Press used for sintering of the 80GeSe ₂ –20Ga ₂ Se ₃ glass powder, a) global view; b) inside view of the furnace.....	126
Figure 4.10: Thermal treatment applied during sintering of the 80GeSe ₂ –20Ga ₂ Se ₃ glass powder.....	127
Figure 4.11: a) Inhomogeneous 80GeSe ₂ –20Ga ₂ Se ₃ sample obtained by sintering glass powder; b) Crystallized sample; c) SEM micrograph of the inside of a sintered sample	128
Figure 4.12: Transmission graph of a 10mm thick ZnSe window prepared by CVD. Image from Wuhan Sintec Optronics [119].....	129
Figure 4.13: Evolution of the ZnSe powder coloration with milling time.....	130
Figure 4.14: Evolution of the XRD spectra of the ZnSe powder with milling time.....	131
Figure 4.15: Thermal treatment applied during sintering of ZnSe powder	132
Figure 4.16: a) Bulk material obtained; b) and c) SEM micrograph of the material; d) zinc particles observed.....	133
Figure 4.17 : Dr. Sinter 505 Syntex machine.....	135
Figure 4.18: Optical transmission of the GeSe ₄ glass sintered by SPS	136
Figure 4.19: XRD spectra of a glass sintered by SPS with and without use of Ta foil as a diffusion barrier	138
Figure 4.20: a) Visible picture of the glasses of 9mm, 20mm and 36 mm in diameter sintered by SPS ; b) Infrared picture of the same three glasses observed with a 8-12μm thermal camera.....	139
Figure 4.21: Comparison of the optical transmission of glasses sintered by SPS (2 min at 390°C, 50MPa)	140
Figure 4.22: X-Ray microdiffraction patterns of the 36mm diameter sample from the center (a) to the periphery (p)	141
Figure 4.23 Experimental setup	145
Figure 4.24: Pictures of the GeSe ₄ sample obtained by melting of the powder prepared by mechanosynthesis, a) bottow view; b) top view; c) inside view.....	147
Figure 4.25: Optical transmission of the obtained GeSe ₄ sample.....	147
Figure 4.26: Pictures of the Ge ₂₅ Ga ₅ Se ₇₀ sample obtained by melting of the powder prepared by mechanosynthesis, a) bottow view; b) top view; c) inside view.....	149
Figure 4.27: SEM micrographs of the bulk material obtained after melting, a) unmelted powder grains on the surface; b) crystals ; c) unmelted powder grains and crystals ; d) porosity observed	150
Figure 5.1: Free energy of a particle as a function of its radius.....	157

LIST OF FIGURES - Continued

Figure 5.2: Typical representation of nucleation and growth curves.....	158
Figure 5.3: Particle size distribution of the $80\text{GeSe}_2\text{-}20\text{Ga}_2\text{Se}_3$ glass powder used for the SPS experiments	161
Figure 5.4: Optical transmission of the $80\text{GeSe}_2\text{-}20\text{Ga}_2\text{Se}_3$ glass-ceramics obtained after 2 min, 15 min, 30 min and 60 min of SPS treatment at 390°C	162
Figure 5.5: XRD spectra of the initial $80\text{GeSe}_2\text{-}20\text{Ga}_2\text{Se}_3$ glass powder used (80h of milling) and of samples obtained after 2 min, 30 min and 60 min of SPS treatment at 390°C	164
Figure 5.6: SEM images of glass-ceramics obtained from the $80\text{GeSe}_2\text{-}20\text{Ga}_2\text{Se}_3$ base glass powder for SPS treatment time of a) 2 min b) 15 min, c) 30 min, d) 60 min of SPS treatment at 390°C ; e) Ga_2Se_3 and f) GeSe_2 crystals observed under TEM observation on the glass ceramic treated for 60 min at 390°C	165
Figure 5.7: SEM images (x20,000) of the $80\text{GeSe}_2\text{-}20\text{Ga}_2\text{Se}_3$ glass-ceramics etched in "piranha" solution for a) 0 min, b) 5 min, c) 10 min, d) 30 min, e) 60 min, f) 120 min.	170
Figure 5.8: SEM images (x5,000) of the $80\text{GeSe}_2\text{-}20\text{Ga}_2\text{Se}_3$ glass-ceramics etched in "piranha" solution for a) 60 min and b) 120 min	171
Figure 5.9: Evolution of the thickness of the $80\text{GeSe}_2\text{-}20\text{Ga}_2\text{Se}_3$ glass-ceramic pellets as a function of etching duration in a "piranha" solution.....	172
Figure 5.10: SEM observation of the cross section of the $80\text{GeSe}_2\text{-}20\text{Ga}_2\text{Se}_3$ glass-ceramics etched in a "piranha" solution for a,b) 5 min, c,d) 10 min, e,f) 30 min and g,h) 60 min	173
Figure 5.11: Optical transmission of the $80\text{GeSe}_2\text{-}20\text{Ga}_2\text{Se}_3$ glass-ceramics as a function of etching duration in a "piranha" solution	174
Figure 5.12 : Absorbance spectrum of $80\text{GeSe}_2\text{-}20\text{Ga}_2\text{Se}_3$ glass-ceramics functionalized with APTS.....	180
Figure 5.13: Configurations used for etching of $80\text{GeSe}_2\text{-}20\text{Ga}_2\text{Se}_3$ glass-ceramics in a "piranha" solution, a) without agitation, b) with agitation system.....	181
Figure 5.14: $80\text{GeSe}_2\text{-}20\text{Ga}_2\text{Se}_3$ glass-ceramics after a) 2 h and b) 20 h of etching in a "piranha" solution with no agitation system, c) white layer observed on the surface	182
Figure 5.15: a,b) canals, c) pores observed on the glass-ceramics after 20h of etching in a NaOH 0.1M solution; d) remaining crystals observed in the canals	183
Figure 5.16: $\text{GeSe}_2\text{-Ga}_2\text{Se}_3\text{-In}_2\text{Se}_3$ glassy domain	187
Figure 5.17: Evolution of the thermal properties of the $80\text{GeSe}_2\text{-(}20\text{-x)}\text{Ga}_2\text{Se}_3\text{-(x)}\text{In}_2\text{Se}_3$ as a function of x.....	188
Figure 5.18: Evolution of the optical band gap wavelength and density of the $80\text{GeSe}_2\text{-(}20\text{-x)}\text{Ga}_2\text{Se}_3\text{-(x)}\text{In}_2\text{Se}_3$ as a function of x	189

LIST OF FIGURES - Continued

Figure 5.19: GeSe ₂ -Ga ₂ Se ₃ -PbSe glassy domain.....	190
Figure 5.20: Evolution of the thermal properties of the (100-x)(80GeSe ₂ -20Ga ₂ Se ₃), xPbSe glasses as a function of x	192
Figure 5.21: Evolution of the optical cut-band gap wavelength and density of the (100- x)(80GeSe ₂ -20Ga ₂ Se ₃), xPbSe glasses as a function of x	193
Figure 5.22: XRD spectra of In1 glass-ceramics	195
Figure 5.23: Optical transmission of the In1 glass-ceramics heat treated at 386°C for different durations	196
Figure 5.24: SEM images of the In1 glass-ceramic heat-treated for 29 h at 386°C (T _g +30°C)	197
Figure 6.1: The Dieke diagram	203
Figure 6.2: Experimental setup	207
Figure 6.3: Raman spectrum of the 80GeSe ₂ -20Ga ₂ Se ₃ glass	208
Figure 6.4: DSC curve of the 80GeSe ₂ -20Ga ₂ Se ₃ + 0.1 %Er bulk glass	210
Figure 6.5: XRD spectra the 80GeSe ₂ -20Ga ₂ Se ₃ + 0.1% Er glass and glass-ceramics heat treated at 380°C for increasing time durations.	211
Figure 6.6: XRD spectra the 80GeSe ₂ -20Ga ₂ Se ₃ + 0.1% Nd glass and glass-ceramics heat treated at 380°C for increasing time durations.	211
Figure 6.7: SEM micrographs (x20,000) of the 80GeSe ₂ -20Ga ₂ Se ₃ + 0.1% Er composition after a) 0h, b) 10h, c) 20h, d) 50h and e) 80h of heat treatment at 380°C .	212
Figure 6.8: SEM micrographs (x20,000) of the 80GeSe ₂ -20Ga ₂ Se ₃ + 0.1% Nd composition after a) 0h, b) 10h, c) 20h, d) 50h and e) 80h of heat treatment at 380°C .	213
Figure 6.9: Optical transmission of the 80GeSe ₂ -20Ga ₂ Se ₃ + 0.1% Er glass and glass- ceramics	214
Figure 6.10: Optical transmission of the 80GeSe ₂ -20Ga ₂ Se ₃ + 0.1% Nd glass and glass- ceramics	215
Figure 6.11: Emission spectrum of the 80GeSe ₂ -20Ga ₂ Se ₃ + 0.1% Er glass and glass- ceramics	216
Figure 6.12: Energy diagram of the 80GeSe ₂ -20Ga ₂ Se ₃ + 0.1% Er glass	217
Figure 6.13: Emission spectrum of the 80GeSe ₂ -20Ga ₂ Se ₃ + 0.1% Nd glass and glass- ceramics	218
Figure 6.14: Energy diagram of the 80GeSe ₂ -20Ga ₂ Se ₃ + 0.1% Nd glass	219
Figure 6.15: Decay curve measured on Er-doped 80GeSe ₂ -20Ga ₂ Se ₃ glass-ceramics ..	220
Figure 6.16: Decay curve measured on Nd-doped 80GeSe ₂ -20Ga ₂ Se ₃ glass-ceramics .	223

LIST OF TABLES

Table 2.1: Optical and thermal properties of some materials used for thermal imaging lenses	46
Table 3.1: Position of characteristic absorption bands in the infrared region	71
Table 3.2: Melting and boiling temperatures of the elements commonly used to prepare chalcogenide glasses	78
Table 3.3: Thermal properties of the $\text{Ge}_{25}\text{Ga}_5\text{Se}_{70}$ glass before and after melting/casting process.....	85
Table 3.4: Electron Dispersive X-Ray Spectroscopy analysis of the obtained material ..	93
Table 3.5: Hardness of some commercially available materials used as milling elements	100
Table 3.6: Characteristic temperatures of the $80\text{GeSe}_2\text{-}20\text{Ga}_2\text{Se}_3$ powder obtained and of a $80\text{GeSe}_2\text{-}20\text{Ga}_2\text{Se}_3$ glass prepared in sealed silica tube.....	111
Table 5.1: Mechanical properties of the glass-ceramics obtained after SPS treatment and of a $80\text{GeSe}_2\text{-}20\text{Ga}_2\text{Se}_3$ glass prepared in sealed silica tube	166
Table 5.2: Surface area of the $80\text{GeSe}_2\text{-}20\text{Ga}_2\text{Se}_3$ base glass, the glass-ceramic before etching and after 10 min of treatment in a “piranha” solution.....	177
Table 5.3: Mechanical properties of the In1 glass-ceramics.....	194
Table 6.1: The number of 4f valence electrons in trivalent rare earth ions	202
Table 6.2: Some emissions reported in the near- and mid-infrared regions for RE-doped chalcogenide glasses	206
Table 6.3: Origin and purity of the elements used for the study.....	208
Table 6.4: Lifetimes calculated for the Er-doped $80\text{GeSe}_2\text{-}20\text{Ga}_2\text{Se}_3$ glass-ceramics as a function of ceramization time	221
Table 6.5: Lifetimes calculated for the Nd-doped $80\text{GeSe}_2\text{-}20\text{Ga}_2\text{Se}_3$ glass-ceramics as a function of ceramization time	223

ABSTRACT

Chalcogenide glasses and glass-ceramics present a high interest for the production of thermal imaging lenses transparent in the 3-5 μm and 8-12 μm windows. However, chalcogenide glasses are conventionally synthesized in sealed silica ampoules which have two major drawbacks. First, the low thermal conductivity of silica limits the sample dimensions and second the silica tubes employed are single use and expensive, and represent up to 30% of the final cost of the material. The present work therefore addresses the development of innovative synthesis methods for chalcogenide glass and glass-ceramics that can present an alternative to the silica tube route.

The first synthesis method investigated involves melting the raw starting elements in reusable silica containers. This method is suitable for the synthesis of stable chalcogenide glasses compositions such as GeSe_4 but uncontrolled crystallization and homogenization problems are experienced for less stable compositions.

The second approach involves preparation of amorphous chalcogenide powders by ball milling of raw elements. This mechanosynthesis step is followed by consolidation of the resulting powders to produce bulk glasses. Hot Uniaxial Pressing is suitable for compositions stable against crystallization. However, uncontrolled crystallization occurs for the unstable $80\text{GeSe}_2\text{-}20\text{Ga}_2\text{Se}_3$ glass composition. In contrast consolidation through Spark Plasma Sintering (SPS) allows production of bulk glasses in a short duration at relatively low temperatures and is appropriate for the synthesis of unstable glasses. A sintering stage of only 2 min at 390°C is shown to be sufficient to obtain infrared

transparent $80\text{GeSe}_2\text{-}20\text{Ga}_2\text{Se}_3$ bulk glasses. This method enables the production of lenses with a 4-fold increase in diameter in comparison to those obtained by melt/quenching technique. Moreover, increasing the SPS treatment duration yielded infrared transparent glass-ceramics with enhanced mechanical properties. This innovative synthesis method combining mechanosynthesis and SPS has been patented in the framework of this study.

The controlled etching of $80\text{GeSe}_2\text{-}20\text{Ga}_2\text{Se}_3$ glass-ceramics in acid solution yields nanoporous materials with enhanced surface area. The porous layer created on the surface of the glass-ceramic is shown to play the role of anti-reflection coating and increase the optical transmission in the infrared range by up to 10%. These materials may have potential for the production of sensors with increased sensitivity in the infrared.

The influence of indium and lead addition on the thermal and optical properties of the $80\text{GeSe}_2\text{-}20\text{Ga}_2\text{Se}_3$ glass has also been assessed. Increased In or Pb contents tend to decrease the T_g of the glasses and shift the optical band gap toward higher wavelengths. A systematic ceramization study emphasizes the difficulty of controlling the crystallization for glasses in the systems $\text{GeSe}_2\text{-Ga}_2\text{Se}_3\text{-In}_2\text{Se}_3$ and $\text{GeSe}_2\text{-Ga}_2\text{Se}_3\text{-PbSe}$. No crystallization of the In_2Se_3 and PbSe crystalline phase was obtained.

Finally, the possibility of producing rare-earth doped $80\text{GeSe}_2\text{-}20\text{Ga}_2\text{Se}_3$ glass-ceramics transparent in the infrared region up to $16\text{ }\mu\text{m}$ is demonstrated. Enhanced photoluminescence intensity and reduced radiative lifetimes are observed with increased crystallinity in these materials.

CHAPTER 1: INTRODUCTION

Thermal imaging devices were first developed in the 1940s for military applications, motivated by the need to detect objects in dark conditions. Thermal cameras are based on the detection of the thermal radiation emitted by hot bodies in the second and third atmospheric windows located in the 3-5 μm and 8-12 μm wavelength range, respectively. Notably, bodies near room temperature such as human bodies emit a maximum of radiation around 10 μm , emphasizing the need for materials transparent in the 8-12 μm range.

Since the 1940s, the improvement and miniaturization of detectors, electronics and computing systems has led to shrinkage of infrared cameras as well as to improvement in resolutions and cost reductions of the thermal cameras. Consequently, thermal imaging has reached the industrial market for maintenance and process control applications, firefighting, surveillance or medical applications, and is now expanding to civilian applications such as driver's vision enhancement devices which represent its fastest growing market. This application is currently reserved to up-market cars, but the progressive decrease in the cost of thermal cameras is expected to extend driver's vision enhancement devices to lower price cars.

Among all the components of thermal imaging cameras, optical lenses still represent an important part of the final cost of the devices. Currently, the lenses which need to be transparent in the second and third atmospheric windows are predominantly made of single-crystalline germanium or polycrystalline zinc selenide. These materials

are expensive and need costly grinding and polishing processes to be shaped. Thus, development of materials intrinsically cheaper and easier to shape is important in the perspective of cost reduction of thermal imaging devices.

Glasses are a category of material combining optical transparency, ease of shaping by molding and low production costs. For these reasons, they are employed in multiple forms in our everyday life, such as decorative objects, windows, drinking vessels, cookware, light bulbs, displays, optical fibers or as construction material in architecture. By definition, glasses are amorphous (non-crystalline) solid materials that exhibit a glass transition. Their composition dictates their properties and thus their applications. Notably, three families of optical glasses are distinguished: oxide, fluoride and chalcogenide. Due to their high transparency in the visible region and extremely low intrinsic optical losses, oxide glasses are by far the most produced and employed glasses. However, their optical transmission is limited to $4\text{ }\mu\text{m}$ in the infrared range, making them inadequate for production of thermal imaging optics. Fluoride glasses possess a wider domain of transparency than oxide glasses, but their transmission is limited to $7\text{ }\mu\text{m}$. Consequently, their use as infrared optics is also limited. However, these glasses have low phonon energies and very high rare earth solubility, making them good materials for optical amplification and laser sources.

Chalcogenide glasses are a family of glasses containing at least one of the chalcogen elements (sulfur, selenium or tellurium), but no oxygen. The extended optical transmission of chalcogenide glasses in the infrared range offers a wide range of potential applications such as biological and chemical sensing, non-linear optics, or optical fibers.

Notably, selenium-based glasses transmit in the second (3-5 μm) and third (8-12 μm) atmospheric windows. Their lower cost as compared to germanium or zinc selenide, and their ease to be shaped by molding represent major advantages for the production of infrared optic and some selenium-based glasses are currently used for equipping low-cost thermal cameras. However, mechanical properties are known to be the weak point of chalcogenide glasses and limit their use. Moreover, chalcogenide glasses are highly sensitive to contamination by oxygen and their synthesis process is generally carried out in sealed silica ampoules. The silica tubes utilized are single use as they have to be broken at the end of the synthesis process to extract the chalcogenide glass and they can represent up to 30% of the final cost of the material.

Over the past decades, studies have shown that the controlled development of a crystalline phase within the glassy matrix allows production of glass-ceramics with enhanced mechanical properties while keeping a good transparency. Notably the interesting potential of the $80\text{GeSe}_2\text{-}20\text{Ga}_2\text{Se}_3$ glass-ceramics for production of thermal imaging optics has been demonstrated in recent studies.

The objective of this PhD work is to develop new methods for the synthesis of chalcogenide glasses and glass-ceramics without use of silica tubes and thus to reduce their production costs and increase the attractiveness of these materials for low-cost thermal imaging devices and other applications in the infrared region.

In the second chapter of this dissertation, the basic principles governing thermal imaging will be described and the main components of thermal imaging devices will be presented. The materials currently used for infrared optics as well as their major

advantages and drawbacks will be detailed. Notably, the interesting potential of chalcogenide glasses and glass-ceramics for this application will be emphasized.

In the third chapter, different synthesis methods will be studied. The first one involves melt/quenching technique in reusable silica containers while the second method involves mechanosynthesis by mechanical milling of the elements to produce amorphous powders. The production of infrared transparent bulk glasses from the powders prepared by mechanosynthesis will be presented in chapter 4. Three consolidation processes will be considered: melting, Hot Uniaxial Pressing and Spark Plasma Sintering.

In chapter 5, the production of chalcogenide glass-ceramics by combining mechanosynthesis and Spark Plasma Sintering will be presented. New applications for the $80\text{GeSe}_2\text{-}20\text{Ga}_2\text{Se}_3$ glass-ceramics will also be explored. The production of nanoporous materials for biosensing applications by chemical etching of glass-ceramics will be described. Finally, the effect of the addition of indium and lead on the $80\text{GeSe}_2\text{-}20\text{Ga}_2\text{Se}_3$ glass properties will be investigated for the development of new glass-ceramic families. A systematic ceramization study will be realized to assess the potential of these materials for glass-ceramic production.

Chapter 6 addresses the use of glass-ceramics for photoluminescent applications. Selenium-based glass-ceramics will be doped with rare-earth elements and the effect of crystallinity on photoluminescence intensity and radiative lifetime of erbium- and neodymium-doped $80\text{GeSe}_2\text{-}20\text{Ga}_2\text{Se}_3$ glass-ceramics will be presented.

CHAPTER 2: THERMAL IMAGING

2.1. Introduction

Thermal imaging is a technique that is currently used for numerous applications. Based on the detection of infrared radiations emitted by bodies at temperatures above absolute zero, this technique was first reserved to military applications, but is now encountered in many industrial and civil applications. In this chapter, we will first describe the development of thermal imaging and its applications. After defining the infrared region of the electromagnetic spectrum, the laws governing thermal radiations will be detailed. Subsequently, the main component parts of thermal imagers (or thermal cameras) will be outlined. One of the practical motivations for the work performed during this PhD was the reduction of the production costs of infrared optical elements and in particular to identify low-cost routes for the synthesis of chalcogenide glasses and glass-ceramics for use as infrared lenses. Thus, special attention will be paid to materials currently used for thermal imaging optical systems in the last part of this chapter.

2.1.1. Development of thermal imaging

Thermal imaging devices were first developed in the 1940s by the US Army, motivated by the need to detect objects in dark conditions. Infrared radiations are emitted by all bodies above absolute zero according to the black body radiation law and thermal imaging devices make it possible to detect them with or without visible illumination.

Thermal imaging has to be differentiated from image intensification performed by devices which although cheaper and smaller in volume, only magnify existing light and are unable to see through smoke and haze, thus providing limited applications.

The frequency and amount of radiation emitted by an object increases with temperature. Therefore, variations in temperatures can be monitored by thermal cameras and warm objects can be differentiated from a cooler background. Thermal cameras provide a non-contact and non-destructive way to collect and visualize temperatures maps over large areas. It can thus be operated to monitor temperatures in hazardous areas or inaccessible to other methods. Furthermore, thermal cameras exhibit fast operation and are capable of monitoring moving target in real time.

Early thermal cameras were large in size thus difficult to handle, and their price ranged in the order of tens of thousands of US dollars due to the high costs of their different parts, and in particular of the infrared lenses. To this day, the major drawback of thermal imaging devices remain their high production cost, however, over the past decade, thermal cameras have dropped in size, weight, power consumption and cost [1]. The improvement and miniaturization of detectors, electronics and computing systems has led to the shrinkage of infrared cameras as well as to improvement in resolutions. Therefore, thermal cameras are not anymore reserved to military use and numerous applications have reached the civil domain. The evolution of the sales of thermal cameras in the world ranked by applications between 2005 and 2009, and the sales forecasts up to 2011 is presented in figure 2.1. As the prices keep decreasing, the amount of global sales increases. This emphasizes the need for low-cost thermal cameras.

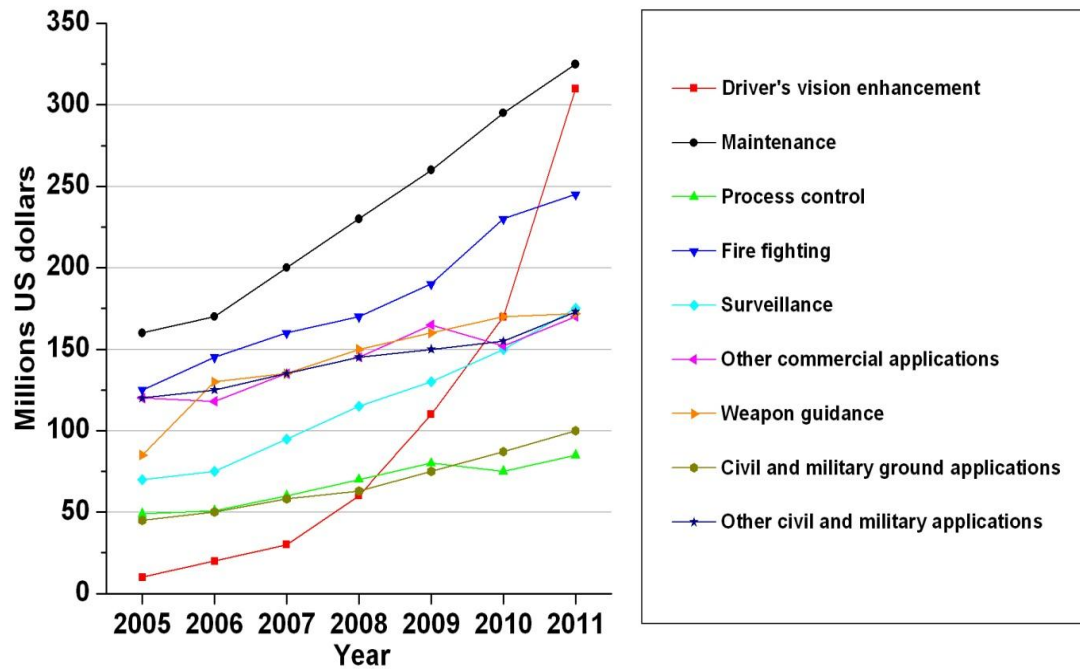


Figure 2.1: Evolution of the sales of thermal cameras in the world ranked by applications between 2005 and 2009, and the sales forecasts up to 2011 (Dadas provided by Umicore IR Glass)

2.1.2. Applications

As mentioned previously, the first applications of thermal cameras were in the military domain for surveillance, night vision and weapon guidance. Following cost reduction, the thermal imaging market has extended to industrial applications, and is now expanding to broader consumer markets. The main applications of thermal imaging are described below.

Industrial maintenance widely uses thermal cameras to find deteriorating, i.e. overheating components before their failure or to find defects in shafts, pipes and other metallic or plastic parts. Thermal imaging is also used to check heat loss in houses caused by air infiltrations through junctions between roofs and walls, as illustrated in figure 2.2.



Figure 2.1: Thermal isolation of an habitation monitored by thermal imaging

After the September 11, 2001, attacks, the need for devices enhancing vision through smoke and locating bodies was recognized as a high priority for firefighting and rescue applications. Thermal cameras have proven to be an excellent tool and more and more firefighters are equipped with such thermal imagers. The decreasing costs and the miniaturization of the equipments favor the development of this market. Imagers used for firefighting and rescue applications are of special design and construction. They have to withstand harsh environmental conditions and need to be light and at the same time robust. They can be either handheld or helmet mounted in order to free the hands of the firefighters.

Another application involves driver's vision enhancement which is one of the fastest growing markets for thermal cameras. Thermal imaging devices are located in the front bumpers of cars and produce a thermal image which is retransmitted on the dashboard as shown in figure 2.3 on a BMW Class 5 car [2]. This device increases driver's detection range to more than 300 meters, gaining over 7 seconds additional time

at an average speed of 100 Km per hour [3]. Driver's detection range is limited to 150 meters in dark conditions without these devices.

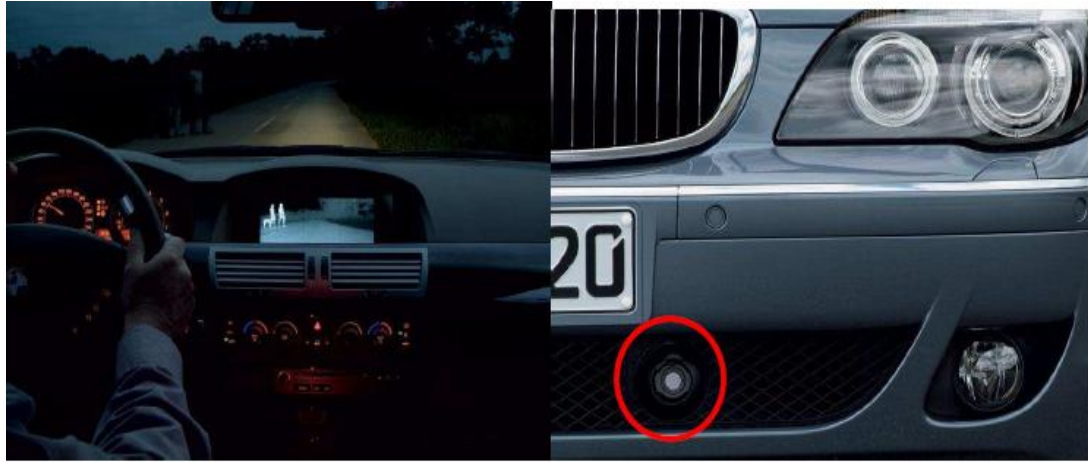


Figure 2.2: Driver's vision enhancement system on a BMW Class 5 vehicle

The motivation for developing this product results from the fact that while 75% of car traffic happens during the day, 50% of the deadly accidents happen at night. It has been proven that 50% of the accidents are due to a lack of attention and to a lack of visibility of the drivers. Thus, the need for driver's vision enhancement systems clearly appears [4]. This system is currently reserved to up-market cars, but the decreasing cost of thermal cameras tends to extend driver's vision enhancement devices to lower range cars.

Another growing area for thermal cameras involves the medical field. The non-destructive nature of thermal imaging and the progress in thermal resolution (ability to differentiate small variations in temperatures) of detectors make this technique more and more used for medical applications, such as detection of breast cancer [5], inflammations or vascular problems [6]. In fact, anomalies in human body result in local changes in temperatures that can be detected in a non-intrusive way using thermal cameras.

Notably, airports were fitted with thermal cameras during the SARS epidemic to detect incoming passengers who had a high fever and might have been infected with the virus [7]. Other notable applications involving thermal imaging include safety assessment and food quality [8], volcanology, or unconventional applications such as anxiety detection [9] or lie detection [10].

2.2. The principles of thermal imaging

2.2.1. The Infrared region of the electromagnetic spectrum

Following the wave-particle duality, light can either be described as a particle (photon) or an electromagnetic wave. An electromagnetic wave results from the oscillation of an electric and magnetic field having a velocity of propagation equal to the speed of light in vacuum. It is characterized by its wavelength λ or its frequency ν .

Photons are particles carrying a quantity of energy defined by the light wavelength λ according to the relation:

$$E = \frac{hc}{\lambda} \quad \text{and} \quad \nu = \frac{c}{\lambda}$$

with: h: Planck's constant (6.63×10^{-34} J.s)

c: speed of light in vacuum ($299,792,458 \text{ m.s}^{-1}$)

Depending on the phenomenon observed, either the wave nature or the particle nature of the light is used to describe optical effect. This represents a fundamental principle of quantum mechanics.

The whole range of radiations of wavelengths λ is called the electromagnetic spectrum. It is divided in several regions, as shown on figure 2.4. The infrared (IR) region comprises wavelengths ranging from $\sim 0.74 \mu\text{m}$ to $1000 \mu\text{m}$. It is located between the low-energy radio wavelengths and the visible range. The visible range corresponds to the wavelengths to which human eyes are sensitive. Therefore, infrared radiations cannot be directly seen by humans and special devices have to be employed to observe them. The IR region is usually divided in subdomains:

- NIR: Near Infrared
- SWIR: Short-Wave Infrared
- MWIR: Mid-Wave Infrared
- LWIR: Long-Wave Infrared
- VLWIR: Very Long-Wave Infrared

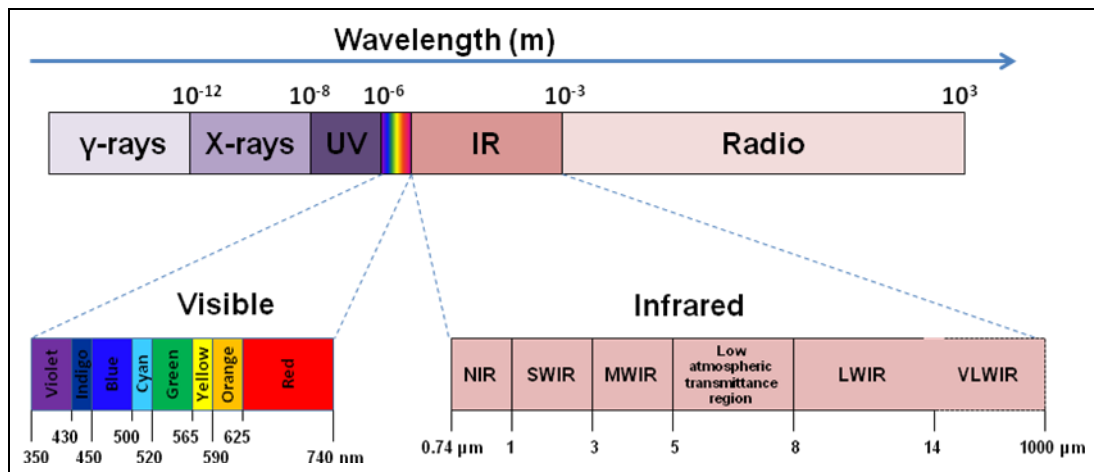


Figure 2.3: The electromagnetic spectrum

2.2.2. Thermal radiations

All matter emits electromagnetic radiations when it has a temperature above absolute zero (0K or -273.15°C). These radiations result from the thermal motion of

charged particles (ions, electrons, nuclei) and are thus called thermal radiations. They represent a conversion of thermal energy into electromagnetic energy. The wavelengths corresponding to thermal radiations range from 0.1 μm and 100 μm . Therefore, they fall in the visible and the IR regions of the electromagnetic spectrum. Examples of thermal radiation include the visible light emitted by an incandescent light bulb or by the surface of the Sun.

2.2.3. Laws of thermal radiation

2.2.3.1. Black bodies and Planck's law

For a given wavelength and temperature, the quantity of radiation emitted by a body is limited. A surface attaining this limit is called a black body. A black body can be described as an ideal solid absorbing all incident radiations, regardless of direction and wavelength, and reemitting the corresponding energy with 100% efficiency according to Planck's law [11, 12]. The maximum radiation energy than can be emitted by a body at a given wavelength is a function of its temperature and its surface emissivity for that particular wavelength. Planck's Law defines the spectral distribution of the monochromatic luminescence energy (or radiance) of a black body as a function of its temperature.

The monochromatic luminescence energy L of a body represents the flow of energy emitted at a given wavelength and in a given direction per apparent unit surface area of this body. It is spatially and angularly uniform and only depends on the

wavelength and the temperature of the body. It is expressed in $\text{W.m}^{-2}.\text{sr}^{-1}.\text{m}^{-1}$ (S.I. units) and is defined by the following relation:

$$\left(\frac{dL}{d\lambda}\right)_T = \frac{2hc_\lambda^2}{\lambda^5} \frac{1}{\exp\left(\frac{hc_\lambda}{k_B\lambda T}\right) - 1}$$

with: h : Planck's constant ($6.63 \times 10^{-34} \text{ J.s}$)

k_B : Boltzmann constant ($1.38 \times 10^{-23} \text{ J.s}^{-1}$)

$c_\lambda = c/n_\lambda$: velocity of the electromagnetic radiation in a propagation media of refractive index n_λ at the wavelength λ ($c = 299,792,458 \text{ m.s}^{-1}$ for electronic radiation in vacuum)

λ : wavelength (in meters)

T : temperature at the surface of the black body

2.2.3.2. Wien's displacement law

Wien's displacement law states that the wavelength distribution of thermal radiation from a black body at any temperature has essentially the same shape as the distribution at any other temperature, except that each wavelength is displaced on the graph. Figure 2.5 shows the monochromatic luminescence energy of a black body as a function of its temperature calculated from Planck's law. At a given temperature, the maximal monochromatic luminescence energy is given by Wien's displacement law:

$$\lambda_{max} = \frac{hc_\lambda}{4.9651 k_B T}$$

Thus, the wavelength corresponding to the maximal monochromatic luminescence energy is inversely proportional to the temperature. This maximal luminescence is shifted toward shorter wavelengths for bodies at higher temperatures.

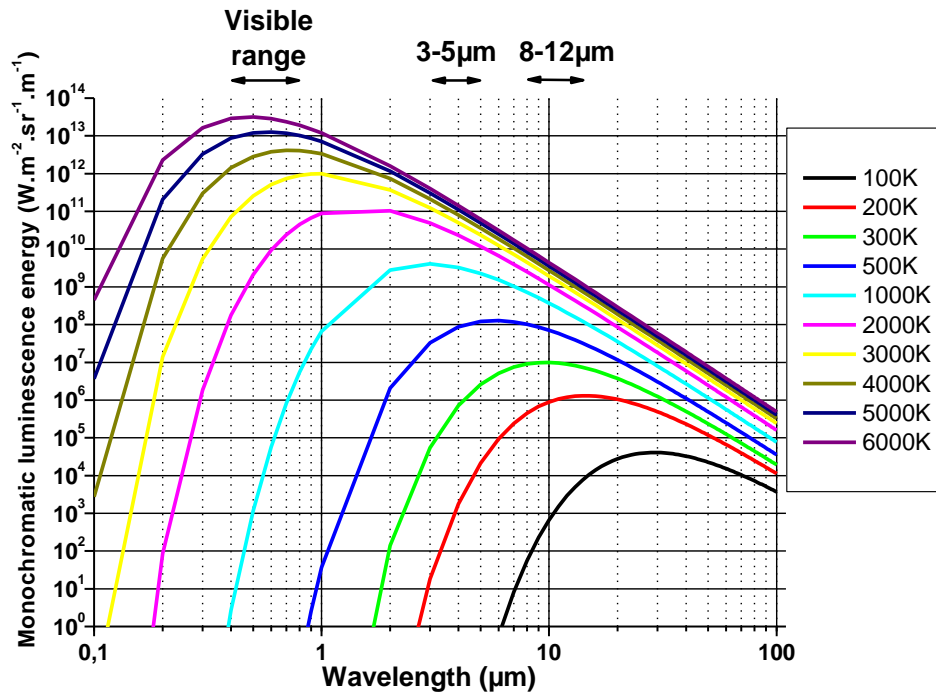


Figure 2.4: Monochromatic luminescence energy of a black body as a function of its temperature

From figure 2.5, it clearly appears that bodies with temperatures of about 3000K, such as a lamp filament, or 6000K such as the surface of the Sun, have their maximum radiations in the visible region. These radiations fall into the human eye sensitivity range and correspond to “visible light”. The monochromatic luminescence energy of black bodies at room temperature (about 300K) does not fall in visible range of the electromagnetic spectrum and are thus out of reach of human eyes. We can therefore only see them by reflection if they are illuminated by an external visible source such as the sun. However, they emit radiations in the 3-5 μm and 8-14 μm windows.

2.2.3.3. Stefan-Boltzmann law

The mathematical integration of Planck's law yields Stefan-Boltzmann law. It states that the total energy radiated per unit surface area of a black body (P , in W.m^{-2}) is directly related to its temperature, as described by the following equation:

$$P = \sigma T^4$$

where σ is the Stefan's constant ($5.67 \times 10^{-8} \text{ W.m}^{-2}.\text{K}^{-4}$) and T is the temperature of the black body (in K).

Thus, the total energy radiated (or emissive power) is only dependant on the temperature of the black body. The fourth power emphasizes the strong dependence of emissive power to temperature. Knowing the energy radiated by a body allows the evaluation of its temperature, without the need for direct contact with this body.

2.2.3.4. Real bodies and emissivity

As described previously, a black body is an ideal body absorbing all incident radiations and presenting no loss by reflection or transmission of the radiation flux. Therefore, a black body in thermal equilibrium radiates a thermal flux equal to the incident energy reaching its surface.

However, real bodies do not absorb 100% of the incident energy. Some of the incident energy is reflected at the body surface, some is absorbed by the body and some is transmitted through the body. Thus the incident radiation is equal to:

$$R_I = R_R + R_A + R_T$$

where R_I is the incident radiation, R_R is the reflected radiation, R_A is the absorbed radiation and R_T is the transmitted radiation.

Therefore, a reflection coefficient R , a transmission coefficient T and an absorption coefficient A can be defined for a real body subject to a radiation. These three coefficients depend on the wavelength of the incident radiation. In accordance with the law of conservation of energy, the following equation can be written:

$$R(\lambda) + T(\lambda) + A(\lambda) = 1$$

As a result, a body cannot reemit all the energy it receives, and the thermal radiation emitted is referenced to the thermal radiation of a black body at the same temperature. For each wavelength λ and at a given temperature, the monochromatic luminescence energy of a real body (X) is proportional to the one of a black body (BB) at the same temperature and to its absorption coefficient, according to Kirchhoff's law:

$$\left[\frac{dL}{d\lambda} \right]_X^T = A(\lambda) \cdot \left[\frac{dL}{d\lambda} \right]_{BB}^T$$

The thermal radiation of a body being proportional to its spectral absorption factor, the later is also called spectral emissivity factor. The spectral emissivity, noted $\varepsilon(\lambda)$ with $\varepsilon(\lambda)=A(\lambda)$, is not a constant, as it depends on the wavelength and the temperature of the body, but also on the direction to which the body is observed and on the surface conditions. The variations in $\varepsilon(\lambda)$ can be important in regard to the direction of observation.

2.2.4. Atmospheric transmission

Thermal radiations are attenuated in passage through terrestrial atmosphere by the processes of absorption and of scattering by gas molecules, molecular clusters, rain, snow, and suspensions such as smoke, haze and smog. Water vapor (H_2O), carbon dioxide (CO_2) and ozone (O_3) are the most significant absorbers. Figure 2.6 illustrates the atmospheric transparency spectrum in the visible and IR regions.

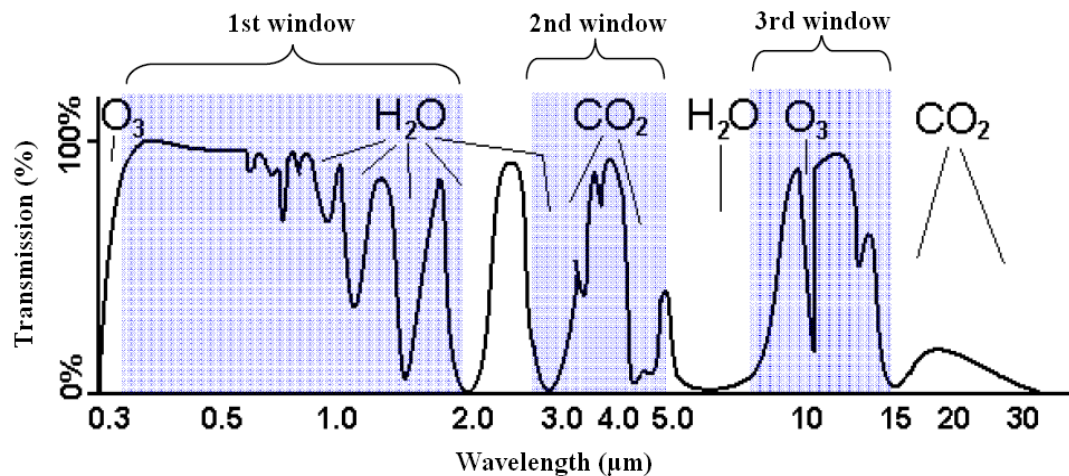


Figure 2.5: Atmospheric transmission spectrum

From this illustration, three windows where the energy is transmitted well are identified. The first window extending from 0.4 μm to 2 μm corresponds to the visible region and a part of the near-IR region. The two other transparency windows are located in the IR, from 3 μm to 5 μm and from 8 μm to 14 μm for the second and third windows, respectively. The third window is sometimes referred as “thermal window” since the peak of emitted radiation from a body at room temperature (about 300K) occurs in this window, while the second window is sometimes referred as the “hot window” since

heated objects emit at shorter wavelengths in this range [13]. Thermal imaging devices work in these two windows.

2.3. Thermal imagers and their component parts

2.3.1. A basic thermal imager

A basic thermal imager, illustrated schematically in figure 2.7 is composed of the main following parts [14]:

- An optical system that form an image of an external scene using radiation in the thermal wavelength range
- A detection system that converts this radiation into electrical signals proportional to the incident radiation received
- An electronic processor that can process the detector outputs and convert them into a video signal
- A display unit that generates a visual image from the video signal

Various configurations are available and result in different performances in term of resolution and sensitivity to temperature differences. As part of this study on chalcogenide glasses for infrared optics, specific attention will be given to optical systems and more specifically to infrared lens systems. Detection systems will be briefly described. No further details will be given on electronic processors and displays. Detailed reviews concerning these components can be found elsewhere [14].

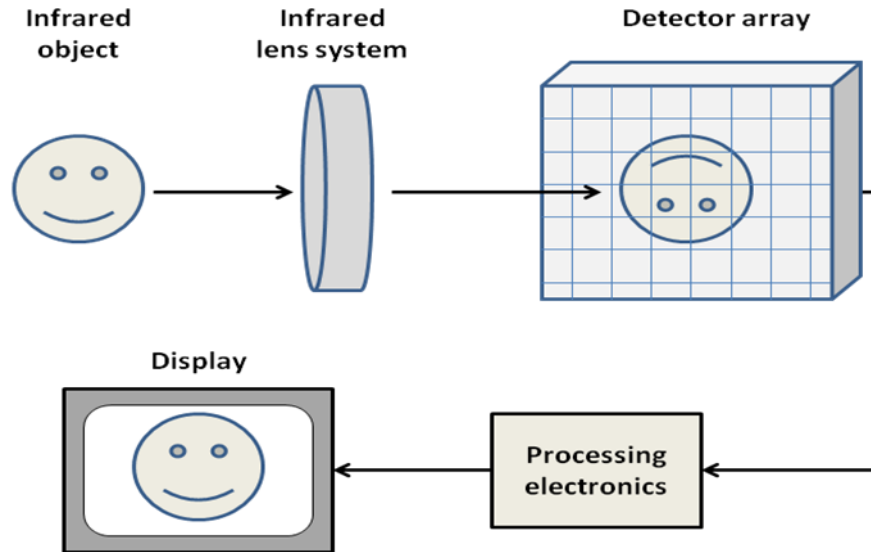


Figure 2.6: Schematic of a basic thermal imager

2.3.2. Detection systems

The detection system determines the potential level of thermal and spatial resolution that can be achieved by the thermal imager. Based on the principles used for thermal radiation detection, detectors can be classified into two main categories: thermal detectors and quantum detectors (photon detectors). In general, photon detectors provide greater sensitivity than thermal detectors but need the use of a cooling system to be operated, increasing the cost of the detection system. For that reason, photon detectors are sometimes referred as cooled detectors while thermal detectors are referred as uncooled detectors. It is worth noting that cooling systems are a major factor influencing both the design and application of thermal imagers. Recently, the development of uncooled focal plan array detector (FPA) has led to a major breakthrough in cost reduction for thermal cameras [15].

2.3.2.1. Thermal detectors

All matter at a temperature above absolute zero emits radiations in the IR. In the same manner, all matter receiving infrared radiations undergoes an increase in temperature. The resulting temperature rise triggers some change in physical properties that is used as a measure of the radiation incident on the detector. The physical properties involved define a classification amongst thermal detectors. The most commonly used thermal detectors are described below:

- Resistive bolometer arrays: monitors the change in electrical resistance with temperature. These detectors are usually made of vanadium oxides (V_2O_2 , V_2O_3 , V_3O_5 , V_4O_7 , V_5O_9) or amorphous silica.
- Ferroelectric/pyroelectric arrays: similar in construction to resistive bolometer arrays, but the detection is based on using pyroelectric (generation of a voltage with variations in temperature) or ferroelectric (changes in electric polarization with temperature) effect.
- Bimetallic cantilever arrays: a very fine bimetallic strip bends as its temperature changes. The degree of bending is a measure of its temperature and can be detected by measuring the capacitance between the end of the strip and the base wafer on which it is supported.

For accurate measurements, thermal detectors need a stable reference in temperature. In general, this reference is close to room temperature (25°C).

2.3.2.2. Quantum detectors

The signal is generated by the direct absorption of photons by electrons. These interactions induce changes in energy states of electrons in the detector material. Quantum detectors usually operate either as photoconductors (the incident radiation changes the electrical conductivity of the detector element) or as photovoltaic devices (the radiation generates a voltage across a p-n junction). These detectors are mainly semiconductors with suitable doping to achieve the desired characteristics. The choice of the material depends on the wavelength range of interest for detection. Thus, for thermal imagers working in the 3-5 μm window, indium-antimony (InSb) or platinum silicide (PtSi) are commonly used. Mercury-cadmium-tellurium (MCT) or quantum well devices (QWP) are used for the 8-14 μm window. As mentioned previously, quantum detectors need to be cooled in order for electron to populate the low quantum energy levels where they can have the desired interaction with the incident photons.

It is worth noting that the performance of the detectors is often limited in the third atmospheric window (8-14 μm). In general, their response does not extend farther than 12 μm . For this reason, thermal imagers working in this wavelength band are referred as thermal imagers for the 8-12 μm band.

2.3.3. Image-forming optical systems

2.3.3.1. Important factors to consider

The optical systems comprise the lenses or reflectors required to collect and focus incident radiations on the detectors. Optical systems used in thermal imagers are designed and function in the same way as optical systems for visible wavelengths. However, a major difference resides in the materials used for thermal wavelengths. In fact, materials used for visible wavelengths are generally not transparent to thermal radiations. This transparency is the key factor for the choice of the material constituting the image-forming optical system. Different materials are used for optical systems working at thermal wavelengths. Each material has a specific range of wavelength in which it can be operated, thus materials used in the 3-5 μm band may differ from materials used in the 8-12 μm band. The choice of the lens material has a direct impact on the design of a thermal imager (number of lenses, focal lens, correction systems...). The aim of thermal imager designers is to tend to the miniaturization of the devices.

Besides high mechanical properties required to ensure the use of the lens without fracture, several optical factors have to be considered. One of the most important parameter is the refractive index. In general, materials used for thermal imaging lenses have relatively high refractive indices, inducing high reflectivity on their surface. On the other hand, this allows achieving a high degree of optical correction with fewer elements than would be required in the case of a visible optical system.

2.3.3.2. Reflectivity and anti-reflection coatings

Radiations incident upon the surface of an infrared optical material are separated into reflected, transmitted, absorbed and scattered fractions. Refractive indices, absorption, homogeneity and perfection of the surfaces of the material determine the fraction of available energy distributed amongst these phenomena. Depositing interference coatings is found to be useful in altering and controlling the fraction of energy reflected and transmitted on both surfaces of the components. The fraction of energy reflected at an air/material interface is dependent on the wavelength of the incident radiation and is defined by:

$$R(\lambda) = \left[\frac{n_m(\lambda) - 1}{n_m(\lambda) + 1} \right]^2$$

with $n_m(\lambda)$ the refractive index of the material m at the wavelength λ . It appears from this equation that materials with higher values of n will present higher losses due to reflections. For instance, the transmittance of a plane parallel plate glass window with a refractive index of $n=1.5$ is 92%, while that of a similar plane parallel plate of germanium of refractive index $n=4.0$ (for $\lambda=10 \mu\text{m}$) is 47%. These values take no account of material absorption and scatter. Thus, antireflection coatings are essential in optical systems in order to achieve a usable image. Much effort is involved in the development of these antireflection coatings and in the manufacturing of coated materials presenting high transmissions in the atmospheric windows. Figure 2.8 shows the transmission of a chalcogenide Gasir 1® glass ($n=2.49$ at $10 \mu\text{m}$) with and without antireflection coating

[16]. The average transmission in the range 8-12 μm is increased from about 70% for uncoated sample to approximately 97% for a coated sample.

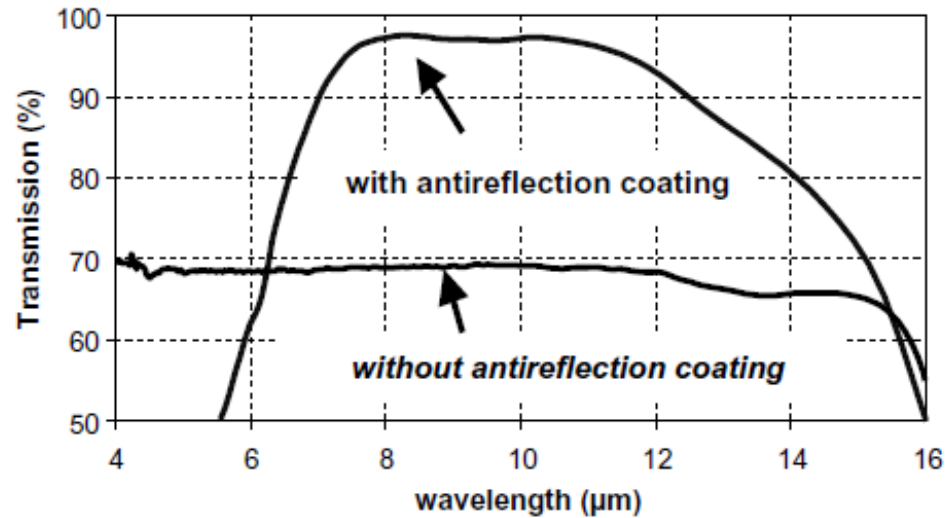


Figure 2.7: Transmission of a chalcogenide Gasir 1® glass with and without antireflection coating [16]

2.3.3.3. Variations of the refractive index with wavelength and temperature

The refractive index may vary with wavelength and temperature, inducing aberrations that have to be corrected to ensure a good resolution of the thermal imager. Change in refractive index with wavelength is called optical dispersion. The refractive index n of a material is defined as:

$$n = \frac{c}{v}$$

with: c : speed of light in vacuum

v : speed of light in the material considered

A variation in n yield a change in optical path of a radiation according to Snell-Descartes' refraction laws ($\sin\theta_1/\sin\theta_2 = v_1/v_2 = n_2/n_1$). In a dispersive medium, the

velocity of propagation of the radiation, thus its refractive index, will depend on its wavelength. Thermal imagers cover a large range of wavelength (3-5 μm or 8-12 μm). Therefore, this chromatic dispersion $dn/d\lambda$ is an important parameter. It is evaluated by calculating the Abbe number (also called constringence or V-number) for a given material in the wavelength range of interest. Materials with high values of Abbe number show low chromatic dispersion. The constringence is calculated using the following relations:

$$V_{3-5} = \frac{n_4 - 1}{n_2 - n_5} \quad \text{and} \quad V_{8-12} = \frac{n_{10} - 1}{n_8 - n_{12}}$$

with: V_{3-5} : Abbe number in the 3-5 μm region

V_{8-12} : Abbe number in the 8-12 μm region

n_x : refractive index of the material at the wavelength x (in μm)

The variation of refractive index with temperature dn/dT also has an effect on the optical systems performance. Significant values of dn/dT induce aberrations that have to be compensated. Two techniques of corrections may be used. The first one is based on monitoring the temperature of the optical system and mechanically adjusting the focus accordingly (active compensation). The second technique relies on careful optical and mechanical design (passive compensation). Changes in refractive indices of lens elements are compensated by adjustment of the mechanical spacing between the lenses using spacers made from materials with appropriate thermal coefficients of expansion. The optical and physical properties of some materials used for thermal imaging lenses are presented in table 2.1.

Table 2.1: Optical and thermal properties of some materials used for thermal imaging lenses

Material	V8-12 at 298K	dn/dT at 298K ($\times 10^{-4} \text{ K}^{-1}$)	Coefficient of thermal expansion at 298K ($\times 10^{-4} \text{ K}^{-1}$)	Index of refraction at 10 μm at 298K
Ge single crystal	865	4	5.9	4.003
ZnS	23	0.54	6.5	2.200
ZnSe	58	0.6	7.0	2.407
GaAs	99	0.49	5.7	3.274
CdTe	159	1.47	5.9	2.672
Gasir 1® glass Ge ₂₂ As ₂₀ Se ₅₈	120	55	17.0	2.494
Amtir 1® glass Ge ₃₃ As ₁₂ Se ₅₅	113	72	12.0	2.498
IG5® glass Ge ₂₈ Sb ₁₂ Se ₆₀	102	91	14.0	2.604

2.4. Materials for thermal imager optical systems

2.4.1. The ideal material

J.M. Lloyd described the ideal thermal imaging lens material as a highly transparent material in the IR region combining all the following properties [17]:

- A high refractive index to minimize lens curvatures and the number of lens elements in a given system
- A zero thermal coefficient of refractive index (no change in index with temperature) to prevent aberration unbalancing and focal length as the lens temperature changes

- A zero dispersion (no change in refractive index with wavelength) to minimize chromatic aberration and the number of lenses necessary to compensate for it
- A zero coefficient of thermal expansion (no change in lens dimensions with temperature) to avoid aberration-unbalancing and focal length changes, and to simplify lens mountings
- High surface hardness to prevent scratching and abrasion
- High mechanical strength to allow thin lenses to be used (high diameter-to-thickness ratio)
- Chemical stability to assure lens integrity in rain and high humidity conditions
- Compatibility with antireflection coatings because lens surface reflection losses increase with increasing refractive indices
- Low radiation absorbance to minimize absorption losses and to allow efficient system design

No known material possesses all of these desirable qualities. However, materials partly satisfying some of these conditions are known and are employed for thermal imagers optical systems. These materials can be classified as either working in the 3-5 μm or the 8-12 μm windows. Materials that can be used in both windows are referred as multispectral materials. Most of the materials described below are multispectral. Only the materials limited to the mid-infrared are listed as materials for the mid infrared. Multispectral materials are listed as materials for the far infrared, but one has to keep in

mind that most of these materials are also suitable for applications in the 3-5 μm band, even though their transmittance properties have generally been optimized for 8-12 μm wavelengths [18].

2.4.2. Materials for the mid-infrared (3-5 μm band)

2.4.2.1. Silicon (Si)

Silicon is the world's most common semiconductor material. It is thus readily available in high quality and quantity for use in infrared optical applications. Commercial Si monocrystals up to 150mm in diameter are routinely grown by the Czochralsky technique. Its transparency in the infrared region extends from 1 μm to 6 μm and its refractive index is relatively high ($n=3.4316$ at 3 μm). Its mechanical properties are conducive with production of infrared lenses and reflectors. Therefore, silicon is widely used for applications in the 3-5 μm range. However, at high temperatures, free carriers absorption reduces its transparency, and Si optical components are limited to applications at temperatures below 200°C.

2.4.2.2. Oxides and oxynitrides

Sapphire (Al_2O_3) combines excellent chemical durability and excellent optical and mechanical properties, making it a special choice for a variety of demanding optical applications. Its transparency range extends from 0.15 μm up to 5.5 μm . Sapphire is one of the hardest of the oxide crystals and maintains a good strength at high temperatures. However, its high hardness makes it difficult to shape the material into complex optical

elements. Cleavage is possible but its properties are anisotropic because of its hexagonal crystal structure and cuts have to be made along specific axis.

Spinel (MgAl_2O_4) presents optical and mechanical properties similar as sapphire, making it another material of choice for designing infrared optics. As spinel, monocrystals are grown using Czochralsky technique.

Aluminum oxynitride (or AlON, $5\text{AlN}.9\text{Al}_2\text{O}_3$), which transparency range and mechanical properties are equivalent to the properties of spinel and sapphire, is also used for the production of optical components for the mid infrared. Nevertheless, it is worth noting that this material presents isotropic physical properties and is relatively easy to produce.

2.4.2.3. Fluorides

Calcium fluoride (CaF_2) and barium fluoride (BaF_2) have a good transparency in the UV, visible and mid-infrared regions, as shown in figure 2.9 [19]. They are readily produced in excellent quality up to diameters of the order of 150mm by the Bridgman process and possess excellent physical properties. These two materials are commonly used for the production of thermal imaging optics for applications in the 3-5 μm wavelength range. Unlike CaF_2 which is not moisture-sensitive, BaF_2 lenses need a protective coating due to problems of water solubility and surface absorption. Magnesium fluoride (MgF_2), despite excellent physical properties and a good transparency range, is not used for the production of optical systems due to the birefringent character of this material.

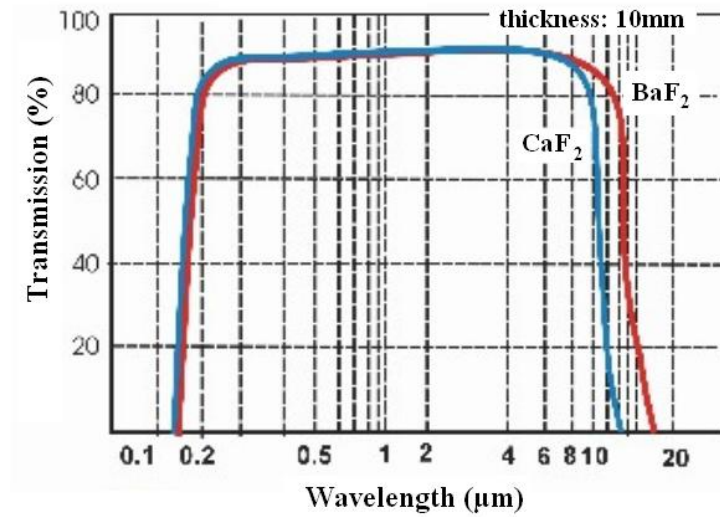


Figure 2.8: Transmission spectra of CaF_2 and BaF_2 [19]

2.4.2.4. Hot pressed ceramics (Irtran)

Hot pressed ceramics for airborne infrared windows used in the 3-5 μm wavelength band were developed by Eastman Kodak Co USA in the early 1970s. Different materials were manufactured, based on the hot pressing of previously prepared powders. These materials are known as Irtran 3 (CaF_3) and Irtran 5 (MgO), both possessing good mechanical properties and a transparency ranging from the visible up to 8 μm . However, the technique used to prepare the lenses raise problems of contamination of the powder, non-uniformity and scattering. Nowadays, the other materials described previously are preferably used instead of Irtran materials.

2.4.3. Materials for the far-infrared (8-12 μm band)

2.4.3.1. Germanium (Ge)

Germanium is the most commonly used lens material for the 8-12 μm window. Its spectral transmission extends from 2 μm to 12 μm , as shown in figure 2.10. The high refractive index of germanium allows high optical power to be generated in thin optical components. Its low dispersion in the 8-12 μm range reduces chromatic aberration in lens systems which thus need low corrections. Due to its semiconductor behavior, absorption of germanium increases with temperature, and severe losses are experienced when used above 80°C. Its high value of dn/dT (about $4 \cdot 10^{-4} \cdot \text{K}^{-1}$) also has to be emphasized and may involve the use of thermal control devices.

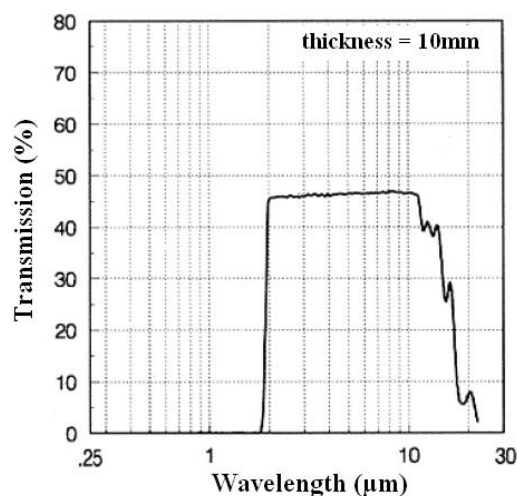


Figure 2.9: Transmission spectrum of single-crystalline germanium

Single-crystalline germanium presents a high degree of hardness and mechanical strength, making it an ideal candidate for applications where ruggedness is a prime factor. It also presents a high resistance to thermal shocks and corrosion. Ge single-crystals with

dimensions up to 350mm in diameter are commercially available, allowing the production of lenses with high dimensions. However, germanium does not occur in major ore deposits but is found in low concentrations, typically 0.005-0.2% in certain lead, copper or zinc ores, and its extraction process is laborious. Furthermore, germanium lenses have to be made from single-crystals. Although cheaper to produce, polycrystalline germanium is not adequate for optical applications as structural defects located at the grain boundaries generate local refractive index variations [20]. The Czochralski (or crystal pulling) technique is employed to produce the single-crystalline Ge. In addition to the expensive cost of the material itself [21] (about 90\$ for a wafer of 1” in diameter and 0.5mm in thickness in 2011), the high hardness of germanium imposes the use of highly expensive diamond grinders to shape lenses [22]. Therefore, despite the remarkable optical and mechanical properties of germanium for production of optical systems, the high final cost of germanium lenses lead to investigate other materials for thermal imaging devices.

2.4.3.2. Gallium Arsenide (GaAs)

In the same way as single-crystalline Ge, GaAs has a high transparency in the IR ranging from 2 μm to 12 μm , but is less subject to increase of absorption with temperature. The mechanical properties of GaAs and Ge are comparable. Therefore, gallium arsenide lenses are often used to replace germanium lenses for applications involving temperatures of use between 70°C and 200°C. However, GaAs has to be used as single-crystals, and the important cost of elemental gallium and the complexity of the

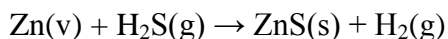
process employed for the shaping of lenses make this material expensive. GaAs lenses have notably been produced by Amorphous Materials Inc (AMI) [23].

2.4.3.3. Cadmium Telluride (CdTe)

CdTe shows a wide range of transmission in the infrared region, ranging from 2 μm to 20 μm and therefore presents a high interest for applications requiring large wavelengths windows. However, its mechanical properties are relatively poor and it is easily damaged by scratching [24]. CdTe was commercially produced with the reference Irtrans 6, but is no longer manufactured due to the complexity of the process involved and the toxicity of Cd.

2.4.3.4. Zinc Sulfide (ZnS)

Polycrystalline ZnS is commonly used for thermal imaging optical lenses. It is referred as Irtran 2. It is produced by chemical vapor deposition technique (CVD). The chemical reaction involves zinc vapors and gaseous hydrogen sulfide.



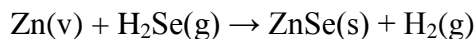
The as-prepared zinc sulfide is mainly composed of the spharelite cubic phase, but a small amount of hexagonal wurtzite remains. The presence of this phase induces light scattering at the shorter wavelengths and giving a yellow coloration to the material [25]. To eliminate these defects, an additional treatment by hot isostatic pressing (HIP) is performed. The heat-treated ZnS, called multispectral CVD ZnS possess a large transparency in the infrared region, from 0.4 μm to 12 μm . However, for lenses with

thickness greater than 10mm, a significant decrease in transmission is observed for wavelength above 10 μm . For this reason, ZnS lenses use is limited to thermal imagers working in 3-5 μm or 8-10 μm ranges.

ZnS has relatively good mechanical properties, although less than those of Ge or GaAs. Its shaping is done by mechanical grinding but diamond grinders are not necessary, leading to lower costs of production in comparison to Ge and GaAs lenses. The toxicity of the gaseous H_2S employed during the synthesis process has to be noticed.

2.4.3.5. Zinc Selenide (ZnSe)

Zinc selenide optical systems are also produced by CVD. The reaction involves gaseous H_2Se , which toxicity is higher than H_2S .



The optical transmission of ZnSe is greater than of ZnS, extending from 0.6 μm up to 15 μm , as seen on figure 2.11.

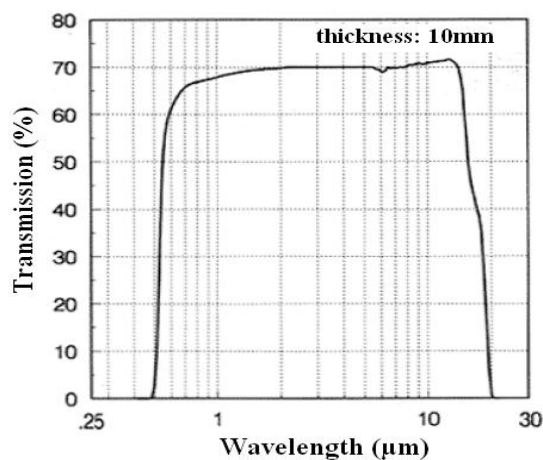


Figure 2.10: Transmission spectrum of ZnSe

The low absorption coefficient of zinc selenide at 10.6 μm allows its use for applications involving high power CO_2 lasers. The mechanical properties are relatively low in comparison to ZnS and limit its use as material for external optical applications. However, ZnSe lenses are used extensively in conjunction with germanium in multi-element objectives for the 8-12 μm band.

2.4.3.6. Halides

Thallium bromo-iodide (TlBr-TlI, also known as KRS5) has been widely studied for infrared optical applications due to its high transparency from 0.6 μm to 25 μm [26]. However, the use of KRS5 is very limited due to the extremely high toxicity of thallium, the poor aging behavior of this material and its difficulty to be shaped.

Silver chloride (AgCl) and silver bromide (AgBr) have been studied as infrared fiber materials. Despite their good transparency range extending up to 17 μm , the polycrystalline nature of these materials induce variations of optical properties with time and the presence of UV-sensitive silver particles limit their applications [27].

Alkali halides (KBr, KCl, NaCl, CsBr or CsCl) have a good transparency ranging from visible to the mid-infrared. These materials are inexpensive and single-crystals with large dimensions can be easily prepared [27]. Their low absorption coefficients at 10.6 μm make them interesting materials for applications involving high power CO_2 lasers. For these reasons, alkali halides have been used for optical materials at the laboratory-scale. However, their poor mechanical properties and their high hygroscopic behavior

(except for KBr) limit their application to laboratory-scale devices, and few commercial thermal imaging applications involve alkali halide-made lenses.

2.4.3.7. Diamond

Diamond can be considered the ultimate infrared optical material because of its superior optical and mechanical properties [18]. The purest diamonds are multispectral, transmitting in the UV (from 0.2 μm), visible and IR (up to 100 μm). However, diamond optical systems are extremely expensive and are mainly reserved to space optics applications.

2.4.4. Chalcogenide glasses as materials for thermal imagers

Due to their good transparency in the mid and far infrared regions, chalcogenide glasses have been widely studied for applications as thermal camera lenses material [28]. Compared to the crystalline or semiconductor materials described above, chalcogenide glasses present some significant advantages. The synthesis process is relatively simpler than growth of single crystals and lead to lower production costs (see chapter 3). In addition, due to their glassy behavior they can be easily shaped by molding or drawn into fibers, reducing the processing costs of lenses. Furthermore, variations in the glass stoichiometry can be easily carried out to adjust specific parameters such as the refractive indices. This cannot be done for crystalline materials.

Meanwhile, they generally suffer from relatively poor mechanical properties. In addition, their high coefficients of thermal expansion ($12\text{-}30 \times 10^{-6} \text{ K}^{-1}$ at 298K) associated

with low thermal conductivities ($2\text{-}4 \times 10^{-3} \text{ W.cm}^{-1}.\text{K}^{-1}$ at 298K) make them weaker to thermal shocks than single-crystalline germanium. Their refractive index is significantly lower and their chromatic dispersion is higher than for Ge in the 8-12 μm wavelength range (see table 2.1). However, their low production costs combined to their ability to be shaped by molding make them materials of high interest for the production of low cost thermal imaging optical components. Numerous compositions suitable with these applications have been developed over the past few decades and will be described below.

2.4.4.1. Selenide glasses

Selenium as a pure single element is a good glass former presenting a large transparency in the infrared region. However, its poor mechanical properties are not conducive to the production of lenses [29]. To enhance these properties, other elements such as germanium, arsenic or antimony are added to the composition to obtain glasses suitable for the production of infrared optics.

- *Glasses of the system As-Se*

Arsenic-selenium glasses have a transparency ranging from about 1 μm to 16 μm . The absence of the expensive germanium in these compositions reduces the cost of these materials. Among all the compositions in this binary diagram, As_2Se_3 presents the best thermal and mechanical properties. Its glass transition temperature is about 185°C. This glass composition has been commercially distributed by the society Vitron (composition

referenced as IG6®) [30]. Amorphous Materials Inc also commercialized As-Se glasses, known as AMTIR 2® and AMTIR 5® [23].

- *Glasses of the systems Ge-As-Se and Ge-Sb-Se*

Systematic studies showed that selenide glasses with contents of about 20-30% of germanium and 10-20% of arsenic or antimony lead to compositions having interesting mechanical and optical properties for the manufacturing of lenses [31, 32]. The addition of germanium enhances the thermal behavior of optical elements (lower thermal expansion, higher T_g and better thermal conductivity) in comparison to glasses in the As-Se binary system and also increases the mechanical strength.

The society Umicore IR Glasses developed two compositions that are commercially available under the references Gasir 1® ($\text{Ge}_{22}\text{As}_{20}\text{Se}_{58}$) and Gasir 2® ($\text{Ge}_{20}\text{Sb}_{15}\text{Se}_{65}$) [33]. Their optical transmission covers the 2-14 μm wavelength range. The low germanium content of these glasses yield a low production cost while maintaining good mechanical properties. Infrared lenses are produced by a molding process schematically presented in figure 2.12. An example of lenses produced by this technique is also shown.

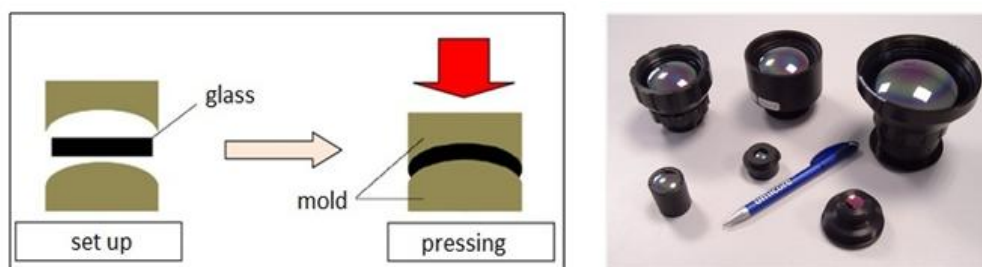


Figure 2.11: Process of chalcogenide glass lenses molding developed by Umicore IR Glass and example of lenses produced with this technique

Other compositions among these ternary systems are commercially available such as the glasses IG2® ($\text{Ge}_{33}\text{As}_{12}\text{Se}_{55}$), IG4® ($\text{Ge}_{10}\text{As}_{40}\text{Se}_{50}$) and IG5® ($\text{Ge}_{28}\text{Sb}_{12}\text{Se}_{60}$) commercialized by Vitron [30] and the glasses AMTIR 1® (Ge-As-Se) et AMTIR 3® (Ge-Sb-Se) commercialized by Amorphous Materials Inc [23]. The presence of arsenic or antimony in these glasses, both toxic, can be problematic in the future due to more severe environmental standards concerning these elements (notably the European law about Registration, Evaluation, Authorization and Restriction of Chemical substances, or REACH). Much effort is spent on finding As- and Sb-free compositions with equivalent properties to Gasir® glasses.

2.4.4.2. Telluride-Selenide glasses

- *Glasses of the system Ge-As-Se-Te*

The addition of tellurium induces higher refractive indices and slightly lower dispersions [18]. However, tellurium is a poor glass former and its presence during the synthesis process decreases the glass stability and may induce undesirable crystallization. Up to 30% of Te can be added to Ge-As-Se glasses [34]. Higher contents of Te yield lower glass transition temperatures [35]. However, higher Abbe number (thus lower dispersion) can be achieved. This latter point lead Vitron to commercialize a glass named IG3® ($\text{Ge}_{30}\text{As}_{12}\text{Se}_{32}\text{Te}_{25}$) [30].

- *Glasses of the system Te-As-Se (TAS glasses)*

These glasses present a transmission range that extends up to 17 μm and are generally stable toward crystallization when the tellurium content does not exceed 30%. It has been shown that fibers made of glasses from this ternary system can have extremely low optical losses [36], making them materials of high interest for the detection of biological or chemical species for instance [37]. Amorphous Materials Inc commercializes glass fibers of TAS glasses under the reference C1 [23].

2.4.4.3. Telluride glasses

In the 1980s, telluride-halide glasses, known as TeX glasses have been discovered at the Glass and Ceramics laboratory of the University of Rennes 1, France [38, 39]. These glasses showing a wide transparency in the infrared region up to more than 20 μm were commercially distributed by the society Vertex, now Umicore IR Glasses.

Other interesting compositions in the Ge-Ga-Te [40] and Te-Ge-I [41] ternary diagrams showing large transmission ranges in the infrared and which can be drawn into fibers are extensively studied at the Glass and Ceramics laboratory of the University of Rennes 1.

2.4.5. Chalcogenide glass-ceramics

Chalcogenide glasses generally show a large transparency in the infrared region but suffer from poor mechanical properties in comparison to single-crystalline germanium or zinc selenide. However, a controlled crystallization of these glasses can

yield glass-ceramics presenting higher mechanical properties than the base glass while maintaining a sufficient transparency range for thermal imaging applications.

The first chalcogenide glass-ceramics transparent in the 8-12 μm wavelength range were developed in 1973 by Mecholsky by crystallization of a $\text{PbSeGe}_{1.5}\text{As}_{0.5}\text{Se}_3$ glass [42], and Cheng Jijian in 1980 from As-Ge-Se-Sn glasses [43-45]. The possibility to shape glass-ceramics from the system Ga-Ge-Sb-Se was demonstrated at the Glasses and Ceramics Laboratory of the University of Rennes 1 [46]. However, while presenting good optical properties and enhanced mechanical properties, the poor reproducibility of these glass-ceramics was not conducive to industrial production.

The first reproducible chalcogenide glass-ceramics were obtained in 2004 by Zhang et al. by controlled crystallization of $\text{GeSe}_2\text{-Sb}_2\text{S}_3\text{-CsCl}$ glasses [47]. The materials obtained this way present stronger mechanical properties and a transparency range up to 11.5 μm . Other interesting materials with a transparency extended up to 15 μm were produced from the $\text{GeSe}_2\text{-Sb}_2\text{Se}_3\text{-X}$ systems, where X is a alkali halide (CsCl, RbI, CsI, KI, CsBr....) or a metallic compound (ZnS or CdTe) [48-52]. Additional compositions with X = PbS, PbSe or CdSe have also been studied and showed interesting properties for infrared applications [53-57].

In 2008, Yang et al. demonstrated the possibility of molding glass-ceramics in a one-step process with a $40\text{GeSe}_2\text{-}30\text{Ga}_2\text{Se}_3\text{-}30\text{CsI}$ glass composition [58]. While keeping a good transparency in the 8-12 μm wavelength range, the toughness of the glass-ceramics was more than doubled in comparison to the base glass. In 2010, Rozé et al. showed that lenses made of glass-ceramics with a composition of $72\text{GeSe}_2\text{-}18\text{Ga}_2\text{Se}_3\text{-}$

10CsI can be produced with diameters as high as 50mm and better mechanical properties than the Gasir 1® glass commercially produced for thermal imaging optics [59]. The possibility to shape the glass by molding and to deposit antireflection coating with good optical properties has been successfully demonstrated. However, the presence of hygroscopic CsI yields glass-ceramics sensitive to humidity.

Recently, glass-ceramics with a composition $80\text{GeSe}_2\text{-}20\text{Ga}_2\text{Se}_3$ have been studied and their ability to be shaped and crystallized in a one-step molding process has been demonstrated [60, 61]. The good transparency range and the enhanced toughness of these glass-ceramics make them a material of interest for the production of thermal camera lenses.

2.5. Summary

This chapter described the fundamentals of thermal imaging and emphasized the need for low cost optical components required to expand the thermal cameras market to civilian consumer applications. No ideal material currently exists and compromises have to be made when selecting the optical component composition. The most commonly used materials for infrared cameras lenses is currently single-crystalline germanium (Ge). Although presenting a high transparency range and high mechanical properties, the intrinsic cost of the material itself and of the shaping process prevents its use for low-cost thermal imagers. Other materials presenting lower mechanical properties exist, such as zinc sulfide (ZnS), zinc selenide (ZnSe) or silicon (Si, limited to the 3-5 μm

applications), but their production process remain complicated and sometimes involve the use of highly toxic compounds.

Due to their good transmission properties in the mid- and far-infrared regions, combined to lower production costs and their ability to be shaped by molding, chalcogenide glasses present a major interest for the production of thermal imaging components. The mechanical properties remain the major drawback of chalcogenide glasses, however some glassy compositions of the systems Ge-As-Se or Ge-Sb-Se (Gasir® glasses) are commercially available and currently equip low-cost thermal imaging devices. Moreover, studies show that a controlled crystallization of some chalcogenide glass compositions yield glass-ceramics with enhanced mechanical properties while maintaining transparency in the infrared.

2.6. Objectives of this study

Chalcogenide glasses and chalcogenide glass-ceramics may represent a good alternative to germanium and Gasir® glasses for the production of thermal cameras lenses. Nevertheless, the synthesis of chalcogenide glasses currently requires the use of expensive single use silica ampoules that represent an important fraction of the final cost of the glass. Moreover, silica has a low thermal conductivity which reduces heat dissipation during quenching and limits the diameter of glass cylinders that can be obtained without risk of crystallization.

The objective of this study therefore focuses on the development of innovative methods for the synthesis of chalcogenide glass and glass-ceramics without the use of silica tubes. Several approaches including open synthesis in inert atmosphere as well as mechanosynthesis of amorphous powders will be addressed. Powder sintering will emerge as a very promising approach and will be the focus of detailed investigations for the production of glass and glass ceramic lenses.

In the last part of this study, the potential of these glasses for hosting luminescent rare earth ions will be investigated for the development of laser sources in the mid-infrared region. In particular, the effect of nucleation on the luminescent properties will be reported.

CHAPTER 3: NEW SYNTHESIS METHODS FOR CHALCOGENIDE GLASSES

3.1. Introduction

Due to their high transparency in the infrared region, their ability to be shaped by molding and their lower cost as compared to other materials transmitting in the second and third atmospheric windows such as single crystalline germanium, chalcogenide glasses are used for a wide range of applications in the infrared optics. These applications comprise night vision, non linear optics, chemical and biological sensing or optical fibers. The development of thermal imaging devices for the civilian market must be driven by a reduction of the production costs of the materials used, while simultaneously improving their mechanical and optical properties. Chalcogenide glasses and glass-ceramics represent good candidates for achieving this goal.

Currently, chalcogenide glasses are synthesized in silica ampoules sealed under vacuum. The silica ampoules involved in the process are expensive and single use. They can represent up to 30% of the final cost of the glass. The development of cheaper synthesis techniques would reduce the final costs of the glasses and increase its marketability for infrared optics. This motivates the development of new synthesis method involving reusable containers.

Another source of high cost is the lenses molding process. The molding step is performed on bulk samples that have been previously cut to the mold size. This cutting step generates materials loss and even if the residual glass can be collected, remelted and

reused after purification for production of other optics, the corresponding cost increase is over 20%.

In this chapter, different techniques for producing chalcogenide glasses without the need for single use silica ampoules will be investigated. In the first section, an open synthesis method involving traditional melting of raw elements under inert atmosphere will be attempted. In the second section, a different approach for glass formation involving mechanical energy rather than thermal energy will be presented. The specific materials under focus for this study are glasses from the Ge-Ga-Se ternary system, which present a high interest for infrared cameras optics. The following section reviews the general physical properties of these materials.

3.2. Chalcogenide glasses

3.2.1. Introduction

By definition, chalcogenide glasses are glasses which contain at least one of the three chalcogen elements, sulfur, selenium or tellurium, but no oxygen. Depending on the desired application, other chemical elements may be added to the composition to improve the mechanical, thermal or optical properties. Commonly used elements include germanium, gallium, arsenic, antimony, alkali halides or metals such as lead, silver or copper. It is worth noting that among the three chalcogen elements, only selenium easily forms a stable glass as a pure single element.

3.2.2. Optical properties

As mentioned previously, chalcogenide glasses present a wide transparency window in the infrared region. At the shorter wavelengths, the optical transmission window of a glass is limited by its band-gap, while at longer wavelengths it is limited by multi-phonon absorption.

3.2.2.1. Band gap

The glass transmission at shorter wavelengths is limited by the optical absorption due to electronic transitions between the valence band (VB) and the conduction band (CB) of the material. The energy difference between these two bands corresponds to the forbidden band-gap of the glass. Photons with sufficient energies are absorbed by exciting electrons across the forbidden band-gap. The electrons are excited from the top of the VB to the bottom of the CB, as shown in figure 3.1.

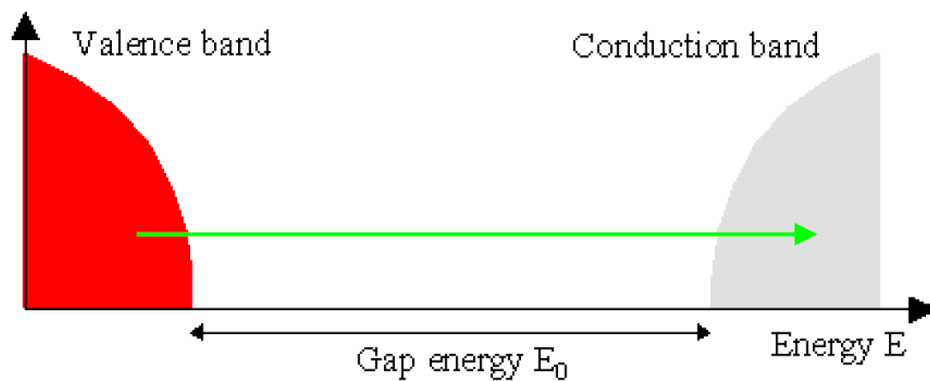


Figure 3.1: Band-gap

The band-gap energy is correlated to its wavelength by the following relation:

$$E_g = \frac{hc}{\lambda_g} = \frac{1.24}{\lambda_g}$$

where E_g is the band gap energy (eV), h is Planck's constant (eV.s), c is the speed of light ($\mu\text{m.s}^{-1}$) and λ_g is the wavelength (μm). The optical band-gap energy E_g is usually estimated as the photon energy corresponding to an absorption coefficient α equal to 10 cm^{-1} . The absorption coefficient α is related to the material's thickness x according to:

$$I = I_0 e^{-\alpha x} \quad \text{thus} \quad \alpha = \frac{1}{x} \ln \left(\frac{I_0}{I} \right)$$

where α is the linear attenuation coefficient (cm^{-1}), I_0 is the incident intensity and I is the intensity transmitted by the glass at a given wavelength. This equation does not take into account the high reflectivity due to the high refractive indices of chalcogenide glasses. To be more accurate, the Fresnel losses, due to the reflections of light at the surface of the material, have to be considered:

$$T = \frac{I}{I_0} = \frac{(1-R)^2 e^{-\alpha x}}{1-R^2 e^{-\alpha x}} \quad \text{with} \quad R = \left(\frac{n-1}{n+1} \right)^2 = \frac{1-T_0}{1+T_0}$$

where T_0 is the maximal transmission, T is the percentage of transmission at a given wavelength, R is the reflectivity of the glass and n is the refractive index of the glass.

Therefore, the absorption coefficient of the glass is given by the relation:

$$\alpha = \frac{1}{x} \ln \left(\frac{2TR^2}{-(1-R)^2 + \sqrt{(1-R)^4 + 4T^2R^2}} \right)$$

The band-gap energy can then be estimated from a transmission measurement by determining the wavelength corresponding to a value of α equal to 10 cm^{-1} .

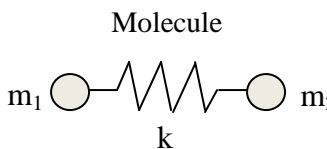
In chalcogenide glasses, the top of the valence band is composed of lone pair electrons of the chalcogen elements: S, Se or Te. The lone pair electrons of selenium ($4s^2p^4$) or tellurium ($5s^2p^4$) are higher in energy than the lone pair electrons of sulfur ($3s^2p^4$). The band gap energy will be greater for sulfur-based glasses than for selenium-

based and tellurium-based glasses. Therefore, the band gap shifts from visible with sulfur-based glasses to near infrared for selenium and tellurium-based glass.

3.2.2.2. Multi-phonon absorption

The transmission at longer wavelengths is limited by the multi-phonon absorption. This absorption is due to interactions between light and vibrational modes of the glass network. Considering a simplified two body oscillator model, the phonon energy is correlated to the force constant of the bond (k) and to the reduced mass (μ) of the atoms constituting the bond, following the relations:

$$E = h\nu \quad \text{with} \quad \nu = \frac{1}{2\pi} \sqrt{\frac{k}{\mu}} \quad \text{and} \quad \frac{1}{\mu} = \frac{1}{m_1} + \frac{1}{m_2}$$



where ν is the vibration frequency of the bond, m_1 and m_2 are mass of the atoms 1 and 2, and h is Planck's constant. From these equations, it appears that phonon energies are inversely proportional to the mass of the atoms constituting the glass. Glasses composed of heavy elements will therefore present multi-phonon absorptions at longer wavelengths. From the periodic table of the elements, we have $M_{\text{Oxygen}} < M_{\text{Fluor}} < M_{\text{Sulphur}} < M_{\text{Selenium}} < M_{\text{Tellurium}}$. Thus, as shown in figure 3.2, chalcogenide glasses present a transmission extending far in the infrared region, up to 11 μm for sulfide glasses, 16 μm for selenide glasses, and more than 20 μm for tellurium glasses, while the transmission of silica and fluoride glasses is limited to about 4 μm and 7 μm respectively.

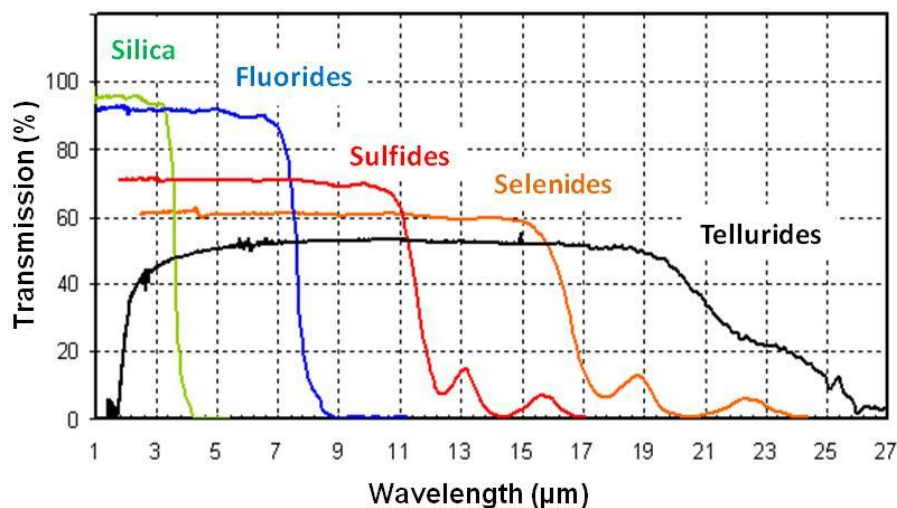


Figure 3.2: Optical transmissions of different families of glasses

3.2.2.3. Absorption bands due to impurities

During the synthesis process, chalcogenide glass melts are highly sensitive to the presence of contaminants, particularly to oxygen and water, which provoke strong absorption bands within the transparency windows of the resulting glass. For an optical glass, the oxygen content should not exceed 1ppm to ensure good transparency [18]. Impurities can also generate optical losses by inducing crystallization and scattering in the glass. These undesirable phenomena are highly detrimental to the transmission in the infrared region and are not conducive to the production of glasses for optical applications.

Figure 3.3 shows the transmission spectra of a selenium-based glass. The non-purified glass shows important absorption bands. When the glass is purified, i.e. prepared with specific care to eliminate the contamination sources during the synthesis process, no absorptions are observed on the transmission spectrum.

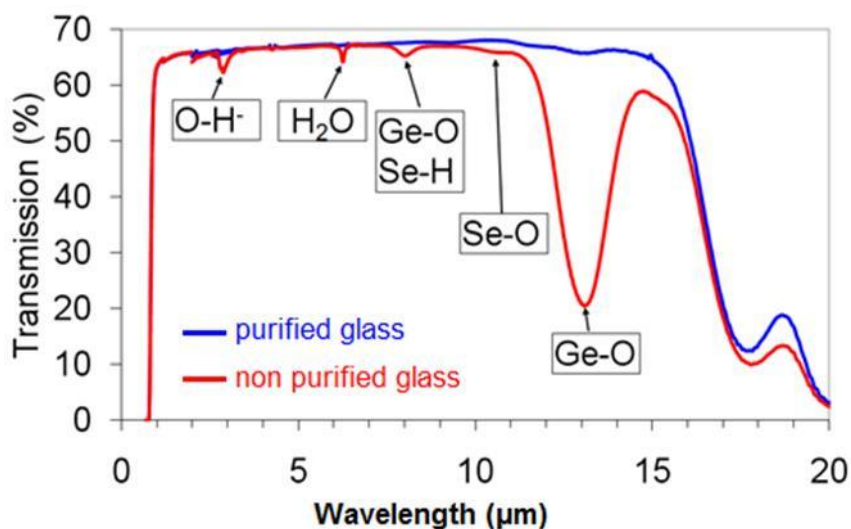


Figure 3.3: Effect of oxygen contamination on the optical transmission of a chalcogenide glass

The position of some of the characteristic absorption bands in the infrared region due to the presence of impurities in chalcogenide glasses are listed in table 3.1 [28]. It is worth noting that all the absorptions listed on the table below may not be observed simultaneously on the transmission spectrum of a glass.

Table 3.1: Position of characteristic absorption bands in the infrared region

Chemical bond	Position of the absorption bands (μm)
H-O ⁻	2.73 ; 2.78 ; 2.84 ; 2.9
S-H	2 to 2.1 ; 2.55 ; 3.1 ; 3.64 to 4.1
Se-H	2.3 ; 3.5 ; 4.1 ; 4.3 to 4.9 ; 7.2 ; 7.8
H ₂ O	2.3 ; 6.3 ; 10.7
Se-O	10.7 ; 16
Ge-O	8 ; 11.1 ; 12.5 ; 12.7 ; 13
C-S	4.94 ; 7.6

3.2.3. Thermal properties

Glasses are defined as amorphous materials that exhibit a glass transition temperature T_g . For temperatures below T_g , glasses show an infinite viscosity (solid state). Above T_g , the viscosity decreases with increasing temperature. The glass

transition temperature corresponds to a viscosity of 10^{13} poises. As the viscosity decreases, the mobility of atoms in the glassy matrix increases and rearrangements of the constituting atoms in organized lattices may occur. This phenomenon corresponds to the crystallization of the glass, characterized by the crystallization temperature T_x . At higher temperature, melting occurs at the melting point of the glass (T_m). Glass transition and melting are endothermic phenomena, while crystallization is exothermic.

The knowledge of these temperatures gives an estimate of the stability of a given glass against crystallization. One of the most used criterion is the Hruby criterion [62], calculated from the following relation:

$$Hr = \frac{T_g - T_x}{T_m - T_x}$$

High values of Hr correspond to stable glasses. However, it is sometimes difficult to measure the melting temperature T_m . In this case, the difference $\Delta T = T_x - T_g$ is a good criterion to assess the stability of the glass against crystallization. Chalcogenide glasses showing values of ΔT higher than 100°C are considered stable, as their molding or drawing into fibers is feasible. It is worth noting that crystallization may not be observed in some chalcogenide glasses, such as the TAS glass ($\text{Te}_2\text{As}_3\text{Se}_5$) [36].

In this study, the thermal properties of the chalcogenide glasses were determined using Differential Scanning Calorimetry (DSC). This technique is based on the difference in heat flow between a sample and a reference. Figure 3.4 shows a schematic DSC curve for a chalcogenide glass undergoing a crystallization phenomenon.

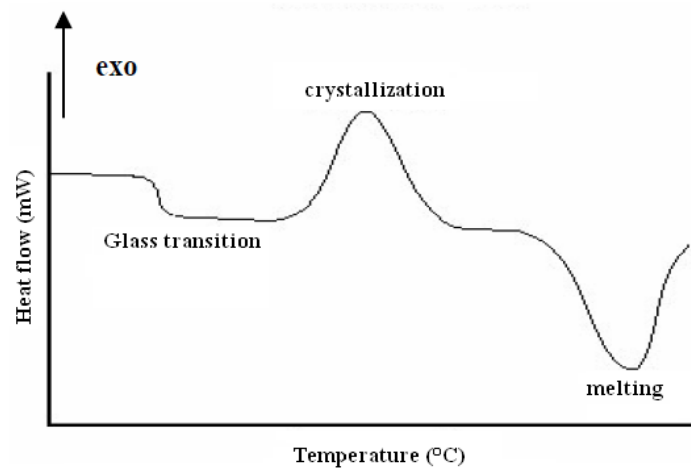


Figure 3.4: Typical DSC curve of a glass

3.2.4. Mechanical properties

3.2.4.1. Density

It is necessary to know the density of a glass to calculate its other physical characteristics, such as Young's modulus. The density is measured using the Archimedes' double weighing technique. The glass sample is first weighed in air (m_{air}) then in distilled water ($m_{\text{H}_2\text{O}}$). The density of the sample, ρ ($\text{g}\cdot\text{cm}^{-3}$), is obtained using the following equation:

$$\rho = \frac{m_{\text{air}}}{(m_{\text{air}} - m_{\text{H}_2\text{O}})} * \rho_{\text{H}_2\text{O}}$$

where $\rho_{\text{H}_2\text{O}}$ is the density of water in $\text{g}\cdot\text{cm}^{-3}$.

3.2.4.2. Coefficient of thermal expansion

The coefficient of thermal expansion (CTE, or α) is the tendency of matter to change in volume in response to a change in temperature. In the case of glasses, the

knowledge of the CTE allows characterizing the resistance of the glass to thermal shocks. The lower the CTE, the more resistant the glass is. Generally, chalcogenide glasses show higher values of α than oxide glasses [63], thus are more sensitive to thermal shocks.

In this study, the CTE has been measured with a TMA 2940 equipment (T.A. Instruments). Glass discs with a thickness ranging from 4 to 6mm are heated with a heating ramp of 2°C/min from room temperature to 200°C and the dilatation of the sample is probed by the instrument.

3.2.4.3. Hardness

The hardness of a material corresponds to the resistance it opposes to the penetration of a harder body, i.e. its resistance to deformation. Even though this notion of hardness is rather intuitive, its translation into a measurable value is more delicate. Different scales are used to define hardness, according to the method employed to measure it. Hardness testing methods include, Brinell, Rockwell, Meyer or Leeb techniques. During this study, we chose to use Vickers hardness [19].

All the hardness techniques rely on the same principle: apply a force on a flat, polished surface of a sample for a given duration and observe the deformation of the material. For Vickers hardness tests, we used a square-based pyramidal indenter, with an angle of 136° between two triangular faces. Tests were performed using a Matzuzawa WMT-7S indenter. In the present study, all samples were tested using a small charge of 100 g applied for 5 seconds. Considering the small resulting indentation area these tests are often called micro-hardness. After the indentation, a square-shaped print with cracks

starting at the tips and with a dimension of some tens of micrometers can be observed on the surface of the glass. A schematic of the print obtained on a glass surface after micro-indentation tests is presented in figure 3.5.

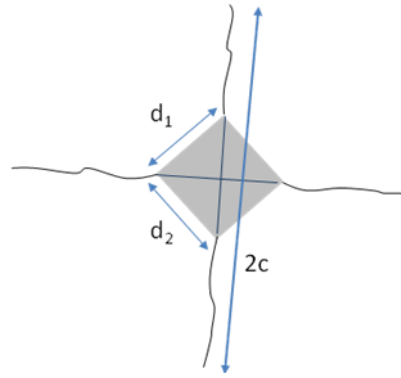


Figure 3.5: Print obtained on a glass surface after micro-indentation tests

A measure of the length of the diagonal of the square-based print (d) allows the calculation of Vickers hardness (H_V). For practical purposes, the average value of the lengths d_1 and d_2 (figure 3.5) is taken to calculate Vickers hardness according to the following relation:

$$H_V = \frac{p}{S} = \frac{2p \cdot \sin\left(\frac{\theta}{2}\right)}{d^2} = 1.854 * \frac{p}{d^2}$$

Where p is the indentation load (N), S is the surface of the print (mm^2), d is the average value of the diagonal of the print (μm) and θ is the angle at the top of the indenter (136°). In order to broaden the comparison to other materials, Meyer hardness (H_M) can be calculated by the ratio:

$$H_M = \frac{P}{2a^2} \quad \text{and} \quad H_V = 1.854 * H_M$$

with $2a$: length of the indentation diagonal.

3.2.4.4. Young's modulus

Young's modulus is defined as the ratio of the stress applied to a material over the resulting strain [64]. The measures of Young's modulus E , shear modulus G (matrix of coefficients linking a tangential constraint applied to a single layer and the resulting deformation to a variable area), and Poisson's ratio ν (characterizing the contraction of a material perpendicularly to the direction of the applied stress) are performed by ultrasonic testing using the pulse-echo method. This non-destructive technique monitors the propagation of longitudinal waves (traction/compression waves) and transversal waves (shear waves) in the material. A wave is generated by inducing an electric potential difference in a piezoelectric transducer. This wave is propagated inside the material and reflected on the opposite face of the sample following the Snell-Descartes law. The elastic chemical bonds induce a temporal shift of the material's response. This shift increases with increasing propagation distance. Thus, the propagation velocity of the wave depends directly on the rigidity of the bonds inside the material. The time difference between two successive echoes is measured and enables the calculation of the propagation velocity of the transversal and longitudinal waves.

In isotropic materials such as glasses, Young's modulus (E), shear modulus (G) and Poisson's ratio (ν) can be calculated using the following relation:

$$E = \rho \left(\frac{3V_L^2 - 4V_T^2}{\left(\frac{V_L}{V_T} \right)^2 - 1} \right) \quad ; \quad G = \rho V_T^2 \quad ; \quad \nu = \frac{E}{2G} - 1$$

Where ρ is the density of the material (g.cm^{-3}), V_L and V_T are the propagation velocities of the longitudinal and transversal waves (m.s^{-1}), respectively, E is the Young's modulus (Pa), G is the shear modulus (Pa) and ν is the Poisson's ratio (no unit).

3.2.4.5. Toughness

Toughness (K_C) is defined as the resistance of a material to fracture when stressed. This notion is used for isotropic materials. However, its approach is delicate in the case of composite materials due to their heterogeneous and anisotropic nature. Generally, tough materials show low brittleness. The calculation of toughness values is done using the equation proposed by B.R. Lawn and D.B. Marshall [65]:

$$K_C = 0.016 \left(\frac{E}{H} \right)^{\frac{1}{2}} \left(\frac{p}{c^{3/2}} \right)$$

Where K_c is toughness value derived from indentation technique ($\text{MPa.m}^{1/2}$), E is the Young's modulus (GPa), H is the Meyer hardness (GPa), p is the indentation load (N) and c is the half-length of the cracks (m).

3.2.5. Synthesis of chalcogenide glasses in sealed silica ampoule under vacuum

The elements commonly used for the production of chalcogenide glasses (S, Se, Te, Ge, Ga, As, Sb...) show an important disparity in their thermal properties. The melting and boiling temperatures of these elements under atmospheric pressure are listed in table 3.2 [66]. The classic glass synthesis process is ensured by reaction of the elements in a liquid or vapor phase. Thus, high temperatures have to be reached.

Depending on the composition, synthesis temperatures ranging from 600°C to 1000°C have to be reached for homogenization of chalcogenide glasses.

Table 3.2: Melting and boiling temperatures of the elements commonly used to prepare chalcogenide glasses

Element	T _m (°C)	T _b (°C)
S	115.2	444.6
Se	221	685
Te	449.5	988
Ge	938	2833
Ga	29.7	2204
As		603 (sublimation)
Sb	630.6	1587

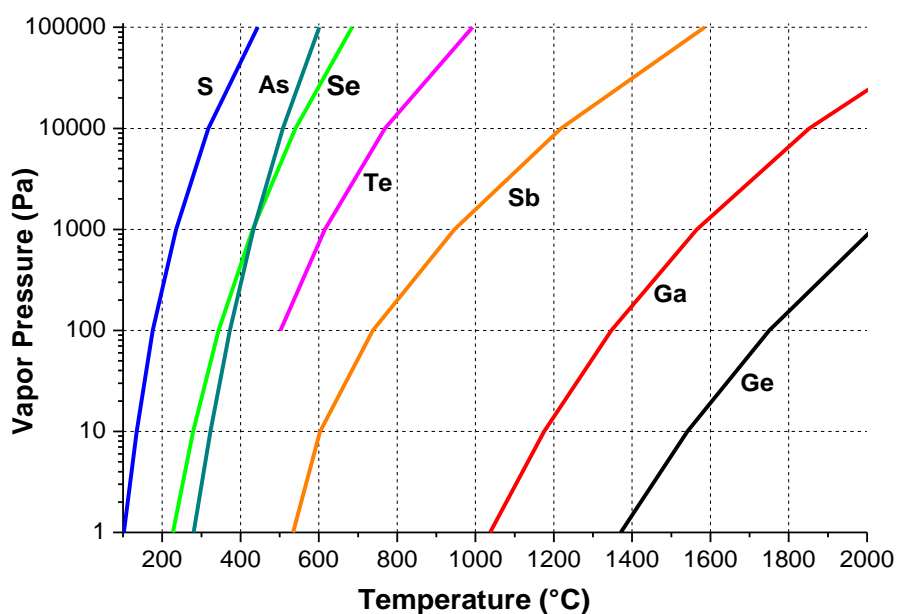


Figure 3.6: Vapor pressures of the elements commonly used to prepare chalcogenide glasses

As shown in figure 3.6, the elements commonly used in chalcogenide glasses compositions possess different vapor pressures. While elements such as sulfur, selenium or arsenic show relatively high vapor pressures, thus high volatilities, gallium and germanium have extremely low vapor pressures below 1000°C. Therefore, to ensure

reaction between the elements and avoid their evaporation during the synthesis process, closed systems are employed.

As mentioned previously, chalcogenide glasses are highly sensitive to the contamination by oxygen or other impurities. To limit this phenomenon, their synthesis is generally carried out using sealed silica ampoules. The standard set-up used is shown in figure 3.7. The pure raw starting elements (typically with 99.999% purity) are introduced in a silica tube and pumped under vacuum (the empty silica tube is previously cleaned and dried under vacuum to avoid the presence of impurities and moisture). A trap cooled with liquid nitrogen is used to retain potential volatile compounds and protect the vacuum pump. After some time, the tube is sealed to obtain a silica ampoule containing the raw starting elements.

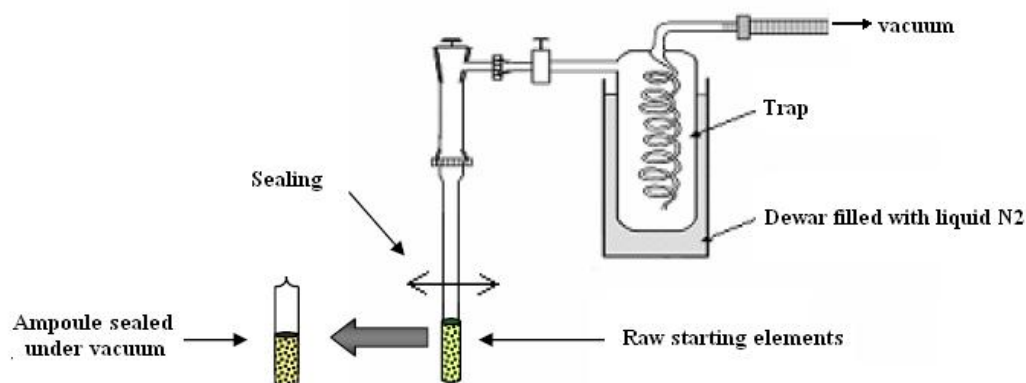


Figure 3.7: Typical setup used for synthesis in sealed silica ampoules under vacuum

The ampoule is then placed into a rocking furnace and heated up to high temperatures to melt the mix of elements [67]. The furnace is held at high temperature while rocking for several hours to ensure the reaction between the elements. The ampoule is then quenched, typically in air or water, to vitrify the melt and avoid crystallization

such as to obtain a bulk glass. The quenching step induces stress inside the glass due to the rapid decrease in temperature. In order to relax these constraints, the glass (still in the silica ampoule) is annealed in an annealing furnace at a temperature close but below the glass transition temperature (typically 10°C below T_g). After the annealing step, the silica ampoule is cautiously broken to remove the bulk chalcogenide glass. A bulk chalcogenide glass synthesized in sealed silica ampoule and a typical thermal treatment profile are presented in figure 3.8-a and 2.8-b, respectively.

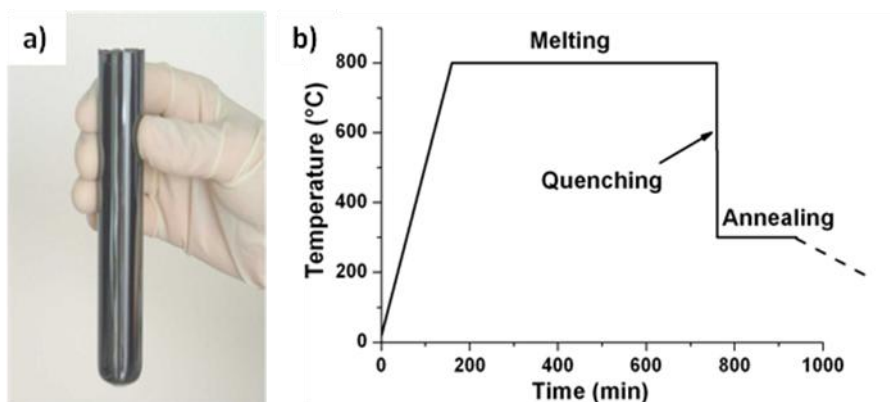


Figure 3.8: a) bulk chalcogenide glass synthesized in sealed silica ampoule; b) typical heat treatment profile used for glass synthesis

3.3. Synthesis in open system under argon atmosphere

3.3.1. Introduction

The cost of the single use silica ampoules used in the conventional synthesis technique represents a significant part of the final price of chalcogenide glasses. The aim of this study is the development of an innovative synthesis route based on open synthesis in reusable containers. The sensitivity of chalcogenide glasses to oxygen contamination during the synthesis process requires the experiments to be performed in a controlled,

oxygen-free atmosphere. The important differences in the thermal properties of the elements used to synthesize glasses in the Ge-Ga-Se system also bring technical challenges when open crucibles are used and high temperatures are involved. Two different approaches are presented in the following section, The first involves synthesis in a rocking furnace placed in a glove box maintained under argon atmosphere. The second involves synthesis in a silica chamber equipped with a rotating helix for homogenization purposes and placed under argon flux.

3.3.2. Preliminary tests in rocking furnace

The preliminary tests were performed on the $\text{Ge}_{25}\text{Ga}_5\text{Se}_{70}$ composition. This glass possesses the highest stability toward crystallization for glasses from the Ge-Ga-Se system, with a ΔT value ($T_x - T_g$) of 197°C [68].

3.3.2.1. Experimental setup

A rocking furnace was used to perform preliminary tests. The furnace, shown in figure 3.9, is placed on a vertical axis. An engine allows it to be swung to an angle up to 30° from the vertical. The elements to be melted are placed in a reusable open silica crucible. A two-position lever system enables to place the crucible in the central part of the furnace during the melting process or to lift it to the top of the furnace for the casting process. Once the glass is molten, the furnace is rotated 180° from the vertical to cast the melt. A holding system retains the crucible during the casting process.

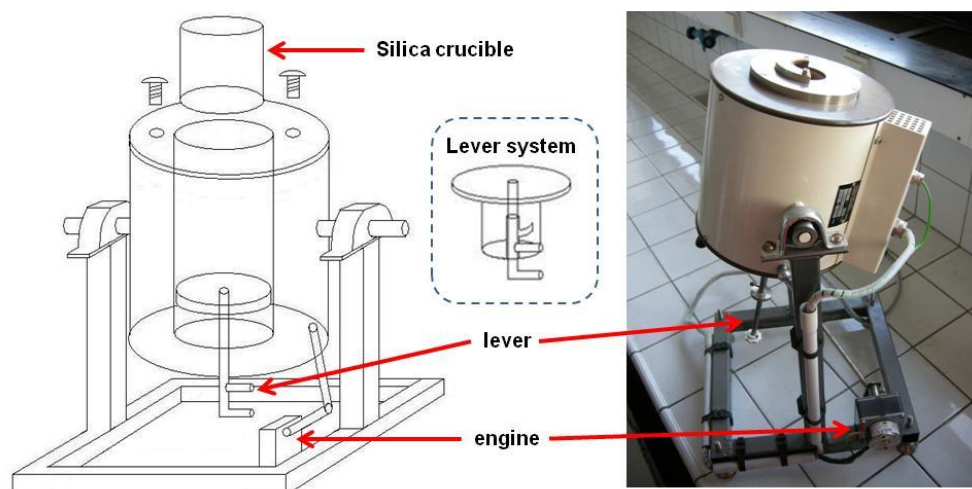


Figure 3.9: Rocking furnace used for preliminary tests

3.3.2.2. Melting of a previously synthesized bulk glass

To assess the ability of a glass to be melted in an open system and casted, bulk pieces of a $\text{Ge}_{25}\text{Ga}_5\text{Se}_{70}$ glass previously synthesized in a sealed silica ampoule were used and placed in the silica crucible.

The furnace temperature has to be sufficient to induce a low viscosity of the melt suitable for casting. However, high temperatures favor volatilization of the glass, yielding important weight losses. Thus, the temperature of melting and the experiment duration have to be carefully optimized to ensure the glass casting while avoiding an excessive volatilization of high vapor pressure elements. The minimal temperature necessary to rapidly attain an appropriate viscosity for $\text{Ge}_{25}\text{Ga}_5\text{Se}_{70}$ glass was determined to be 720°C .

The crucible containing 30.88 grams of bulk glass pieces was introduced in the rocking furnace at 720°C and homogenized for 10 minutes before casting it on a cold metallic plate. The casted melt was quickly pressed with a cold metallic weight to ensure

a rapid cooling of both faces of the glass. The weight was then removed and the glass was annealed at 253°C ($T_g - 20^\circ\text{C}$) for two hours.

A release of yellow/orange fumes was observed during the melting process. After the melting/casting process, 29.98 grams of glass were collected (casted glass and glass remaining in the melting crucible). A weight loss of 2.9% occurred during the process. The casted glass is shown in figure 3.10-a. Composition fluctuations or insufficient melting and homogenization time led to the presence of solid inclusions in the central part of the glass (figure 3.10-b).

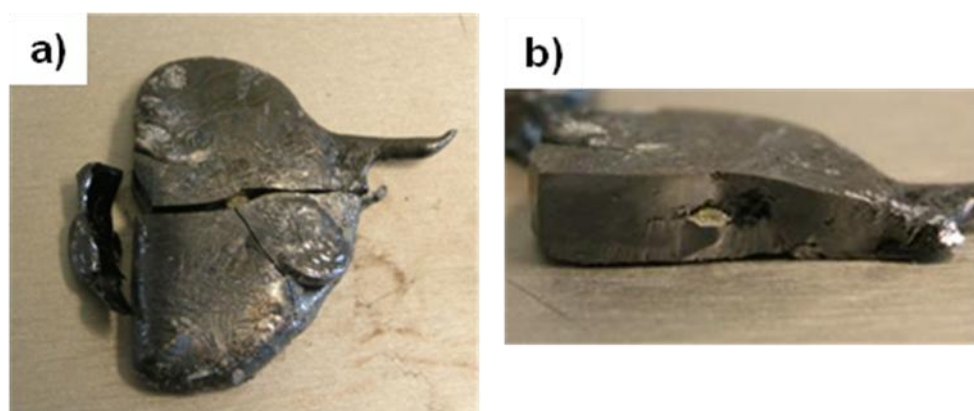


Figure 3.10: Casted $\text{Ge}_{25}\text{Ga}_5\text{Se}_{70}$ glass, a) top view and b) side view of the bulk sample

A piece of the casted glass was taken out and polished to obtain a 2mm thick sample with plane parallel faces (figure 3.11-a). An infrared camera operating in the 3-5 μm range was used to assess the homogeneity of the material after the process. The glass is transparent in the infrared, as seen in figure 3.11-b. Some defects are observed and may correspond to solid inclusions. An observation of the surface with an optical microscope (x10) shows the presence of bubbles (figure 3.11-c) and confirms the presence of inclusions (figure 3.11-d)

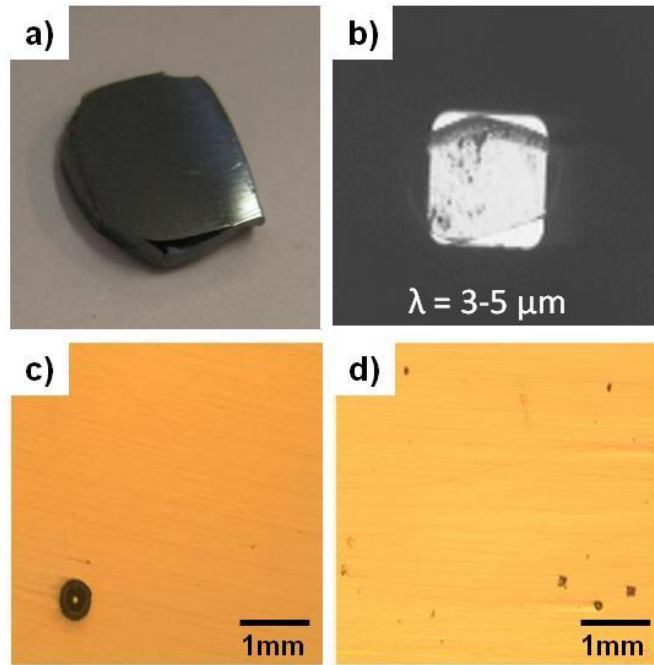


Figure 3.11: Casted $\text{Ge}_{25}\text{Ga}_5\text{Se}_{70}$ glass, a) after polishing and b) observed with a 3-5 μm thermal camera; c) bubbles and d) impurities observed on the glass surface with an optical microscope (magnification $\times 10$)

The optical transmission of the $\text{Ge}_{25}\text{Ga}_5\text{Se}_{70}$ glass was measured before and after the melting/casting process. The transmission (figure 3.12) is not significantly altered during the process. The glass remains transparent in the infrared range. This confirms the observation made with the infrared camera working in the 3-5 μm region (figure 3.11-b). The slight decrease of the maximum of transmission can be attributed to scattering induced by the bubbles observed within the casted glass.

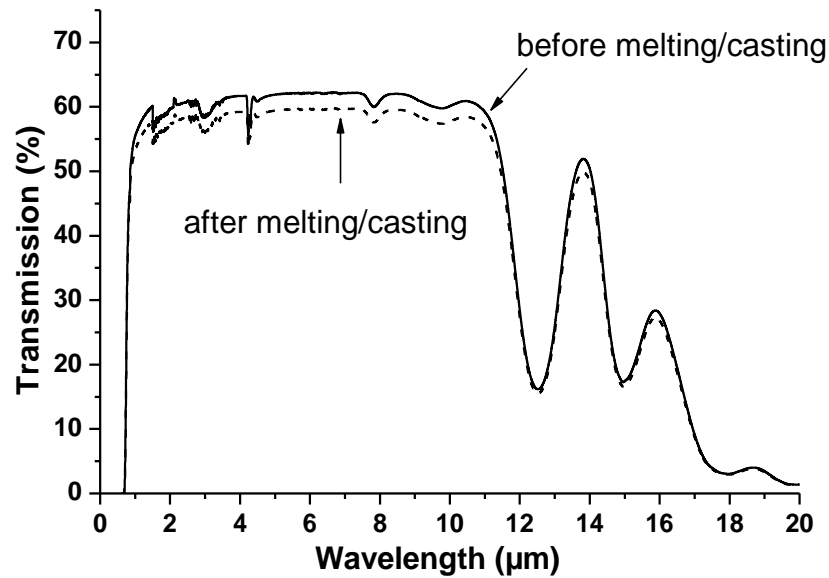


Figure 3.12: Optical transmission of the $\text{Ge}_{25}\text{Ga}_5\text{Se}_{70}$ glass before and after melting/casting process

The characteristic temperatures of the glass have been measured before and after the melting/casting process and are presented in table 3.3. The glass transition temperature (T_g) of the $\text{Ge}_{25}\text{Ga}_5\text{Se}_{70}$ glass remains stable. The crystallization temperature (T_x) is decreased by 18°C , yielding a lower ΔT value of 180°C after the process.

Table 3.3: Thermal properties of the $\text{Ge}_{25}\text{Ga}_5\text{Se}_{70}$ glass before and after melting/casting process

	$T_g (\pm 2^\circ\text{C})$	$T_x (\pm 2^\circ\text{C})$	$\Delta T (\pm 4^\circ\text{C})$
Before process	275	473	198
After process	277	457	180

The fumes observed during melting were collected and analyzed by EDS. A small silica plate placed on the top of the crucible was used to deposit the evaporated material. Dendritic crystals were observed (figure 3.13). Their composition was determined to be GeSe_2 . No gallium was detected in the fumes. Thus, the weight loss occurring during the melting of the glass is due to losses of germanium and selenium.

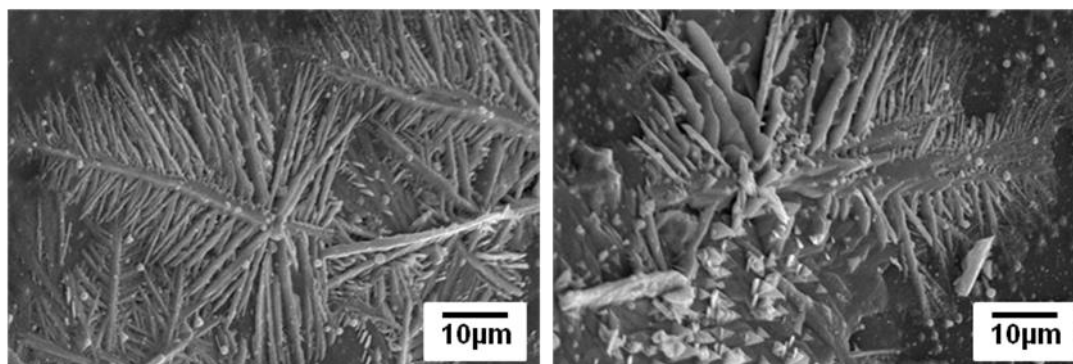


Figure 3.13: GeSe₂ crystals observed in the fumes deposited after melting/casting process

This preliminary study showed the possibility to remelt and cast a chalcogenide glass presenting a good optical transmission. The obtained material contained some defects and bubbles and a slight weight loss due to evaporation of the material was observed. The aim of this initial experiment was uniquely to assess the feasibility of the melting and casting process and the experimental parameters were not optimized. However, these preliminary tests performed with pieces of a glass previously synthesized in sealed silica ampoules confirm the possibility of casting chalcogenide glasses in an open environment. The next step is then to test this experimental setup for synthesis from the pure raw elements.

3.3.2.3. Melting/casting from the pure raw elements

Pure raw Ga, Ge and Se were introduced in the silica crucible in stoichiometric quantities to obtain a glass with composition of Ge₂₅Ga₅Se₇₀. The elements were introduced as fine powders to enhance their specific surface area, thus their reactivity. The crucible was introduced in the furnace at room temperature to avoid excessive evaporation of selenium. The temperature was then slowly increased with a heating ramp of 2°C/min.

Abundant emanations of fumes were observed and required to stop the process before a temperature of 600°C was reached. Most of the selenium was evaporated, while the germanium remained unmelted. Important weight losses were calculated (>60%), corresponding to a nearly total evaporation of the selenium. It was not possible to obtain a reaction between the different elements with this experimental setup. This emphasizes the difficulty to synthesize a glass of the Ge-Ga-Se ternary system from the raw elements in an open system, due to the important difference in melting temperatures of selenium and germanium.

3.3.2.4. Conclusion on the preliminary tests

Melting and casting of a glass of the Ge-Ga-Se ternary system with no loss of optical transmission is possible. However, this has been realized using glass pieces previously prepared in sealed silica ampoules, and the experimental setup studied does not appear suitable for synthesis from the raw starting elements. Poor homogenization obtained in the rocking furnace did not allow for good reaction between the elements and important materials losses were observed when open crucibles were used. These poor results led to the study of another experimental setup, comprising a closed, reusable silica chamber equipped with a homogenization device.

3.4. Synthesis in closed silica chamber with homogenization device

3.4.1. Experimental setup

In 2009, Erwan Guillevic at the University of Rennes 1, France, utilized a reusable closed silica crucible equipped with a rotating helix to synthesize As-Se glasses from the pure raw starting elements [69]. The experimental setup is shown in figure 3.14-a. The raw elements were introduced in a silica tube with an inner diameter of 60mm and a silica cap placed on its top. Vacuum grease was used to seal the two parts of the system. A constant flux of argon was applied inside the silica chamber to avoid contamination by oxygen during the synthesis process. The temperature of the furnace was progressively increased to 430°C to ensure the reaction between the elements while homogenization was performed by rotations of the helix. Then, after 50h of reaction, the helix was removed from the melt and the silica tube was taken out of the furnace. The tube was quenched in air and introduced in an annealing furnace at a temperature slightly below the T_g of the glass. After annealing, the silica tube was cut to extract the glass sample. It is important to note that only the bottom of the silica tube is cut and can be re-sealed for subsequent experiments. The consumption of silica is thus limited in this process.

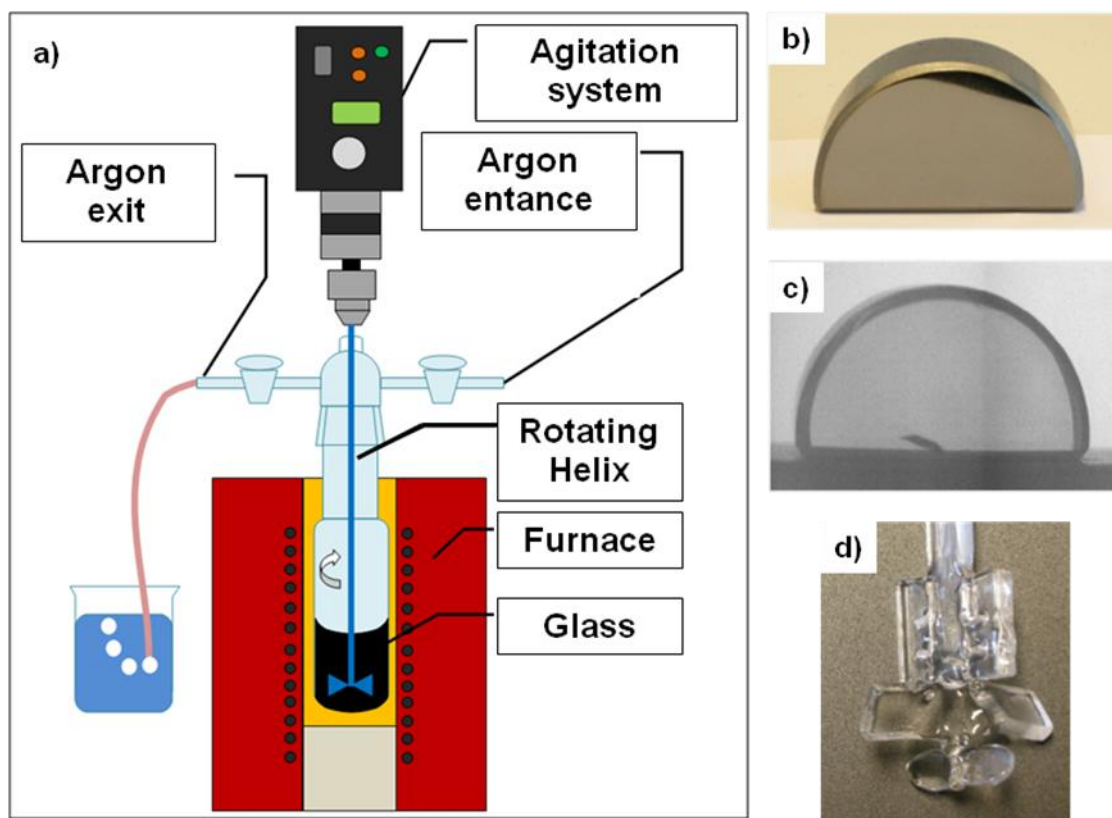


Figure 3.14: a) Experimental setup used for synthesis in closed silica chamber; b) As_2Se_3 bulk glass obtained by Guillevic and c) observed with a 3-5 μm thermal camera; d) rotating helix used for experiments [11]

Reproducible bulk As_2Se_3 glasses with a mass of more than 400 grams were produced (figure 3.14-b). A picture taken with a thermal camera working in the 3-5 μm range shows an excellent homogeneity and optical transparency of the sample (figure 3.14-c). The study by Guillevic emphasized the role of the rotating helix to obtain homogeneous, bubble-free bulk glass. The shape of helix giving the best results is presented in figure 3.14-d.

The same experimental setup was used to synthesize $\text{Ge}_{25}\text{Ga}_5\text{Se}_{70}$ glasses. It is important to remember that while bulk As_2Se_3 glasses were produced with this process, arsenic and selenium possess close thermal properties. The introduction of germanium and gallium, which melting temperature and vapor pressure are strongly different than

that of selenium, induces additional technical challenges when these three elements are melted together.

3.4.2. Synthesis of the $\text{Ge}_{25}\text{Ga}_5\text{Se}_{70}$ glass

The raw starting elements were introduced in the silica tube in stoichiometric proportions to prepare 300 grams of $\text{Ge}_{25}\text{Ga}_5\text{Se}_{70}$ glass. Selenium and germanium were milled into fine powders and manually mixed together before introduction in the tube to increase their specific surface area, thus their reactivity. Gallium, which melts at low temperatures (30°C), was introduced as bulk pieces. The homogenization helix was placed in the setup and the silica cap was sealed with vacuum grease on the top of the tube. The silica chamber was pumped under vacuum for 30 min, and then filled with argon. This vacuum/argon filling process was conducted three times to evacuate the oxygen inside the experimental setup. Subsequently, a constant flux of argon was applied during the complete duration of the experiment.

The temperature was rapidly increased to 350°C to avoid an excessive evaporation of selenium. At this temperature, both Ga and Se are molten. The speed of the helix was set at 4 rotations per minute to enhance reaction between the elements and increase homogeneity. A heating ramp of $2^\circ\text{C}/\text{min}$ was then applied.

The helix was blocked in the reaction mix when the temperature reached 400°C . This is likely due to the reaction of germanium which higher coordination results in a higher melt viscosity at the temperature of the experiment. The helix remained blocked until the furnace reached a temperature of 700°C . At this temperature, important

emanations of fumes were observed inside the silica chamber. This led to an increase of the pressure resulting in a loss of integrity of the sealing between the two parts of the silica setup. Due to important releases of fumes outside the reaction setup, the experiment had to be stopped. The setup containing the molten glass was rapidly removed from the furnace and quenched in cold water. During the process, some of the fumes crystallized on the upper part of the silica chamber. The crystals were analyzed by EDS and determined to be pure selenium.

After the experiment, the reaction product was extracted from the tube. As shown in figure 3.15-a, an inhomogeneous block was obtained. The blades of the helix do not allow homogenization on the entire diameter of the silica tube. A portion of the initial powder remained in the outer part of the melt during the process and formed a shell of compacted powder as observed in figure 3.15-a.

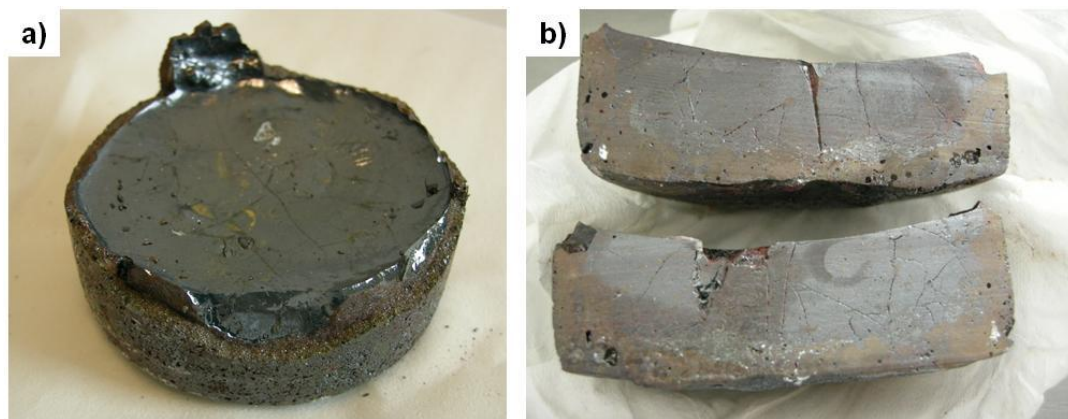


Figure 3.15: a) Bulk material obtained by synthesis in closed silica chamber of $\text{Ge}_{25}\text{Ga}_5\text{Se}_{70}$ composition and b) cross section

The central part of the material, which benefited from a better homogenization, presented an amorphous glassy aspect. A lateral cut was performed to analyze a cross section of the block. As seen on figure 3.15-b, the resulting material presents an

inhomogeneous aspect. The presence of bubbles is also noted. Some elemental metallic gallium remains and appears as shiny grey dots. Gallium ($d=5.90\text{g.cm}^{-3}$) is more dense than Se ($d=4.82\text{g.cm}^{-3}$) and Ge ($d=5.32\text{g.cm}^{-3}$) and due to the lack of homogenization, the unreacted gallium is found at the bottom sample (figure 3.15-b). Energy Dispersive X-Ray Spectroscopy (EDS) analyses were carried out on four different zones of the block. The atomic percentage of gallium, germanium and selenium in the different zones are presented in table 3.4. The atomic contents are probed on volumes of $1\text{ }\mu\text{m}^3$. The three elements are detected in different proportions throughout the sample. This indicates that only partial reaction has occurred between Ga, Ge and Se.

SEM micrographs of material cross section reveals the presence of unmelted elements (figure 3.16-a) and crystalline inclusions (figure 3.16-b). The composition of the crystals was determined by EDS to be GeSe_2 .

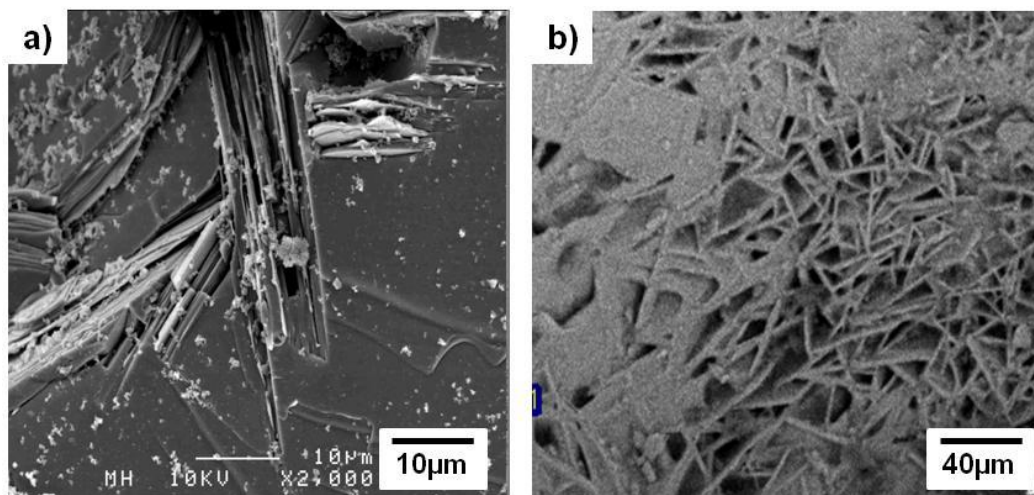
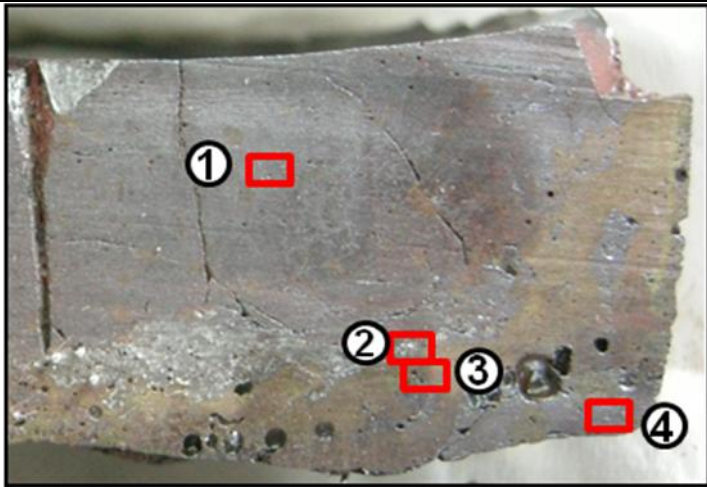
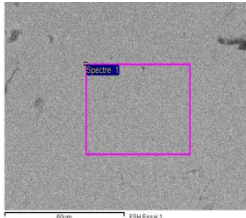
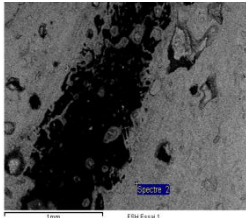
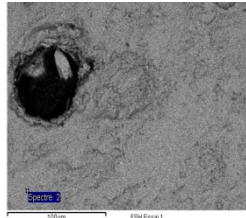
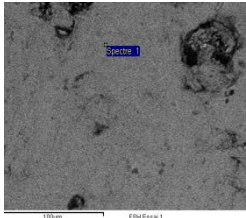


Figure 3.16: a) Unmelted powder grains and b) GeSe_2 crystals observed in the bulk material

Table 3.4: Electron Dispersive X-Ray Spectroscopy analysis of the obtained material

			
Zone 1	Zone 2	Zone 3	Zone 4
			
Ga: 2.0 at% Ge: 22.2 at% Se: 75.8 at%	Ga: 5.8 at% Ge: 29.6 at% Se: 64.6 at%	Ga: 23.7 at% Ge: 25.9 at% Se: 50.4 at%	Ga: 0.0 at% Ge: 48.1 at% Se: 51.9 at%

3.4.3. Conclusion on the synthesis in open system

Previous studies by Erwan Guillevic have demonstrated successful production of As-Se glasses in sealed silica chamber under argon atmosphere [69]. The use of germanium in synthesis of glasses from the Ge-Ga-Se system with this process brought additional technical challenges. The melting temperature of Se (221°C) is significantly lower than that of Ge (938°C). Prolonged stages at high temperatures are required to

ensure the reaction between the elements. The high vapor pressure of selenium led to important emanations of fumes and the integrity of the silica chamber was impaired before a complete reaction could be reached. The importance of the homogenization of the melt was also pointed out. The lack of homogenization in the outer region of the silica tube led to the formation of a shell composed of compacted, partially molten powder grains. Partial crystallization of the material and incomplete melting of the initial powder were also observed. Therefore this synthesis method does not appear suitable for synthesis of Ge-based glasses starting from the raw elements.

Controlling the melt viscosity for optimal homogenization is the key factor when glass synthesis is performed by melting of raw elements. Compositional fluctuations during the reaction process lead to large variations in melt viscosity which is difficult to control thermally. The challenges encountered during the synthesis of Ge-Ga-Se glasses in open systems therefore lead to investigate alternative approach for homogenization and reaction of raw elements. The next section presents an alternative synthesis route based on mechanosynthesis where the reaction is driven by mechanical energy instead of thermal energy.

3.5. Mechanosynthesis

3.5.1. Introduction

By definition, mechanosynthesis is a powder processing technique that allows production of homogeneous materials starting from blended powder mixtures [70].

Mechanosynthesis can be distinguished as either mechanical alloying (MA) or mechanical grinding (MG). The difference between MA and MG resides in the nature of the powder mixture. When elemental powders are used, the process is termed MA, while MG corresponds to mixtures of alloy powders.

In the mechanosynthesis process, the energy required for the reactions is of mechanical nature, contrarily to thermal energy used to produce materials by melting of the elements. High energy mills with high milling speeds and equipped with milling jars and grinding balls are used to furnish this mechanical energy. Different types of mills are commercially available (planetary ball mills, attritors, shaker mills, knife mills...), and different materials may be used for the grinding jars and balls (steel, alumina, zirconium oxide, agate, tungsten carbide...).

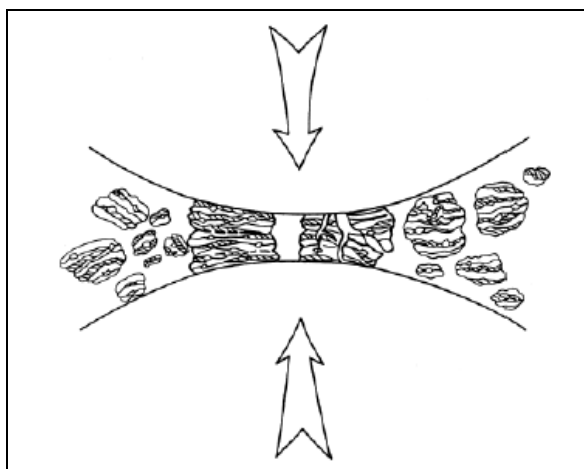


Figure 3.17: ball-powder-ball collisions of powder mixture during mechanosynthesis

The actual process of mechanosynthesis starts with mixing of the raw starting elements in the right proportion and loading the mix into the mill along with the grinding medium (generally steel balls). Ball-powder-ball collisions of the powder mixture ensure the reaction between the elements by repeated welding, fracturing, and rewelding, as

shown in figure 3.17. This mix is milled for the desired length of time until a steady state is reached when the composition of every powder particle is the same as the proportion of the elements in the starting powder mix. The important parameters of the mechanosynthesis process are:

- Raw starting elements
- Mill
- Milling container
- Milling speed and duration
- Milling medium
- Ball-to-powder weight ratio
- Atmosphere
- Temperature of milling
- Potential process control agents

Mechanosynthesis was developed in the 1960s and the first industrial application occurred few years later, when the International Nickel Company (INCO) used this process to produce nickel superalloys [71], oxide dispersion strengthened (ODS) aluminum and aluminum-magnesium alloys [72, 73]. Mechanical alloying has since been widely used to produce metallic alloys at room temperature such as Fe-Al [74] and ZnSe [75] binary systems, CoNbSn [76] ternary system, or PbMgNbTi alloys [77]. It allows the formation of alloys and compounds that are difficult or impossible to produce by the conventional melting and casting technique. For example, the large difference in the melting points between Al (933K) and Ta (3293K) restricts the production of Al-Ta binary alloys by melting while mechanosynthesis allows its formation at room temperature [78].

Mechanical alloying is an easily scalable process (from laboratory scale to industrial scale) that offers a variety of attributes, including the production of fine dispersion of second phase (usually oxide) particles, the extension of solid solubility limits, the refinement of grain sizes down to nanometer range, the possibility to synthesize novel crystalline and quasi-crystalline phases, the development of amorphous (glassy) phases, the disordering of ordered intermetallics, the possibility of alloying elements which are difficult to alloy and the activation of chemical reactions at low temperatures.

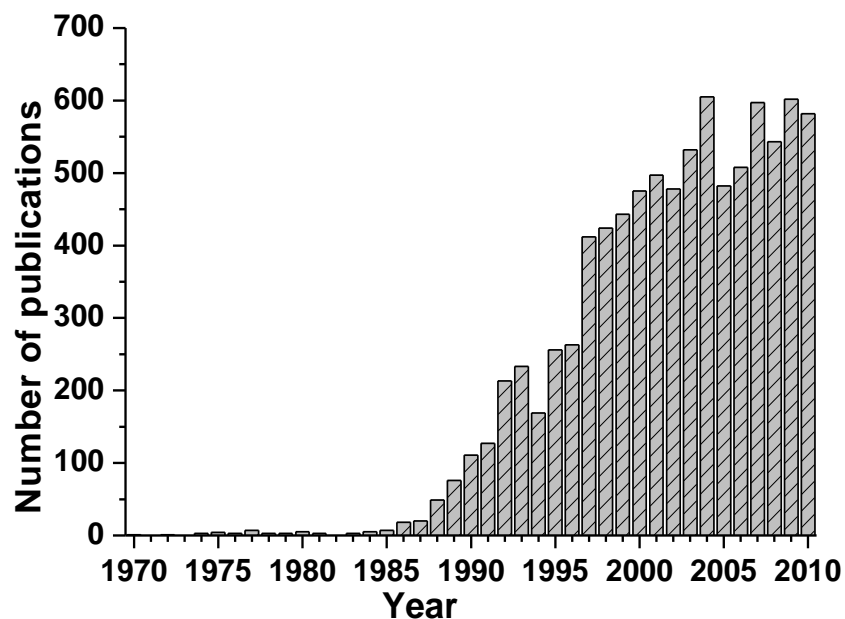


Figure 3.18: number of publications per year reporting synthesis of materials by mechanical alloying

This variety of applications and the relatively inexpensive equipment needed (on the laboratory scale) has made this method very popular for the preparation of many novel compounds. This is emphasized by the increased number of publications reporting the use of mechanical alloying in the last few decades, as shown in figure 3.18. Since the

first publication by Benjamin in 1970, this number has continuously increased to reach over 600 annual publications in recent years.

3.5.2. Amorphization by mechanical alloying

As mentioned previously, amorphous materials can be prepared by mechanosynthesis. In 1983, Koch et al. were the first to study the amorphization of $\text{Ni}_{60}\text{Nb}_{40}$ by mechanical alloying of pure elemental metallic powders. Strong similarities in X-Ray diffraction patterns and crystallization behavior were shown between the as-prepared alloy and alloys synthesized by conventional melt-quenching technique [79]. Preparation of amorphous metallic materials (metallic glasses) by mechanosynthesis have since been widely studied. The main reason is that MA offers the possibility to easily prepare amorphous materials while the melt-quenching technique sometimes requires high quenching rates of the liquid, which can be difficult to achieve. In fact, studies report amorphization of numerous metallic alloys by MA, such as Hf-Al, Hf-Cu, Zr-Co, Zr-Fe, Cu-Al, Sn-Ni or Al-Ni-Fe-Gd alloys. More recently, amorphization of molecular compounds such as lactose-mannitol or budesonide/ α -lactose molecular alloys using ball milling have been reported [80-83]. Only a few studies have reported amorphization of compounds including chalcogenide elements. These studies are limited to Ga-Se, Ge-Se and Ge-GeSe mixtures [84-90]. It is important to notice that no bulk materials were prepared and that studies were limited to the powder properties.

The mechanism of amorphization induced during mechanosynthesis is not clearly understood. However, two models have been developed to explain this phenomenon: the

liquid quenching (LQ) model and the solid state amorphization reaction (SSAR) model [91].

3.5.2.1. Liquid Quenching model

LQ model assumes partial melting of the powder particles under the impact of the colliding balls followed by ultra-rapid quenching. The deformation of the particles trapped in balls collisions induces a local rise in temperature that may result in local melting of the powder. The liquid layer formed this way rapidly solidifies by heat dissipation into the cooler regions of the particle. The repetition of this rapid melting-solidification process yield amorphous powder. However, the theoretical quenching rates implied in LQ model (as high as 10^6K/sec) may not be consistent with experimental conditions. Moreover, even if measurements of the temperature change during ball collisions are not possible, theoretical calculations showed that the temperature increase is limited to a few hundreds of kelvins [92] and would therefore be insufficient to induce melting of the powder particles. The LQ model was the first model developed to explain amorphization by MA, but its inability to rationalize the results of mechanosynthesis experiments carried out at a temperature significantly below T_g led to the development of an alternative model called the Solid State Amorphization Model (SSAR).

3.5.2.2. Solid state amorphization model

This model assumes a fine chemical reaction between each element of the powder mixture. Amorphization has been shown to happen in metallic alloys with a high negative

heat of mixing and elements with significantly different atomic sizes. This difference in atomic radii is believed to induce a high difference in chemical diffusivity of the elements in each other, kinetically hindering the formation of stable crystalline compound in favor of the amorphous alloy [91]. Caron et al. studied a series of trehalose/mannitol molecular alloys prepared by MA at room temperature and showed that amorphization follows the SSAR model instead of LQ model when milling temperature is lower than the T_g of the alloy [93].

3.5.3. Choice of milling balls

During the mechanosynthesis process, collisions occur between the milling jar, the raw elements and the grinding balls. These high energy collisions may result in a contamination of the powder by the milling balls. Studies showed that the mechanical alloying of nickel-tungsten alloy powders using grinding elements made of steel (which is much softer than tungsten) resulted in an important contamination of the final powder by iron [94]. A solution to limit this phenomenon is to use a container and a grinding medium harder/stronger than the powder to be milled. Table 3.5 summarizes the hardness of the raw elements used during this study, germanium, selenium and gallium.

Table 3.5: Hardness of some commercially available materials used as milling elements

Material	Hardness (Mohs)
Germanium	6
Gallium	1.5
Selenium	2
Stainless steel	5
Hardened steel	6
Agate	6.5-7
Tungsten Carbide	9
Zirconium oxide	8.5

The hardness values for the different milling balls commercially available from Retsch (stainless steel, hardened steel, agate, tungsten carbide, zirconium oxide) are also listed [95]. Mohs' Hardness was chosen as a reference scale. It is applied to non-metallic elements and minerals. In this scale, hardness is defined by how well a substance resists scratching by another substance. A scale of 1 to 10 with half-step increments is employed. Members with higher scale numbers will scratch the surface of members of equal or lower scales.

Though selenium and gallium are rather ductile materials, germanium shows a substantial hardness. The use of steel or agate as grinding medium would lead to an important deterioration of the milling elements and thus to important contamination. To limit this potential contamination, tungsten carbide (WC) was chosen as the material of choice for the milling jar and the milling balls used to perform the experiments. Figure 3.19 shows the planetary ball mill Retch PM100 used for the mechanosynthesis tests.



Figure 3.19: Retch PM100 planetary ball mill

3.5.4. Mechano-synthesis of GeSe₄

Preliminary tests were performed on the well known GeSe₄ glass. This composition comprising both Ge and Se has already been widely studied when synthesized by conventional melt/quenching technique [96-98]. The keen knowledge of the properties of this glass facilitates the evaluation of the mechano-synthesis process.

3.5.4.1. Experimental procedure

Pure raw metallic germanium (5N, Umicore) and selenium (5N, Umicore) were introduced in the WC milling jar in stoichiometric quantities to obtain 20 grams of material. Six WC grinding balls, with a total weight of 375g were added, yielding a 19:1 ball-to-powder weight ratio. The jar was then sealed. The weighing of the elements and their introduction in the milling jar was done in a glove box under argon atmosphere to limit oxygen contamination. The following steps of the mechano-synthesis were performed outside the glove box.

The milling jar was introduced into the planetary ball mill. Milling cycles of 3 min at 400rpm were scheduled with direction reversal and a pause of 3 min between each cycle. The jar was opened inside the glove box at different milling durations to collect powder samples. After each sample collection, the jar was re-sealed and the milling was pursued. The total duration of milling was 100h.

3.5.4.2. Coloration of the powder

Photographs of the powder obtained after 0 h, 20h, 30 h, 40 h and 50 h of milling are shown in Figure 3.20, and indicate a change in coloration with milling duration.

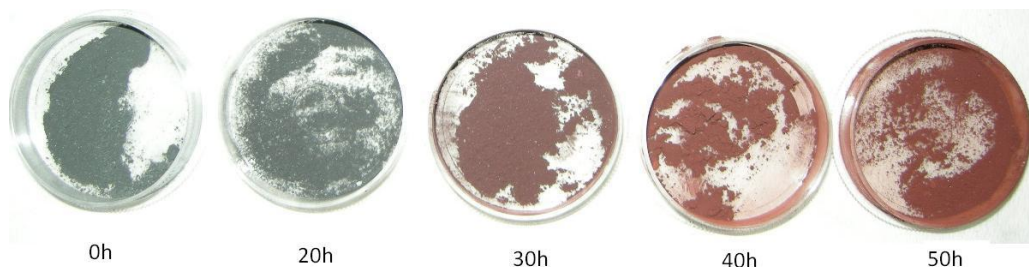


Figure 3.20: Evolution of the powder coloration with milling time

Before milling (0 h), the powder presents a dark grey aspect, corresponding to a mix of the metallic selenium and germanium powders. The color progressively turns to red as the milling time increases, indicating a lowering of particle size and a progressive reaction between the raw elements.

3.5.4.3. X-Ray Diffraction

The XRD spectra carried out on the powders at different milling durations are presented in figure 3.21. Before milling, peaks corresponding to the pure Ge and Se metallic elements are observed. After 5 hours of milling, all the selenium has been amorphized, leading to the disappearance of the corresponding characteristic diffraction peaks located at 21.0 ; 23.2 ; 25.0 ; 29.1 ; 32.2 ; and 39.8° (2θ). A part of the germanium remains in the metallic form.

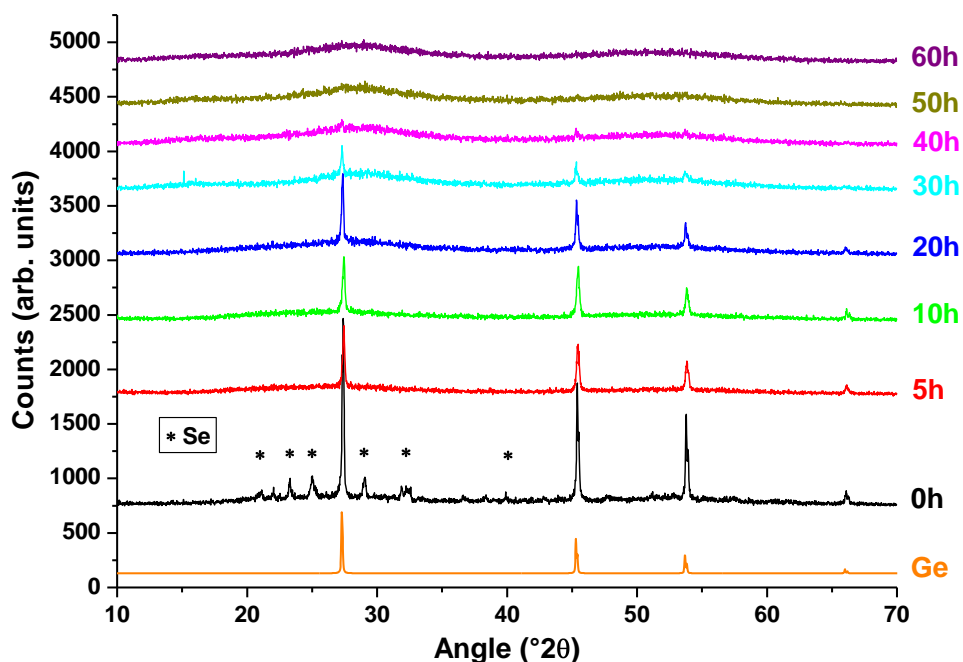


Figure 3.21: Evolution of the XRD spectra of the GeSe_4 powder with milling time

With longer durations of milling, the proportion of metallic germanium decreases, and the diffraction peaks progressively disappear, indicating a progressive microstructural change to amorphous powder. No more peaks are observed after 50h of milling. The shape of the XRD spectra is typical of an amorphous state. All the germanium has reacted with the selenium to form a glass powder.

3.5.4.4. Differential Scanning Calorimetry

The DSC curves obtained from 10mg of powder with a heating ramp of $10^\circ\text{C}/\text{min}$ are presented in figure 3.22 and show the evolution of the thermal properties of the powder after different milling durations. The T_g of the powder remains near 50°C up to 10 h of milling and a crystallization peak is observed at temperatures below 150°C . With

longer durations of milling, the glass transition of the samples shifts toward higher temperatures and no crystallization peaks are observed up to 250°C. After 50 h of milling, the T_g is stabilized at 165°C, and remains unchanged after 100 h of experiment.

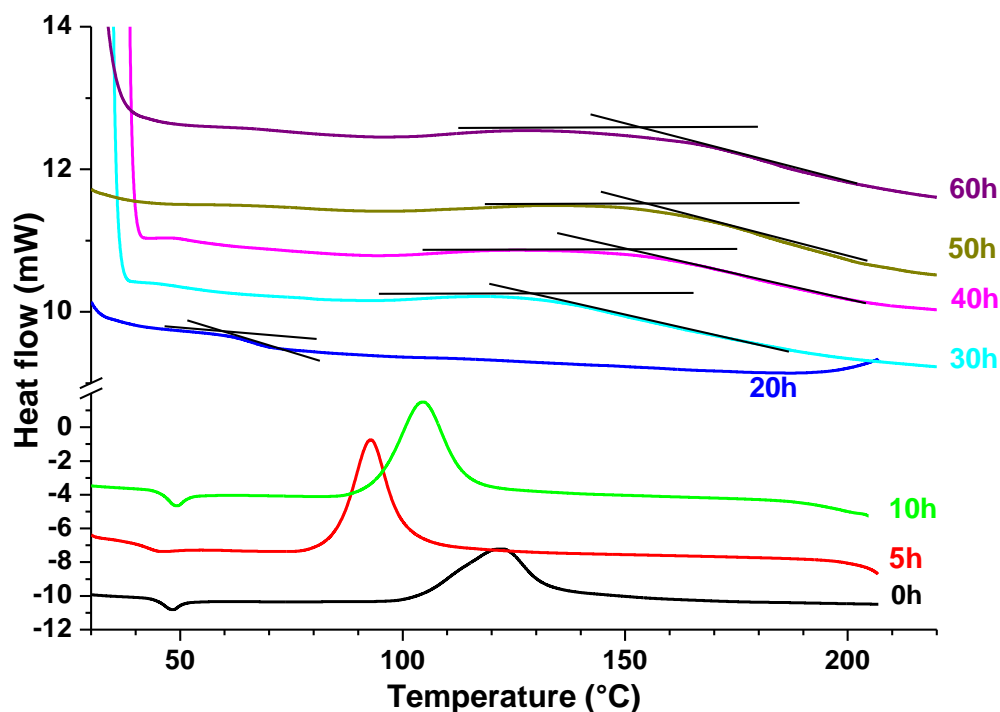


Figure 3.22: Evolution of the characteristic temperatures of the GeSe_4 powder with milling time

Figure 3.23 shows the evolution of the glass transition temperature of the powder with milling duration. The T_g of different Ge-Se glasses (prepared by melt/quenching technique in sealed silica ampoule) is indicated [98]. The T_g of ~50°C observed up to 10h of milling is consistent with the T_g of pure selenium (0at% of Ge), indicating that the selenium has been amorphized but that Se and Ge have not yet reacted to a significant extent. The subsequent increase in T_g indicates a progressive reaction of the two elements to form an amorphous Ge_xSe_y phase with an increasing content of germanium.

The value of the T_g is stabilized at 165°C after 50 h and does not change afterwards. This temperature corresponds to the T_g of the GeSe_4 glass.

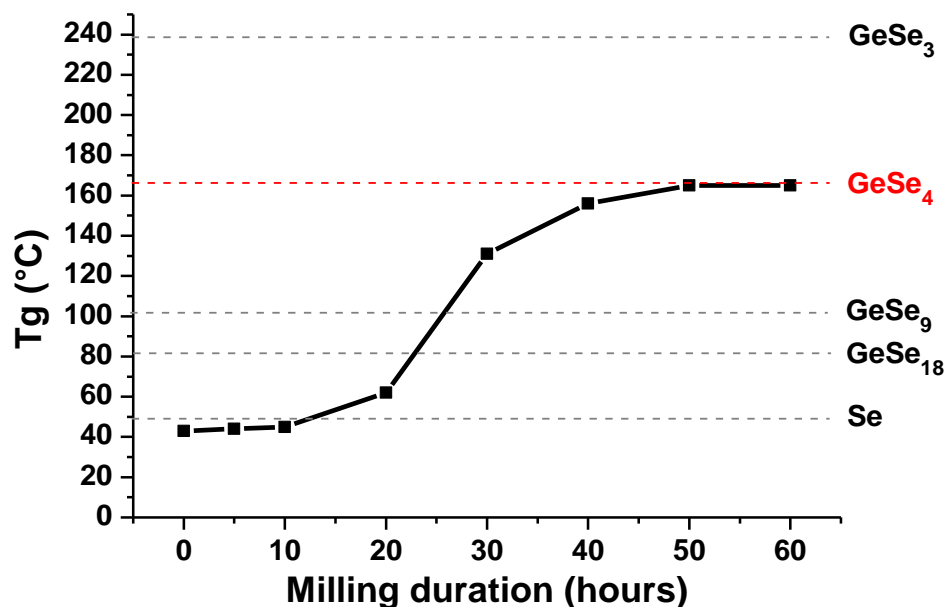


Figure 3.23: Evolution of the glass transition temperature (T_g) of the powder with milling duration

3.5.5. Mechanochemical synthesis of $80\text{GeSe}_2\text{-}20\text{Ga}_2\text{Se}_3$

3.5.5.1. Experimental procedure

The experimental procedure used to prepare the $80\text{GeSe}_2\text{-}20\text{Ga}_2\text{Se}_3$ was similar to that of GeSe_4 . A stoichiometric quantity of pure raw metallic germanium (5N, Umicore), gallium (6N, Cerac) and selenium (5N, Umicore) equivalent to 45 grams of material were introduced in a glove box and mixed in the WC milling jar containing the grinding balls, for a 8:1 ball-to-powder weight ratio. After sealing, the jar was taken out of the glove box and introduced into the planetary ball mill. Milling cycles of 3 min at 400rpm were

performed with direction reversal and a pause of 3 min between each cycle. Powder samples were collected at given milling durations by opening the jar to perform analyses. After each sample collection, the jar was re-sealed and the milling was pursued. The total duration of milling was 100h. The collected powder samples were analyzed by X-Ray diffraction, DSC, Raman spectroscopy and solid state NMR.

3.5.5.2. Coloration of the powder

The powders obtained after 0 h, 3 h, 5 h, 8 h, 10 h, 20 h, 40 h and 80 h of milling are shown in figure 3.24 and indicate a change in coloration with milling duration. Before milling (0 h), the powder presents a dark grey aspect, corresponding to a mix of the metallic raw elements. The color progressively turns into a red/orange powder as the milling time increases, indicating a lowering of particle size and a progressive reaction between the raw elements.

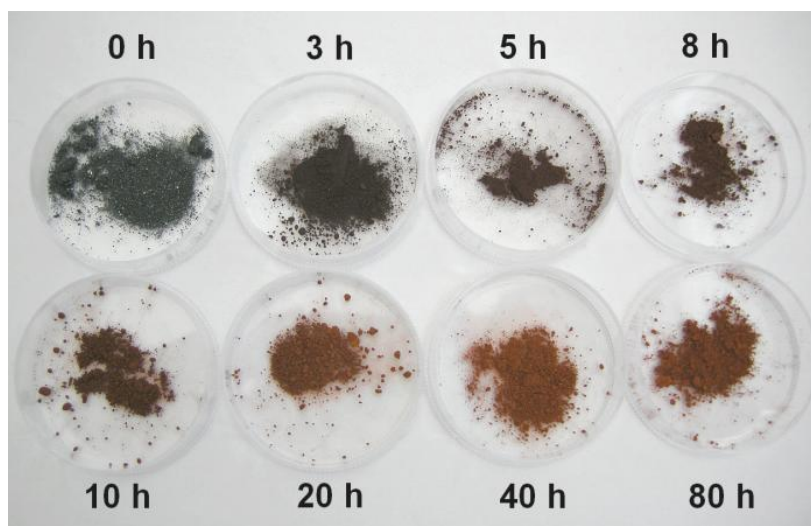


Figure 3.24: Evolution of the $80\text{GeSe}_2\text{-}20\text{Ga}_2\text{Se}_3$ powder coloration with milling time

3.5.5.3. Particle size distribution

The evolution of particle size distribution with milling duration is presented in figure 3.25.

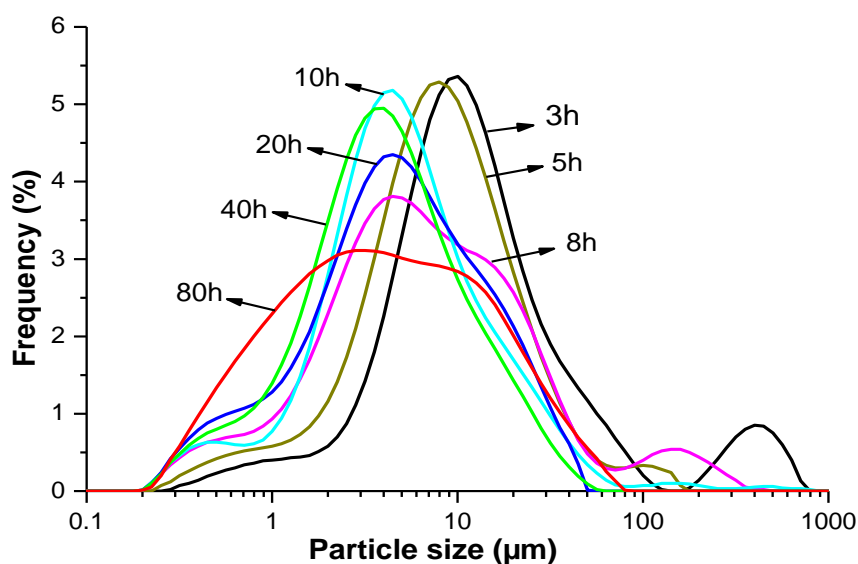


Figure 3.25: Evolution of the particle size distribution with milling time

After 3 hours of milling, the distribution is bimodal. A part of the powder is composed of particles smaller than 100 μm , while some particles between 200 μm and 800 μm remain. The proportion of big particles decreases with milling duration, and no particles bigger than 100 μm are observed after 10h. Then, the distribution of the particles size tends to smaller dimensions, more and more particles with a size less than 1 μm are observed. After 80 h of milling, the size of the particles is evenly distributed and their dimensions range from 0.2 μm to 80 μm .

Increased milling duration leads to increased amount of particles with small dimensions (below 1 μm). The median value (or D50, defined as the threshold size where half of the population is larger, and half is smaller) is 3.72 μm .

3.5.5.4. X-Ray Diffraction

The X-Ray diffraction spectra recorded on the sample powders after 3 h, 5 h, 8 h, 10h, 20 h, 40 h and 80 h of milling are presented in figure 3.26. After 3 h of milling, only the three main characteristic diffraction peaks of the crystalline germanium are observed. No peaks corresponding to Se or Ga phases appear, indicating that these two elements have already been amorphized.

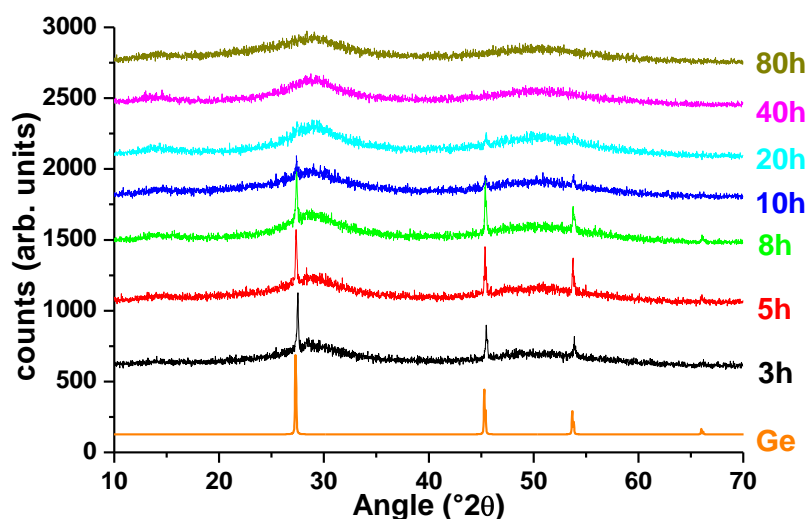


Figure 3.26: Evolution of the XRD spectra of the 80GeSe₂-20Ga₂Se₃ powder with milling time

For longer milling durations, the height of the Ge peaks progressively decreases while a broader background appears. This can be attributed to a progressive reaction of Ge to form an amorphous compound. After 40 h, a broad spectrum corresponding to an

amorphous powder is obtained. After 80 h of milling the peak slightly broadens indicating further amorphization of the powder.

It is interesting to note that the amorphization of the powder occurs in shorter times for the $80\text{GeSe}_2\text{-}20\text{Ga}_2\text{Se}_3$ powder than for the GeSe_4 powder. The gallium melts at low temperatures ($T_m=29.7^\circ\text{C}$). Due to the small increase in temperature induced during the milling process, this element is in its liquid form during mechanosynthesis. It is believed that this liquid phase acts as a milling medium enhancing the reaction between the elements. Thus, the reaction between the Ge and Se occurs in shorter duration as compared to GeSe_4 mechanosynthesis, in which all elements are in solid state.

3.5.5.5. Differential Scanning Calorimetry

The DSC curves obtained on ~10mg of powder at different milling durations are presented in figure 3.27. The heating ramp was $10^\circ\text{C}/\text{min}$. The measured glass transition temperatures (T_g) and temperatures of crystallization (T_x) are indicated in table 3.6. The characteristic temperatures of $80\text{GeSe}_2\text{-}20\text{Ga}_2\text{Se}_3$ glass made in sealed silica tube under vacuum are also given. A magnification of the DSC curves obtained on the powders after 3h and 5h of milling is presented in figure 3.28.

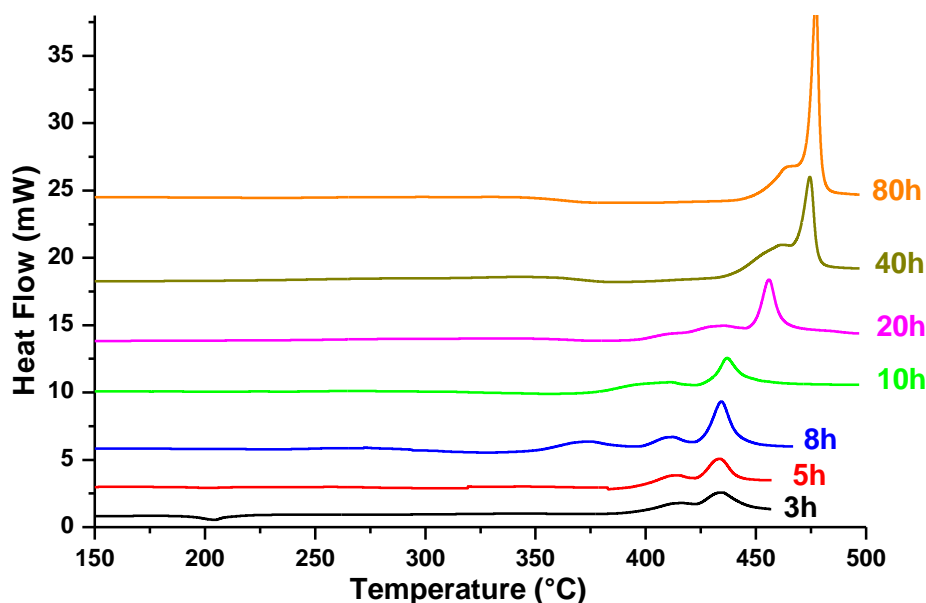


Figure 3.27: Evolution of the characteristic temperatures of the 80GeSe₂-20Ga₂Se₃ powder with milling time

The first peak observed in DSC analysis at about 200°C after 3 h and 5 h of milling is due to the melting of residual crystalline Se which was not yet amorphized. A glass transition temperature is clearly identified (figure 3.28) and confirms the production of an amorphous powder after 5 h of milling. It is important to notice that due to the inhomogeneity of the powders at the shorter milling times, several DSC measurements were performed to ensure the accuracy of the measurements.

Table 3.6: Characteristic temperatures of the 80GeSe₂-20Ga₂Se₃ powder obtained and of a 80GeSe₂-20Ga₂Se₃ glass prepared in sealed silica tube

Duration of milling (hours)	T _g (±1°C)	T _x (±1°C)
3h	191	391 / 416
5h	180 / 276	388 / 420
8h	289	346 / 396 / 423
10h	315	377 / 402 / 425
20h	350	396 / 411 / 443
40h	355	439 / 459
80h	347	449 / 470
<i>Silica tube</i>	367	449 / 463

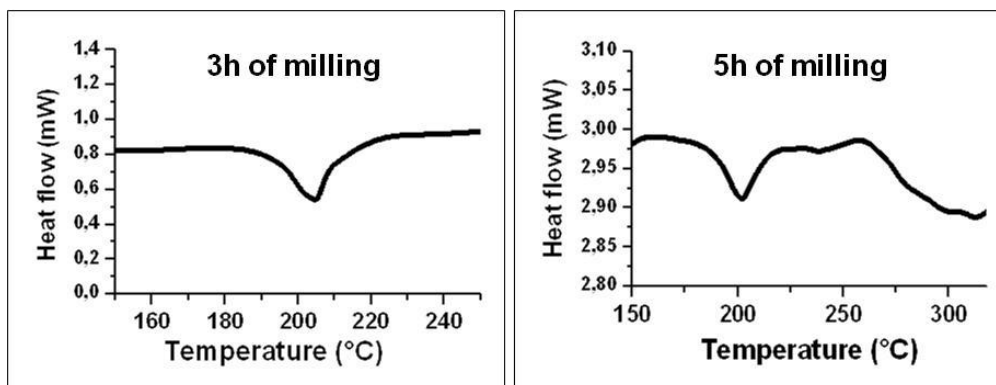


Figure 3.28: Magnification of the DSC curves obtained on the powders after 3h and 5h of milling showing the glass transition temperatures

With increasing milling time, the melting peak of Se vanishes and a shift of both glass transition temperature and crystallization temperature is observed. What is surprising is the presence of three crystallization peaks on the DSC curves from 8h to 20 h of milling. A XRD analysis was carried out on the powder collected after the DSC experiments performed at 10°C/min up to 470°C to identify the three crystalline phases precipitated. Results showed the crystallization of GeSe, GeSe₂ and Ga₂Se₃ (or Ga₄GeSe₈, as both phases present extremely close patterns) [51, 61].

As shown in figure 3.27, the glass transition temperature evolves according to the milling time. From table 3.6, it appears that a T_g close to that of a glass prepared in sealed silica tube is reached after 20 hours of milling, however the recrystallization temperature T_x is significantly lower, possibly due to unreacted particles acting as heterogeneous nucleation sites. Upon further ball milling duration the T_x increases until it reaches a value similar to the melted glass after 80 hours of ball milling. It can then be assumed that an equivalent glass microstructure is obtained using both techniques.

3.5.5.6. Mechanism of amorphization

The amorphization process could be explained by two phenomena. The first one consists in a fine chemical reaction between each element (Solid State Amorphization model), while the second one could be attributed to the localized melting/quenching process due to the high energy of the impact characteristic of ball milling process (Liquid/Quenching model).

V. Caron has demonstrated that the first process occurs when the milling temperature is lower than the glass transition temperature, T_g [93]. Measuring the temperature inside the milling jar during the process is not possible. However, considering the high T_g of the $80\text{GeS}_2\text{-}20\text{Ga}_2\text{Se}_3$ glass composition (around 350°C), we can assume that a fine chemical reaction occurs between the raw materials leading to an amorphous powder, according to the solid state amorphization model. For information purpose only, the temperature inside the milling jar has been measured using a thermal camera device just after the end of a milling cycle. A temperature of 50°C was measured.

3.5.6. Conclusion on mechanosynthesis

Chalcogenide glass powders have been prepared by mechanosynthesis. Mechanical milling of raw starting elements allowed the production of amorphous powders with the desired final composition without melting and quenching. Furthermore, mechanosynthesis does not involve use of expensive, single use silica set ups. In fact, multiple powder batches can be prepared using the same milling elements (jar and

grinding balls). These elements only need to be cleaned between each mechanosynthesis experiment.

Mechanosynthesis is a promising synthesis route for chalcogenide glasses. It also potentially opens the way for the production of glass compositions which cannot be obtained by the conventional melt/quenching technique in sealed silica ampoule. In fact, compositions considered as “unstable”, which crystallize when prepared by conventional synthesis, may be prepared by mechanical milling. Finally, mechanosynthesis does not involve prolonged heat treatments at high temperatures and could thus lead to cheaper production costs. The high interest of this technique highlighted during this study led to the filing of a patent by the Glass and Ceramics Lab of the University of Rennes 1 [99].

3.6. Conclusion

In this chapter, different alternatives to melt/quenching in sealed silica ampoules technique for synthesis of chalcogenide glasses from the Ge-Ga-Se system have been studied. Two approaches were considered to provide the energy necessary to induce a reaction between the raw starting elements: thermal energy (melt/quenching) and mechanical energy (mechanosynthesis). Major technical challenges appeared for synthesis experiments based on melting the raw starting elements in open crucibles or in closed silica chamber under argon atmosphere. The important differences in thermal properties of the elements used, and the high vapor pressure of Se were the main issues. The high temperatures used to ensure a reaction between Ge, Ga and Se led to uncontrolled crystallization and important weight losses by evaporation before a

complete reaction could be achieved. Also, homogenization of the elemental mix appeared problematic due to uncontrolled increase in viscosity. Thus, these two methods were deemed inadequate for synthesis of glasses from the Ge-Ga-Se system.

On the other hand, preparation of glass powders by mechanical milling of a mix of the raw starting elements appeared as a promising technique. Amorphous powders with similar thermal characteristics than glasses prepared by the conventional melt/quenching in sealed silica tube technique were synthesized. Mechanosynthesis does not involve melting and uncontrolled crystallization induced by thermal treatment is avoided. Furthermore, as no quenching is needed, unstable glass composition which cannot be produced due to the low thermal conductivity of silica may be produced by mechanical alloying.

Overall, this study has paved the way for a new synthesis route for chalcogenide glass powders. Further studies are required to identify the influence of the different milling parameters (ball-to-powder weight ratio, the size and number of the grinding balls used, the milling speed and duration, and the atmosphere on the reaction kinetics) and will be the subject of future work at the Glass and Ceramics Lab at the University of Rennes 1, France.

Finally, while the formation of amorphous powders is a noteworthy achievement, it is of little interest for practical applications. Infrared optics application requires large monolithic bulk samples for the production of optical elements. The production of bulk materials from the powders obtained by mechanosynthesis will therefore be the focus of chapter 4.

CHAPTER 4: PRODUCTION OF BULK MATERIALS FROM POWDERS OBTAINED BY MECHANOSYNTHESIS

4.1. Introduction

The study presented in chapter 3 showed the possibility of synthesizing chalcogenide amorphous powders by mechanosynthesis of the raw starting elements. This new synthesis route paves the way for the production of chalcogenide glasses at a lower cost and for the production of compositions which cannot be obtained in sealed silica ampoules due to the limited quenching rate resulting from the low thermal conductivity of silica.

Though production of glass powders by mechanosynthesis is an important achievement, it only represents the first step for the production of bulk chalcogenide glasses for thermal imager optics. The second step involves the consolidation of the powders obtained by mechanosynthesis to produce compact monolithic glasses. To the best of our knowledge, no such studies have been reported for chalcogenide glasses, although bulk metallic glasses such as $\text{Al}_{75}\text{Ni}_{10}\text{Ti}_{10}\text{Zr}_5$ [100] or $\text{Tm}_{60}\text{Ti}_{40}$ [101] have been prepared by sintering of amorphous powders obtained by grinding of the starting metals.

Two approaches will be considered for the production of bulk materials from the chalcogenide glass powders previously synthesized: sintering and melting. Both approaches involve heating of the powder and thus require special attention during their respective processes. The two critical factors that must be monitored and controlled are

the crystallization of the glass due to the low stability of the glasses compositions and a loss of material due to the high vapor pressures of the elements constituting the glasses.

4.2. Sintering of glasses: Principle and Techniques

4.2.1. Definition

Sintering involves the fusion of powder particles at high temperatures without melting [102]. According to Frenkel's theory, sintering of glasses occurs by viscous flow under the influence of surface stress [103, 104]. Two stages are distinguished during sintering. In the first stage, bridges, or necks, are formed between adjacent particles of powder, with little or no change in density. The second stage corresponds to the densification of the material by reduction of the porosity. Large volume changes can be observed during the second stage. The two sintering stages may overlap.

Theoretical models of sintering processes assume a distribution of particles with spherical shape and equal diameters. In most cases, these conditions are not achieved, with particles varying in both sizes and shapes. However, the fundamentals principles remain valid. The theoretical model of sintering of glass powders by viscous flow first introduced by Frenkel is briefly described below.

The driving force for sintering is a decrease of the high surface energy inherent to powders. The sintering process is therefore associated with a reduction of surface curvature and a decrease in surface area. The surface energy per unit volume is inversely proportional to the particle diameter. The isothermal neck growth in the case of sintering

by viscous flow is measured by the neck size ratio X/D , and is described by the following relation:

$$\left(\frac{X}{D}\right)^2 = \frac{3\gamma}{2\eta D^2} t$$

where X is the neck diameter, D is the particle diameter, t is the isothermal sintering time, γ is the surface energy and η is the viscosity. This equation indicates that smaller particles with high specific surface areas and higher surface energy sinter faster. The initial stage of neck growth between two adjacent particles relies on the motion of atoms by diffusion at the grain boundaries. The diffusion is a thermally activated process, thus diffusion rates are higher at high temperatures. Figure 4.1 illustrates neck growth during the sintering of two spherical particles of diameter D . Prolonged sintering causes the two particles to coalesce into a single sphere with a final diameter equal to 1.26 times the original diameter.

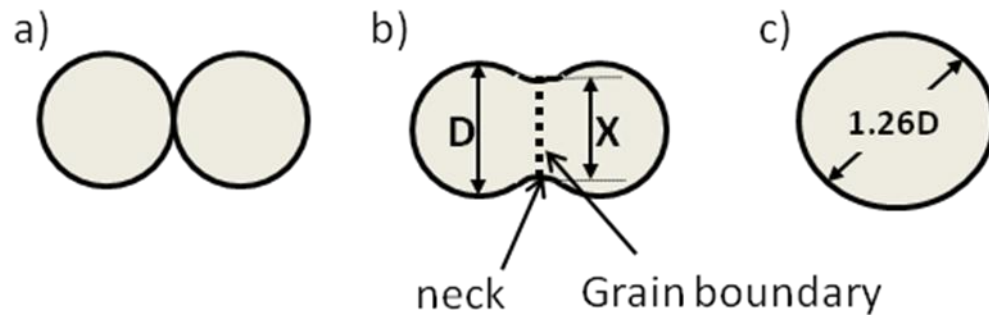


Figure 4.1: Neck growth between two particles during sintering

The neck growth stage induces the creation of porosity inside the material. Porosity is divided into open pores (connected to the surface) and closed pores (enclosed in the bulk material) as illustrated in figure 4.2-a). The second stage of the sintering process is the elimination of this porosity to obtain a dense material. This corresponds to

densification. In most cases, densification comes with shrinkage. The elimination of the pores occurs via diffusion through the material and is therefore thermally activated. Elimination of open porosity happens first. This step leads to materials with a density about 92% of the theoretical full density of the glass. The remaining 8% correspond to the closed porosity. Figure 4.2-b) shows the variation in the open and closed pore fractions versus the total porosity for urania sintering at 1400°C [105]. The elimination of the closed porosity is a slow process wherein isolated, spherical pores shrink by a bulk diffusion mechanism and is critical to achieve full density.

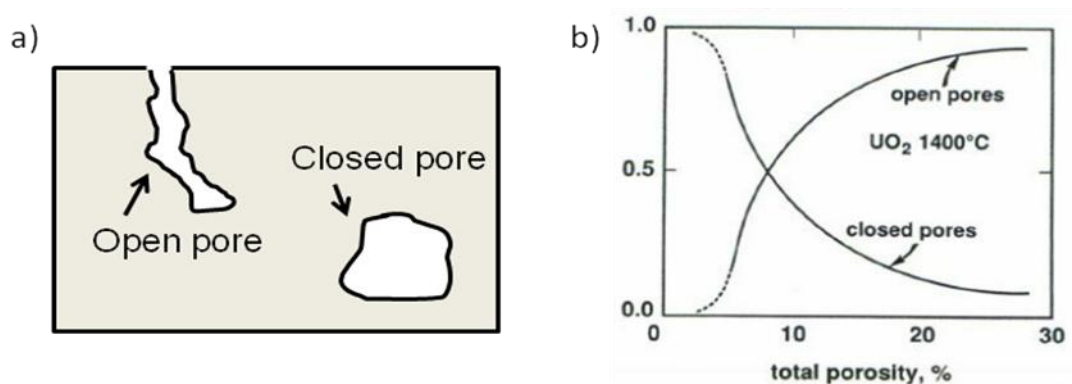


Figure 4.2: a) Illustration of closed and open porosity; b) variation in the open and closed pore fractions versus the total porosity for urania sintering at 1400°C [105]

Sintering can be carried out with or without application of an external pressure. Mixers and binders may be used for a better handling of the powder before the sintering process. The present work focuses on two sintering techniques where a pressure is applied on the powder during the process: Hot Uniaxial Pressing (HUP) and Spark Plasma Sintering (SPS). These techniques are briefly described in the following paragraphs. No mixers or binders were used during the experiments.

4.2.2. Hot Uniaxial Pressing

In this process, the powder to be sintered is placed inside a mold between two removable pistons, as illustrated in figure 4.3. Protective plates are used to isolate the pistons from potential contamination by the powder. The mold is then placed in a press and a pressure is applied on the pistons. In the case of Hot Uniaxial Pressing (HUP), the pressure is applied along one axis only. HUP has thus to be differentiated from Hot Isostatic Pressing (HIP), where pressure is applied isostatically along all directions.

The whole system (mold+pistons) is enclosed in a heating chamber producing the heat necessary for sintering. The heat is transferred to the mold and then to the powder by convection. The temperature and pressure applied on the powder can be monitored and adjusted for each experiment.

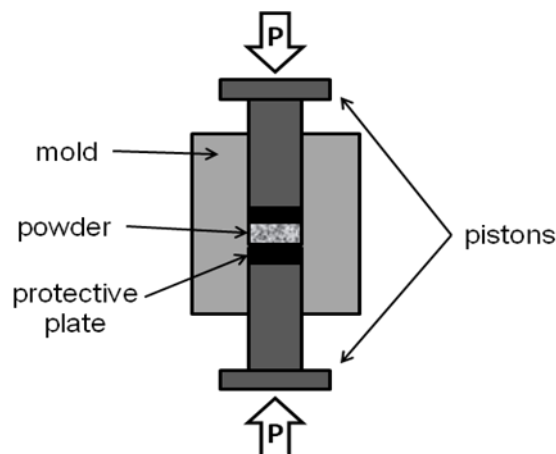


Figure 4.3: Illustration of Hot Uniaxial Pressing process

The shape and size of the sample prepared by this technique are defined by the shape and the dimension of the mold. Thus, by using appropriately shaped molds, lenses may be directly molded by sintering of a glass powder [16].

4.2.3. Spark Plasma Sintering (SPS)

Spark Plasma Sintering (SPS), also referred as Pulsed Electric Current Sintering (PECS) or Field Activated Sintering Technique (FAST), utilizes pulsed high DC current along with uniaxial pressure to consolidate powders [106]. Even though this technique was first investigated and patented in 1906 [107, 108], its main development actually happened during the last decade following a reduction in costs of the commercial equipments.

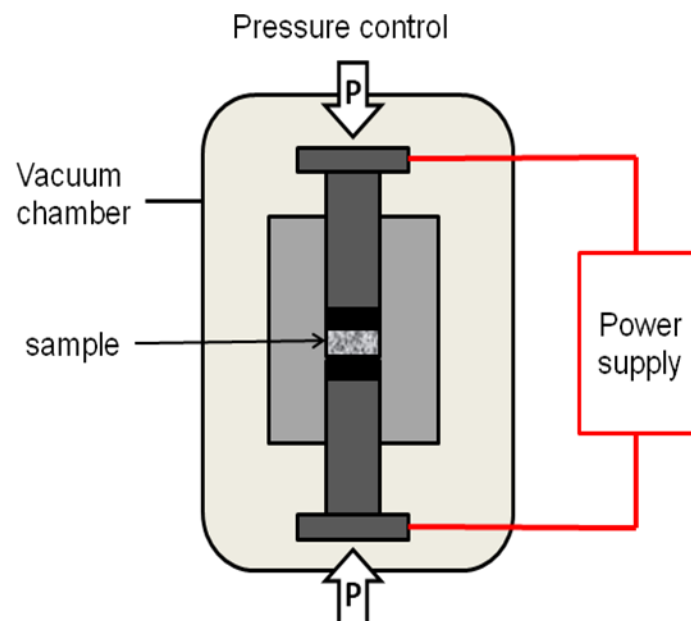


Figure 4.4: Illustration of Spark Plasma Sintering process

The main difference between SPS and HUP lies in the heating process. Conductive dies, generally graphite, have to be used for SPS experiments. The pulsed DC current directly passes through the die. In the case of conductive powders, current also passes through the sample. This current allows a rapid heating of the powder by Joule heating [109], with heating rates as high as 1000°C/min, considerably greater than

heating rates achieved with conventional Hot Pressing. A schematic of the SPS process is presented in figure 4.4.

The fast heating rates achieved with SPS generally lead in sintering in shorter times and at lower temperatures, thus can minimize material loss due to vaporization, undesirable phase transformation, and suppression of grain growth. Enhancement of the mechanical properties (three-point bending strength and Vickers hardness) of materials consolidated by SPS has also been observed [110, 111]. As for the HUP technique, the size and shape of the mold dictate the geometry of the final product. Examples of bulk materials with different shapes are presented in figure 4.5 [112].

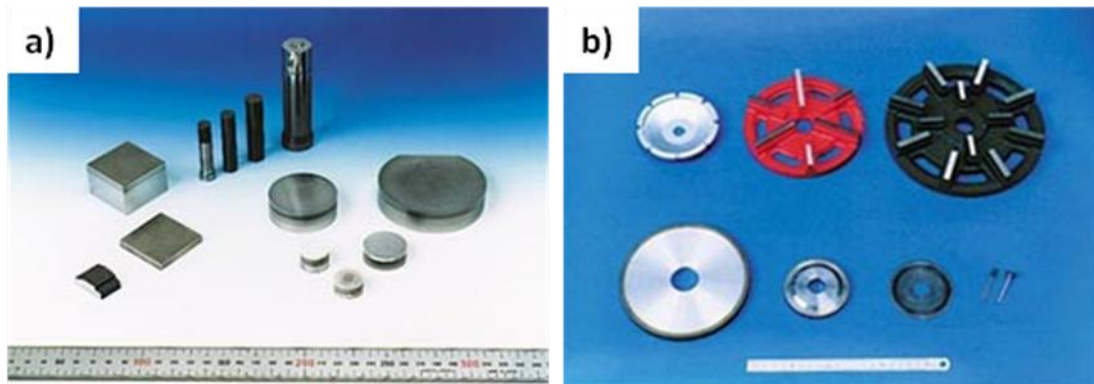


Figure 4.5: a) Functionally graded WC/Co materials, b) diamond grinding tools prepared by SPS. Images from Fuji Electronic Industrial Co., Ltd [112]

Spark Plasma Sintering technique is currently used to produce a wide variety of materials, including oxide ceramics [113], SiC-TiC ceramics for tool applications [114, 115], hydroxyapatite compacts [116], or metallic alloys [117, 118].

4.3. Sintering of Chalcogenide Glass Powder by Hot Uniaxial Pressing

4.3.1. Sintering of GeSe₄ powder

4.3.1.1. Experimental procedure

A hot press built in the Glass and Ceramics Lab at the University of Rennes 1 was used to sinter the GeSe₄ powder prepared by mechanosynthesis. The setup, shown in figure 4.6-a, comprises a hot chamber connected to a vacuum pump. The experiments can be run either under vacuum or under argon atmosphere. The temperature inside the chamber can be raised up to 400°C. A piston allows applying a pressure up to 2 tons. A stainless steel mold with an inner diameter of 20mm was used for the experiments (figure 4.6-b).

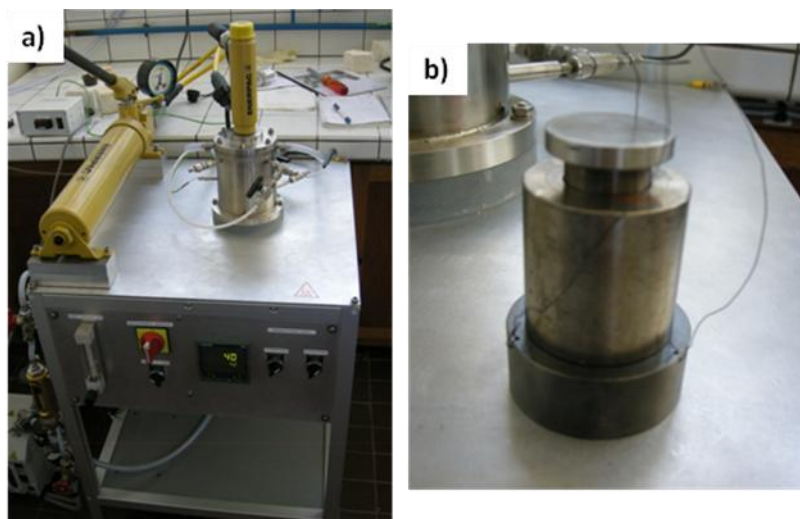


Figure 4.6: a) Experimental setup and b) mold used for sintering of GeSe₄ powder

A mass of 2g of GeSe₄ powder obtained after 80h of ball milling was introduced in the mold and placed inside the hot press. The preparation of the glass powder is

described in chapter 3. The chamber was closed and evacuated under vacuum. The vacuum was maintained during the complete sintering process. The temperature was raised up to 350°C degrees for 1h while applying a pressure of 1ton (31 MPa). Then, the temperature was decreased to 150°C ($T_g - 15^\circ\text{C}$) for 15 min to relax the constraints in the glass. The pressure was released and the temperature was slowly decreased to room temperature in 2h.

4.3.1.2. Results

A bulk sample of 2.50mm thickness was obtained. The theoretical density of the GeSe_4 glass prepared with the melting/quenching technique in sealed silica ampoule is $4.37\text{g}\cdot\text{cm}^{-3}$. The glass prepared by sintering of the powder prepared by mechanosynthesis presents a density of $4.36\text{g}/\text{cm}^3$. Therefore, densification of 99.8% was achieved, indicating a low residual porosity inside the glass.

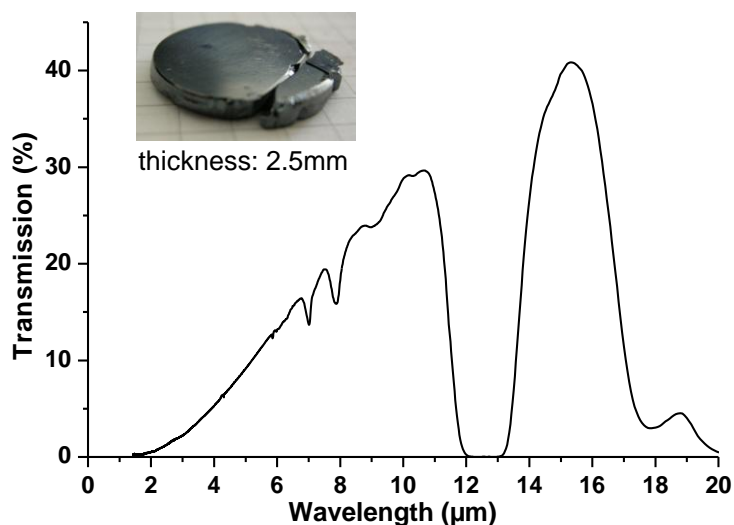


Figure 4.7: Optical transmission of the GeSe_4 glass sintered by HUP

After polishing the sample on both faces, the optical transmission was recorded. The sintered glass shows a transmission in the infrared ranging from 2 μm to 17 μm (figure 4.7). The maximum transmission is 40%. A strong absorption band is observed at 12.5 μm , corresponding to vibrations of Ge-O bonds. This indicates a contamination by oxygen during the process.

During mechanosynthesis of the GeSe_4 powder, the planetary ball mill was operating in ambient atmosphere. Even though the jar was sealed in a glove box under argon atmosphere, the high rotational speed involved during milling (400rpm) may have induced a leakage in the sealing and contamination of the powder by oxygen occurred. However, the possibility of preparing a bulk glass transmitting in the infrared by sintering of a powder previously synthesized by mechanosynthesis has been demonstrated. The sample was subsequently analyzed by Energy Dispersive Spectroscopy (EDS). The glass presents a homogeneous aspect (figure 4.8). Atomic contents of 20% Ge and 80% Se were determined in agreement with the expected GeSe_4 stoichiometry.

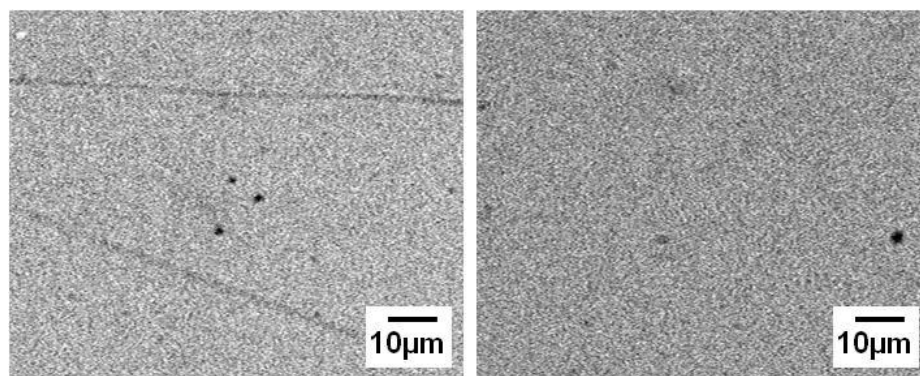


Figure 4.8: Impurities on the surface of the GeSe_4 sintered glass

4.3.2. Sintering of $80\text{GeSe}_2\text{--}20\text{Ga}_2\text{Se}_3$ powder

4.3.2.1. Experimental procedure

The glass transition temperature of the $80\text{GeSe}_2\text{--}20\text{Ga}_2\text{Se}_3$ glass (370°C) is higher than that of the GeSe_4 glass (165°C) [61, 98]. The maximum temperature achievable on the hot press used to sinter the GeSe_4 powder (400°C) is insufficient to sinter $80\text{GeSe}_2\text{--}20\text{Ga}_2\text{Se}_3$ powder prepared by mechanosynthesis. Thus, a different hot press was utilized (figure 4.9-a). It comprises a graphite furnace enclosed in a chamber and equipped with pistons in a vertical position (figure 4.9-b). Temperatures up to 2200°C and pressures up to 150MPa can be achieved. The experiments can be run under vacuum, or inert gas atmosphere (nitrogen or argon).

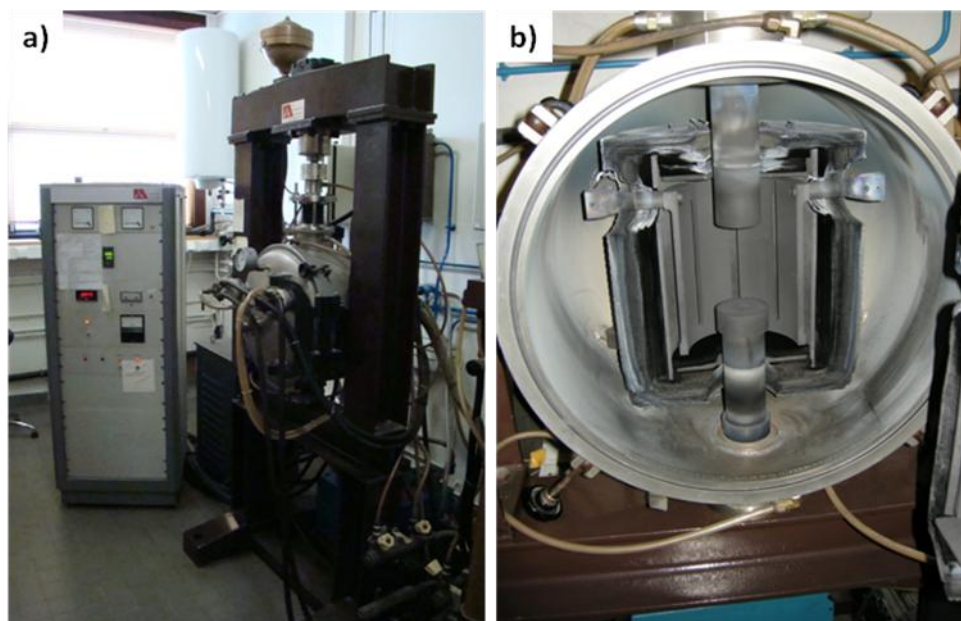


Figure 4.9: Hot Press used for sintering of the $80\text{GeSe}_2\text{--}20\text{Ga}_2\text{Se}_3$ glass powder, a) global view; b) inside view of the furnace

A mass of 2g of $80\text{GeSe}_2\text{--}20\text{Ga}_2\text{Se}_3$ powder prepared by mechanosynthesis with a total duration of milling of 80h was introduced in a graphite mold with an inner diameter

of 13mm. The preparation of the powder is described in chapter 3. To limit the contamination of the sample by carbon diffusion from the graphite die and to avoid that the glass sticks to the walls, a layer of boron nitride (BN) was applied on the surface of the die before introduction of the glass powder. The thermal treatment and the pressure applied during the sintering process are presented in figure 4.10. The temperature was raised to 500°C degrees for an hour while applying a pressure of 35 MPa. Then, the temperature was decreased to 350°C ($T_g - 20^\circ\text{C}$) for 20 min to anneal the constraints in the glass. The pressure was released and the temperature was slowly decreased to room temperature in 2h.

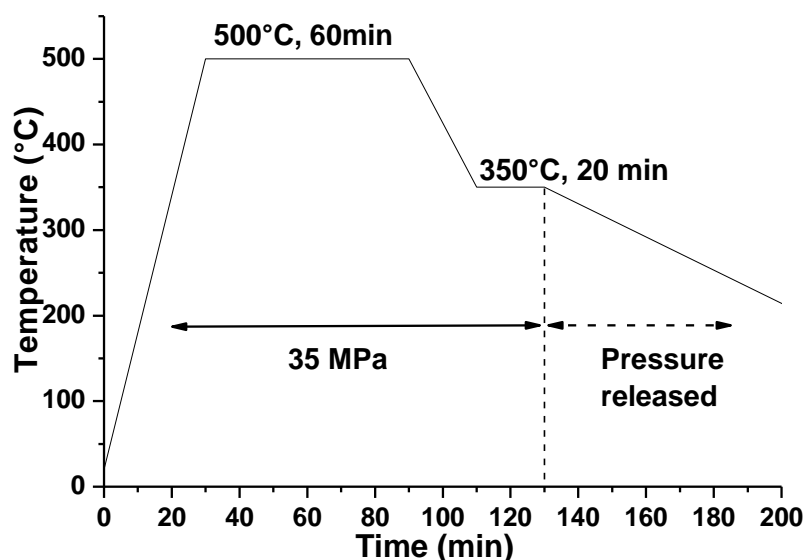


Figure 4.10: Thermal treatment applied during sintering of the $80\text{GeSe}_2\text{-}20\text{Ga}_2\text{Se}_3$ glass powder

4.3.2.2. Results

The first samples obtained showed an inhomogeneous profile (figure 4.11-a). The upper part of the sample presented a black glassy aspect, while the lower part had a red

coloration and was composed of compact, not sintered powder. The white particles observed on the surface of the sample correspond to the boron nitride used to cover the mold. An inhomogeneous temperature profile inside the furnace is responsible for the uneven character of the sintered glass powder. The position of the sample was slightly below the central point of the furnace. The bottom part of the glass powder was thus in a zone where the temperature is lower and insufficient to ensure its sintering. Therefore, the shape of the mold was adjusted to ensure the positioning of the glass powder in the central part of the furnace and obtain a homogeneous heating profile. The following sintering experiments resulted in crystallized bulk materials, as can be seen on figure 4.11-b, and on the SEM image of the inside of a sintered sample (figure 4.11-c). No optical transmission was obtained on the $80\text{GeSe}_2\text{--}20\text{Ga}_2\text{Se}_3$ bulk samples prepared by Hot Uniaxial Pressing. The low stability of this glass towards crystallization ($\Delta T = 97^\circ\text{C}$) and the important specific surface area of the powder led to the precipitation of crystals during the sintering process.

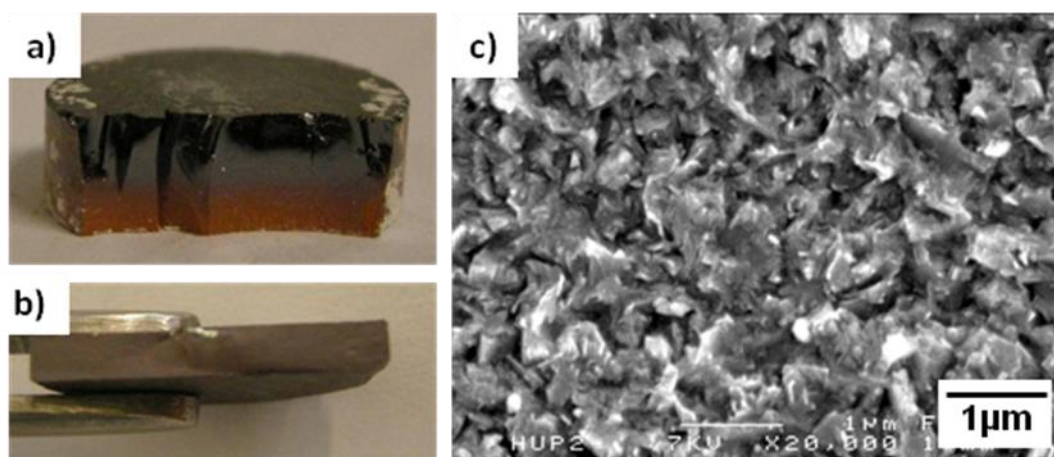


Figure 4.11: a) Inhomogeneous $80\text{GeSe}_2\text{--}20\text{Ga}_2\text{Se}_3$ sample obtained by sintering glass powder; b) Crystallized sample; c) SEM micrograph of the inside of a sintered sample

4.3.3. Sintering of ZnSe powder

Polycrystalline zinc selenide (ZnSe) is currently used to produce thermal imaging optics due to its wide range of transmittance in the infrared range (figure 4.12).

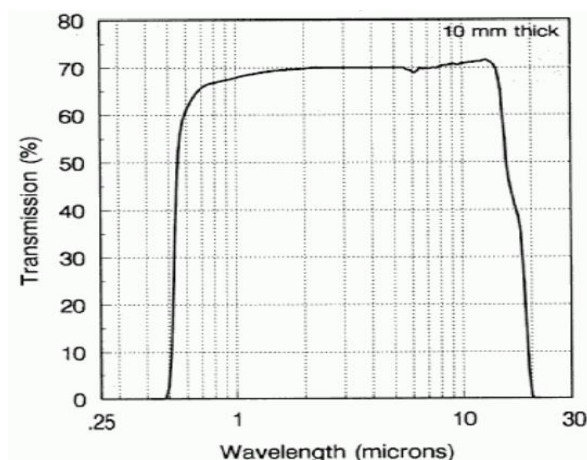
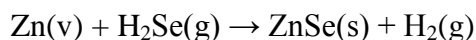


Figure 4.12: Transmission graph of a 10mm thick ZnSe window prepared by CVD. Image from Wuhan Sintec Optronics [119]

The lenses are prepared by chemical vapor deposition (CVD) [120]. This synthesis method necessitates use of zinc vapors and highly toxic gaseous H_2Se , according to the following reaction:



The preparation of bulk ZnSe samples by sintering of a powder prepared by mechanosynthesis has been studied. Recently, the possibility to synthesize ZnSe powder by mechanical alloying has been demonstrated [121-123]. However, no bulk material was prepared from this powder. Combining mechanosynthesis and sintering of ZnSe powder should permit to produce bulk materials without use of toxic gaseous H_2Se .

4.3.3.1. Preparation of ZnSe powder by mechanosynthesis

The pure raw metallic zinc (5N, Strem) and selenium (5N, Umicore) were introduced in stoichiometric quantities to obtain 20 grams of material in the WC milling jar. Six WC grinding balls, for a total weight of 375g were added, yielding a 19:1 ball-to-powder weight ratio. The milling jar was introduced into the planetary ball mill. Rotation cycles of 3 min at 400rpm were scheduled with direction reversal and a pause of 3 min between each cycle. The evolution of the color of the powder with milling duration is shown in figure 4.13. The initial grey powder corresponding to a mix of pure zinc and selenium progressively turns to an orange powder.

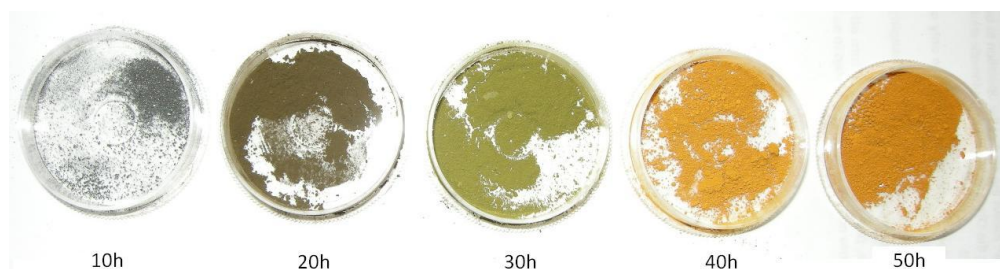


Figure 4.13: Evolution of the ZnSe powder coloration with milling time

The XRD spectra recorded on the powders are presented in figure 4.14. After 10h of milling, the characteristic diffraction peaks of metallic zinc and selenium are observed and no peaks corresponding to a ZnSe cubic zincblende crystalline phase are detected. The presence of a hexagonal wurtzite ZnSe phase would be characterized by two peaks located at 25.5° and 29° (2θ) [124]. After 20h of milling, the Se peaks vanish and ZnSe peaks appear. Metallic zinc is still present in the powder. For milling times of 30h and longer, the XRD spectra only show presence of a crystalline ZnSe phase and metallic Zn

peaks are no longer observed. The shape of the spectra remains stable after 30h of milling.

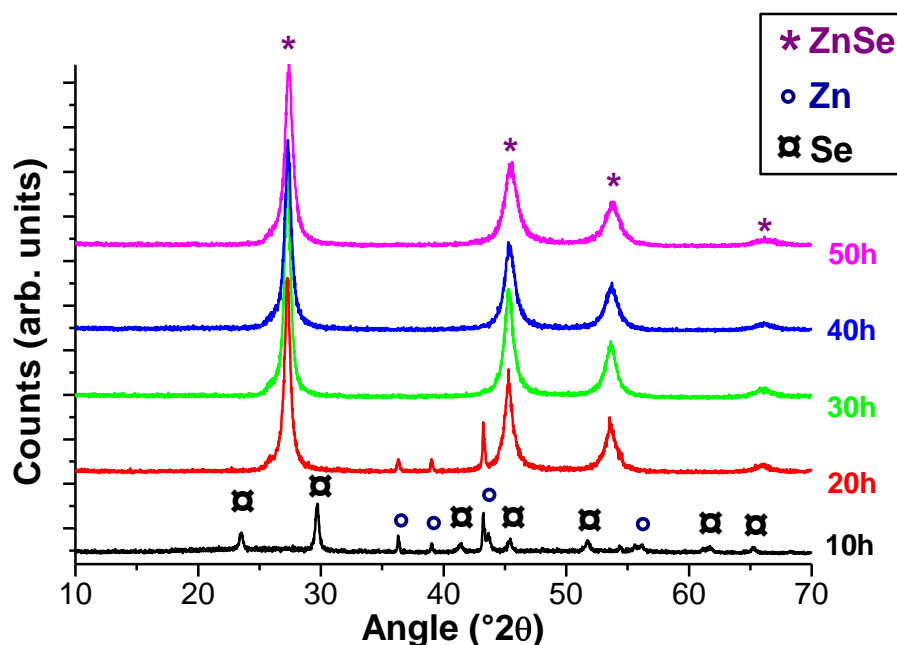


Figure 4.14: Evolution of the XRD spectra of the ZnSe powder with milling time

4.3.3.2. Hot Uniaxial Pressing

A mass of 2g of ZnSe powder milled for 50 h was introduced in a graphite die with a diameter of 20mm. The die was covered with boron nitride to prevent ZnSe powder to stick to the mold and limit contamination by diffusion of carbon from the mold. The thermal treatment and the pressure applied are presented in figure 4.15. The temperature was quickly raised to 600°C with an applied pressure of 12bars. Below this temperature, no sintering of the powder occurs. Then, the temperature was slowly increased to 1000°C, with a pressure of 20bars applied. The choice of this sintering

temperature was based on several criteria. Below 1000°C, it is complicated to sinter correctly the ZnSe powder. Above 1000°C, losses by evaporation of the material or a phase change from zincblende (cubic) to wurtzite (hexagonal) phase may occur [125]. After a dwell of 60 min, the sample was slowly cooled down to room temperature.

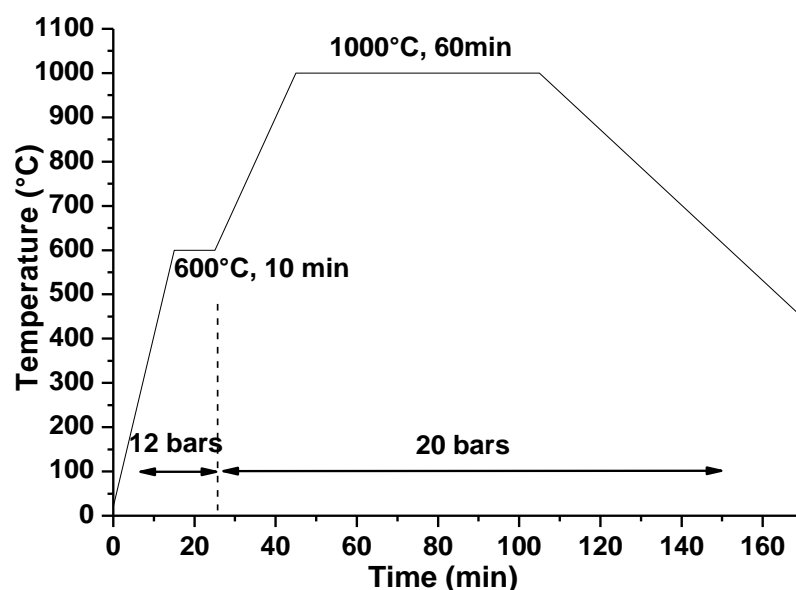


Figure 4.15: Thermal treatment applied during sintering of ZnSe powder

An opaque, yellow bulk sample was obtained (figure 4.16-a). SEM micrographs of the inside of the material shows the highly crystalline nature of the sample, as seen on figures 3.16-b and figure 4.16-c. Some particles of approximately 2 μm in diameter are observed inside the sample (figure 4.16-d). An EDS analyses identified these particles as being pure zinc. Thus, the mechanosynthesis of ZnSe was incomplete and some pure metallic zinc remains in the powder. This may be due to a small excess of zinc during the synthesis process, or an insufficient milling duration to ensure a complete reaction between Zn and Se. The absence of peaks corresponding to Zn on the XRD spectrum of

the powder milled for 50h indicates that only a few zinc particles have not reacted. However, this low content is sufficient to yield an opaque bulk material presenting no optical transmission in the infrared.

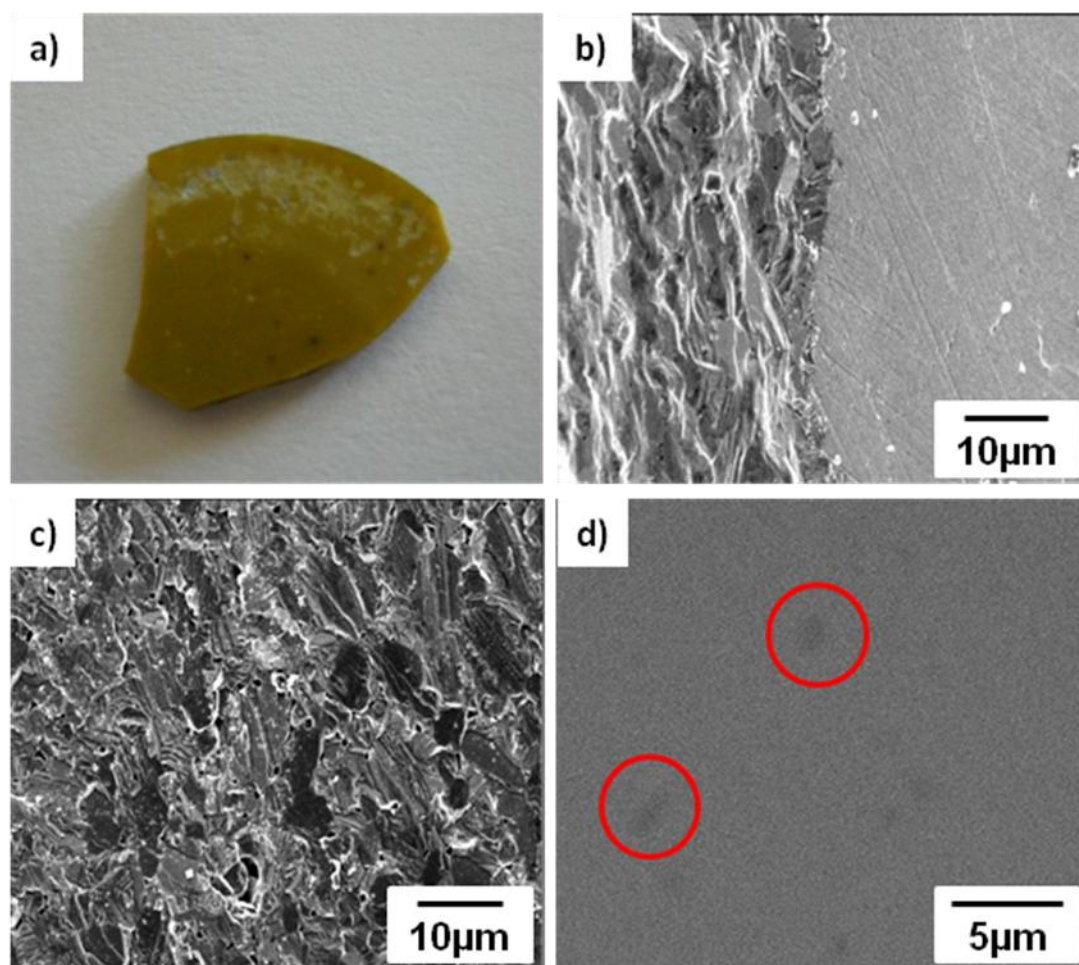


Figure 4.16: a) Bulk material obtained; b) and c) SEM micrograph of the material; d) zinc particles observed

4.3.4. Conclusions on sintering by Hot Uniaxial Pressing

The possibility of preparing GeSe_4 bulk glasses transparent in the infrared region by Hot Uniaxial Pressing of a powder prepared by mechanosynthesis has been demonstrated. High densification rates were achieved (up to 99.8%). This composition

was studied in a first step because of its high stability toward crystallization but does not present an interest for infrared cameras optics. Sintering by Hot Uniaxial Pressing of the $80\text{GeSe}_2\text{--}20\text{Ga}_2\text{Se}_3$ composition, which is of high interest for thermal imaging applications, led to uncontrolled crystallization of the material during the process and opaque materials were obtained. The sintering of ZnSe appeared unsuccessful, due to the remaining presence of a small amount of metallic zinc particles in the powder prepared by mechanosynthesis. Experiments will have to be performed on powders prepared with longer milling durations.

Overall, HUP appears to be a viable technique for the production of bulk glass from stable composition but it is shown to be inappropriate for unstable glasses due to uncontrolled crystallization. Prolonged stages at temperatures above the glass transition temperature favor the development of a crystalline phase. Production of unstable glasses will therefore require a reduction of the heat treatment duration to avoid this uncontrolled crystallization. With this perspective in mind, the sintering of the powders obtained by mechanosynthesis using Spark Plasma Sintering (SPS) technique has been studied and is presented in the following section.

4.4. Sintering of Chalcogenide Glass Powder by Spark Plasma Sintering

4.4.1. Experimental procedure

The Spark Plasma Sintering (SPS) experiments were carried out with a Dr. Sinter 505 Syntex machine (figure 4.17) at the “Plate-forme de Frittage de Paris”, Thiais,

France. The densified bulk samples were prepared by introducing a proper amount of glass powder into a graphite die. The sintering was performed under vacuum, with a pressure applied up to 100MPa. The temperature is controlled via a thermocouple in the wall of the die which adjusts the power output during the experiments.



Figure 4.17 : Dr. Sinter 505 Syntex machine

4.4.2. Sintering of GeSe_4 powder

The goal of this experiment was to assess the feasibility of the process. A mass of 0.5 grams of GeSe_4 powder obtained after 80h of milling was introduced in an 8mm diameter graphite die. The temperature was quickly raised to 180°C in 5 min. A dwell of 2 min at 180°C was performed, and then the temperature was decreased to room temperature. A pressure of 100MPa was applied during the sintering. The duration of the entire process is 7 min, as compared to more than 2 hours for Hot Uniaxial Pressing.

A bulk glass with a thickness of 0.6mm was obtained. The optical transmission ranging from 2 μm to 17 μm (figure 4.18) is similar to that obtained on samples sintered by Hot Uniaxial Pressing. A strong absorption band located at 12.5 μm due to vibration of Ge-O bonds is observed. This indicates a contamination of the initial powder by oxygen during the mechanosynthesis process. The maximum transmission reaches 20%. The density of the bulk sample is $4.31\text{g}\cdot\text{cm}^{-3}$, which corresponds to a densification rate of 99%. An EDS analysis revealed atomic contents of 20 at% Ge and 80 at% Se. This confirms the production of a GeSe_4 glass. No loss of elements occurred during the SPS process.

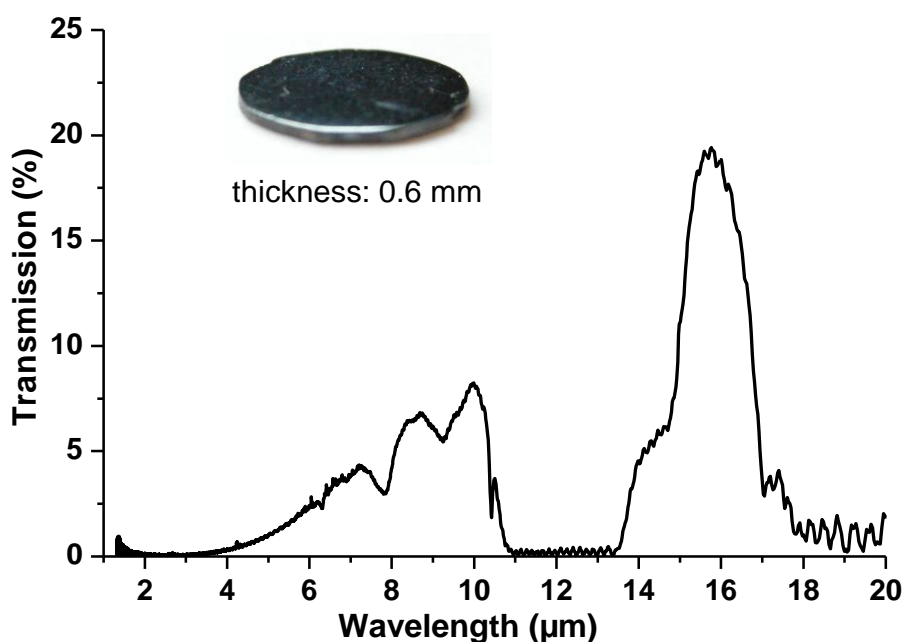


Figure 4.18: Optical transmission of the GeSe_4 glass sintered by SPS

This experiment demonstrates the possibility of obtaining bulk glasses by Spark Plasma Sintering of a powder prepared by mechanosynthesis. It is important to point out

that SPS led to similar results than HUP in a shorter time and at a significantly lower temperature. In fact, the duration of the sintering process is reduced by a factor 17 for SPS experiments and the temperature is lowered to 20°C above T_g . This will constitute a significant advantage for the production of unstable glass compositions.

4.4.3. Sintering of 80GeSe₂–20Ga₂Se₃ powder

The powder obtained after 80h of mechanical milling was sintered under vacuum at 390°C. This temperature was reached in 4 minutes and kept constant for 2 minutes before cooling down to room temperature. The total duration of the sintering process is 10 min, as compared to more than 2 hours for sintering by Hot Uniaxial Pressing.

4.4.3.1. Contamination by carbon

The first experiments were performed using a Papyex® inner foil (flexible graphite [126]) to cover the graphite die. The XRD spectra of the obtained bulk materials present an important diffraction peak at 26.8° corresponding to the diffraction peak of the Papyex® foil, indicating a diffusion of carbon graphite inside the glass during the sintering process. Subsequent experiments were carried out using a tantalum (Ta) inner foil as a diffusion barrier. The XRD spectrum recorded on the bulk material sintered using a Ta foil do not present a diffraction peak at 26.8° and has a broad shape characteristic of amorphous materials, as shown in figure 4.19.

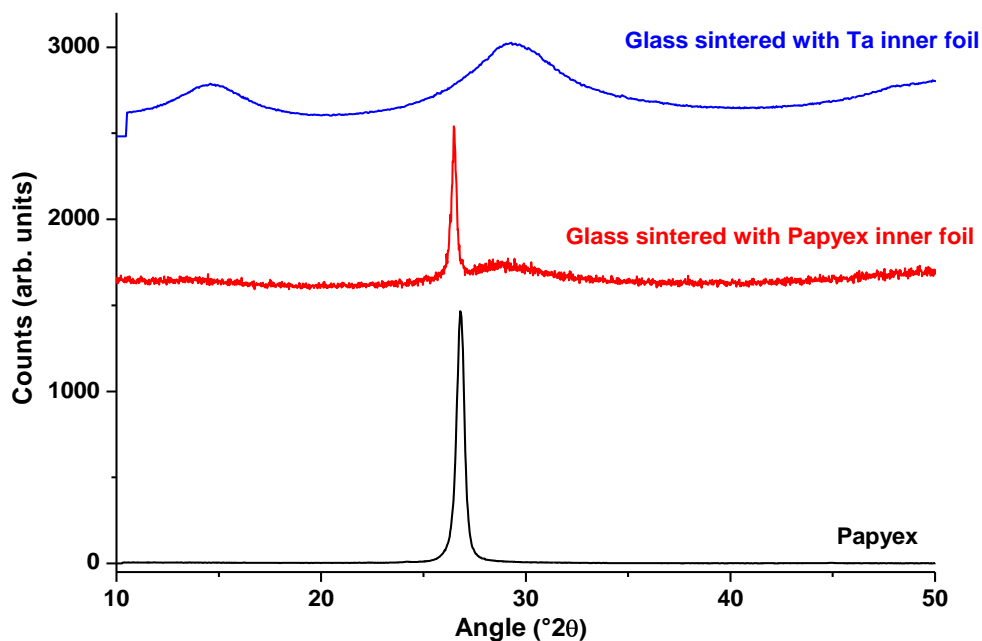


Figure 4.19: XRD spectra of a glass sintered by SPS with and without use of Ta foil as a diffusion barrier

4.4.3.2. Optical properties

Bulk glasses with diameters of 8mm, 20mm and 36mm were obtained (figure 4.20-a). A picture of the samples taken with a 8-12 μm thermal camera (figure 4.20-b) shows that the $80\text{GeSe}_2\text{--}20\text{Ga}_2\text{Se}_3$ glasses present a good infrared transmission whatever their dimension. All the samples, including the 36mm diameter, present good mechanical handling and no cracks even though the cooling rate was not controlled during the SPS experiment. The density of the sintered glasses is 4.37g.cm^{-3} . The theoretical density of this composition is 4.38g.cm^{-3} , thus a densification rate of more than 99% was reached.

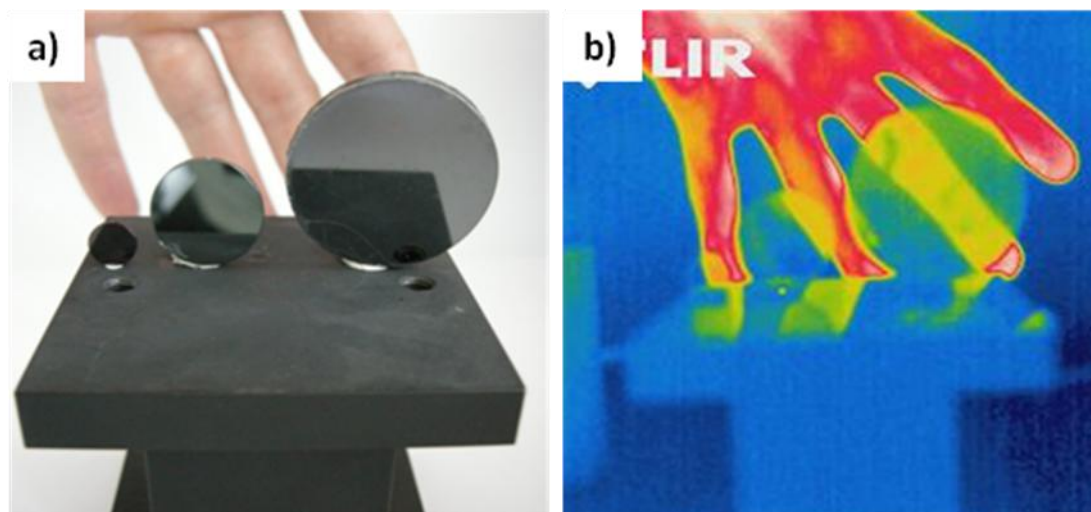


Figure 4.20: a) Visible picture of the glasses of 9mm, 20mm and 36 mm in diameter sintered by SPS ; b) Infrared picture of the same three glasses observed with a 8-12 μ m thermal camera

The absorption observed on figure 4.20-b is firstly due to reflection on both faces because of the high refractive index of the glass ($n \sim 2.4$). Secondly, the presence of oxygen, leading to the formation of Ge-O bonds inside the bulk glass, induces phonon absorption. Finally, a slight diffusion of carbon graphite or tantalum from the mold may also generate losses.

The optical transmissions of a glass sintered from a powder prepared by mechanosynthesis and a sample prepared from a powder obtained by grinding a glass previously prepared by the melting/quenching technique in sealed silica tube have been compared (figure 4.21). The glass prepared by sintering of the glass synthesized in silica tube then ground shows an optical transmission up to 17 μ m, similar to the optical transmission of the $80\text{GeSe}_2\text{-}20\text{Ga}_2\text{Se}_3$ bulk glass prepared by the conventional melting/quenching technique [68]. The transmission of the glass obtained by sintering $80\text{GeSe}_2\text{-}20\text{Ga}_2\text{Se}_3$ powder prepared by mechanosynthesis is limited to 11 μ m. The intensity of the vibrations of Ge-O bonds, which signature is located at 12.5 μ m, leads to

an important absorption and makes the glass opaque beyond 11 μm . The glass prepared by sintering powder of a bulk $80\text{GeSe}_2\text{--}20\text{Ga}_2\text{Se}_3$ obtained by melting/quenching technique and ground also presents a Ge-O absorption band, but its intensity is significantly weaker.

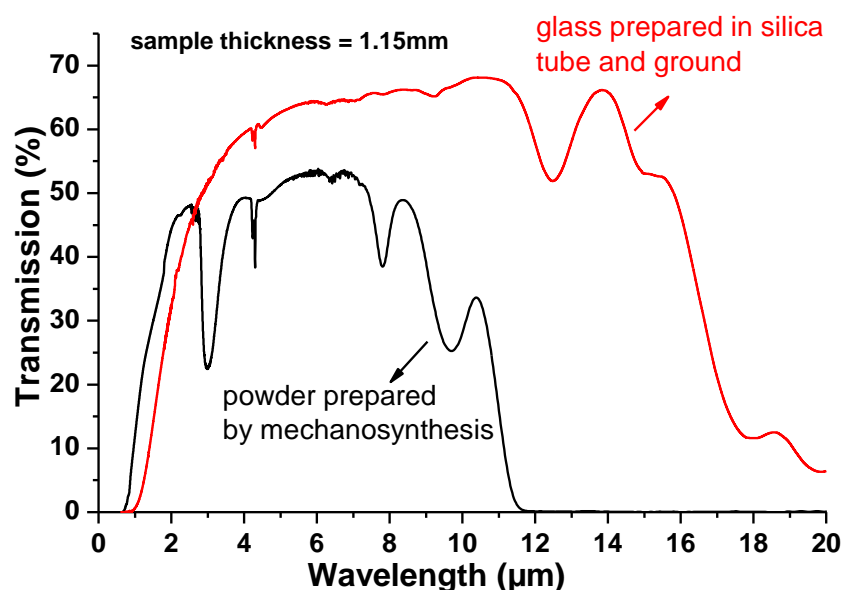


Figure 4.21: Comparison of the optical transmission of glasses sintered by SPS (2 min at 390°C, 50MPa)

The comparison of the optical transmissions reveals an important contamination by oxygen during the mechanosynthesis process. Although introduction of the raw elements and sealing of the milling jar take place in a glove box, the planetary ball mill operates in air. The high energies involved during the milling process are likely to break the hermetic seal of the jar and lead to a contamination by ambient oxygen. The planetary ball mill will have to be placed in a glove box in order to conduct the entire process under controlled, oxygen-free atmosphere.

4.4.3.3. Homogeneity of the samples

Some thermal gradients may appear when using large diameter dies in SPS experiments, especially when using insulator powder such as $80\text{GeSe}_2\text{--}20\text{Ga}_2\text{Se}_3$ [127]. An X-Ray microdiffraction experiment was carried out to investigate the amorphous character of the glass bulk along the diameter. Results show that no crystallization peaks are observed in the 36mm diameter sample. The glass is still amorphous and homogeneous (figure 4.22).

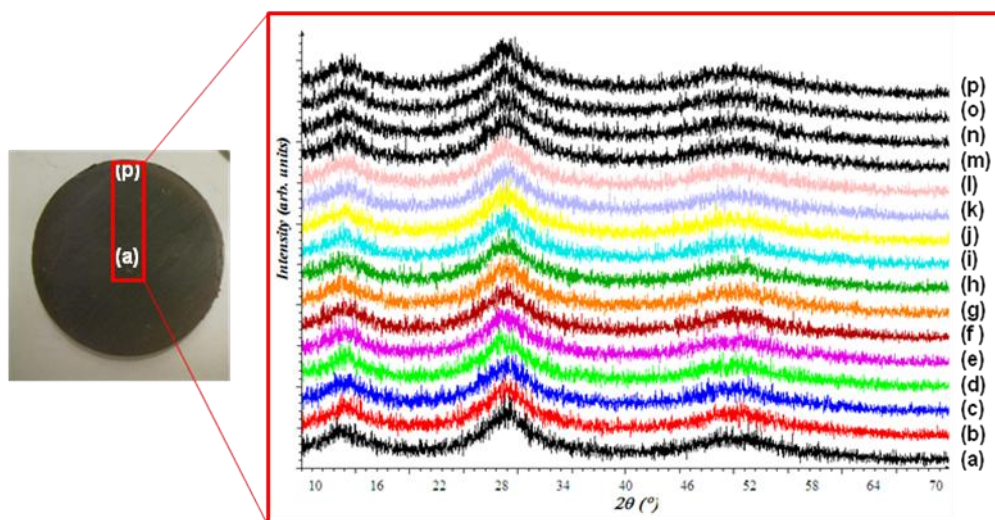


Figure 4.22: X-Ray microdiffraction patterns of the 36mm diameter sample from the center (a) to the periphery (p)

4.4.3.4. Comparison with other synthesis techniques

It is important to point out that the normal synthesis route involving melting/quenching in sealed silica tube limits the quenching rate because of the low thermal conductivity of silica ($1.4 \text{ W.m}^{-1}.\text{K}$ [66]). Thus, unstable glasses ($T_x\text{--}T_g < 100^\circ\text{C}$), such as the $80\text{GeSe}_2\text{--}20\text{Ga}_2\text{Se}_3$ composition may present risks of crystallization. Indeed,

increasing the silica tube diameter irremediably leads to uncontrollable crystallization of the melt bath during quenching. Several attempts have been made with the $80\text{GeSe}_2\text{-}20\text{Ga}_2\text{Se}_3$ glass composition using different silica tube diameters. Samples with a maximum diameter of 9mm can be synthesized without crystallization but any larger diameters irremediably lead to uncontrollable crystallization. Likewise, the sintering experiments using Hot Uniaxial Pressing led to uncontrolled crystallization of the glass powder and no transparent materials were obtained with this method.

In comparison, Spark Plasma Sintering of $80\text{GeSe}_2\text{-}20\text{Ga}_2\text{Se}_3$ glass powder previously prepared by mechanosynthesis yielded samples with a diameter up to 36mm corresponding to a 4-fold increase compared to samples obtained in sealed silica ampoules. This is equivalent to a 16-fold increase in surface which opens the way to the manufacture of optical elements for many applications such as thermal imaging, new laser source if doped with rare earth, non linear applications such as optical switching, etc. Furthermore, this sintering process is only limited by the size of the die utilized. The maximum diameter available for the experiments was 36mm in our case but synthesis of glasses with higher dimensions should be possible using dies with larger diameters. However, the thermal gradients which may appear when using bigger diameter dies in SPS experiments may require several adjustments of the instrument parameters and of the thermo-mechanical cycle.

4.4.4. Conclusion on Spark Plasma Sintering

Spark Plasma Sintering appears to be a successful method for synthesizing bulk glasses from powders previously prepared by mechanosynthesis. Homogeneous samples with good transparency in the infrared and with high densification rates (>99%) have been obtained. The short sintering stages permits to produce amorphous bulk samples from unstable compositions such as $80\text{GeSe}_2\text{-}20\text{Ga}_2\text{Se}_3$ glass. In comparison, sintering of glass powders from this composition by Hot Uniaxial Pressing led to uncontrolled crystallization. In addition, the SPS technique permits to produce samples with large diameters up to 36mm, while the diameter of the $80\text{GeSe}_2\text{-}20\text{Ga}_2\text{Se}_3$ glass samples is limited to 9mm by the conventional melting/quenching technique in sealed silica ampoules.

The optical transmission measured on the sintered glasses showed an important contamination of the initial powder by oxygen. A better control of the atmosphere by placing the planetary ball mill in a glove box and conducting the whole mechanosynthesis process in an oxygen-free environment should solve this issue.

The aim of this study was merely to assess the feasibility of the technique and no specific attention was paid to the effect of particle size distribution of the initial powder. This parameter will be the subject of future studies. Meanwhile, this new route for the synthesis of bulk chalcogenide glasses optically transparent in the infrared by sintering of a powder previously prepared by mechanosynthesis has been patented [99].

4.5. Melting of amorphous powder in open system under argon atmosphere

4.5.1. Introduction

As described in the previous chapter, the production of chalcogenide glasses in the Ge-Ga-Se system by melting the raw starting elements in open systems yielded inhomogeneous samples. Prolonged stages at high temperatures are required to ensure a complete reaction of the elements. The important differences in thermal properties of the elements led to important evaporation of Se and precipitation of GeSe_2 crystals before a complete reaction could be achieved. Thus, melting of the raw starting elements in open systems appeared inadequate for synthesis of glasses containing both Ge and Se.

As an alternative, the mechanosynthesis studies presented in chapter 3 demonstrated the possibility of preparing amorphous chalcogenide glass powders in which the elements have fully reacted to yield the desired glass composition. Melting of these previously reacted powders in open system under argon atmosphere should preclude evaporation of selenium and lead to homogeneous bulk glasses. The next section presents the result of synthesis attempts following this route.

4.5.2. Experimental procedure

The general setup used for this experiment (figure 4.23) was described in chapter 3. In the present experiment, a mass of 120g of glass powder previously prepared by mechanosynthesis was introduced in silica tube with a diameter of 60mm. A rotating helix was used for homogenization, and a silica cap was sealed with vacuum grease on

the top of the silica tube. Prior to thermal treatment, the silica chamber was evacuated under vacuum and subsequently filled with argon. Then, a constant flow of argon was applied for the complete duration of the experiment.

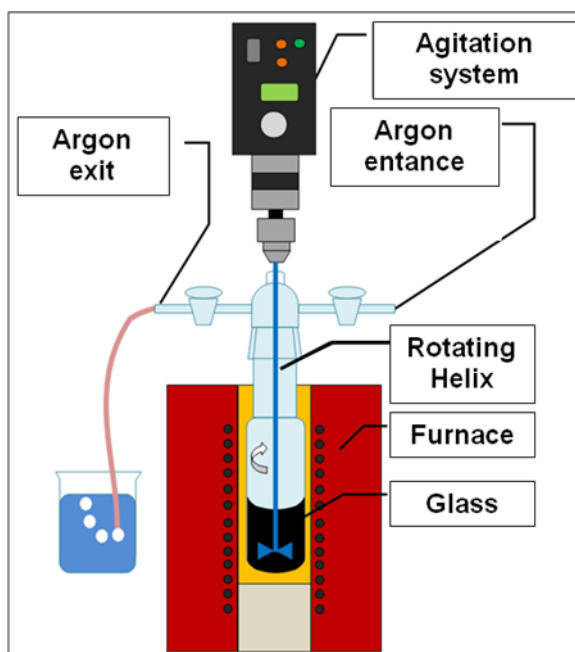


Figure 4.23 Experimental setup

Contrarily to synthesis attempts using raw elements, the powder used in this experiment already possesses the desired composition. The risk of undesired evaporation of selenium is reduced. The process only requires melting and densification of the powder. The tube was introduced in the furnace at high temperature in order to reduce the experiment duration. The helix was first rotated at a speed of 15rpm, then rotation was slowed to 4rpm for 15 min and finally stopped to allow the evacuation of bubbles [69]. The rotating helix was removed from the melt. The silica chamber was taken out of the furnace and soaked in cold water to quench the melt. Then, the glass was introduced in a furnace below T_g to anneal the constraints generated during quenching. At the end of the

process, the bottom part of the silica tube was cut to extract the glass. It is important to notice that the reaction tube can be re-sealed after the process, limiting the consumption of silica.

Initial experiments were performed on GeSe_4 glass to assess the feasibility of the technique. This composition possesses a low glass transition temperature (165°C) and is highly stable toward crystallization [98]. Further experiments focused on glasses from the Ge-Ga-Se system, which present higher interest for the production of infrared optics.

4.5.3. GeSe_4 powder

A glass powder obtained after 80h of milling was used. The preparation of the powder is described in chapter 3. The synthesis temperature was set to 680°C . A bulk glass with a thickness of 10mm was obtained. The bottom part of the glass presents a shiny aspect (figure 4.24-a) while the upper part is dusky (figure 4.24-b). This is likely due to impurities floating on the top of the melt during the process. Small bubbles are observed in the bulk material, as shown on figure 4.24-c, hence the homogenization process will require optimization to eliminate these bubbles.

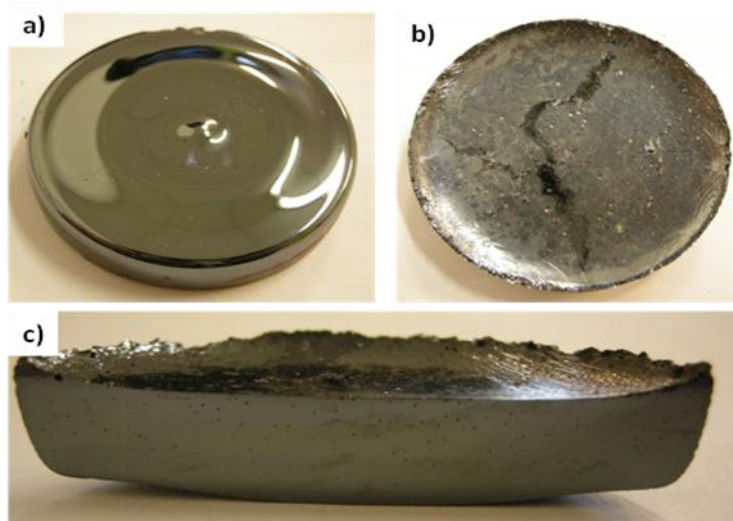


Figure 4.24: Pictures of the GeSe_4 sample obtained by melting of the powder prepared by mechanosynthesis, a) bottom view; b) top view; c) inside view

The optical transmission measured on a 2mm thick sample extends up to 17 μm (figure 4.25). A strong absorption due to vibrations of Ge-O bonds is observed at 12.5 μm and indicates a contamination of the initial powder by oxygen during the mechanosynthesis process.

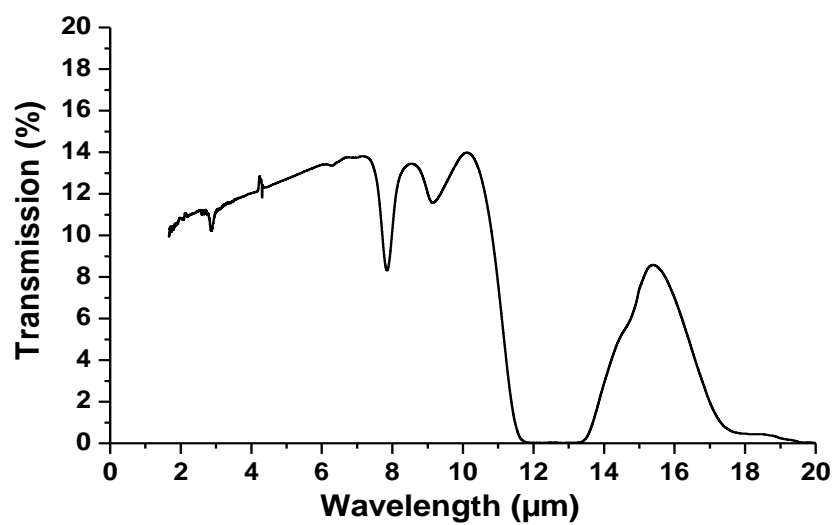


Figure 4.25: Optical transmission of the obtained GeSe_4 sample

An EDS analysis performed in three different areas of the sample yielded homogeneous atomic percentages of 20% Ge and 80% Se, confirming the production of a bulk glass of composition GeSe_4 .

4.5.4. $\text{Ge}_{25}\text{Ga}_5\text{Se}_{70}$ powder

A glass powder obtained after 80h of milling was used. The preparation of the powder is described in chapter 3. The melting temperature was set to 630°C . An inhomogeneous bulk material was obtained. The bottom part of the sample shows a glassy aspect (figure 4.26-a) while the upper part appears crystallized (figure 4.26-b). The central part of the material also presents a highly crystallized aspect and bubbles are observed (figure 4.26-c). The bottom part is in direct contact with the silica and is thus cooled more rapidly during the quenching. The inside and bottom part are cooled down at lower rates. This difference in cooling rates leads to uncontrolled crystallization. It is worth noting that no emanation of fumes was observed during the melting of the powder.

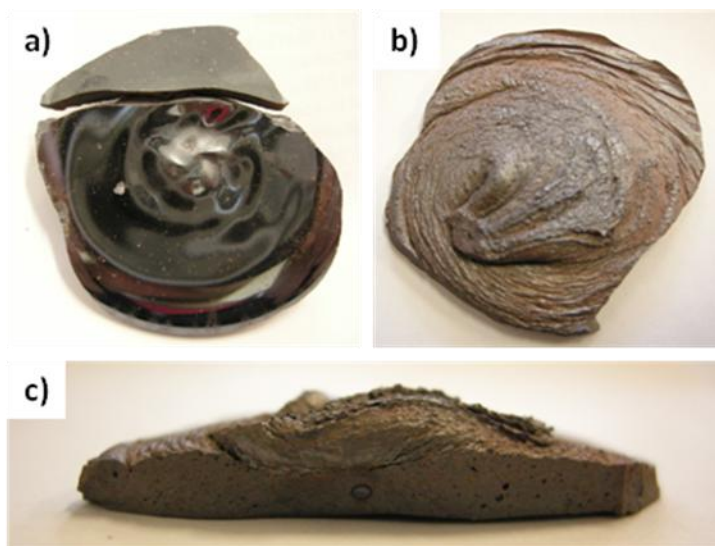


Figure 4.26: Pictures of the $\text{Ge}_{25}\text{Ga}_5\text{Se}_{70}$ sample obtained by melting of the powder prepared by mechano-synthesis, a) bottom view; b) top view; c) inside view

The microstructure of the bulk material was observed by SEM. The bottom part (figure 4.27-a) appears smooth but residual unmelted powder grains are observed. Micrographs of the inside part of the material confirm the presence of an important crystalline phase (figure 4.27-b). Clusters of powder grains and pores were also observed (figures 3.27-c and 3.27-d).

Silica tube of smaller diameters might reduce the time needed to melt the powder and allow a more rapid quenching of the whole melt, thus reducing uncontrolled crystallization. However, homogenization of the melt inside tubes of small diameters might be a major obstacle. Furthermore, it is important to point out that bulk glasses with high dimensions are required for the production of infrared optics. Thus, reducing the dimensions of the samples prepared may not present an interest for this application.

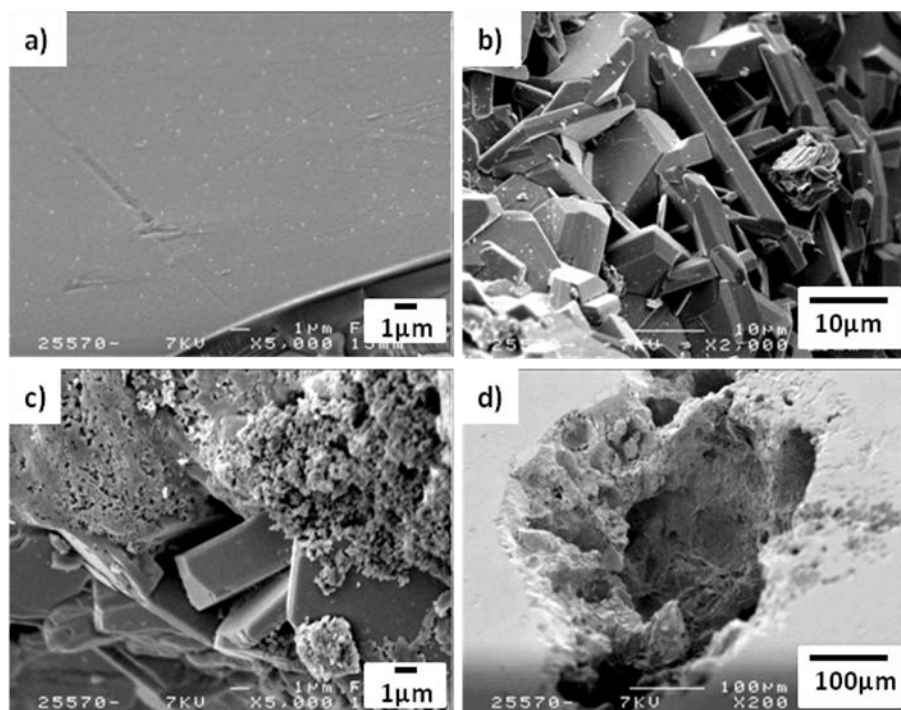


Figure 4.27: SEM micrographs of the bulk material obtained after melting, a) unmelted powder grains on the surface; b) crystals ; c) unmelted powder grains and crystals ; d) porosity observed

4.5.5. Conclusion

A GeSe_4 bulk glass with large dimensions and transmitting in the infrared region was produced by melting a powder previously prepared by mechanosynthesis. This constitutes a new route for the synthesis of chalcogenide glasses, which are normally prepared by melting the raw starting elements in a sealed silica tubes and quenching the melt. However the homogenization parameters need improvement to remove bubbles entrapped during quenching. The mechanosynthesis step will also have to be optimized to prevent oxygen contamination. The contamination of the initial powder by oxygen leads to detrimental absorptions bands on the infrared transmission of the final bulk material.

Performing the entire mechanosynthesis process in controlled, oxygen-free atmosphere should yield production of glasses with enhanced transmission in the infrared range.

The $\text{Ge}_{25}\text{Ga}_5\text{Se}_{70}$ composition possesses the highest stability toward crystallization for glasses from the Ge-Ga-Se system, with a ΔT value ($T_x - T_g$) of 200°C . However, the melting of $\text{Ge}_{25}\text{Ga}_5\text{Se}_{70}$ glass powder prepared by mechanosynthesis yielded uncontrolled crystallization of the material. Furthermore, the remaining powder grains observed on the material after the process indicate incomplete melting. This synthesis route thus appears inadequate for the production of bulk glasses in the Ge-Ga-Se system. Less stable glasses would irretrievably crystallize when using this technique.

4.6. Conclusion

Mechanosynthesis allows the preparation of glass powders without use of silica tubes sealed under vacuum. Different methods for producing bulk chalcogenide glasses from the as-prepared powders have been assessed. Melting the powder in a closed silica chamber under argon flux yielded good results for the stable GeSe_4 composition, although homogenization parameters still require optimization to remove remaining bubbles. A bulk glass transmitting in the infrared region was produced despite the observation of remaining unmelted powder grains. However, this method did not prove successful for less stable glass compositions such as the $\text{Ge}_{25}\text{Ga}_5\text{Se}_{70}$ glass. Despite being the most stable glass in the Ge-Ga-Se system, uncontrolled crystallization occurred during the synthesis process. This undesired phenomenon will undoubtedly occur when melting less stable glass powders such as the $80\text{GeSe}_2\text{-}20\text{Ga}_2\text{Se}_3$ composition.

The second approach considered for consolidation of powders prepared by mechanosynthesis was sintering. Hot Uniaxial Pressing yielded good results for the stable GeSe_4 composition but crystallization problems occurred for the less stable 80GeSe_2 - $20\text{Ga}_2\text{Se}_3$ composition. The prolonged heat treatments necessary to consolidate the material combined with the high specific surface area of the powder irretrievably lead to undesired crystallization and material opaque in the infrared region were obtained.

Overall, Spark Plasma Sintering appears to be the most promising method for consolidation of powders prepared by mechanosynthesis. The short sintering time at a temperature slightly above the glass transition of the glass allows production of infrared transmitting bulk glasses, even for the 80GeSe_2 - $20\text{Ga}_2\text{Se}_3$ composition. This innovative method to produce bulk chalcogenide glasses by combining mechanosynthesis and SPS and without use of expensive silica tubes sealed under vacuum has been patented by the Glass and Ceramics Lab of the University of Rennes 1, France.

While the resulting glasses still showed a contamination of the initial powder by oxygen during the mechanosynthesis process, this issue should be easily resolved by performing the synthesis under controlled atmosphere. The planetary ball mill will have to be placed in a glove box filled with argon to obtain materials with optimized optical transmission in the infrared. This will be the subject of future studies at the Glass and Ceramics Lab of the University of Rennes 1.

CHAPTER 5: CHALCOGENIDE GLASS-CERAMICS FOR INFRARED APPLICATIONS

5.1. Introduction

Selenium-based chalcogenide glasses typically possess a good transmission in the second and third atmospheric windows. Their ability to be shaped by molding is a major advantage as compared to materials currently used for infrared optics such as single crystalline germanium or polycrystalline ZnSe. Indeed, those materials require costly grinding and polishing steps to be formed into lenses. However, the poor mechanical properties of chalcogenide glasses have somewhat limited their widespread use in infrared optics. In that respect, previous studies have shown that controlled crystallization of the glass can improve its mechanical properties (toughness, hardness, coefficient of thermal expansion) while retaining a good transmission in the infrared [47, 56, 58, 59, 128]. Hence, chalcogenide glass-ceramics could serve as a promising low-cost alternative for the production of thermal imaging optics.

Among chalcogenide glass candidates, the composition $80\text{GeSe}_2\text{-}20\text{Ga}_2\text{Se}_3$ is particularly promising because of its controllable crystallization behavior and its ability to be shaped by molding [60]. However, the sample diameter of this glass composition is limited to diameters of 9mm when synthesized in sealed silica tube. Uncontrolled crystallization occurs during quenching in tubes with larger diameters. Nevertheless, the study presented in the previous chapter showed the possibility to produce $80\text{GeSe}_2\text{-}20\text{Ga}_2\text{Se}_3$ glasses with higher dimensions by sintering a glass powder previously prepared

by mechanosynthesis with the SPS technique. Production of bulk glasses with diameters up to 36mm have been demonstrated using this technique. These dimensions are adequate for the production of infrared optics but larger diameters are also achievable since the sample size is only limited by the size of the die employed.

In the following chapter we investigate the possibility of producing 80GeSe_2 - $20\text{Ga}_2\text{Se}_3$ glass-ceramics by SPS for the production of thermal imaging optics. The potential of these glass-ceramics for the design of nanoporous ceramics is also investigated. Previous studies have demonstrated that infrared transparent porous glass-ceramics may present high interest for production of ATR (Attenuated Total Reflections) plates with enhanced detection sensitivity [129, 130]. The etching of 80GeSe_2 - $20\text{Ga}_2\text{Se}_3$ glass-ceramics is therefore assessed with this perspective in mind. Finally, the addition of indium and lead in the GeSe_2 - Ga_2Se_3 system is explored with the aim of improving the thermo-mechanical properties as well as the crystallization behavior of the glass.

5.2. General Principles of Glass-ceramics

5.2.1. Background

By definition, glass-ceramics are polycrystalline materials resulting from the controlled crystallization of a glass. They are composed of one or more crystalline phases embedded in a glassy matrix. Glass-ceramics combine the advantages of both the glassy phase (ability to be shaped by molding, chemical durability) and the crystalline inclusions (mechanical properties, thermal conductivity, low coefficients of thermal expansion). A

controlled crystallization process permits to adjust the properties of the glass-ceramic to fit the specifications of a targeted application. Therefore, these materials present a major interest and have been widely studied over the past decades.

The first glass-ceramic was produced in the mid-18th century by Réaumur who heated a glass bottle for several days and obtained a partially vitreous, polycrystalline material [131]. However, Réaumur had no control on the ceramization process and was not able to obtain reproducible glass-ceramics. More systematic investigations of glass-ceramics started in the 1950s, when Donald Stookey from Corning accidentally produced a material with unexpected strength while trying to precipitate silver particles in a lithium silicate glass. From this discovery, Stookey developed a new class of materials combining unique physical properties. The first investigations were focused on the production of glass-ceramics containing the low thermal expansion β -spodumene crystalline phase conferring a high resistance to thermal shocks to the material. The first commercially available glass-ceramics were distributed in 1958 by Corning under the name Corningware®. Their selling point was focused on the fact that Corningware® products could be taken from the freezer directly to the oven with no risk of thermal shock, thus no risk of breakage of the cookware. Many other glass-ceramics have been commercially developed for a wide variety of applications, such as Fotoceram® (Corning) for electronic devices, Zerodur® (Schott) used for telescope mirrors, or Neoceram™ (Nippon Electric Glass) for high temperature applications [132, 133].

Oxide glass-ceramics are by far the most studied and used materials, but glass-ceramics can also be produced from fluoride glasses [134, 135]. Recently, the first

reproducible chalcogenide glass-ceramics have been produced in the Glasses and Ceramics laboratory at the University of Rennes 1, France [47]. The enhanced mechanical properties of these materials combined with a wide transparency in the infrared region are of particular interest for the production of thermal cameras lenses. The principal challenge in producing chalcogenide glass-ceramics consists in controlling the crystallization process, i.e. crystal size, distribution and proportion of crystalline phase. Uncontrolled crystallization in the glasses leads to unwanted physical properties and makes the materials unusable for potential commercial applications.

5.2.2. Nucleation

Nucleation in a glass initiate from the clustering of atoms into an embryo which can grow into a stable nuclei. This phenomenon is linked to the diminution of the free energy (ΔG) of the system where the crystalline phase generated is more stable than the supercooled liquid. According to Turnbull [136], the free energy needed to create a cluster (or nucleus) of radius r of the crystalline phase is defined by the relation:

$$\Delta G = \frac{4}{3}\pi r^3 \Delta G_v + 4\pi r^2 \sigma$$

where ΔG_v is the change in free energy per volume and σ is the interfacial energy per unit volume. The first term (negative) of this equation shows the energy gain of creating a new volume and the second term (positive) shows the energy loss due to surface tension (σ) of the new interface. The two terms are counterbalancing each other and a nucleus can form only if it reaches a critical radius r_c as illustrated in figure 5.1 where ΔG_t is the change in total free energy and ΔG_c ($\Delta G_c = 16\pi\sigma^3/3\Delta G_v^2$) is the critical value of free

energy needed for the creation of a stable nucleus. The value of the critical radius corresponds to $r_c = -2\sigma/\Delta G_v$.

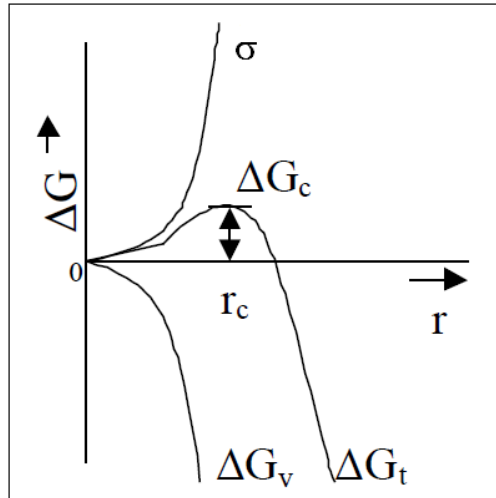


Figure 5.1: Free energy of a particle as a function of its radius

While this mechanism describes a homogeneous nucleation process, heterogeneous nucleation can also commonly occur. Heterogeneous crystallization occurs on low energy sites such as phase boundaries or from impurities and consequently results in a decrease of ΔG_c . In most cases, heterogeneous crystallization is not controlled and is undesirable. However, it can be intentionally generated by addition of small particles inside the glassy matrix during the synthesis process. These particles, called nucleating agents, are spread homogeneously in the glass and nuclei are formed preferentially on their surfaces. This process is commonly used for the production of oxide glass-ceramics such as Corningware® or Zerodur®. Nucleating agents include compounds such as TiO_2 , ZrO_2 , SnO_2 or metallic particles. In the case of this study, only homogeneous nucleation will be considered.

5.2.3. Crystal growth

Crystals grow from the nuclei formed during the nucleation phase. The crystal growth cannot occur without prior nucleation. Glass-ceramics for optical applications must contain a large amount of very small crystals in order to significantly enhance the mechanical properties while still avoiding optical losses induced by Rayleigh scattering.

The homogeneous nucleation-growth process in a glass can be divided along three temperature zones, as shown in figure 5.2. At lower temperatures (zone 1), only nucleation occurs. At higher temperatures (zone 3), crystals grow from the nuclei present in the glassy matrix but no more nuclei are generated. Finally, in the central range of temperature, nucleation and growth happen simultaneously (zone 2).

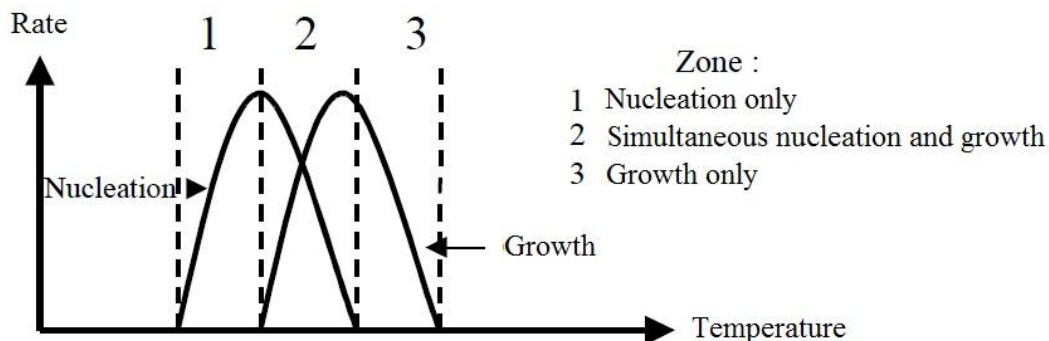


Figure 5.2: Typical representation of nucleation and growth curves

To obtain a large number of crystals with homogeneous size and distribution within the glassy matrix, zone 2 should be as small as possible and the nucleation domain should well separated from the growth domain. However, this is often difficult to achieve with chalcogenide glasses, and the potential presence of impurities within the glass may also result in heterogeneous crystallization.

5.2.4. Ceramization processes

There are three main heat-treatment processes commonly used for the preparation of chalcogenide glass-ceramics.

- One-stage process: a temperature located within zone 2 (figure 5.2) is chosen, thus nucleation and crystal growth happen simultaneously. The temperature has to be optimized to favor an important nucleation and a slow growth rate.
- Two-stage process: a first stage is conducted at a temperature located in zone 1 to generate an important number of nuclei in the glassy matrix. A second stage is then conducted at a temperature located in zone 3 to grow the crystals.
- Heating ramp process: this process consists in slowly heating the glass with a low heating ramp, typically lower than 1°C/min. The glass is heated in a temperature range between its glass transition temperature (T_g) and its crystallization temperature (T_x). It is important to note that a homogeneous distribution of crystals is difficult to achieve with this process. For this reason, one-stage and two-stage processes are more commonly used for preparation of chalcogenide glass-ceramics.

5.3. Production of glass-ceramics by Spark Plasma sintering

5.3.1. Introduction

In 2010, Delaizir et al. showed the possibility of producing chalcogenide glass-ceramics by combined effects of pressure, time, and temperature using SPS. A controlled

crystallization of CsCl crystals in $\text{GeS}_2\text{-Sb}_2\text{S}_3\text{-CsCl}$ glasses was obtained in a short times in comparison with conventional heat treatments [137]. However, the $\text{GeS}_2\text{-Sb}_2\text{S}_3\text{-CsCl}$ powder used in this study was not obtained by mechanosynthesis but by grinding a glass prepared by the conventional melt/quenching technique.

The present study investigates the possibility of producing $80\text{GeSe}_2\text{-}20\text{Ga}_2\text{Se}_3$ glass-ceramics from amorphous powders obtained by mechanosynthesis. In chapter 4, bulk glasses transparent in the infrared were produced with Spark Plasma Sintering treatments of only 2 minutes. Prolonged stages at high temperatures may allow inducing a controlled crystallization of the bulk glass to produce $80\text{GeSe}_2\text{-}20\text{Ga}_2\text{Se}_3$ glass-ceramics as will be shown in the following sections.

5.3.2. Experimental procedure

The Spark Plasma Sintering (SPS) experiments were carried out with a Dr. Sinter 505 Syntex machine at the “Plate-forme de Frittage de Paris”, Thiais, France. An appropriate quantity of $80\text{GeSe}_2\text{-}20\text{Ga}_2\text{Se}_3$ glass powder obtained after 80h of mechanical milling was introduced into a graphite die and sintered under vacuum at a temperature of 390°C ($T_g+20^\circ\text{C}$). This heat-treatment temperature was reached in 4 minutes and kept constant for different dwell durations ranging from 2 minutes to 60 minutes before cooling. The pressure applied during the sintering was 50MPa. A tantalum foil was used to cover the mold to avoid contamination by diffusion of carbon.

The particle size distribution of the powder used is shown in figure 5.3. It is composed of particles from $0.2\text{ }\mu\text{m}$ to $80\text{ }\mu\text{m}$, with most of the particles (75%) having a

size between 1 μm and 20 μm . The impact of the particle size distribution on the sintering was not studied here.

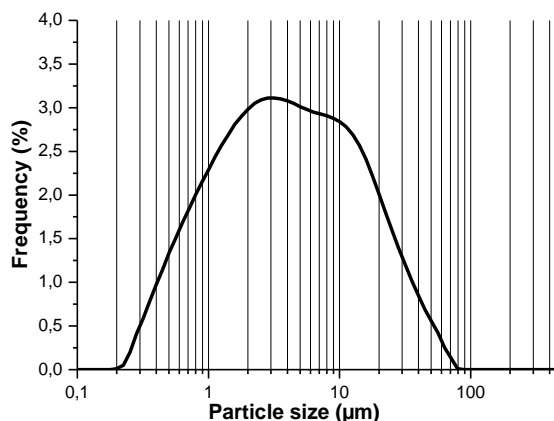


Figure 5.3: Particle size distribution of the $80\text{GeSe}_2\text{-}20\text{Ga}_2\text{Se}_3$ glass powder used for the SPS experiments

5.3.3. Optical properties

The optical transmission of the $80\text{GeSe}_2\text{-}20\text{Ga}_2\text{Se}_3$ glass-ceramics obtained after dwells of 2 min, 15 min, 30 min and 60 min at 390°C is presented in figure 5.4. As a comparison, the transmission of a glass sintered from a $80\text{GeSe}_2\text{-}20\text{Ga}_2\text{Se}_3$ glass powder obtained by grinding a sample prepared by melt/quenching in sealed silica ampoule is also presented. This glass is referred as “base glass” on the following figure.

Absorption bands are observed on the transmission spectra of the sintered glass-ceramics. The band located at $2.9\ \mu\text{m}$ corresponds to vibrations of O-H bonds. Vibrations of Se-H bonds induce absorption bands at $4.3\ \mu\text{m}$ and $7.8\ \mu\text{m}$.

The absorption band at $12.5\ \mu\text{m}$ corresponds to the vibration of Ge-O bonds and its intensity is significantly lower for the base glass. This clearly indicates air leakage in

the milling jar during the process. To optimize the infrared transmission, the planetary ball mill will have to be placed in a glove box under controlled atmosphere.

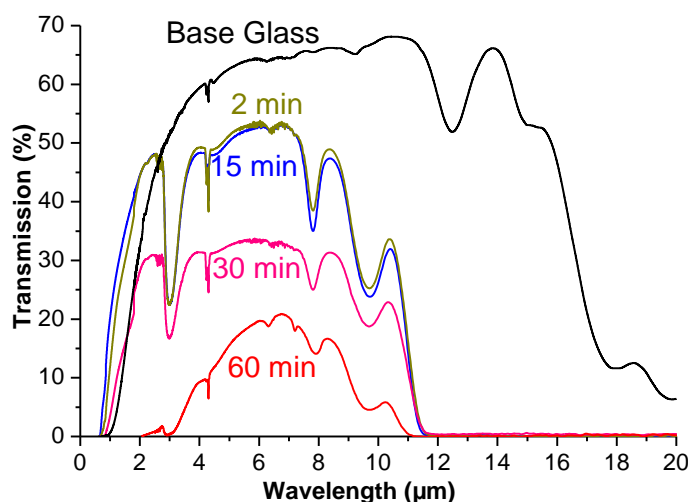


Figure 5.4: Optical transmission of the $80\text{GeSe}_2\text{-}20\text{Ga}_2\text{Se}_3$ glass-ceramics obtained after 2 min, 15 min, 30 min and 60 min of SPS treatment at 390°C

The transmission of the samples extends from $2\ \mu\text{m}$ up to $11\ \mu\text{m}$. The maximum transmission reaches 50% for samples sintered for 2 min and 15 min. After 30 min and 60 min, the transmission decreases. However, after 60 min at 390°C , the sample still remains partially transparent in the infrared range. Rayleigh scattering also becomes more prominent for longer dwell time as the crystal size increases [51, 138]. Surface oxidation of the initial powder may also provoke Rayleigh scattering due to localized differences in refractive indices at the grain boundaries. The decrease of the maximum of transmission is mainly due to the crystallization of particles with bigger dimensions (microcrystals) inducing MIE scattering.

Finally it is important to note that 80GeSe₂-20Ga₂Se₃ glass-ceramics have been obtained within minutes by SPS treatments. The conventional technique used to prepare equivalent glass-ceramics by heating bulk glass samples in a ventilated furnace takes tens of hours [68]. The production time is thus considerably shortened.

5.3.4. X-Ray Diffraction

The XRD spectra of the initial 80GeSe₂-20Ga₂Se₃ glass powder (80h of milling) and of samples obtained after sintering for 2 min, 30 min and 60 min at 390°C are presented in figure 5.5. After 2 min of sintering, the XRD pattern shows that the sample is still amorphous, i.e. is a bulk glass. The results obtained for a 30 minutes SPS treatment time clearly show that the Ga₂Se₃ (or Ga₄GeSe₈) crystalline phase has nucleated and grown inside the glassy matrix. The preference for the formation of this crystalline phase has been discussed in a study by Calvez et al. [51]. For longer treatment time (60 minutes) a second phase, GeSe₂ is appearing.

The Ga₂Se₃ crystalline phase is responsible for the Rayleigh scattering observed on the optical transmission of the 80GeSe₂-20Ga₂Se₃ glass-ceramics (figure 5.4). The uncontrolled development of GeSe₂ crystals leads to the important MIE scattering observed after 60 min of SPS treatment as will be shown later by SEM and TEM.

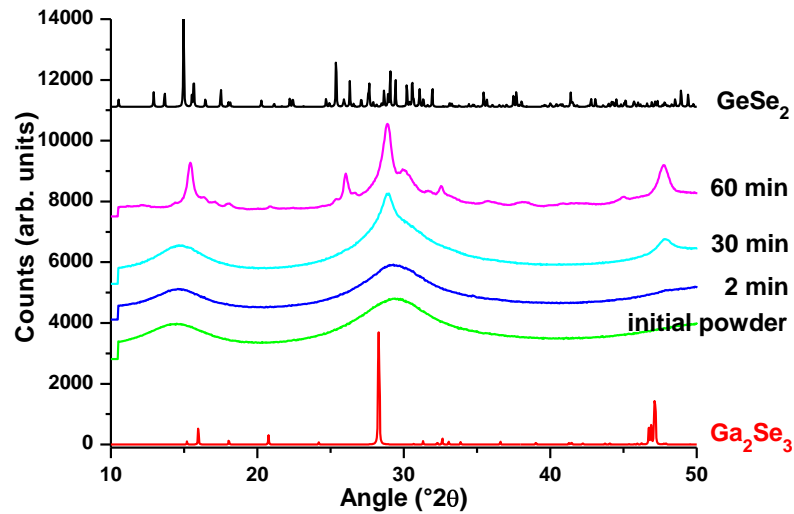


Figure 5.5: XRD spectra of the initial 80GeSe₂-20Ga₂Se₃ glass powder used (80h of milling) and of samples obtained after 2 min, 30 min and 60 min of SPS treatment at 390°C

It was not possible to find values for the refractive indices (n) of Ga₂Se₃ and GeSe₂ bulk crystals in the literature. However, values of refractive index of 2.55 for GeSe₂ [139] and 2.40 for Ga₂Se₃ [140] at 800 nm have been measured on amorphous thin films. From these values, it can be assumed that the refractive indices of both crystalline phases are close to the value of the refractive index of the 80GeSe₂-20Ga₂Se₃ glass (2.42 at 1.33 μm [68]). Thus, the scattering provoked by the slight variation in refractive indices between the glassy matrix and the crystals precipitated should be limited. Thereby, the important scattering observed at shorter wavelengths for the glass-ceramics obtained after 60 min of SPS treatment (figure 5.4) is more likely due to precipitation of GeSe₂ crystals with large dimensions (several hundreds of nm). The observation of the glass-ceramics microstructure presented in the following paragraph confirms this hypothesis.

5.3.5. Microstructure

The microstructure of the glass-ceramics obtained has been investigated by Scanning Electron Microscopy (FEG-SEM JEOL 7400F) and Transmission Electron Microscopy (TEM, JEOL 2100F) as shown in figure. 4.6. No crystals are observed after 2 min at 390°C, as seen on figure 5.6-a. A crystallization of about, 15%, 40% and 70% of nanoparticles with size ranging from 50 nm to 200 nm is observed after 15 min (figure 5.6-b), 30 min (figure 5.6-c) and 60 min (figure 5.6-d) of SPS treatment, respectively. The TEM picture (figure 5.6-e) shows the mechanism of growth of Ga_2Se_3 nanocrystals ranging from 50 nm to 200 nm which are progressively constituted of aggregates of particles of 5 nm to 10 nm as previously observed for this composition [61]. For longer treatment time (60 minutes), crystals 500 nm in size, thus five to ten times bigger than the Ga_2Se_3 crystals appear (figure 5.6-f) and are attributed to the GeSe_2 crystalline phase observed by XRD (figure 5.5) [127].

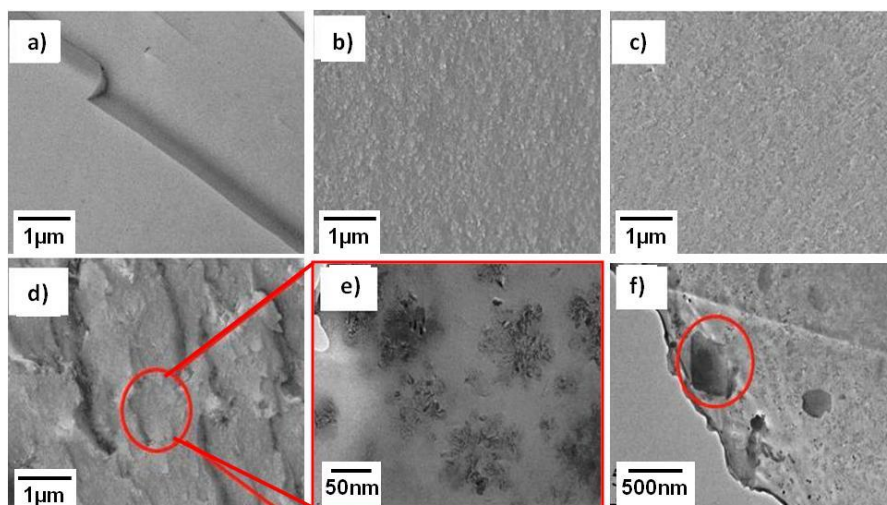


Figure 5.6: SEM images of glass-ceramics obtained from the 80GeSe₂-20Ga₂Se₃ base glass powder for SPS treatment time of a) 2 min b) 15 min, c) 30 min, d) 60 min of SPS treatment at 390°C; e) Ga₂Se₃ and f) GeSe₂ crystals observed under TEM observation on the glass ceramic treated for 60 min at 390°C

5.3.6. Mechanical properties

The mechanical properties of the glass-ceramics obtained by SPS are compared to the base glass made by the conventional melt/quenching technique in table 5.1. The measurement techniques have been described in chapter 3.

Table 5.1: Mechanical properties of the glass-ceramics obtained after SPS treatment and of a $80\text{GeSe}_2\text{-}20\text{Ga}_2\text{Se}_3$ glass prepared in sealed silica tube

Sample	Density (ρ) $\pm 0.03 \text{ Kg.m}^{-3}$	Young's modulus (E) $\pm 0.3 \text{ GPa}$	Vickers Hardness (Hv) $\pm 1 \text{ Kg.mm}^{-2}$	Toughness (K_{IC}) $\pm 0.005 \text{ Mpa.}\sqrt{\text{m}}$
<i>Base glass</i>	4.39	22.7	201	0.186
<i>2 min</i>	4.39	22.6	199	0.180
<i>15 min</i>	4.42	23.6	200	0.194
<i>30 min</i>	4.47	24.3	203	0.206
<i>60 min</i>	4.30	----	167	No cracks

The glass obtained after 2 min of SPS treatment at 390°C present similar physical and mechanical properties than the base glass, with a density of 4.39 ± 0.2 , a hardness of $199 \pm 2 \text{ Hv}$, toughness K_{IC} of $0.186 \pm 0.005 \text{ MPa.m}^{1/2}$. These results are in good agreement with those of glasses synthesized in silica tubes reported in a previous study by Rozé et al. [61]. In order to make a comparison, it is important to notice that the GASIR[®] glass ($\text{Ge}_{22}\text{As}_{20}\text{Se}_{58}$), currently one of the most used chalcogenide glasses for infrared devices, presents a hardness of 170 Hv, a Young's Modulus of 17.89 GPa and a thermal expansion coefficient of $17.10^{-6} \text{ K}^{-1}$ [141]. The thermal expansion coefficient of $80\text{GeSe}_2\text{-}20\text{Ga}_2\text{Se}_3$ glass and glass-ceramics is also lower at $12.10^{-6} \text{ K}^{-1}$ and independent of the crystallization time. Since glass-ceramics typically have higher thermal conductivity than glasses [133], the combination of this low thermal expansion

coefficient value and higher thermal conductivity leads to an increase in the resistance of this material to thermal shocks.

Finally, an important increase of toughness is observed with longer SPS treatment duration. This is linked to the growing percentage of generated nanoparticles inside the glassy matrix and then to the growing size of nanoparticles from 50 nm to 200 nm (figure 5.6 and table 5.1). The hardness remains constant with increasing number of Ga_2Se_3 particles but drastically decreases when GeSe_2 particles start growing, inducing a decrease in the glass-ceramic density.

5.3.7. Conclusion

Bulk $80\text{GeSe}_2\text{-}20\text{Ga}_2\text{Se}_3$ glass-ceramics transparent in the infrared were prepared with enhanced mechanical properties by combining mechanosynthesis and Spark Plasma Sintering [127]. The controlled crystallization of nanoparticles obtained with this technique is significantly faster than the conventional technique which consists in heating bulk glassy samples in a ventilated furnace.

A strong absorption band due to Ge-O vibrations located at $12.5\text{ }\mu\text{m}$ indicates a contamination of the initial powder by oxygen during the mechanosynthesis process. For future studies, the planetary ball mill will have to be placed in a glove box under controlled atmosphere since optical transmission is a key factor for thermal imaging applications.

The diameter of $80\text{GeSe}_2\text{-}20\text{Ga}_2\text{Se}_3$ bulk glasses and glass-ceramics is limited to 9mm when using the conventional melt/quenching technique, thus limiting the

applications for this composition. The innovative synthesis route developed during this study allows producing samples of larger diameters adequate for infrared applications. It also reduces the production time to a few minutes. Thus, this new process would lead to lower manufacturing costs of chalcogenide glasses and glass-ceramics which could be adapted to numerous set-ups such as thermal imaging, infrared laser sources, waveguides or infrared sensors.

5.4. Porous glass-ceramics

5.4.1. Introduction

In 2007, Delaizir et al. showed an enhancement of the detection sensitivity of Attenuated Total Reflection (ATR) plates made of $\text{GeSe}_2\text{-Sb}_2\text{S}_3\text{-CsCl}$ nanoporous glass-ceramics [129, 130]. The porosity was obtained by chemical etching of quasi- CsCl nanocrystals precipitated in the glass-ceramics. Etching was carried out with a “piranha” solution, composed of 70% of concentrated H_2SO_4 (98%) and 30% of H_2O_2 (35%). This acid solution has been used previously for chemical polishing of chalcogenide glasses from the Te-As-Se system [142].

As demonstrated in the previous section, the $80\text{GeSe}_2\text{-}20\text{Ga}_2\text{Se}_3$ composition also shows controllable crystallization behavior and might therefore presents high interest for the design of nanoporous optical elements. The behavior of glass-ceramics in acid and basic solutions has therefore been investigated in order to assess the possibility of producing porous glass-ceramics of that composition by chemical etching. While CsCl is

highly hygroscopic and relatively easy to dissolve, the Ga_2Se_3 nanoparticles generated in the $80\text{GeSe}_2\text{-}20\text{Ga}_2\text{Se}_3$ glass-ceramics should be more difficult to dissolve. In the following section, it is shown that etching $80\text{GeSe}_2\text{-}20\text{Ga}_2\text{Se}_3$ in acid solution can nonetheless lead to highly porous surfaces.

5.4.2. Etching in acid solution

Glass-ceramics pellets with a composition of $80\text{GeSe}_2\text{-}20\text{Ga}_2\text{Se}_3$ were used. The crystallization process for this composition has been described by Rozé et al. [61]. For ceramization processes shorter than 61h, a Ga_2Se_3 crystalline phase precipitates in the form of aggregates of about 100 nm in size uniformly distributed within the glassy matrix. Longer ceramization durations lead to precipitation of larger crystals of GeSe_2 phase inducing important Rayleigh and MIE scattering. In our case, $80\text{GeSe}_2\text{-}20\text{Ga}_2\text{Se}_3$ glass-ceramics heat treated for 60h were used.

Glass-ceramic pellets with a diameter of 9mm and a thickness of 1.75mm were immersed into a piranha solution for durations ranging from 5 min to 120 min. The piranha solution was stirred with a magnetic stirrer during etching. After the etching treatment, the glass-ceramics were rinsed with deionised water. The microstructure of the etched glass-ceramics was then observed by Scanning Electron Microscopy (figure 5.7).

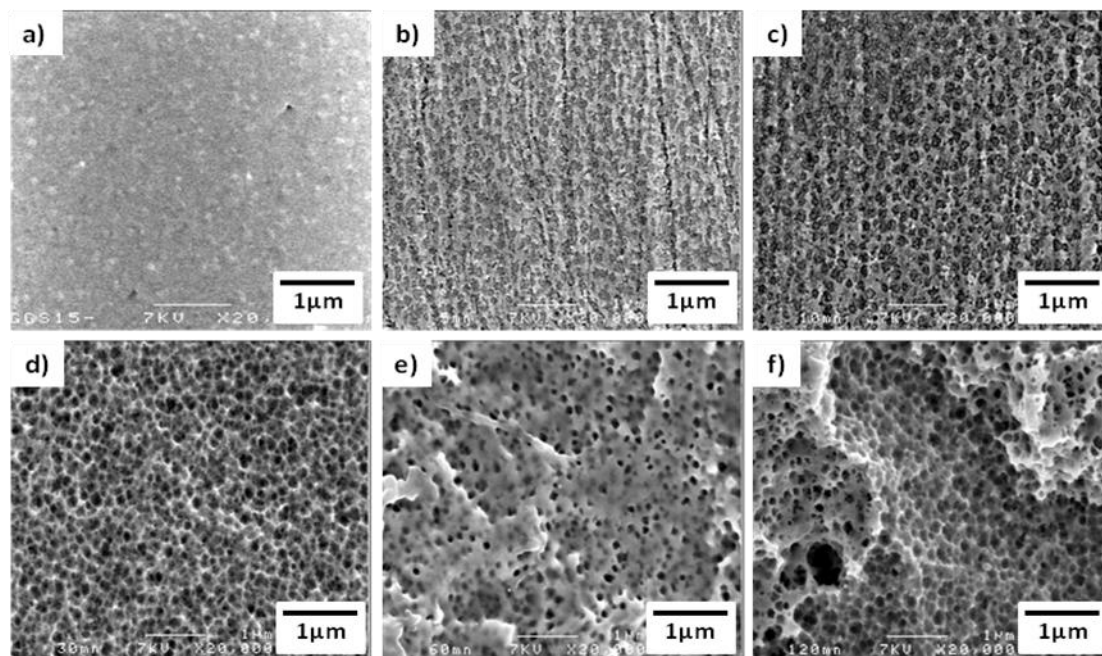


Figure 5.7: SEM images (x20,000) of the $80\text{GeSe}_2\text{-}20\text{Ga}_2\text{Se}_3$ glass-ceramics etched in "piranha" solution for a) 0 min, b) 5 min, c) 10 min, d) 30 min, e) 60 min, f) 120 min

Before etching, the glass-ceramic presents a smooth aspect, and 100 nm crystals homogeneously distributed in the glassy matrix are observed (figure 5.7-a). After 5 min of etching (figure 5.7-b), pores are observed in the material. The pores are homogeneous in size (about 100 nm) and evenly distributed on the surface of the material. The dimensions of the pores correspond to the size of the Ga_2Se_3 crystals dispersed in the glassy matrix [61]. This confirms that the crystalline phase is preferential etched by the "piranha" solution. The size of the pores and their distribution on the surface of the material is similar after 10 min (figure 5.7-c) and 30 min (figure 5.7-d) of etching. Only the depth of the pores increases.

However, the morphology of the glass-ceramic surface changes for longer etching times. After 60 min (figure 5.7-e), the remaining glassy phase has been partially dissolved and crystals previously buried have been exposed to the piranha solution. Pores

of about 100 nm in size are still observed throughout the glass-ceramic but bigger holes are also created on the surface of the material. This observation is similar after 120 min of etching treatment (figure 5.7-f). SEM images collected at lower magnification clearly show the creation of large holes on the surface and a collapse of the structure of the material after 60 min (figure 5.8-a) and 120 min (figure 5.8-b) of etching. However, it is important to point out that the size and distribution of the nanopores (about 100 nm in size) is homogeneous whatever the etching time.

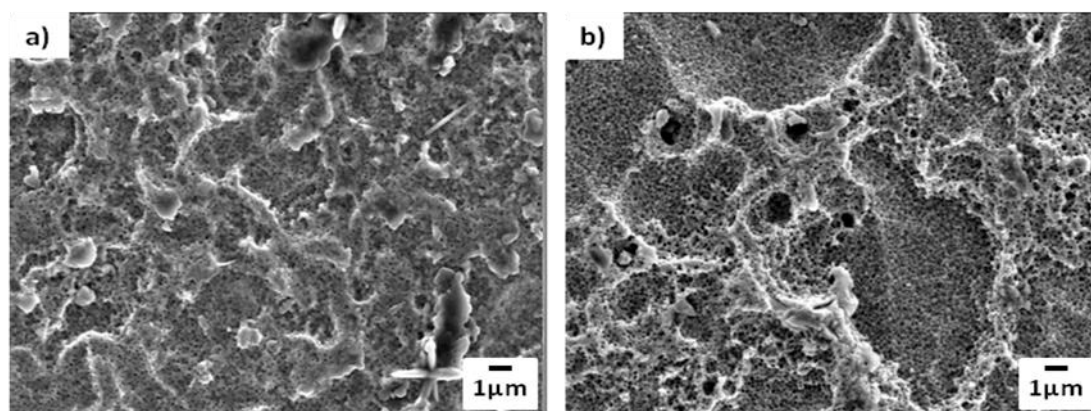


Figure 5.8: SEM images (x5,000) of the 80GeSe₂-20Ga₂Se₃ glass-ceramics etched in "piranha" solution for a) 60 min and b) 120 min

The partial dissolution of the glassy matrix for long etching duration leads to a continuous decrease of the thickness of the material with etching time as illustrated in figure 5.9. After 10 min of etching, the material still presents its initial thickness. It can thus be assumed that only the crystals are dissolved at this time. For longer etching times, the thickness decreases, indicating a progressive leaching of the glassy phase on the surface of the material. It is worth noting that the material is completely dissolved after 20 hours of treatment in the "piranha" solution.

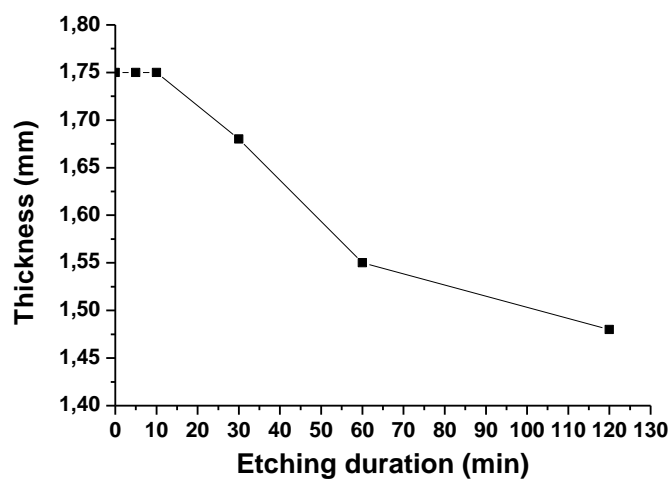


Figure 5.9: Evolution of the thickness of the $80\text{GeSe}_2\text{-}20\text{Ga}_2\text{Se}_3$ glass-ceramic pellets as a function of etching duration in a “piranha” solution

The cross sections of the etched glass-ceramics were observed by SEM to help understanding the dissolution process. Two different angles of observation were used: 45° (observation of the surface and the cross section) and 90° (observation of the cross section). Prior to the observation, the samples were broken to reveal the thickness of the porous layer and the morphology of the bulk material. The pictures of the glass-ceramics etched for 5 min, 10 min, 30 min and 60 min are presented in figure 5.10. The glass-ceramic etched for 120 min is not shown as it presents the same morphology as the glass-ceramics etched for 60 min.

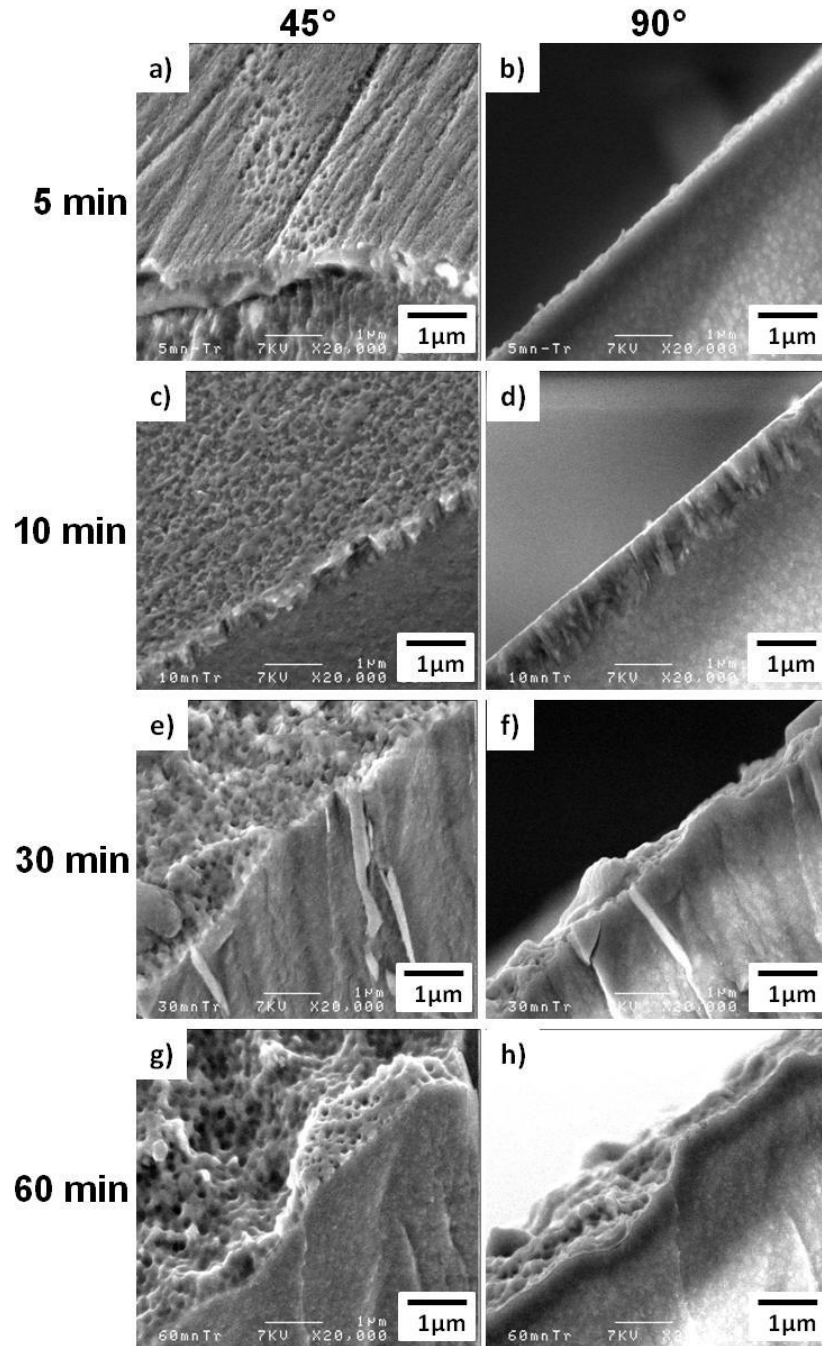


Figure 5.10: SEM observation of the cross section of the $80\text{GeSe}_2\text{-}20\text{Ga}_2\text{Se}_3$ glass-ceramics etched in a "piranha" solution for a,b) 5 min, c,d) 10 min, e,f) 30 min and g,h) 60 min

The depth of porous layer on the $80\text{GeSe}_2\text{-}20\text{Ga}_2\text{Se}_3$ glass-ceramics is about 200 nm after 5 min of treatment (figures 4.10-a and 4.10-b), and reaches about 1 μm after 10

min of etching (figures 4.10-c and 4.10-d). The surface of the material is still flat up to 10 min of etching. After 30 min (figure 5.10-e and 4.10-f) and 60 min (figure 5.10-g and 4.10-h) in the “piranha” solution, it clearly appears that the surface is more severely attacked and becomes rough. A part of the glassy phase remaining on the surface has been progressively dissolved, leading to the decrease in thickness of the glass-ceramics measured (figure 5.9). It is important to note the presence of undissolved crystals below the porous layer, whatever the etching treatment duration. A crystallized fraction of about 60% can be estimated from the SEM pictures and these crystals do not form a highly interconnected phase. Thus, the dissolution of crystals is limited to a thin layer beneath the surface.

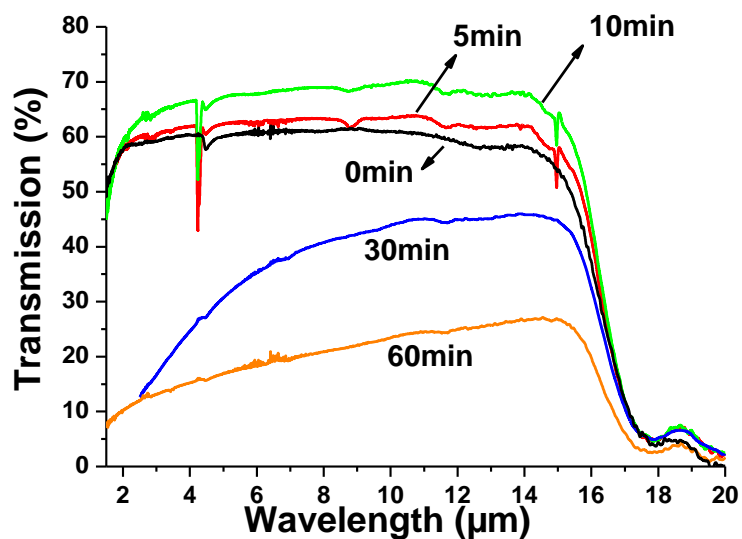


Figure 5.11: Optical transmission of the $80\text{GeSe}_2\text{-}20\text{Ga}_2\text{Se}_3$ glass-ceramics as a function of etching duration in a “piranha” solution

The optical transmission of the etched glass-ceramics is presented in figure 5.11. The glass-ceramics etched for 5 min and 10 min are still highly transparent in the infrared

range up to 17 μm . It is interesting to note the increase from 60% to 70% in the maximum of transmission for short etching time as compared to the glass-ceramic not treated in the “piranha” solution (0 min), even though the thickness of the samples remained the same (1.75mm) after 0 min, 5 min and 10 min (figure 5.9). However, for longer etching times, the porosity affects the optical transmission of the glass-ceramics and while the materials are still transparent in the infrared region up to 17 μm , the maximum of transmission is decreased to 45% after 30 min and to 20% after 60 min. After 120 min of etching, large holes and the irregular morphology of the surface of the material (figure 5.8-b) induce important optical losses and the material becomes opaque.

The increase in the maximum of transmission after 10 min of etching is of particular interest as it would be beneficial for optical applications. This phenomenon could be explained by an anti-reflection effect played by the nanoporous layer on the surface of the glass-ceramic. Two approaches may be considered. The important change in refractive index between air ($n=1$) and the $80\text{GeSe}_2\text{-}20\text{Ga}_2\text{Se}_3$ glass-ceramics ($n\sim 2.6$) induces important losses by reflection, called Fresnel losses. The normal reflection of a light beam of wavelength λ incident on a substrate coated with a homogeneous layer of thickness $\lambda/4$ will be minimized if:

$$n = \sqrt{n_s \cdot n_0}$$

where n is the refractive index of the coating layer, n_s is the refractive index of the substrate and n_0 is the refractive index of air [143]. In our case, this value would be of $n=1.61$. The nanoporous layer on the surface of the etched $80\text{GeSe}_2\text{-}20\text{Ga}_2\text{Se}_3$ glass-ceramics can be considered as a layer composed of a mix of air and glass. Assuming a

ratio air/glass of 60%/40%, its refractive index can be approximated by averaging the refractive indices of the two materials, i.e. $n_{\text{approx}} \approx (0.6 \times 1 + 0.4 \times 2.6) \approx 1.64$. This value is close to that of $n=1.61$ calculated for a minimization of the reflection losses for a coating layer of thickness $\lambda/4$. The thickness of the porous layer was evaluated by SEM to be of 1 μm (figure 5.10-d). This value is on the order of magnitude of $\lambda/4$ for values of λ in the infrared region. Thus, the nanoporous layer on the surface of the etched $80\text{GeSe}_2\text{-}20\text{Ga}_2\text{Se}_3$ glass-ceramics may act as an anti-reflection coating reducing Fresnel losses, thus increasing the observed transmission.

The nanoporous layer may also be considered as a microstructured surface. Sanghera et al. observed a reduction of Fresnel losses in chalcogenide fibers using anti-reflective surface structures imprinted on fiber end faces [144]. The controlled periodic porosity gradient created into the surface of the fibers induces a gradient of refractive indices and reduces the losses by reflection in a similar way that previously described for anti-reflection coating layer. To be efficient, such surfaces should present periodic patterns with pores (or protrusions) with height greater than $\lambda/2$ and a periodicity of less than $\lambda/2n$ to avoid diffraction effects, where λ is the wavelength of operation and n is the index of the substrate. As can be observed on figure 5.7, after 5 min and 10 min of etching, pores of about 100 nm in size are evenly distributed on the surface of the glass-ceramic, with a spacing of less than 100 nm between two pores. While the size of the pores is close but lower than $\lambda/2$, the quasi-periodicity observed may be responsible for the enhanced transmission of the $80\text{GeSe}_2\text{-}20\text{Ga}_2\text{Se}_3$ glass-ceramics after 5 min and 10 min of etching. The collapse of the surface morphology due to excessive dissolution for

longer etching time alters this quasi periodicity and leads to important decreases of the transmission (figure 5.11).

Besides this useful anti-reflection effect, the porous layer may be of interest for sensing application as shown in a previous study by G. Delaizir [129]. In this study, the porosity was obtained by etching of CsCl crystals in glass-ceramics with a composition of $62.5\text{GeS}_2\text{-}12.5\text{Sb}_2\text{S}_3\text{-}25\text{CsCl}$. However, the proportion of crystals in these glass-ceramics was very low (10% to 15%) in comparison to the present $80\text{GeSe}_2\text{-}20\text{Ga}_2\text{Se}_3$ glass-ceramics showing Ga_2Se_3 crystalline fraction of about 60%. The porosity of these glass-ceramics should therefore be significantly enhanced.

The surface area of the $80\text{GeSe}_2\text{-}20\text{Ga}_2\text{Se}_3$ glass-ceramic before etching and after 10 min of treatment in a “piranha” solution was measured on cylindrical samples with a diameter of 9 mm and a thickness of 1.75 mm. The measure was performed on a Micrometrics ASAP 2010 Physisorption analyzer using the BET (Brunauer, Emmett and Teller) gas adsorption method. The results are presented in table 5.2. The creation of porosity on the surface of the $80\text{GeSe}_2\text{-}20\text{Ga}_2\text{Se}_3$ glass-ceramic leads to an important increase in the surface area, from 4.9 m^2 before etching to more than 32 m^2 after 10 min of etching. Thus, the surface area has been multiplied by a factor 6.5 as compared to the glass-ceramic before etching and by a factor 11.5 as compared to the base glass.

Table 5.2: Surface area of the $80\text{GeSe}_2\text{-}20\text{Ga}_2\text{Se}_3$ base glass, the glass-ceramic before etching and after 10 min of treatment in a “piranha” solution

Sample	Glass-ceramic	10 min of etching	Base glass
Surface area	4.9 m^2	32.2 m^2	2.8 m^2

It is worth noting that the surface area measured on the sample before etching is on the order of some square meters while the theoretical value of the surface area of samples with these dimensions (cylinder with diameter of 9mm and thickness of 1.75mm) is 1.77cm². Thus, the actual surface area is more than 25,000 times greater than the theoretical surface area where a perfect planarity of the surface of the sample is assumed. However, the cutting and polishing steps performed during the sample preparation induces micro-scratches and striations on the surface, called roughness which can dramatically increase the actual value of the surface area. The values presented in table 5.2 for glass-ceramics were measured on samples polished using alumina powder with grain size of 1 μ m. Their roughness is on the order of tens of nanometers. To assess the influence of polishing, the surface area of a sample with similar dimensions and optically polished was measured. The roughness of this sample, measured by Atomic Force Microscopy (AFM), is inferior to 5 nm. This sample designated as “base glass” in table 5.2, shows a lower value of surface area due to the decreased roughness. However, this value is still in the order of the square meter.

It is worth noting that in the study by Delaizir, the surface area of samples with initial dimensions of 24 mm x 10 mm x 5 mm was calculated to be 10 cm² before etching and measured to be 7 m² after etching [130]. Therefore, the surface area was estimated to be multiplied by a factor 7000 after etching treatment. However, absorption measurement performed on porous glass-ceramics functionalized with a silane molecule only showed a four- to five-fold increase in absorption in comparison to the glass-ceramic before etching. This discrepancy can be explained by the important difference between the

theoretical value and the experimental surface area as measured for the 80GeSe_2 - $20\text{Ga}_2\text{Se}_3$ glass-ceramics. From these results, it can be assumed that the value of 10cm^2 presented in the study by Delaizir corresponds to the theoretical surface area and that the actual surface area is on the order of the square meter. Thus, the factor of multiplication of the surface area obtained by etching is probably lower than 10, as compared to 7000. This value would then be consistent with the absorption measurements [130].

The glass-ceramic surface was functionalized with 3-aminopropyltriethoxysilane (APTS) by immersing the sample in a solution of toluene containing 10% of APTS for 2 h. Silane molecules are commonly used to functionalize surfaces and permit to anchor layers of molecules with specific recognition sites such as enzymes [145, 146]. The Si-O-Si and amino group vibrations of silanol present characteristic absorptions in the $1000 - 1150\text{ cm}^{-1}$ range [130]. Figure 5.12 shows the absorbance spectra measured after functionalizing a glass-ceramic not etched and glass-ceramics etched in a “piranha” solution for 5 min and 10 min. The surface porosity acts as an anchorage site for silane molecules and the glass-ceramic etched for 10 min shows a 5-fold increase in absorbance in comparison to the flat glass-ceramic. This increase is comparable to that obtained by Delaizir et al. for GeS_2 - Sb_2S_3 - CsCl etched glass-ceramics [130]. This demonstrates the possibility of functionalizing the glass-ceramic surface and consequently the potential of applying these materials to the design of sensors with specific binding capabilities.

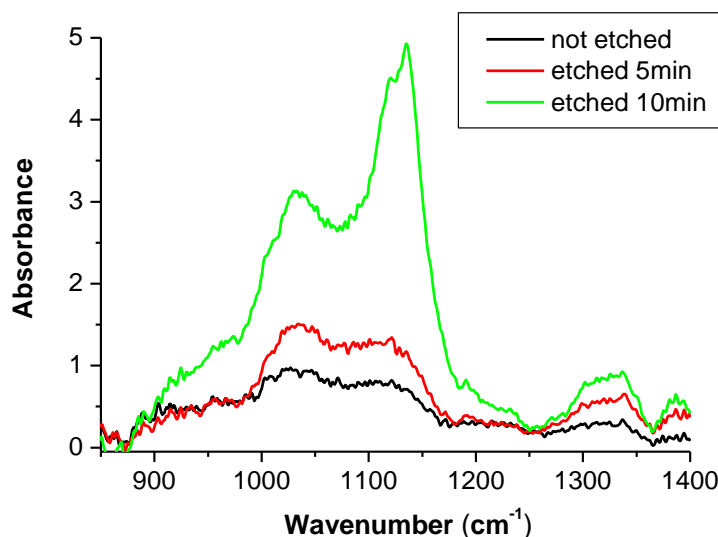


Figure 5.12 : Absorbance spectrum of 80GeSe₂-20Ga₂Se₃ glass-ceramics functionalized with APTS

Overall, the porous glass-ceramics obtained after 10 min of treatment in a “piranha” solution possess surface area enhanced by a factor 11.5 and a transmission increased by 10% in the infrared range as compared to 80GeSe₂-20Ga₂Se₃ glass-ceramics before treatment. These materials could therefore be effectively functionalized and could present a high interest as substrates for infrared sensors or Attenuated Total Reflection (ATR) plates with increased detection sensitivity.

5.4.3. Surface passivation

Two configurations were studied for the etching of the 80GeSe₂-20Ga₂Se₃ glass-ceramics. The first one consisted in laying down the glass-ceramic pellets in the bottom of a beaker containing the “piranha” solution without agitation system, as shown in figure 5.13-a. In the second configuration, the glass-ceramics were held in the “piranha” solution with a clamp and a magnetic stirrer was used for agitation, as shown in figure

5.13-b. It is essential to note that all the results presented in the previous paragraph were obtained using the second configuration.

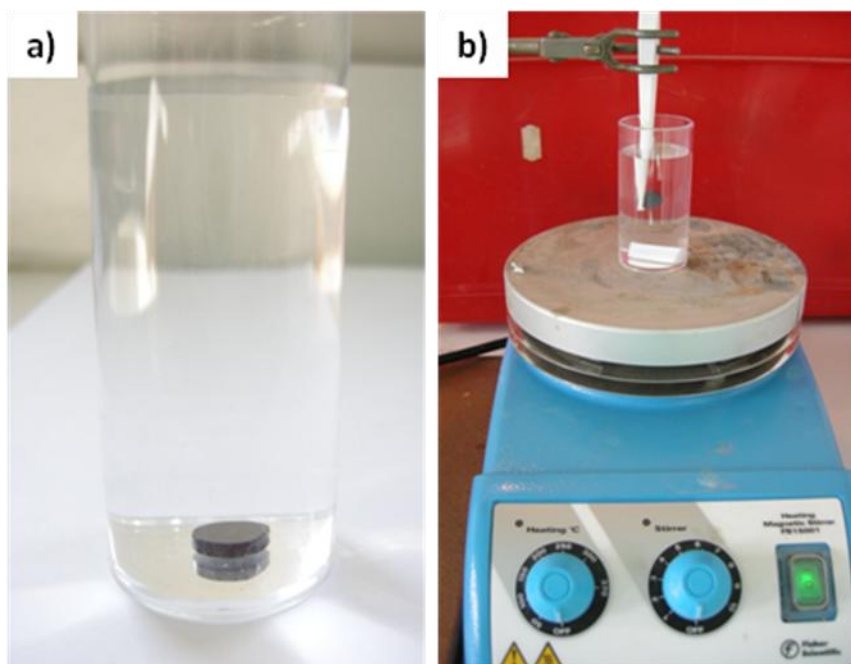


Figure 5.13: Configurations used for etching of $80\text{GeSe}_2\text{-}20\text{Ga}_2\text{Se}_3$ glass-ceramics in a "piranha" solution, a) without agitation, b) with agitation system

The method employed for etching with a “piranha” solution strongly affected the results obtained. With the agitation system, the glass-ceramic was completely dissolved after 20 h in the piranha solution, as mentioned in the previous paragraph. When the glass-ceramic was placed in the bottom of the beaker with no agitation, the material integrity remained and the thickness of the glass-ceramic did not change after 20 h of etching. SEM images of the glass-ceramics etched for 2 h and 20 h in a piranha solution with no agitation are presented in figure 5.14.

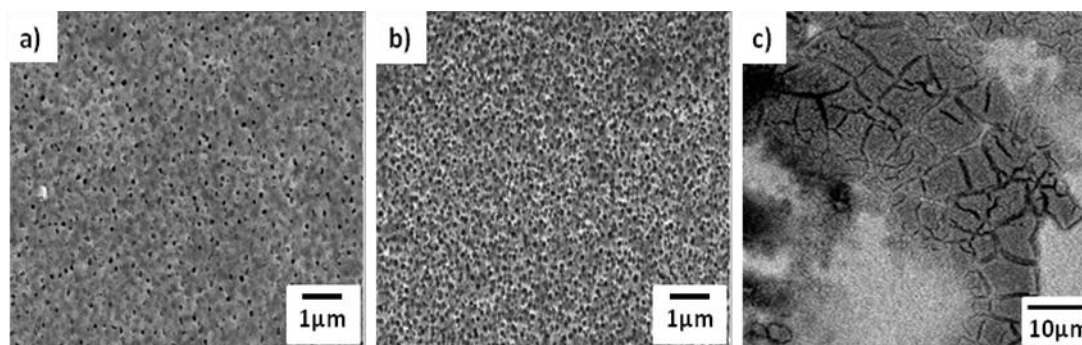


Figure 5.14: 80GeSe₂-20Ga₂Se₃ glass-ceramics after a) 2 h and b) 20 h of etching in a "piranha" solution with no agitation system, c) white layer observed on the surface

Pores of about 100 nm in size are observed after 2 h of etching (figure 5.14-a). Their number increases after 20 h of etching (figure 5.14-b). While this morphology appears somewhat similar to that obtained with agitation of the "piranha" solution the kinetic of etching is much slower and a white layer is observed on the surface of the glass-ceramics as shown in figure 5.13-c. An Electron Dispersive X-Ray Spectroscopy analysis was performed to identify the nature of this layer. It is composed of germanium oxide (GeO₂) and selenium oxide (SeO₂). The dissolution of the glass-ceramic leads to a rapid reaction with the "piranha" solution to form SeO₂ and GeO₂. When no agitation is carried out, these compounds deposit on the surface of the glass-ceramic and act as a passivation layer. When the etching is performed with agitation, such as presented in figure 5.13-b, this deposition cannot occur. This explains the conservation of the material after 20 h of etching when no agitation is performed, while the material is being completely dissolved with agitation of the "piranha" solution for the same etching time. Similar behavior is observed for chemical polishing of silica glasses [147].

5.4.4. Etching in basic solution

The preceding paragraphs describe the behavior of $80\text{GeSe}_2\text{-}20\text{Ga}_2\text{Se}_3$ glass-ceramics in acid solutions. It is known that chalcogenide glasses are more resistant to acid solution than basic solutions, hence the behavior of the glass-ceramics in basic solutions has also been studied. A $80\text{GeSe}_2\text{-}20\text{Ga}_2\text{Se}_3$ glass-ceramic pellet with similar dimensions than the sample used for etching in “piranha” solution and prepared in similar conditions was used. The sample was immersed in a NaOH 0.1M solution for 20 hours.

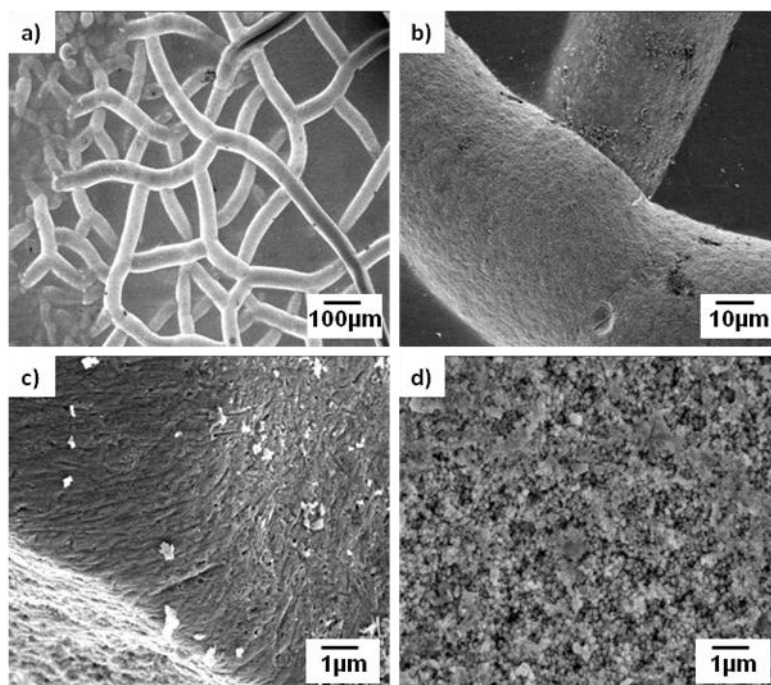


Figure 5.15: a,b) canals, c) pores observed on the glass-ceramics after 20h of etching in a NaOH 0.1M solution; d) remaining crystals observed in the canals

The microstructure was observed using Scanning Electron Microscopy (SEM) as shown in figure 5.15. In contrast to etching in a “piranha” solution, the etching of $80\text{GeSe}_2\text{-}20\text{Ga}_2\text{Se}_3$ glass-ceramics in a NaOH 0.1M was not homogeneous. Canals were formed on the surface of the sample, as seen on figures 4.15-a and 4.15-b. These canals

appear randomly distributed on the surface. Pores are also observed (figure 5.15-c). A closer look inside the canals formed (figure 5.14-d) shows that the glassy phase is preferentially etched and a crystalline phase composed of aggregates of crystals of about 100 nm remains. However, the inhomogeneous character of the dissolution was not explained and no further studies were performed for etching of $80\text{GeSe}_2\text{-}20\text{Ga}_2\text{Se}_3$ glass-ceramics in basic solution. It is worth noting that the glass-ceramic obtained did not present optical transmission in the infrared region after etching.

5.4.5. Conclusion

Chemical etching was used to produce porous $80\text{GeSe}_2\text{-}20\text{Ga}_2\text{Se}_3$ glass-ceramics. It appeared that etching in acid solution yield dissolution of the crystalline phase, while the glassy phase is preferentially dissolved when a basic solution is used.

Controlled etching treatment in a “piranha” solution yielded infrared transparent $80\text{GeSe}_2\text{-}20\text{Ga}_2\text{Se}_3$ glass-ceramics with a porous layer up to one micron in thickness. Pores of 100 nm in size homogeneously distributed on the surface were created. After 10 min of etching, the porous layer plays an anti-reflection role and thus enhances the optical transmission of the glass-ceramic in the infrared region. Moreover, the porosity created enhanced the surface area by a factor 11.5 as compared to the material prior to etching treatment. These materials could be of high interest for applications such as biosensing or production of ATR plates with enhanced detection sensitivity. Such applications will have to be assessed in a subsequent study.

5.5. Exploration of new chalcogenide glassy domains and ceramization

5.5.1. Introduction

As described previously, the $80\text{GeSe}_2\text{-}20\text{Ga}_2\text{Se}_3$ composition shows good crystallization behavior and a high transparency in the infrared region [61] and could therefore serve as a good host matrix for novel multiphase nanoceramics. In that respect, it is known that indium and lead can form crystalline phases with selenium, In_2Se_3 and PbSe respectively which possess interesting properties for optics and optoelectronics applications. Indium selenide crystals possess a high conductivity [148] and may show potential applications in optoelectronic device such as lasers, light emitting diodes (LEDs) and solar cells [149]. The PbSe crystalline phase possesses non-linear optical properties [150-153] and could also present an interest for photovoltaic applications [154, 155].

It has been shown that chalcogenide glass-ceramics containing PbSe micro-crystals can be produced from a $40\text{GeSe}_2\text{-}50\text{As}_2\text{Se}_3\text{-}10\text{PbSe}$ glass [156]. In this study, we investigated the addition of indium ($M_{\text{In}}=114.8 \text{ g/mol}$) and lead ($M_{\text{Pb}}=207.2 \text{ g/mol}$) to glasses from the $\text{GeSe}_2\text{-Ga}_2\text{Se}_3$ tie line in the Ge-Ga-Se ternary diagram. The glassy domains of the $\text{GeSe}_2\text{-Ga}_2\text{Se}_3\text{-In}_2\text{Se}_3$ and $\text{GeSe}_2\text{-Ga}_2\text{Se}_3\text{-PbSe}$ pseudo-ternary systems have been determined. The influence of addition of In and Pb on the properties of the glasses have been analyzed. A ceramization study was performed on some of the glasses obtained and the optical and mechanical properties of the resulting glass-ceramics were characterized.

5.5.2. $\text{GeSe}_2\text{-Ga}_2\text{Se}_3\text{-In}_2\text{Se}_3$ system

5.5.2.1. Exploration of the glassy domain

All glass compositions were prepared in 10 mm inner diameter silica tubes sealed under vacuum, following the synthesis technique described in chapter 3. Raw pure elements with a purity of 5N were used. After melting and quenching, the resulting bulk glasses were systematically cut into slices, polished and optically analyzed using a UV/visible spectrometer (Perkin Elmer Lambda 1050). This technique allows identifying the presence of crystals within the glassy matrix from the shift of the onset of transmission that results from crystals induced scattering. The presence of crystals in the glassy matrix after the synthesis process is undesired and the compositions showing the presence of such particles were considered crystallized, thus indicating the limit of the glassy domain. Most of the studies reporting exploration of glassy domains use X-Ray diffraction to determine which compositions are crystallized. However, in the case of this study, UV/Vis spectroscopy was considered more sensitive for detection of crystalline particles and has thus been employed.

Figure 5.16 shows the glassy domain of the $\text{GeSe}_2\text{-Ga}_2\text{Se}_3\text{-In}_2\text{Se}_3$ pseudo-ternary system. It is worth noting that glasses can only be formed with contents of GeSe_2 higher than 60 mol%.

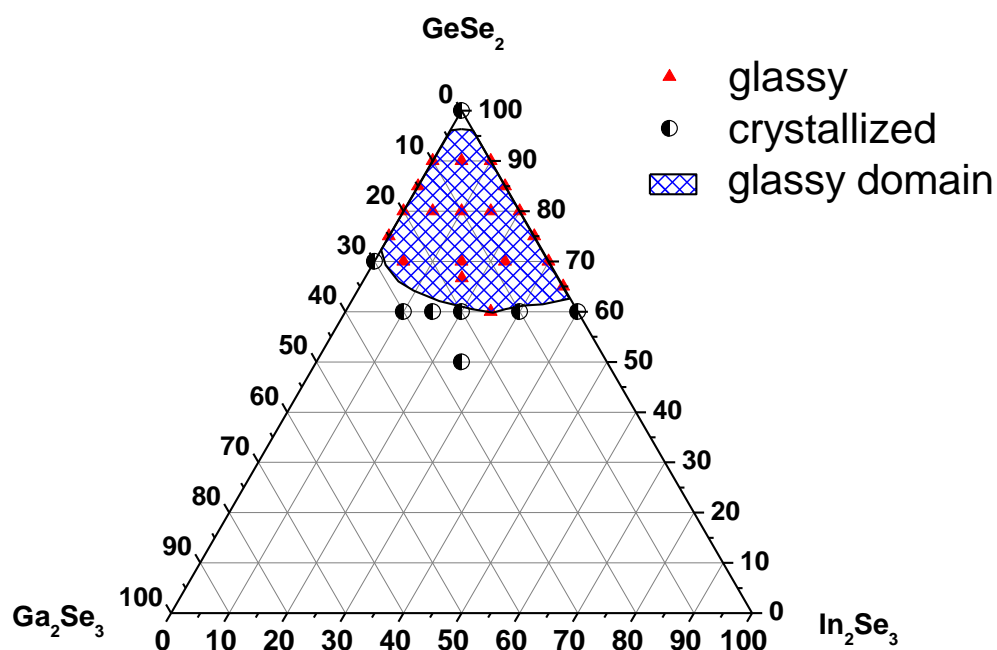


Figure 5.16: $\text{GeSe}_2\text{-Ga}_2\text{Se}_3\text{-In}_2\text{Se}_3$ glassy domain

The thermal, optical and mechanical properties of the $\text{GeSe}_2\text{-Ga}_2\text{Se}_3\text{-In}_2\text{Se}_3$ glasses were determined using the methods described in chapter 3. The results are presented in detail in Appendix A and are discussed in the next section. All the glasses from this system possess relatively high values of T_g ($>320^\circ\text{C}$). Their optical band gap wavelength is above 680 nm, yielding dark glasses. Their hardness is relatively high for chalcogenide glasses, with values around 200 Kg/mm^2 .

5.5.2.2. Influence of indium addition on the glass properties.

The evolution of the thermal properties (T_g , T_x and ΔT) as a function of indium content for $80\text{GeSe}_2\text{-(}20\text{-x)Ga}_2\text{Se}_3\text{-(x)In}_2\text{Se}_3$ glasses is presented in figure 5.17. These

glasses have a constant atomic content for germanium and selenium of 23.53% and 64.71% respectively, and only the Ga/In atomic ratio varies.

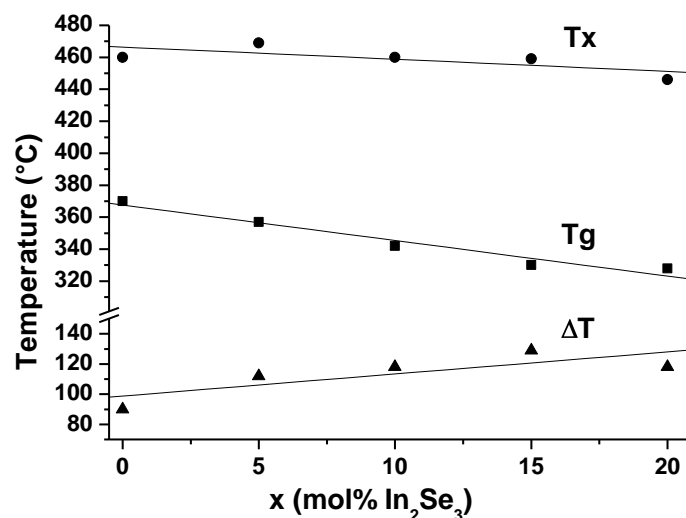


Figure 5.17: Evolution of the thermal properties of the $80\text{GeSe}_2-(20-x)\text{Ga}_2\text{Se}_3-(x)\text{In}_2\text{Se}_3$ as a function of x

The progressive substitution of Ga for In leads to a decrease of the glass transition temperature. The crystallization temperature remains stable, yielding an increase of the values of ΔT . Thus, indium tends to stabilize the glass. This could present a great advantage for production of infrared optics, since wide ΔT values enables the synthesis of bulk glasses of larger dimension.

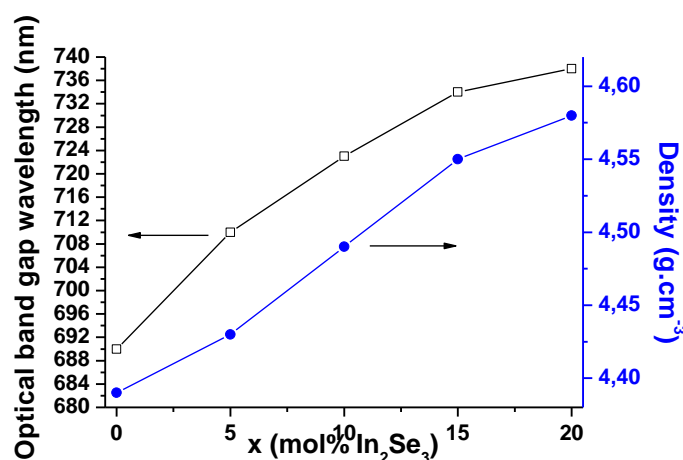


Figure 5.18: Evolution of the optical band gap wavelength and density of the $80\text{GeSe}_2-(20-x)\text{Ga}_2\text{Se}_3-(x)\text{In}_2\text{Se}_3$ as a function of x

The effect of substitution of Ga for In on the optical band gap wavelength and density of the $80\text{GeSe}_2-(20-x)\text{Ga}_2\text{Se}_3-(x)\text{In}_2\text{Se}_3$ is presented in figure 5.18. With increasing indium content, the optical band gap wavelength shifts toward higher wavelengths. Indium and gallium are located in the same column of the periodic table of the chemical elements and adopt the same structure in the network [157]. However, the bond energies differ for the two elements when coordinated to Se. In fact, the bond energy of Ga-Se bonds (65 Kcal/mol [158]) is higher than that of In-Se bonds (61.5 Kcal/mol [159]). Thus, increasing indium content decreases the average bond energy of the system. Studies have shown that the band gap energy of chalcogenide glasses tend to increase with the average bond energy of the system [158, 159]. Thus, the decrease of the average bond energy in the $\text{GeSe}_2\text{-Ga}_2\text{Se}_3\text{-In}_2\text{Se}_3$ by progressive substitution of Ga for In leads to the increase of the optical band gap wavelength (λ_g) observed in figure 5.18. This decreased average bond energy also leads to the lower values of T_g obtained for glasses with higher indium content (figure 5.16).

Finally, the atomic mass of indium ($M_{\text{In}} = 114.82 \text{ g/mol}$) is greater than the atomic mass of gallium ($M_{\text{Ga}} = 69.72 \text{ g/mol}$). Their microstructure being the same, the substitution of Ga for In leads to the increase of the density of the glasses with increasing In content.

5.5.3. $\text{GeSe}_2\text{-Ga}_2\text{Se}_3\text{-PbSe}$ system

5.5.3.1. Exploration of the glassy domain

The glassy domain of the $\text{GeSe}_2\text{-Ga}_2\text{Se}_3\text{-PbSe}$ pseudo-ternary system was explored using the protocol previously described for the $\text{GeSe}_2\text{-Ga}_2\text{Se}_3\text{-In}_2\text{Se}_3$ compositions. The resulting glassy domain is shown in figure 5.19.

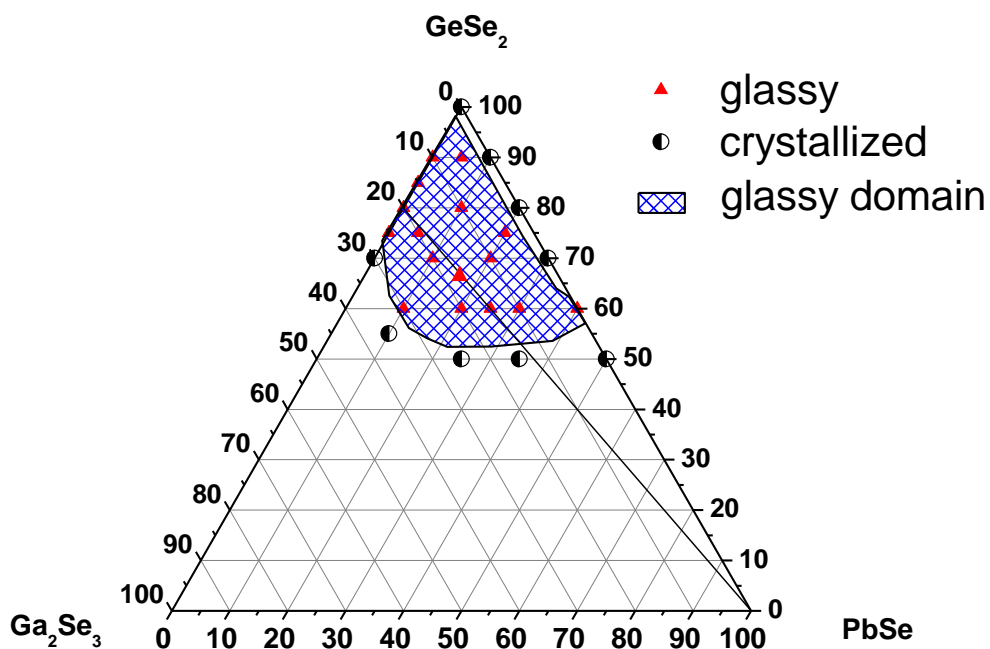


Figure 5.19: $\text{GeSe}_2\text{-Ga}_2\text{Se}_3\text{-PbSe}$ glassy domain

As for the $\text{GeSe}_2\text{-Ga}_2\text{Se}_3\text{-In}_2\text{Se}_3$ system, a high content of GeSe_2 is a required condition to obtain glasses. However, except for the 60 GeSe_2 -40 PbSe composition, pseudo-binary $\text{GeSe}_2\text{-PbSe}$ compositions are not glassy. This differs from the $\text{GeSe}_2\text{-In}_2\text{Se}_3$ pseudo-binary system, where glasses can be obtained for GeSe_2 contents ranging from 65 mol% to 95 mol%.

The optical, mechanical and thermal properties of the glasses are presented in detail in Appendix B and are discussed in the next section. $\text{GeSe}_2\text{-Ga}_2\text{Se}_3\text{-PbSe}$ glasses present glass transition temperatures comprised between 310°C and 365°C. Their crystallization temperatures range from 387°C to 450°C. Most of the glasses have a ΔT value lower than 100°C, indicating a weak stability toward crystallization. Due to their low optical band-gap energy, these glasses are opaque to visible light and present a black metallic coloration. The mechanical properties of the $\text{GeSe}_2\text{-Ga}_2\text{Se}_3\text{-PbSe}$ glasses are constant, with a Vickers hardness of about 200 Hv and a toughness of 0.200 $\text{MPa.m}^{1/2}$.

5.5.3.2. Influence of PbSe addition on the glass properties.

Figure 5.20 shows the evolution of the thermal properties of (100-x)(80 GeSe_2 -20 Ga_2Se_3), x PbSe glasses as a function of PbSe content. In contrast to the addition of indium, the addition of lead yields a decrease of both T_g and T_x . The ΔT values are also lower for glasses with higher contents of PbSe. Thus, addition of PbSe tends to destabilize the glass.

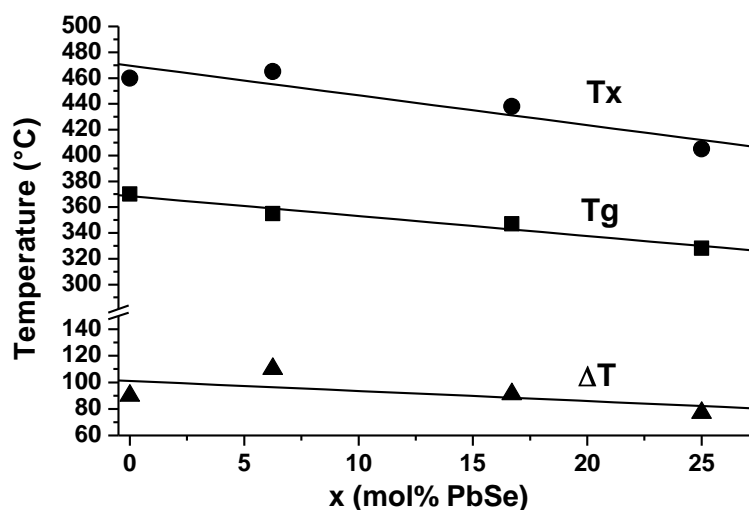


Figure 5.20: Evolution of the thermal properties of the $(100-x)(80\text{GeSe}_2-20\text{Ga}_2\text{Se}_3)$, $x\text{PbSe}$ glasses as a function of x

Similar evolution of the thermal properties with lead content has been reported for other chalcogenide glassy systems such as Ge-Se-Pb [160] and $\text{GeSe}_2\text{-Sb}_2\text{Se}_3\text{-PbSe}$ [161]. This behavior was attributed to the creation of the linear chains Pb-Se-Pb-Se yielding a progressive depolymerization of the glassy network and a decrease of the glass transition temperature with higher Pb content [161, 162].

The optical band gap wavelength is shifted toward higher wavelength with PbSe contents in $(100-x)(80\text{GeSe}_2-20\text{Ga}_2\text{Se}_3)$, $x\text{PbSe}$, as presented in figure 5.21. This might be due to a stronger metallic character of the Pb-Se bonds, as suggested by Parvanov et al. [163].

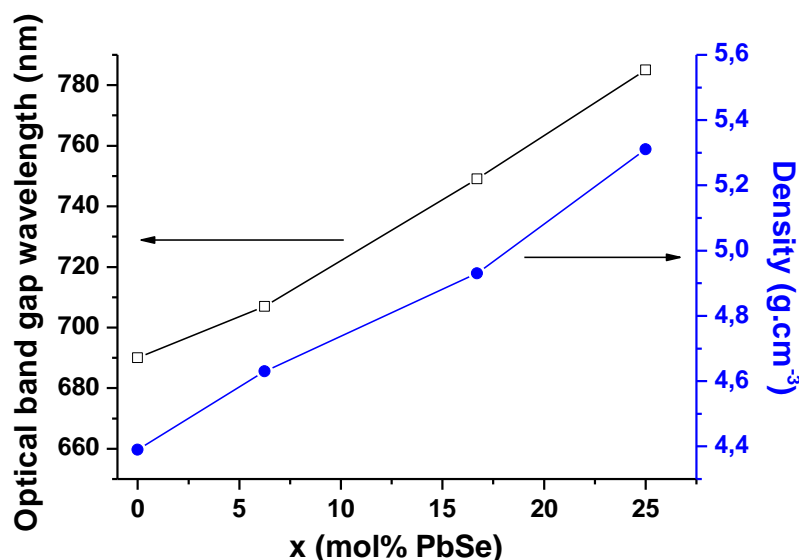


Figure 5.21: Evolution of the optical cut-band gap wavelength and density of the $(100-x)(80\text{GeSe}_2-20\text{Ga}_2\text{Se}_3)_x\text{PbSe}$ glasses as a function of x

Lead possesses a high atomic mass ($M_{\text{Pb}}=207.2\text{g.mol}^{-1}$) hence the progressive introduction of PbSe induces a strong increase in density of the glass, as shown in figure 5.21.

5.5.4. Ceramization study

A systematic ceramization study was performed on the glasses synthesized in the $\text{GeSe}_2\text{-Ga}_2\text{Se}_3\text{-In}_2\text{Se}_3$ and $\text{GeSe}_2\text{-Ga}_2\text{Se}_3\text{-PbSe}$ systems. The process was carried out by heat treatment on glass pellets with a thickness of 2mm polished on both surfaces. The glass samples were heated in a ventilated furnace at a temperature above their glass transition temperature (between 10°C and 50°C above T_g) for several hours. All through the heat treatment process, the samples were regularly monitored by optical transmission

measurements, microscopic observation and X-Ray diffraction to assess the evolution of the crystallization.

The development of a crystalline phase was not achieved in some of the glass compositions studied. The materials remained glassy after prolonged heat treatments up to 100 h at a temperature 50°C above T_g . These compositions were therefore set aside for the ceramization study. Unfortunately, most of the remaining compositions showed an uncontrollable crystallization behavior characterized by a rapid precipitation of crystals of large dimensions (some micrometers) inducing important losses of optical transmission. Also, some of the glass-ceramics produced presented an inhomogeneous distribution of the crystals within the glassy matrix. In the perspective of the production of thermal imaging lenses, these compositions showed no interest and were also set aside. Overall, no controlled crystallization was achieved on compositions from the GeSe_2 – Ga_2Se_3 – PbSe system and only one composition in the GeSe_2 – Ga_2Se_3 – In_2Se_3 system showed a controllable crystallization behavior and was studied in further details: 75GeSe_2 – $18.75\text{Ga}_2\text{Se}_3$ – $6.25\text{In}_2\text{Se}_3$ (referred as In1).

The evolution of the mechanical properties of the glass-ceramics In1 with ceramization treatment at 386°C ($T_g+30^\circ\text{C}$) is given in table 5.3. The XRD spectra measured on these glass-ceramics are presented in figure 5.22.

Table 5.3: Mechanical properties of the In1 glass-ceramics

In1	E ($\pm 0.3\text{Gpa}$)	Hv ($\pm 1\text{Kg/mm}^2$)	K_{IC} ($\pm 0.001\text{ Mpa}\cdot\sqrt{\text{m}}$)	ρ ($\pm 0.03\text{Kg}\cdot\text{mm}^{-3}$)
0h	21.15	197.0	0.191	4.46
4h	21.59	201.8	0.192	4.46
6h	22.99	195.1	0.207	4.47
10h	22.79	191.6	0.212	4.54
29h	23.85	156.7	0.285	4.55

Young's modulus (E), toughness (K_{IC}) and density (ρ) of the In1 glass-ceramics increase with ceramization time. However, Vickers Hardness is substantially decreased after 29 h of heat treatment and can be attributed to the precipitation of GeSe_2 crystals [127]. A similar evolution of the mechanical properties with ceramization duration was observed for $80\text{GeSe}_2\text{-}20\text{Ga}_2\text{Se}_3$ glass-ceramics [61].

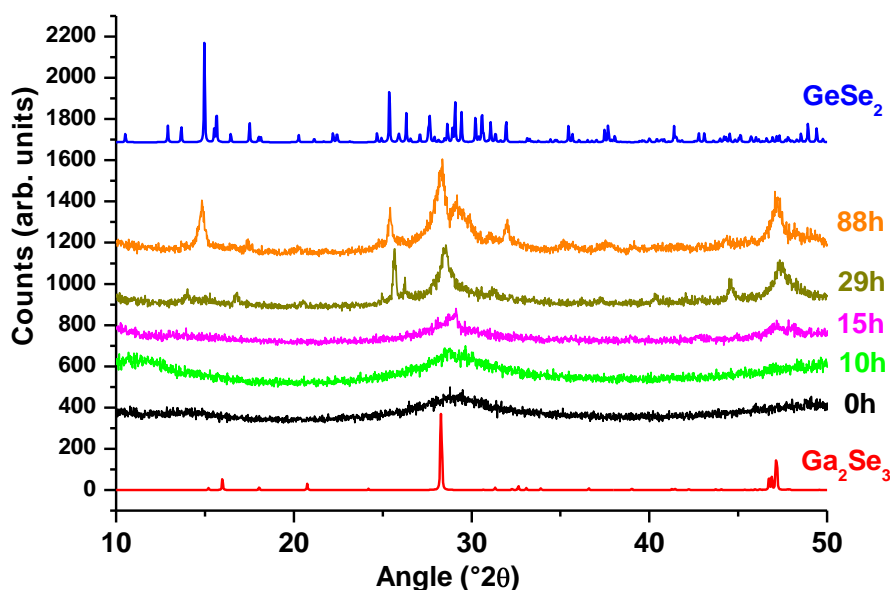


Figure 5.22: XRD spectra of In1 glass-ceramics

As shown in figure 5.22, both GeSe_2 and Ga_2Se_3 precipitate in the In1 glass-ceramics but the In_2Se_3 crystalline phase was not observed, even after 88h of ceramization.

Figure 5.23 shows the evolution of the optical transmission with heat treatment time at 386°C ($T_g + 30^{\circ}\text{C}$) for the composition In1. For short heat treatment times, the development of the crystallinity induces a progressive shift of the beginning of transmission towards longer wavelengths due to Rayleigh scattering. The glass-ceramics

remain transparent in the infrared range up to 15 h of ceramization. After 29 h and 88 h of treatment, the precipitation of GeSe_2 and Ga_2Se_3 crystals with larger dimensions induces MIE scattering. This results in an important decrease of the maximum optical transmission of the glass-ceramics.

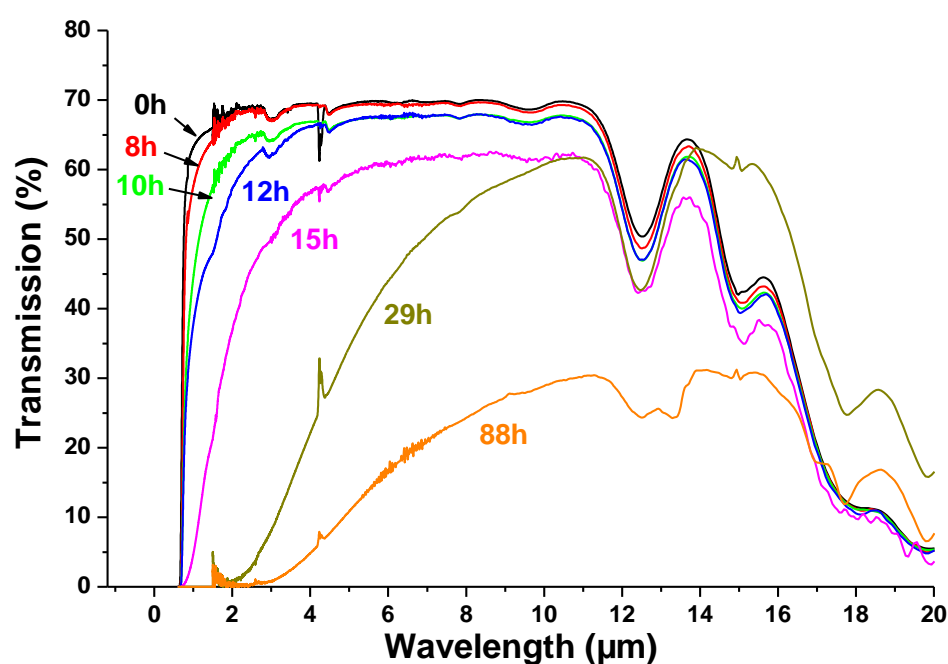


Figure 5.23: Optical transmission of the In1 glass-ceramics heat treated at 386°C for different durations

The microstructure of the In1 glass-ceramic was observed by SEM (figure 5.24). The distribution of crystals is homogeneous within the glassy matrix (figure 5.24-a). The portion of crystalline phase is estimated to be about 40%. The aspect of the crystals precipitated shown in figure 5.24-b is different from those observed for 80GeSe_2 - $20\text{Ga}_2\text{Se}_3$ glass-ceramics [61]. The size of the crystals is on the order of some micrometers, as compared to about 100 nm for 80GeSe_2 - $20\text{Ga}_2\text{Se}_3$ glass-ceramics. The

introduction of indium could be responsible of the difference in crystallization behavior. However, the role of this element on ceramization process has not been determined.

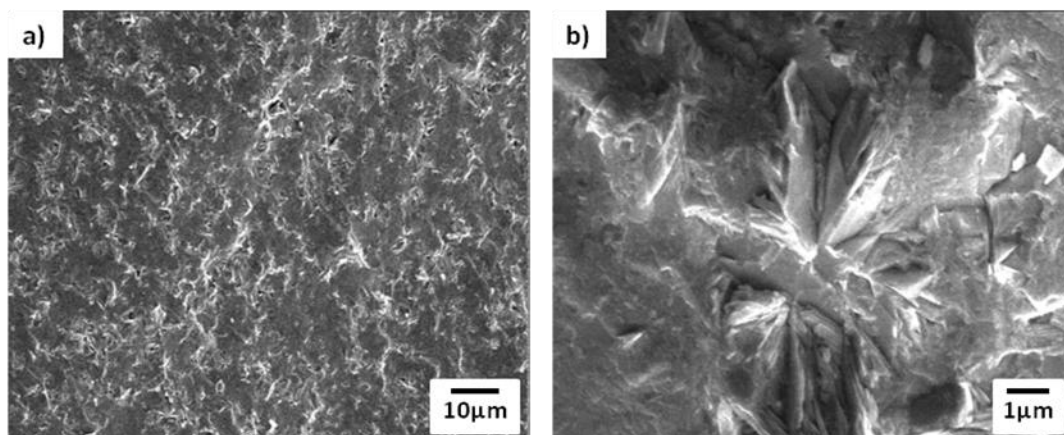


Figure 5.24: SEM images of the In1 glass-ceramic heat-treated for 29 h at 386°C ($T_g+30^\circ\text{C}$)

5.5.5. Conclusion

Two new glassy domains based on $\text{GeSe}_2\text{--Ga}_2\text{Se}_3$ pseudo-binary compositions have been explored. The optical, mechanical and thermal properties of the glasses synthesized in the new glassy domains $\text{GeSe}_2\text{--Ga}_2\text{Se}_3\text{--In}_2\text{Se}_3$ and $\text{GeSe}_2\text{--Ga}_2\text{Se}_3\text{--PbSe}$ glasses have been determined. The influence of In or Pb on the glass properties have been analyzed. It appeared that the addition of these elements leads to a decrease of the glass transition temperature and an increase of the optical band gap wavelength.

The aim of this study was to precipitate In_2Se_3 or PbSe crystalline phases in these new glass compositions to produce glass-ceramics with higher conductivities or non-linear properties, respectively. However, only one of the new compositions studied presented controllable crystallization behavior: $75\text{GeSe}_2\text{--}18.75\text{Ga}_2\text{Se}_3\text{--}6.25\text{In}_2\text{Se}_3$ (In1). Furthermore, XRD analysis revealed that the crystallinity in In1 glass-ceramics is

composed of Ga_2Se_3 (or GeGa_4Se_8) and GeSe_2 crystals. No In_2Se_3 crystals were observed. Finally, In_1 glass-ceramics show a rapid decrease in optical transmission with heat treatment duration. Therefore, this glass-ceramics phase present a limited interest for applications in the infrared region in comparison to $80\text{GeSe}_2\text{--}20\text{Ga}_2\text{Se}_3$.

5.6. Conclusion

In this chapter, various aspects of chalcogenide glass-ceramics have been addressed. Firstly, a new synthesis route combining mechanosynthesis and Spark Plasma Sintering has been demonstrated for the production of glass-ceramics with controlled crystallinity. Infrared transparent $80\text{GeSe}_2\text{--}20\text{Ga}_2\text{Se}_3$ glass-ceramics with enhanced mechanical properties were obtained for sintering treatments shorter than one hour at a temperature slightly above the glass transition temperature. In comparison, several tens of hours of heat treatment in a ventilated furnace are necessary to produce $80\text{GeSe}_2\text{--}20\text{Ga}_2\text{Se}_3$ glass-ceramics from a base glass prepared by melt/quenching technique in sealed silica tubes. Hence, the SPS synthesis technique paves the way for production of chalcogenide glass-ceramics for use as infrared optics at a lower cost. This innovative synthesis approach has been recently patented in France [99] and is now in the process of being patented internationally.

Secondly, the possibility of preparing porous glass-ceramics by chemical etching has been demonstrated. It was shown that basic solutions preferentially dissolve the glassy phase, while acid solutions preferentially dissolve the crystalline phase. Controlled etching treatment in a “piranha” solution yielded infrared transparent $80\text{GeSe}_2\text{--}20\text{Ga}_2\text{Se}_3$

glass-ceramics with pores of 100 nm in size homogeneously distributed on the surface. The depth of the porous layer was controlled by adjusting the etching treatment duration. Nanoporous layer up to 1 μm thickness after 10 min of etching could be achieved. These layers resulted in an increase in optical transmission attributed to an anti-reflective effect. Furthermore, the porosity created enhanced the surface area by a factor 11.5 and could be of high interest for applications such as biosensing or production of ATR plates with improved detection sensitivity. Such applications will have to be assessed in a subsequent study.

Finally, two new glassy domains have been explored: $\text{GeSe}_2\text{-Ga}_2\text{Se}_3\text{-In}_2\text{Se}_3$ and $\text{GeSe}_2\text{-Ga}_2\text{Se}_3\text{-PbSe}$. Notably, it was demonstrated that addition of indium tends to stabilize the glasses while Pb destabilizes it. The aim of this study was to develop new families of chalcogenide glass-ceramics with properties interesting for non-linear optics or photovoltaic by precipitating In-based or Pb-based crystalline phases. However, only one of the new compositions studied showed a controllable crystallization behavior: $75\text{GeSe}_2\text{-}18.75\text{Ga}_2\text{Se}_3\text{-}6.25\text{In}_2\text{Se}_3$ and the crystalline phase precipitated was composed of GeSe_2 and Ga_2Se_3 crystals, and no In-based crystals were observed. Hence, these new glassy systems showed little interest for infrared optic applications.

CHAPTER 6: RARE EARTH DOPED CHALCOGENIDE GLASS-CERAMICS BASED ON SELENIUM

6.1. Introduction

While many commercial laser sources are available in the visible and near IR region, efficient laser sources in the mid-IR are rare or limited to a few wavelengths such as CO₂ laser at 10.6 microns. The low phonon energy of chalcogenide glasses presents two major advantages for the production of laser materials operating in the infrared region. First they generate transparency window that extend far in the infrared, up to 20 μm [164]. Second, low phonons improve the radiative emission quantum efficiency of rare-earth (RE) ions dissolved in the glass matrix.

In addition, several studies have reported an enhancement of the luminescence in sulfur-based glass-ceramics in comparison to the base glass due to the presence of a crystalline environment surrounding the rare-earth ions [165, 166]. It has been postulated that the change in crystalline-field during nucleation results in longer radiative lifetimes.

Such crystallization effects have never been investigated in selenide glass matrixes despite the fact that selenium-based glasses should provide even lower phonon energy and wider infrared transparency thereby enabling the design of laser source at longer wavelength. In addition, selenium-based chalcogenide glasses have shown reproducible and controllable crystallization behavior conducive to the production of controllable and reproducible glass-ceramics with enhanced mechanical properties while

keeping high infrared transparency up to long wavelengths [51, 61]. Hence, selenide glass matrixes are promising candidate for the design of RE doped glass-ceramics. In that respect, gallium-based compositions are of particular interest because several studies have shown that the addition of gallium in chalcogenide glasses enhances the RE ions dissolving capacity [167, 168]. The $80\text{GeSe}_2\text{-}20\text{Ga}_2\text{Se}_3$ glass composition has shown a controllable and reproducible behavior towards crystallization [60, 61]. Furthermore, it possesses a high content of gallium (11.8 at%). Thus, it represents a good potential host for rare-earth ions doped glass-ceramics with enhanced luminescence intensities.

In the following chapter, the introduction of erbium and neodymium in $80\text{GeSe}_2\text{-}20\text{Ga}_2\text{Se}_3$ glasses will be investigated for the production of RE doped glass-ceramics. Their emissions in the infrared as a function of the crystallization will be characterized to study the correlation between the crystalline environment and emission efficiency.

6.2. Luminescence of rare earth ions

Rare earth (RE) ions are commonly used for applications as phosphors, lasers and amplifiers. They are formed by ionization of a number of atoms located after lanthanum in the periodic table. For this reason, RE ions are sometimes referred to as lanthanide ions. Rare earths regroup the elements from cerium (Ce, $Z=58$, outer electronic configuration $5s^25p^65d^14f^16s^2$) to ytterbium (Yb, $Z=70$, outer electronic configuration $5s^25p^64f^{14}6s^2$). RE ions are commonly found as divalent or trivalent cations. In this study, attention will be focused on trivalent cations $(\text{RE})^{3+}$. In these ions, the 5d, 6s and some 4f electrons are removed and result in incomplete 4f electronic layers corresponding to an

outer electronic configuration $5s^25p^64f^n$ where n is the number of electrons on the 4f layer. Table 6.1 gives the number of 4f valence electrons for each trivalent RE ion of the lanthanide series [169].

Table 6.1: The number of 4f valence electrons in trivalent rare earth ions

Ion	Ce ³⁺	Pr ³⁺	Nd ³⁺	Pm ³⁺	Sm ³⁺	Eu ³⁺	Gd ³⁺	Tb ³⁺	Dy ³⁺	Ho ³⁺	Er ³⁺	Tm ³⁺	Yb ³⁺
<i>n</i>	1	2	3	4	5	6	7	8	9	10	11	12	13

Electronic transitions in (RE)³⁺ ions take place between the energy sublevels of the 4f^{*n*} electronic configuration (f→f transitions). The 4f valence electrons of RE ions are shielded by the 5s and 5p outer electrons of the 5s²5p⁶ orbitals. This shielding effect protects the valence electrons from the influence of the crystalline field in the host matrix. The crystalline field induces a shift in the energy states and causes additional level splitting. For transition metal ions, the effect of crystalline field is strong and the splitting of the levels is important, yielding broad absorption bands highly dependent on the environment of the ions. On the opposite, the weak crystalline field observed for RE ions produces only a slight shift in the energy of the states, yielding narrow absorption bands. Consequently, the main features of (RE)³⁺ ion spectrum are similar from one host matrix to another and the energies associated with the different absorption levels vary only slightly from one host matrix to another. In 1968, Dieke and al. made a systematic spectral measurement of the energy levels of rare earths ions in a lanthanum chloride (LaCl₃) host. The resulting diagram presented in figure 6.1, called Dieke diagram, provides essential information for studies of rare-earth doped materials.

An electromagnetic radiation with energy close to the energy difference between an occupied electronic level and a vacant higher energy level has a high probability of

being absorbed and promote an electron into an excited state. The RE ion will then return to its fundamental state through either non-radiative or radiative deexcitation processes.

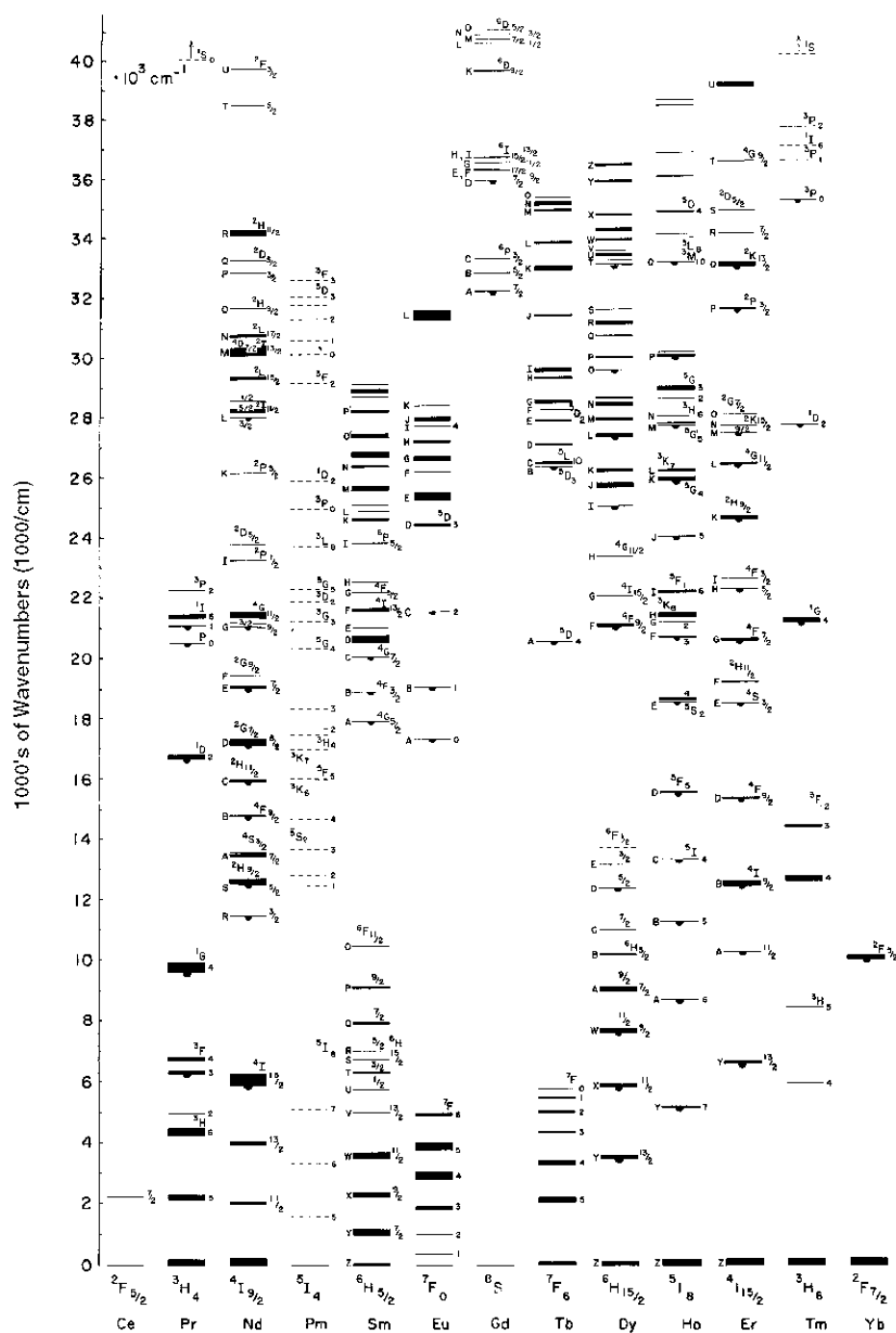


Figure 6.1: The Dieke diagram

Radiative relaxation is accompanied by the emission of a radiation with energy corresponding to the difference between the excited level and the fundamental level. Non-radiative and radiative relaxations are competing deexcitation phenomena. In general, non-radiative rates are dominant over radiative rates and most of the transitions between energy levels are non-light-emitting. The deexcitation rates of excited energy levels are dependent on several factors, including the nature of the host material. To reach lower energy states, electrons from an excited state can release energy to the host matrix in the form of vibrations, called phonons, which are specific to each material. When the energy of an electron is higher than the phonon energy of a given material, several phonons are needed simultaneously to deexcite the ion. This kind of non-radiative deexcitation is called multiphonon relaxation. Materials with lower phonon energies will thus present a lower probability of multiphonon relaxation.

High concentrations of RE ions can also lead to inter-ion multipolar interactions. In this case, energy transfers occur between ions, yielding non-radiative relaxation to the fundamental state. This phenomenon is called quenching. The deexcitation rate (W_T) of an ion is thus dependent on three phenomena: radiative relaxation (A_R) and non-radiative relaxations (Γ_{NR}) due to phonons, and inter-ion quenching (Γ_Q), according to the following relation: $W_T = A_R + \Gamma_{NR} + \Gamma_Q$.

Chalcogenide glasses are then interesting host matrices for RE ions doping because their low phonon energies generate lower probabilities of deexcitation due to multiphonon relaxation. In this study, work has been focused on RE emissions in the near- and mid-infrared region. Table 6.2 summarizes some results found in the literature

for absorptions and emissions observed in the near- and mid-infrared regions for RE-doped chalcogenide glasses. The pumping source used in each case is indicated in brackets, and the corresponding inter-level transitions are given. From this table, it appears that the reported emissions are limited to about 4.5 μm in the mid-infrared region. The non-radiative rate Γ_{NR} from a $(\text{RE})^{3+}$ ion is strongly related to the energy gap between two adjacent levels ΔE . This behavior is described by the following equation:

$$\Gamma_{\text{NR}} = \Gamma_{\text{NR}}^0 e^{-\alpha \Delta E}$$

Where Γ_{NR}^0 and α are constants that depend on the host material (but not on the $(\text{RE})^{3+}$ ion). Thus, the lower the energy gap between two adjacent levels, the higher is the probability of non-radiative multiphonon relaxation. This phenomenon can explain the absence of radiative emissions reported at wavelengths above 4.5 μm , which would imply transitions between levels with low energy differences. It is worth noting that Shaw et al. reported in 2003 an emission at 7.5 μm in Tb^{3+} -doped GeAsGaSe glasses [170]. However, this result has not been reproduced and no other article in the literature has reported similar emissions in the past decade.

Table 6.2: Some emissions reported in the near- and mid-infrared regions for RE-doped chalcogenide glasses

Rare Earth	$\lambda_{\text{absorption}}$	$\lambda_{\text{emission}} (\lambda_{\text{excitation}})$	Transitions	Refs
Pr³⁺	1.06 μm 1.5-1.6 μm 2 μm 4.5 μm	3.5 μm (1.5 μm) 3.8 μm (2 μm) 3.9 μm (1.5 μm)	$(^3\text{F}_2, ^3\text{H}_6) \rightarrow ^3\text{H}_5$	[170] [171]
		4.7 μm (2 μm) 4.9 μm (1.5 μm)	$^3\text{H}_4 \rightarrow ^3\text{H}_5$	[172]
Nd³⁺	586 nm 750 nm 805 nm 876 nm	900 nm (800 nm)	$^4\text{F}_{3/2} \rightarrow ^4\text{I}_{9/2}$	[173] [174]
		1.06 μm (800 nm)	$^4\text{F}_{3/2} \rightarrow ^4\text{I}_{11/2}$	
		1.35 μm (800 nm)	$^4\text{F}_{3/2} \rightarrow ^4\text{I}_{13/2}$	
Tb³⁺	2 μm 3 μm 4.7 μm	3.2 μm (2 μm)	$^7\text{F}_4 \rightarrow ^7\text{F}_6$	[170] [175]
		4.8 μm (2 μm)	$^7\text{F}_5 \rightarrow ^7\text{F}_6$	
		7.5 μm (2 μm)	$^7\text{F}_4 \rightarrow ^7\text{F}_5$	
Dy³⁺	920 nm 1.1 μm 1.31 μm 1.71 μm 2.8 μm	1.15 μm (808 nm)	$(^6\text{H}_{7/2}, ^6\text{F}_{9/2}) \rightarrow ^6\text{H}_{15/2}$	[170] [176] [177] [178]
		1.34 μm (808 nm)	$(^6\text{H}_{9/2}, ^6\text{F}_{11/2}) \rightarrow ^6\text{H}_{15/2}$	
		3.0 μm (1.3 μm)	$^6\text{H}_{13/2} \rightarrow ^6\text{H}_{15/2}$	
		4.5 μm (1.3 μm)	$^6\text{H}_{11/2} \rightarrow ^6\text{H}_{13/2}$	
Er³⁺	550 nm 650 nm 800 nm 980 nm 1.55 μm	980 nm (532 nm)	$^4\text{I}_{11/2} \rightarrow ^4\text{I}_{15/2}$	[165] [179] [180] [181]
		1.55 μm (800 nm)	$^4\text{I}_{13/2} \rightarrow ^4\text{I}_{15/2}$	
		1.72 μm (532 nm)	$^4\text{I}_{9/2} \rightarrow ^4\text{I}_{13/2}$	
		2.8 μm (532 nm)	$^4\text{I}_{11/2} \rightarrow ^4\text{I}_{13/2}$	
		4.3 μm (532 nm) 4.6 μm (804 nm)	$^4\text{I}_{9/2} \rightarrow ^4\text{I}_{11/2}$	
Tm³⁺	700 nm 785 nm 1.2 μm 1.7 μm	1.23 μm (785 nm)	$^3\text{H}_5 \rightarrow ^3\text{F}_6$	[181] [182]
		1.48 μm (785 nm)	$^3\text{H}_4 \rightarrow ^3\text{F}_4$	
		1.8 μm (700 nm)	$^3\text{F}_4 \rightarrow ^3\text{H}_6$	
		2.3 μm (785 nm)	$^3\text{H}_4 \rightarrow ^3\text{H}_5$	
		3.8 μm (785 nm)	$^3\text{H}_5 \rightarrow ^3\text{F}_4$	

6.3. Preparation of rare earth-doped $80\text{GeSe}_2\text{--}20\text{Ga}_2\text{Se}_3$ glass-ceramics

6.3.1. Preparation of the doped base-glass

Starting raw elements with high purity were used to prepare rods of 10g of the doped base glass in 9mm inner diameter silica tubes sealed under vacuum, as illustrated in figure 6.2. The purity and origin of the elements used are presented in table 6.3. Base glasses with compositions $80\text{GeSe}_2 - 20\text{Ga}_2\text{Se}_3 + 0.1\% \text{ Er}$ and $80\text{GeSe}_2 - 20\text{Ga}_2\text{Se}_3 + 0.1\% \text{ Nd}$ (wt%) were prepared. Both erbium and neodymium were used as metallic elements for the synthesis of the glasses.

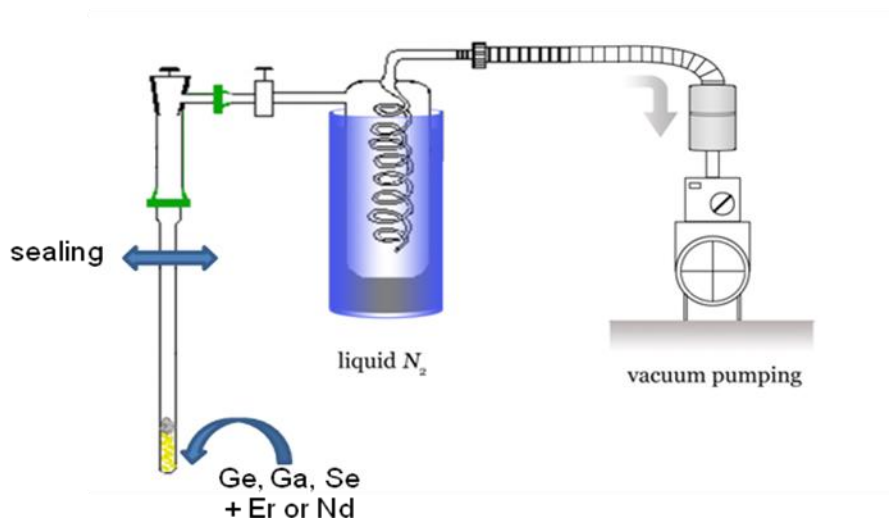


Figure 6.2: Experimental setup

The starting elements were introduced in stoichiometric quantities in the silica tube and evacuated under vacuum ($\sim 10^{-3}$ Pa) for 1h before sealing the tube. The resulting silica ampoule containing the starting elements was inserted into a rocking furnace, heated up with a heating ramp of $2^\circ\text{C}/\text{min}$ up to 850°C . A homogenization dwell was performed for 12 h, and the tube was subsequently quenched in water. The glass sample

was annealed below the glass transition temperature ($T_g - 10^\circ\text{C}$) for 3h to minimize inner constraints, and finally slowly cooled down to room temperature. The glass rod was then cut and polished to produce discs of about 2mm of thickness.

Table 6.3: Origin and purity of the elements used for the study

Element	Retailer	Purity
Germanium	Umicore	5N
Gallium	Cerac	6N
Selenium	Umicore	5N
Erbium	Strem	3N
Neodymium	Strem	3N

6.3.2. Raman study

A Raman spectrum of the $80\text{GeSe}_2\text{-}20\text{Ga}_2\text{Se}_3$ bulk glass was recorded on a Renishaw Invia Reflex spectrometer. The excited wavelength was 785 nm, with a power of 3mW. The resulting spectrum is presented in figure 6.3.

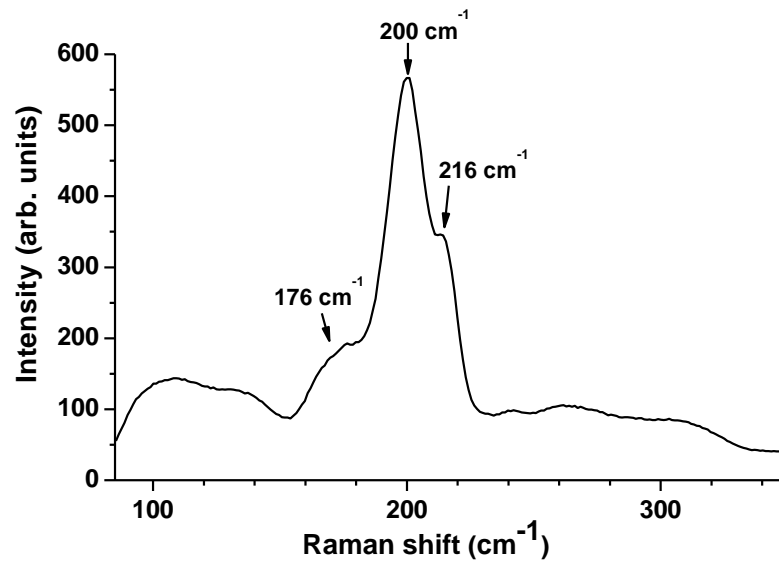


Figure 6.3: Raman spectrum of the $80\text{GeSe}_2\text{-}20\text{Ga}_2\text{Se}_3$ glass

Three vibration bands appear. The lower energy band centered at 176cm^{-1} is associated with $[\text{Se}_3\text{Ge-GeSe}_3]$ and $[\text{Se}_3\text{Ga-GaSe}_3]$ vibrations. The main peak centered at 200cm^{-1} corresponds to the overlap of $\nu_1(\text{A}_1)$ symmetric stretching modes of corner-sharing $[\text{GeSe}_4]$ and $[\text{GaSe}_4]$ tetrahedron. The peak at 216cm^{-1} , called companion peak, is associated to vibration $\nu_1^c(\text{A}_1^c)$ of edge-sharing $[\text{GeSe}_4]$ and $[\text{GaSe}_4]$ tetrahedron [68]. It is worth noting the absence of Se rings in the glass, which A1 modes of vibration would appear at 268cm^{-1} . From this spectrum, the maximum phonon energy of the 80GeSe_2 – $20\text{Ga}_2\text{Se}_3$ glass is 325 cm^{-1} . This low value of phonon energy makes this glass composition a good host for rare earth doping by minimizing the probability of non-radiative multiphonon relaxation.

6.3.3. Ceramization of the doped glasses

The Er-doped and Nd-doped 80GeSe_2 – $20\text{Ga}_2\text{Se}_3$ glass compositions have been ceramized using a one-step ceramization process as described in chapter 5, section II.3. Pellets of the base glass with a thickness of 2mm have been placed in a ventilated furnace at 380°C for durations up to 80h. This corresponds to a temperature 10°C above the T_g of the glass. The glass transition temperature of each sample was obtained on a bulk piece of glass of mass $\sim 10\text{mg}$ using a differential scanning calorimeter QA20 (TA Instrument) with a heating ramp of $10^\circ\text{C}/\text{min}$ up to 500°C . The DSC curve of the base glass is shown in figure 6.4.

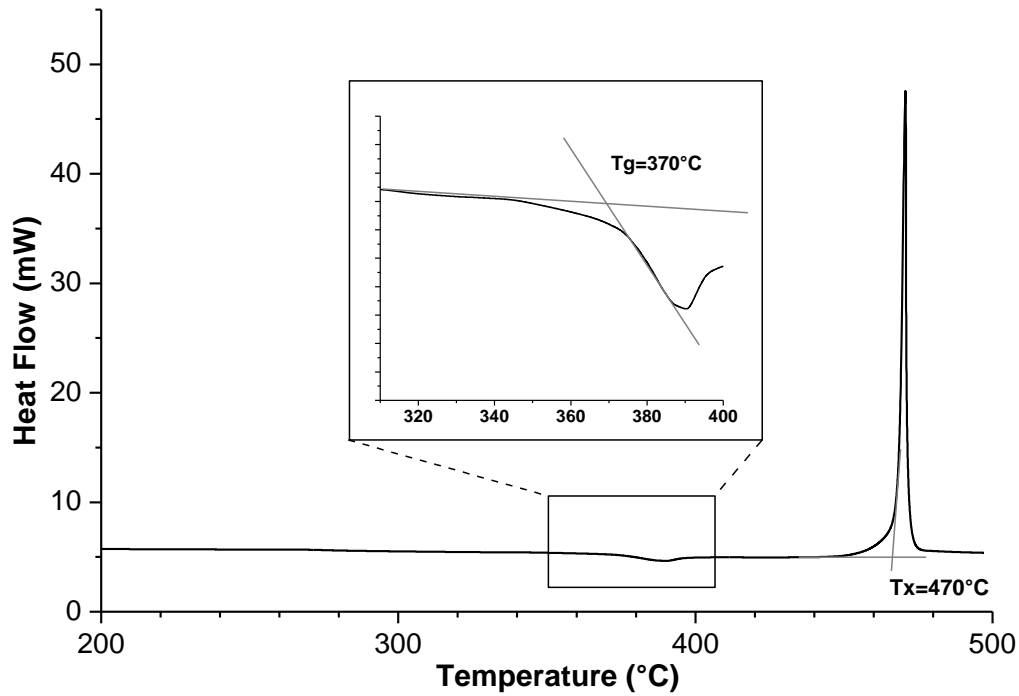


Figure 6.4: DSC curve of the 80GeSe₂–20Ga₂Se₃ + 0.1 %Er bulk glass

6.3.4. X-Ray Diffraction

X-Ray diffraction (XRD) spectra were collected between 10 and 70° (°2θ) on bulk glasses and glass ceramics using a Phillips PW3020 diffractometer (Voltage 40 kV, current 30 mA) with Cu Kα radiation and a step width of 0.02°. The crystallization behavior is similar in both Er-doped (figure 6.5) and Nd-doped (figure 6.6) 80GeSe₂–20Ga₂Se₃ glass-ceramics. The samples show a progressive crystallization of the glass with the duration of heat treatment.

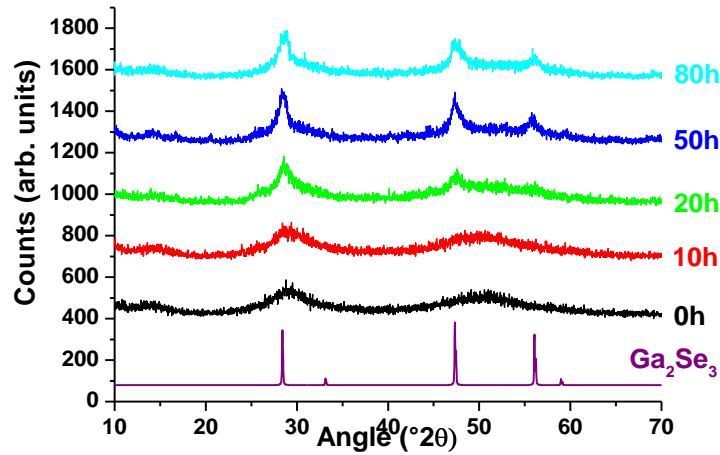


Figure 6.5: XRD spectra the $80\text{GeSe}_2\text{-}20\text{Ga}_2\text{Se}_3 + 0.1\% \text{Er}$ glass and glass-ceramics heat treated at 380°C for increasing time durations.

While a broad signal characteristic of an amorphous material is observed on the base glass (0h of ceramization), crystallization peaks appear on the spectra collected on the glass-ceramics. The peaks become more intense and sharper with the duration of heat treatment. After 20h of heat treatment at 380°C , three crystallization peaks are clearly distinguished. These peaks are attributed to the Ga_2Se_3 crystalline phase.

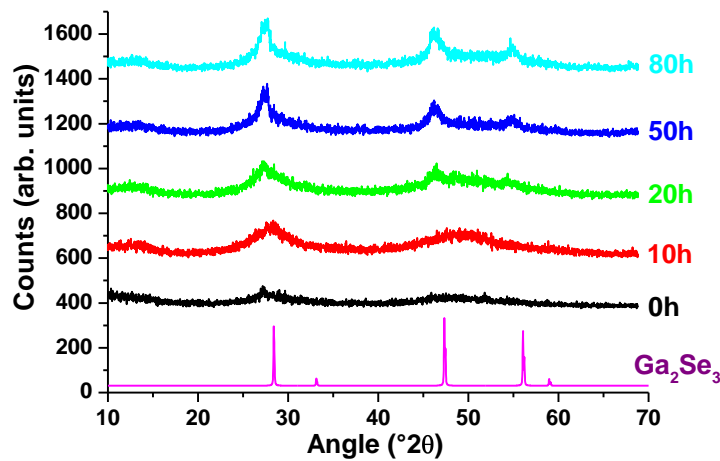


Figure 6.6: XRD spectra the $80\text{GeSe}_2\text{-}20\text{Ga}_2\text{Se}_3 + 0.1\% \text{Nd}$ glass and glass-ceramics heat treated at 380°C for increasing time durations.

6.3.5. SEM observation

The microstructure of the glasses and glass–ceramics were analyzed with a scanning electronic microscope (SEM, JEOL). Due to the insulating character of the $80\text{GeSe}_2\text{--}20\text{Ga}_2\text{Se}_3$ glass, the samples were coated with a gold thin film. Micrographs were taken in fresh cracks made on the surface of the sample.

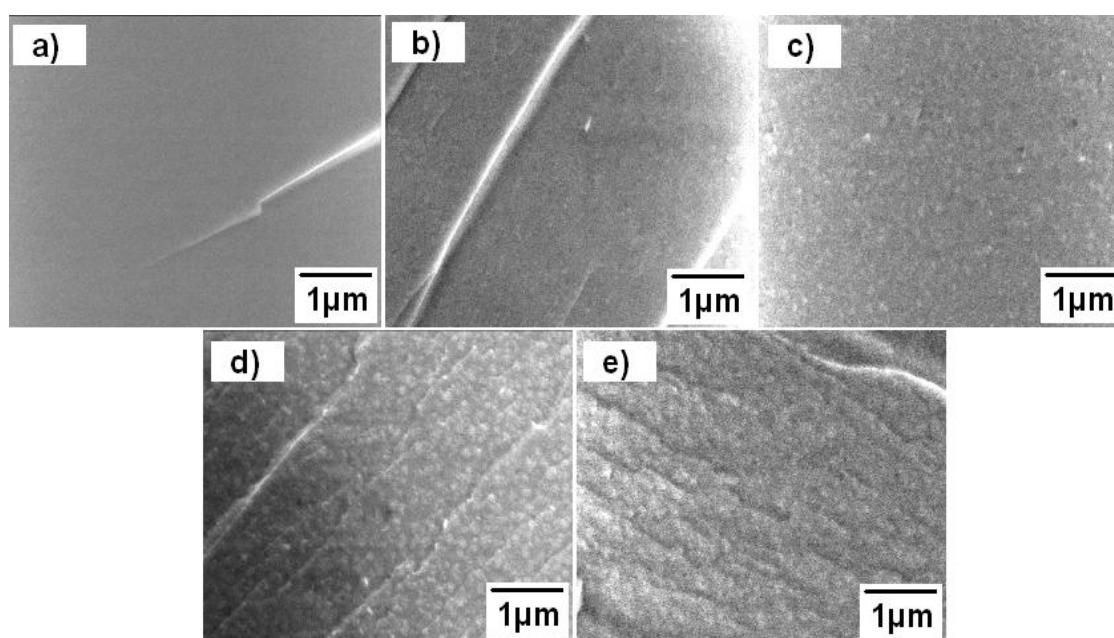


Figure 6.7: SEM micrographs (x20,000) of the $80\text{GeSe}_2\text{--}20\text{Ga}_2\text{Se}_3 + 0.1\% \text{ Er}$ composition after a) 0h, b) 10h, c) 20h, d) 50h and e) 80h of heat treatment at 380°C

No crystals are observed in the $80\text{GeSe}_2\text{--}20\text{Ga}_2\text{Se}_3 + 0.1\text{wt}\% \text{ Er}$ base glass (figure 6.7-a). Submicronic crystals regrouped in aggregates of about 100 nm in diameter appear after 10h of heat treatment (5.7-b). The number of crystals increases after 20h (5.7-c), 50h (5.7-d) and 80h (5.7-e) of ceramization, while the size of the crystals does not increase. From SEM micrographs in figure 6.7, the estimated crystallinity is 10%, 30% and 50% after 10h, 20h and 50h of crystallization, respectively. From the XRD results, the crystalline phase present in the glass correspond to Ga_2Se_3 .

A similar crystallization behavior is observed for the $80\text{GeSe}_2\text{--}20\text{Ga}_2\text{Se}_3 + 0.1\text{wt\% Nd}$ glass and glass-ceramics (figure 6.8). While no crystals are observed on the base glass (5.8-a), an increasing number of submicronic crystals regrouped in aggregates of about 100 nm in diameter appear after 10h of heat treatment (5.8-b). The proportion of crystals increases after 20h (5.8-c), 50h (5.8-d) and 80h (5.8-e) of ceramization. From the XRD measurements, the crystalline phase generated in the glass-ceramics is Ga_2Se_3 .

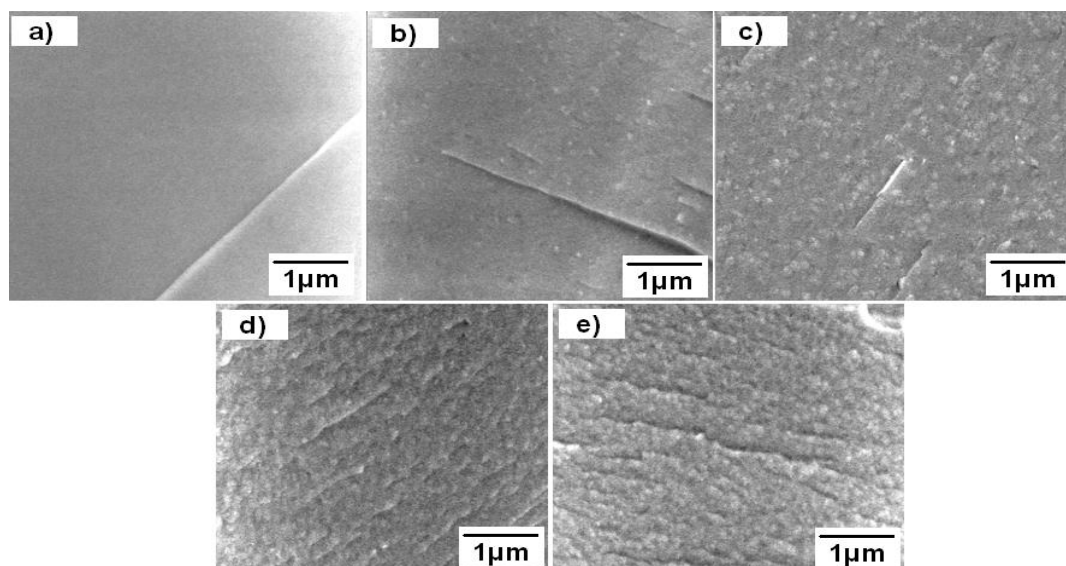


Figure 6.8: SEM micrographs (x20,000) of the $80\text{GeSe}_2\text{--}20\text{Ga}_2\text{Se}_3 + 0.1\% \text{Nd}$ composition after a) 0h, b) 10h, c) 20h, d) 50h and e) 80h of heat treatment at 380°C

6.3.6. Optical Properties

The optical transmission of the Er-doped and Nd-doped $80\text{GeSe}_2\text{--}20\text{Ga}_2\text{Se}_3$ glass-ceramics are presented in figure 6.9 and 5.10, respectively. A progressive shift of the optical band edge towards longer wavelengths with heat treatment duration is observed for the glass-ceramics. This red-shift can be related to the increasing amount of crystals inside the glassy matrix, inducing Rayleigh scattering. However, glass-ceramics transmission in the mid-infrared range remains almost unchanged up to 80h of heat

treatment, demonstrating that no MIE scattering occurs. Both of these observations demonstrate that glass-ceramics are constituted of very small particles, as confirmed by SEM.

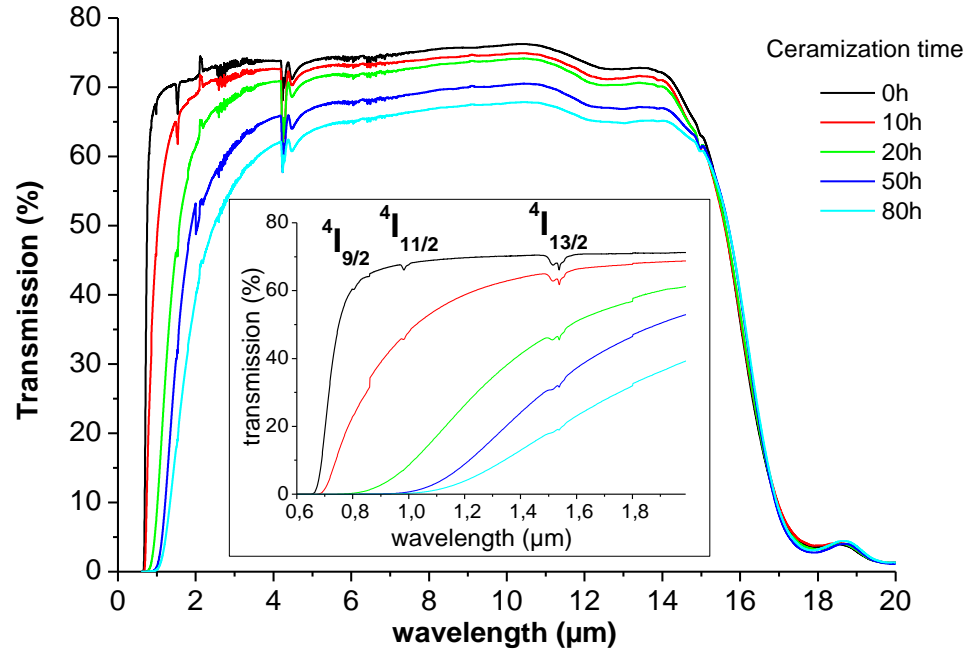


Figure 6.9: Optical transmission of the $80\text{GeSe}_2\text{--}20\text{Ga}_2\text{Se}_3 + 0.1\%$ Er glass and glass-ceramics

After 80h of ceramization, the glass-ceramics remain highly transparent in the infrared range from $3\text{ }\mu\text{m}$ to $16\text{ }\mu\text{m}$. The absorption bands located around $4.5\text{ }\mu\text{m}$ and $12.5\text{ }\mu\text{m}$ correspond to the vibration of Se-H and Ge-O bonds. The presence of impurities during the synthesis process explains these parasite bands. An additional purification step can be used to get rid of these undesired absorptions.

The inset in figure 6.9 shows the optical transmission of the $80\text{GeSe}_2\text{--}20\text{Ga}_2\text{Se}_3 + 0.1\text{wt}\%$ Er glass and glass-ceramics. Absorption bands due to the energy levels $^4\text{I}_{9/2}$, $^4\text{I}_{11/2}$ and $^4\text{I}_{13/2}$ of the Er^{3+} ions are observed at 820 nm , 980 nm and $1.55\text{ }\mu\text{m}$, respectively. The

presence of these absorption bands proves that the erbium ions have been incorporated in the glassy matrix.

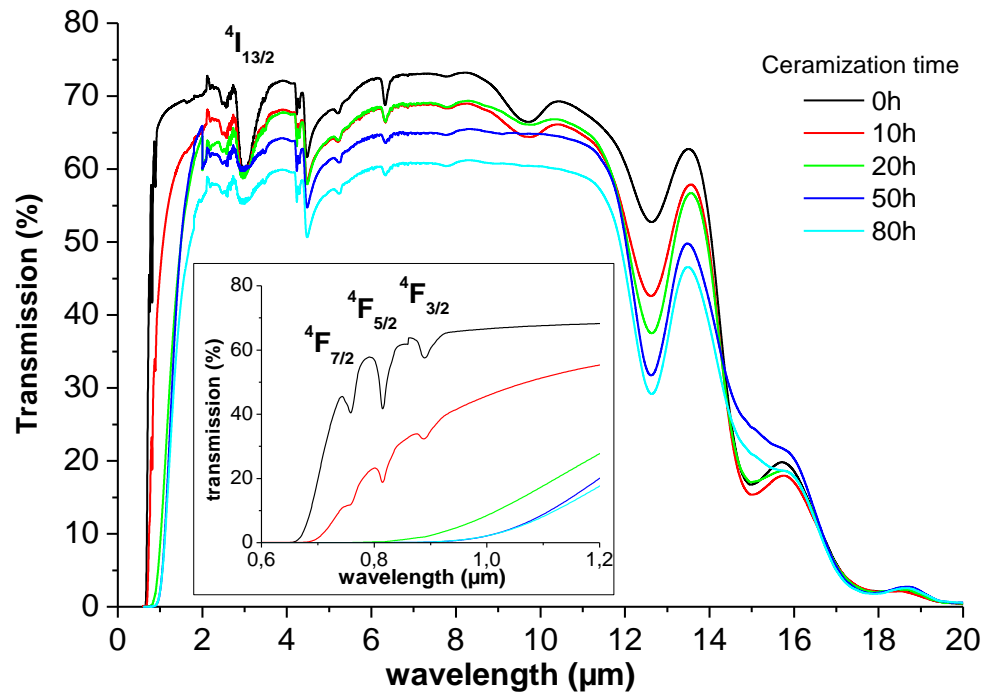


Figure 6.10: Optical transmission of the $80\text{GeSe}_2\text{-}20\text{Ga}_2\text{Se}_3 + 0.1\%$ Nd glass and glass-ceramics

The inset in figure 6.10 shows the optical transmission of the $80\text{GeSe}_2\text{-}20\text{Ga}_2\text{Se}_3 + 0.1\text{wt}\%$ Nd glass and glass-ceramics. The spectrum shows absorption bands at 760 nm, 820 nm, 890 nm and $3.0\ \mu\text{m}$, corresponding to the energy levels $^4\text{F}_{7/2}$, $^4\text{F}_{5/2}$, $^4\text{F}_{3/2}$ and $^4\text{I}_{13/2}$ of the Nd^{3+} ions, respectively. The presence of these absorption bands proves that the neodymium ions have also been incorporated in the glassy matrix

6.4. Luminescence

The near infrared photoluminescence of the erbium-doped and neodymium-doped glasses and glass-ceramics was measured at room temperature with a FLSP920 spectrometer (Edinburgh Instruments) equipped with a nitrogen cooled NIR PMT detector and a tunable CW 450W Xenon Arc Lamp as the excitation source.

6.4.1. Er-doped glass-ceramics

The luminescence intensity for the radiative emission corresponding to the transition ${}^4I_{13/2} \rightarrow {}^4I_{15/2}$ under 823 nm excitation pump is presented in figure 6.11. The energy levels of the Er^{3+} ions, located at 0cm^{-1} , 6450cm^{-1} , 10200cm^{-1} and 12195cm^{-1} , for the ${}^4I_{15/2}$, ${}^4I_{13/2}$, ${}^4I_{11/2}$ and ${}^4I_{9/2}$ levels, respectively, are shown in figure 6.12. After excitation to the ${}^4I_{9/2}$ level, a non-radiative de-excitation leads to the population of the ${}^4I_{13/2}$ level, which then radiatively decay to the ${}^4I_{15/2}$ level with an emission at $1.55\text{ }\mu\text{m}$.

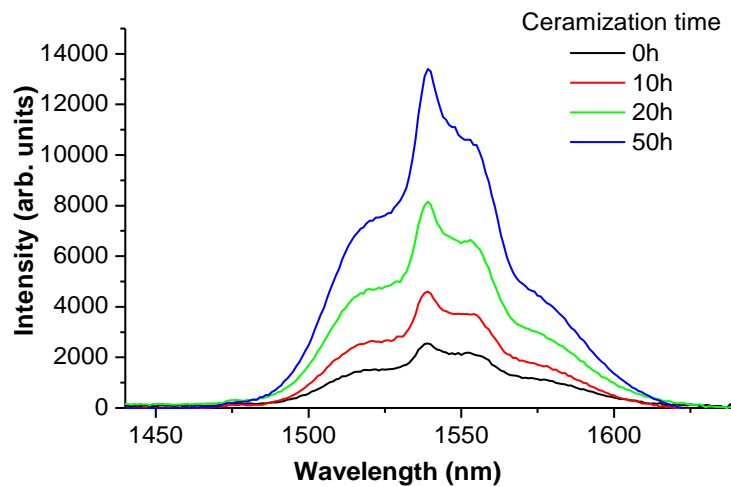


Figure 6.11: Emission spectrum of the $80\text{GeSe}_2\text{--}20\text{Ga}_2\text{Se}_3 + 0.1\% \text{Er}$ glass and glass-ceramics

A broad emission centered at 1535 nm with a full width at half maximum (FWHM) of 50 nm is observed in the base glass and in the glass-ceramics. The maximum intensity of luminescence is progressively enhanced with increasing heat treatment duration. The emission is up to 7 times higher in the sample heat treated for 50h in comparison with the base glass. However, the shape of the peak remains similar whatever the duration of heat treatment, indicating that the Er^{3+} ions remain in the glassy phase and are not incorporated inside the crystals. No emission was observed for the glass-ceramic heat treated for 80h. This absence of emission may be explained by the high crystallinity of the glass-ceramic. An excessive amount of crystals led to a loss of transparency in the 1.55 μm region.

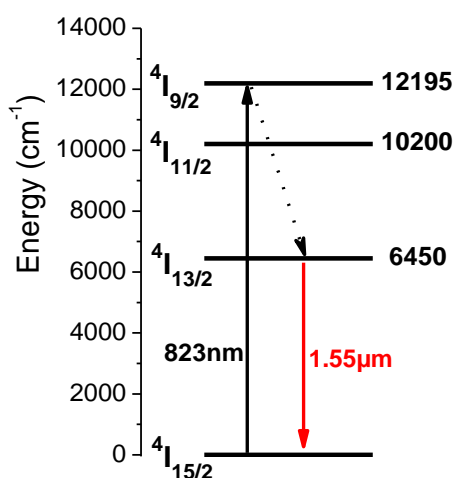


Figure 6.12: Energy diagram of the $80\text{GeSe}_2\text{-}20\text{Ga}_2\text{Se}_3 + 0.1\% \text{Er}$ glass

The enhancement of the luminescence intensity can be explained by the scattering of the pump light due to the crystals present in the glass-ceramics. The optical path of the excitation source is increased with the amount of crystals, increasing its probability to be absorbed by the Er^{3+} ions and then increasing the emission intensity observed.

6.4.2. Nd-doped glass-ceramics

The luminescence intensity for the radiative emission under 823 nm excitation pump is presented in figure 6.13. After excitation to the $^4I_{9/2}$ level, a non-radiative de-excitation leads to the population of the $^4F_{3/2}$ level. Radiative relaxation occurs from the $^4F_{3/2}$ level to the $^4I_{9/2}$, $^4I_{11/2}$ and $^4I_{13/2}$ with emissions centered at 890 nm, 1080 nm and 1380 nm, respectively. The energy levels of the Nd^{3+} ions, located at $0cm^{-1}$, $1980cm^{-1}$, $3300cm^{-1}$, $11240cm^{-1}$, $12195cm^{-1}$ and $13160cm^{-1}$ for the $^4I_{9/2}$, $^4I_{11/2}$, $^4I_{13/2}$, $^4F_{3/2}$, $^4F_{5/2}$ and $^4F_{7/2}$ levels, respectively, are shown in figure 6.14.

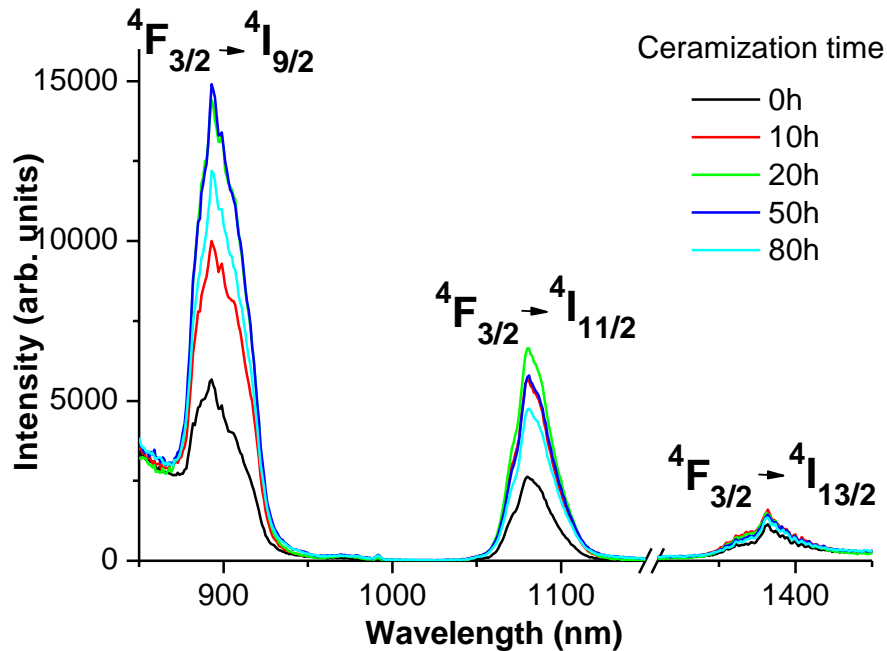


Figure 6.13: Emission spectrum of the $80GeSe_2-20Ga_2Se_3 + 0.1\%$ Nd glass and glass-ceramics

Following a similar pattern as the Er-doped samples, the $80\text{GeSe}_2\text{-}20\text{Ga}_2\text{Se}_3 + 0.1\text{wt\% Nd}$ glass-ceramics show an enhancement in the emission intensity in comparison to the base glass. This increase is more significant for the peaks located at 890 nm and 1080 nm. However, the intensity of the peak observed at 1380 nm remains similar in the base glass and in the glass-ceramics, regardless of the duration of ceramization.

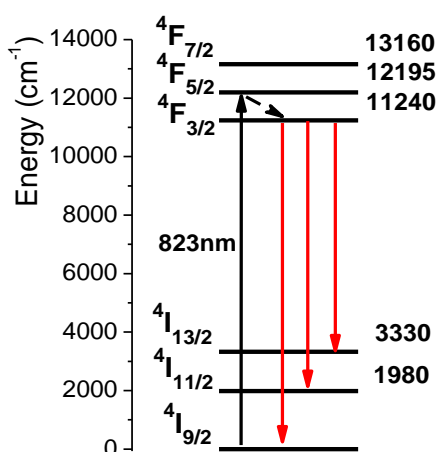


Figure 6.14: Energy diagram of the $80\text{GeSe}_2\text{-}20\text{Ga}_2\text{Se}_3 + 0.1\% \text{Nd}$ glass

The photoluminescence intensity is enhanced by a factor 2 in the glass-ceramic heat treated for 10h. The maximum intensity is obtained after 20h of ceramization. A signal up to three times higher than for the base glass is obtained. After 50h and 80h, the intensity of the peaks progressively decreases, while remaining higher than the signal observed in the base glass.

The shape of the peak remains similar whatever the duration of heat treatment, indicating that the Nd^{3+} ions remain in the glassy phase and are not incorporated inside

the crystals. In the same way as for the Er-doped glass-ceramics, the enhancement of the luminescence intensity can be explained by the scattering of the pump light due to the crystals present in the glass-ceramics, increasing the optical path of the excitation source and thus the probability to be absorbed and re-emitted by the Nd^{3+} ions.

6.5. Lifetime measurements

6.5.1. Er-doped glass-ceramics

The $\text{Er}^{3+} {}^4\text{I}_{13/2}$ energy level lifetime was measured in the base glass and in the glass-ceramics by exciting the ${}^4\text{I}_{9/2}$ level at 823 nm. The fluorescence decay curves for the glass and the glass-ceramics presented a similar shape, illustrated in figure 6.15.

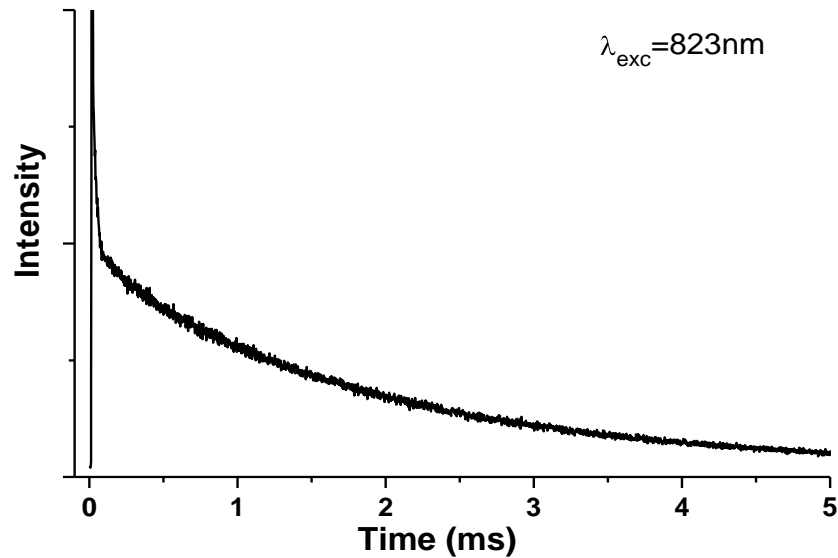


Figure 6.15: Decay curve measured on Er-doped $80\text{GeSe}_2\text{-}20\text{Ga}_2\text{Se}_3$ glass-ceramics

A rise time is observed due to the excitation via the decay of the $^4I_{9/2}$ level followed by the decay of the $^4I_{13/2}$ energy level itself. The decay curves show two different slopes. This indicates that the Er^{3+} ions are found in two different environments in the glass and the glass-ceramics, yielding two different radiative relaxation rates τ_1 and τ_2 . The partial distribution of Er^{3+} ions in the glassy matrix and in nanocrystals could explain this phenomenon. Similar observation was reported in previous studies on Er^{3+} doped glass-ceramics [183].

The lifetimes τ_1 and τ_2 were calculated by fitting the decay curves by a dual exponential expression of the form $I_f(t) = A_1 \exp(-t/\tau_1) + A_2 \exp(-t/\tau_2)$. The results are presented in table 6.4. The population ratio of each erbium site (A_1 and A_2) was calculated. About 2% of the Er^{3+} ions decay with lifetime τ_1 and 98% with lifetime τ_2 , whatever the crystallization time. The proportion of Er^{3+} ions in each environment does not evolve with the proportion of crystals in the glass-ceramics.

Table 6.4: Lifetimes calculated for the Er-doped 80GeSe₂-20Ga₂Se₃ glass-ceramics as a function of ceramization time

Ceramization time	0h	10h	20h	50h
τ_1 (μs)	11	12	15	18
τ_2 (ms)	2.5	2.2	2.1	1.9

The decay curve measured on the doped base glass should present only one relaxation rate, as the host matrix is supposed to be constituted solely of glassy phase. However, two relaxation rates are also observed. Therefore, a weak crystallization probably occurred during the quenching step due to the weak resistance of the 80GeSe₂-20Ga₂Se₃ glass toward crystallization ($\Delta T=90^\circ C$), and a portion of the Er^{3+} ions must be embedded in the nanocrystals generated. Yet, the proportion of crystals in the base glass

must be low, as no crystalline phase is observed on the XRD analysis (figure 6.5) and no crystals are observed by SEM (figure 6.7).

The constant population ratio measured for each erbium site whatever the ceramization duration indicates that no additional Er^{3+} ions are subsequently incorporated in the crystals. This is confirmed by the absence of structuration of the luminescence peaks measured with heat treatment duration (figure 6.11). From the measurements of the lifetimes, it can be assumed that the small proportion of Er^{3+} ions embedded in a crystalline environment decay with the lifetime τ_1 , while the Er^{3+} ions remaining in the glassy matrix decay with lifetime τ_2 .

The values of τ_2 significantly decrease with increased crystallinity. While remaining outside the crystalline structure, the Er^{3+} ions located close to the surface of the crystals are in distorted sites as compared to those in the bulk glassy matrix. These distortions decrease the symmetry of the energy levels, and thus decrease the radiative lifetime [183]. With increased crystallinity, the portion of Er^{3+} ions located close to the surface of crystals is increased, explaining the decreasing lifetime measured (table 6.4). Similar decrease of radiative lifetime with distortion of the rare-earth environment has been reported in the literature, notably by introduction of Zn^{2+} ions [54] or silver nanoparticles [184] in doped glasses.

6.5.2. Nd-doped glass-ceramics

The $\text{Nd}^{3+} {}^4\text{F}_{3/2}$ energy level lifetime was measured in the base glass and in the glass-ceramics by exciting the ${}^4\text{F}_{5/2}$ level at 823 nm. The fluorescence decay curves for

the glass and the glass-ceramics presented a similar shape, illustrated in figure 6.16. The curves show a rise time due to the excitation via the decay of the $^4F_{5/2}$ level followed by the decay of the $^4F_{3/2}$ energy level itself. Contrary to erbium-doped $80\text{GeSe}_2\text{-}20\text{Ga}_2\text{Se}_3$, only one exponential slope is observed for Nd-doped glass-ceramics. Thus, all Nd^{3+} ions remain in the glassy matrix and none are embedded into crystals during the quenching step. The bigger ionic radii of Nd^{3+} ions (1.10\AA) as compared to Er^{3+} ions (1.01\AA) [185] might prevent its insertion within the crystalline phase.

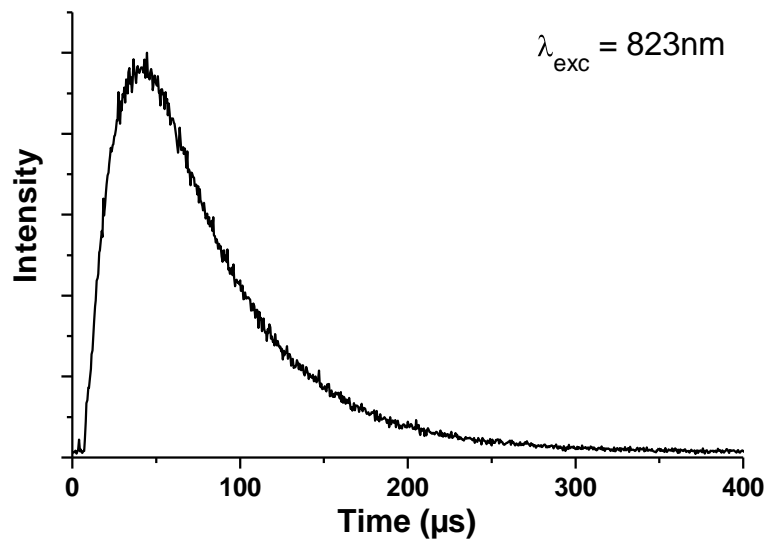


Figure 6.16: Decay curve measured on Nd-doped $80\text{GeSe}_2\text{-}20\text{Ga}_2\text{Se}_3$ glass-ceramics

The lifetimes τ were calculated by fitting the decay curves by a single exponential expression of the form $I_f(t) = A \exp(-t/\tau)$. The values of τ calculated for the base glass and the glass-ceramics (table 6.5) are in the order of some tens of microseconds.

Table 6.5: Lifetimes calculated for the Nd-doped $80\text{GeSe}_2\text{-}20\text{Ga}_2\text{Se}_3$ glass-ceramics as a function of ceramization time

Ceramization time	0h	10h	20h	50h	80h
τ (μs)	55	53	52	49	49

As observed for Er-doped glass-ceramics, the lifetime of Nd^{3+} ions decrease with increased ceramization time. With progressive crystallization, a more important proportion of rare earth ions are located in distorted sites close to the surface of crystals. The perturbation of the symmetry of the energy levels of the Nd^{3+} is thus increased, decreasing the radiative lifetime.

6.5.3. Discussion

The fluorescence decay curves of both Er^{3+} and Nd^{3+} ions exhibit a decrease of the radiative lifetimes with progressive crystallization of the glass matrix. Interestingly, it was previously shown that this process is accompanied by an enhancement of the photoluminescence intensity (figures 5.11 and 5.13). Such a correlation between reduced lifetimes and increased photoluminescence has been previously reported but this phenomenon is still not fully understood [165, 184, 186, 187].

It was suggested that the reduction of the lifetime would lead to an increase of the excitation/radiative emission cycles. Consequently, the number of photons emitted per second would increase, and thus would result in an increase in apparent intensity [184]. However, an alternative explanation for the intensity increase may involve scattering of the pump light by crystals dispersed within the glassy matrix. The scattering process will increase the optical path length of the pump light and enhance the probability of exciting active centers, thus resulting in higher emission intensity. Ultimately, both of these phenomena could occur simultaneously and at this point it is not possible to clearly

assign the increase in photoluminescence activity observed in the doped 80GeSe₂-20Ga₂Se₃ glass-ceramics to either mechanism.

6.6. Conclusion

Rare earth-doped selenium-based glass-ceramics have been prepared for the first time and their luminescence properties have been studied. Base glasses having a composition of 80GeSe₂-20Ga₂Se₃ and doped with 0.1wt% of erbium or neodymium were prepared and heat treated to produce glass-ceramics transparent in the infrared region. In both cases, XRD and SEM analyses showed a progressive crystallization of the Ga₂Se₃ phase inside the glassy matrix, with an increased crystallinity according to the duration of heat treatment. Absorptions due to the energy levels of the (RE)³⁺ ions were observed.

The emission at 1.55 μm has been monitored in the erbium-doped base glass and in the glass-ceramics. A better absorption of the excitation signal by the RE ions due to scattering of the incoming light by crystals leads to 7-fold improvement in emission intensity after 50h of heat treatment. Three emission peaks located at 890 nm, 1080 nm and 1380 nm were observed in the Nd-doped glass and glass-ceramics. As for the Er-doped samples, the luminescence intensity is enhanced and the radiative lifetimes are shortened with increasing crystallinity.

This study demonstrate the possibility of preparing RE doped chalcogenide glass-ceramics based on selenium with a good transparency in the infrared up to 16 μm . The

low phonon energy of the $80\text{GeSe}_2\text{-}20\text{Ga}_2\text{Se}_3$ glass makes it a good potential host for rare-earth doping. This work constitutes the first step towards the design of new materials interesting for the production of new laser sources in the mid-infrared region.

CHAPTER 7: CONCLUSION

Thermal imaging is a fast growing market due to the improvement, miniaturization and the decreasing costs of detectors, electronics and computing systems employed. However, the optics used in thermal cameras require a high transparency in the 3-5 μm and 8-12 μm windows and only a few materials combine good mechanical resistance and satisfying optical transparency. Currently, infrared lenses are predominantly made of expensive and difficult to shape materials such as crystalline germanium or zinc selenide. In contrast, chalcogenide glasses are relatively cheap, easy to shape by molding while presenting extended transmission in the infrared range. Thus, they are of high interest for production of infrared lenses. However, their weak points reside in their relatively low mechanical properties and in their complex synthesis process in sealed silica tubes.

This research work was motivated by the constant need for cheaper materials presenting enhanced properties for thermal imaging applications. The studies presented were focused on the 80GeSe₂-20Ga₂Se₃ glass and glass-ceramics. Two major axes were investigated: first, the development of cheaper synthesis methods and second, the production of glass-ceramics with enhanced mechanical properties and new potential applications in the infrared range.

The main challenge encountered in the development of new synthesis methods consisted in replacing the expensive single use silica tubes currently employed for production of chalcogenide glasses. The first investigations involved the use of open

crucibles and highlighted the difficulty of obtaining a reaction between elements having important differences in thermal properties. These methods generated major weight losses and appeared inadequate for the compositions studied.

The second investigation involved mechanosynthesis by mechanical milling of the starting raw elements which appeared very efficient for preparing chalcogenide glass powders. This synthesis step was followed by a consolidation process to produce bulk materials. Different methods were investigated for preparing bulk chalcogenide glasses transparent in the infrared range. Melting of the as-obtained powders was efficient for compositions stable toward crystallization such as GeSe_4 . However, uncontrolled crystallization was experienced for less stable compositions such as the 80GeSe_2 - $20\text{Ga}_2\text{Se}_3$ glass. Similar results were obtained by sintering of the powders by Hot Uniaxial Pressing. This consolidation process was demonstrated to be inadequate for glass compositions with low thermal stability.

The following investigation demonstrated that Spark Plasma Sintering (SPS) was most promising method for production of chalcogenide glasses from the powders obtained by mechanosynthesis. Bulk 80GeSe_2 - $20\text{Ga}_2\text{Se}_3$ glasses transparent in the infrared region were obtained in short sintering time at a temperature slightly above the glass transition temperature of the glass. The samples produced present a 4-fold increase in diameter in comparison to those obtained by melt/quenching technique. Furthermore, by extending the duration of SPS treatment, glass-ceramics presenting enhanced mechanical properties and transparent in the $3\text{-}5\mu\text{m}$ and $8\text{-}12\mu\text{m}$ windows were obtained.

This innovative synthesis method paves the way for the production of chalcogenide glasses and glass-ceramics at a lower cost.

While the dimensions of glasses produced in silica ampoules are limited by the low thermal conductivity of silica, of the size of samples produced by mechanosynthesis and SPS is only limited by the size of the die used during the sintering process. Thus, many interesting chalcogenide glasses compositions which were set aside due to the impossibility to produce big samples adequate for infrared applications could be prepared by this method. A patent has been filed on this innovative synthesis method in the framework of this study. The aim of this study was the assessment of the synthesis methods for production of chalcogenide glasses. Much more remains to be done on the mechanosynthesis and SPS. The contamination of the powders by oxygen observed in this study will have to be investigated. A high control of the reaction atmosphere during the mechanosynthesis step will have to be carried out to limit this contamination and produce highly transparent materials. It would also be interesting to investigate the effect of the different milling parameters (ball-to-powder weight ratio, milling speed and duration, milling atmosphere and temperature) on the reaction kinetics.

The second axis investigated was the development of new applications for the $80\text{GeSe}_2\text{-}20\text{Ga}_2\text{Se}_3$ glass-ceramics. The interest of this composition for sensing application was explored. A nanoporous layer with a depth of some hundreds of nanometers was created on the surface of the glass-ceramics by controlled etching of the crystalline phase. This porous layer yielded a 6-fold increase in surface area of the material and was shown to have an anti-reflective effect increasing the maximum of

transmission in the infrared range by up to 10%. The possibility of functionalizing the surface with silane was demonstrated and a 5-fold increase in absorbance was obtained on porous glass-ceramics.

Also, the influence of the addition of In and Pb addition on the thermal and optical properties of the $80\text{GeSe}_2\text{-}20\text{Ga}_2\text{Se}_3$ composition was studied. The two new glassy systems $\text{GeSe}_2\text{-Ga}_2\text{Se}_3\text{-In}_2\text{Se}_3$ and $\text{GeSe}_2\text{-Ga}_2\text{Se}_3\text{-PbSe}$ were explored. A decrease of the glass transition temperature and a shift of the optical band-gap toward higher wavelengths was observed with increasing In or Pb contents. The aim of this study was to develop new families of chalcogenide glass-ceramics with properties interesting for non-linear optics or photovoltaic by precipitating In-based or Pb-based crystalline phases. However, only one glass composition in the $\text{GeSe}_2\text{-Ga}_2\text{Se}_3\text{-In}_2\text{Se}_3$ system showed a potential to form controllable and reproducible glass-ceramics, and no In-based crystals were precipitated. Therefore, the two glassy domains explored showed little interest for infrared optic applications.

Finally, the influence of crystallinity on the luminescence properties of erbium- and neodymium-doped $80\text{GeSe}_2\text{-}20\text{Ga}_2\text{Se}_3$ glass-ceramics was studied. The possibility of preparing rare earth doped glass-ceramics transparent in the infrared range up to $16\mu\text{m}$ was demonstrated. An increase in photoluminescence intensity and a decrease of the radiative lifetimes were observed with increased crystallinity. This work constitutes the first step towards design of new materials interesting for the production of efficient laser sources working in the mid-infrared range, where the laser sources currently available are limited to a few wavelengths such as CO_2 lasers at $10.6\mu\text{m}$.

**APPENDIX A: THERMAL, OPTICAL AND MECHANICAL PROPERTIES OF
GLASSES IN THE $\text{GeSe}_2\text{-Ga}_2\text{Se}_3\text{-In}_2\text{Se}_3$ SYSTEM**

Composition (at%)			Atomic contents (at%)				Tg	Tx	ΔT	λg	Hv	K _{i,c}	E	ρ
GeSe ₂	Ga ₂ Se ₃	In ₂ Se ₃	Ge	Ga	Se	In	± 2°C	± 2°C	± 4°C	± 2 nm	±1 Kg.mm ²	±0.005 Mpa.√m	±0.3 GPa	±0.03 Kg/m ³
90	10	0	28.13	6.25	65.62	0	373	477	104	679	200	0.245	19.9	4.20
85	15	0	25.76	9.09	65.15	0	360	466	106	693	202	0.225	20.8	4.36
80	20	0	23.53	11.76	64.71	0	370	460	90	690	193	0.213	22.7	4.39
75	25	0	21.43	14.29	63.88	0	366	437	71	708	-	-	21.4	-
90	0	10	28.13	0	65.62	6.25	340	440	100	710	194	0.218	18.7	4.39
85	0	15	25.76	0	65.15	9.09	331	439	108	723	193	0.221	20.8	4.43
80	0	20	23.53	0	64.71	11.76	328	446	118	736	189	0.210	22.0	4.58
75	0	25	21.43	0	64.28	14.29	325	441	116	745	188	0.171	22.3	4.68
70	0	30	19.44	0	63.89	16.67	321	438	117	757	-	-	22.7	4.71
65	0	35	17.57	0	63.51	18.92	316	445	129	780	-	-	-	4.79
90	5	5	28.13	3.13	65.61	3.13	361	482	121	709	196	0.223	19.2	3.97
80	5	15	23.53	2.94	64.71	8.82	330	459	129	734	192	0.209	22.0	4.55
80	10	10	23.53	5.88	64.71	5.88	342	460	118	723	197	0.219	21.2	4.49
80	15	5	23.53	8.82	64.71	2.94	357	469	112	710	204	0.223	23.1	4.43
75	5	20	21.43	2.86	64.28	11.43	333	460	127	736	194	0.204	21.8	4.64
75	6.25	18.75	21.43	3.57	64.29	10.71	329	458	129	738	192	0.189	21.7	4.56
75	18.75	6.25	21.43	10.71	64.29	3.57	356	462	106	702	197	0.191	21.2	4.49
70	7.5	22.5	19.44	4.17	63.89	12.50	326	453	127	742	-	-	22.8	4.67
70	15	15	19.44	8.33	63.90	8.33	336	453	117	736	-	-	22.6	4.59
70	20	10	19.44	11.11	63.89	5.56	349	461	112	729	207	0.205	22.2	4.52
70	25	5	19.44	13.89	63.89	2.78	360	447	87	720	207	0.204	22.8	4.45
66.67	16.67	16.67	18.18	9.09	63.64	9.09	334	461	127	746	-	-	22.4	4.61
65	10	25	17.57	5.41	63.51	13.51	328	459	131	769	203	0.193	24.2	4.70
65	25	10	17.57	13.51	63.51	5.41	352	435	83	723	213	0.169	20.7	4.53
60	10	30	15.79	5.26	63.16	15.79	323	432	109	756	198	0.207	24.5	4.72
60	15	25	15.79	7.89	63.16	13.16	328	454	126	761	-	-	19.7	4.65

**APPENDIX B: THERMAL, OPTICAL AND MECHANICAL PROPERTIES OF
GLASSES IN THE $\text{GeSe}_2\text{-Ga}_2\text{Se}_3\text{-PbSe}$ SYSTEM**

Composition (mol %)			Atomic contents (at%)				Tg	Tx	ΔT	λ_g	Hv	K _{lc}	E	ρ
GeSe_2	Ga_2Se_3	PbSe	Ge	Ga	Se	Pb	$\pm 2^\circ\text{C}$	$\pm 2^\circ\text{C}$	$\pm 4^\circ\text{C}$	$\pm 2\text{ nm}$	± 1 Kg. mm^{-2}	± 0.001 $\text{Mpa.}\sqrt{\text{m}}$	± 0.3 GPa	± 0.03 Kg/m^3
90	5	5	29.51	3.28	65.57	1.64	365	430 456	65	711	206	0.200	20.2	4.43
80	10	10	25.81	6.45	64.52	3.23	334	447	113	722	203	0.201	22.0	4.56
75	5	20	25.86	3.45	63.79	6.90	322	389	67	797	200	0.214	22.9	4.95
75	18.75	6.25	22.64	11.32	64.15	1.89	355	465	110	707	206	0.190	20.6	4.63
70	10	20	23.33	6.67	63.33	6.67	325	399	74	754	204	0.171	20.2	4.96
70	20	10	21.21	12.12	63.64	3.03	330	450	120	726	212	0.181	22.7	4.57
66.67	16.67	16.67	21.05	10.53	63.16	5.26	347	438	91	749	204	0.186	21.2	4.93
60	15	25	19.67	9.84	62.30	8.19	328	405	77	785	200	0.190	20.6	5.31
60	30	10	17.14	17.14	62.86	2.86	355	418 454	63	745	199	0.211	21.6	4.64
60	20	20	18.75	12.50	62.50	6.25	330	418	88	719	200	0.195	21.0	4.95
60	10	30	20.69	6.90	62.07	10.34	311	387	76	783	-	-	-	-
60	0	40	23.08	0	61.54	15.38	310	391	81	811	196	0.201	29.1	5.61

REFERENCES

1. Richards, A. *Shrinking IR cameras enable new applications*. (<http://www.corebyindigo.com/PDF/articles/LaserFocus3-04.pdf>).
2. BMW. *BMW Night Vision*. (www.bmw.de).
3. Sirica. *Uncooled detector with cool performance at revolutionary prices*. (<http://www.sirica.com/market.asp>).
4. Française, S.R. *Statistiques accidentologiques*. (<http://www.securiteroutiere.equipement.gouv.fr/>).
5. Kerr, J., *Review of the effectiveness of infrared thermal imaging (thermography) for population screening and diagnostic testing of breast cancer*. Nzhta Tech Brief Series, 2004. **3**(3).
6. Wang, H. *IR imaging of blood circulation of patients with vascular disease*. in *SPIE conference Proceedings*. 2004: SPIE.
7. Peacock, G., D. Burleigh and K. Cramer. *Human radiation thermometry and screening for elevated body temperature in humans*. in *SPIE conference Proceedings*. 2004.
8. Gowen, A.A., B.K. Tiwari, P.J. Cullen, K. McDonnell and C.P. O'Donnell, *Applications of thermal imaging in food quality and safety assessment*. Trends in Food Science and Technology, 2010. **21**(4): p. 190-200.
9. Ioannis, P., L. James and B. Paulette, *Thermal Imaging for Anxiety Detection*, in *Proceedings of the IEEE Workshop on Computer Vision Beyond the Visible Spectrum: Methods and Applications (CVBVS 2000)*. 2000, IEEE Computer Society.
10. Pavlidis, I., *Lie detection using thermal imaging*. SPIE proceedings, 2004. **5405**(1): p. 270.
11. Gaussorgues, G., *La thermographie infrarouge: principes-techniques-applications, Quatrième édition revue et argumentée*, ed. Techniques&Documentations. 1999: Lavoisier.
12. Meyzonnette, J.L. and T. Lépine, *Bases de radiométrie optique*, ed. Cépaduès. 1999.
13. Hilton, A.R., *Chalcogenide glasses for infrared optics*. 2010: MacGraw Hill.

14. Williams, T.L., *Thermal Imaging Cameras: characteristics and performance*. 2009: CRC Press.
15. Norton, W. Peter, Cox, Stephen, Murphy, Bob, Grealish, Kevin, Joswick, Mike, Denley, Brian, Feda, Frank, Elmali, Loriann, Kohin and Margaret, *Uncooled thermal imaging sensor and application advances*. Vol. 6206. 2006: Society of Photo-Optical Instrumentation Engineers.
16. Zhang, X.H., Y. Guimond and Y. Bellec, *Production of complex chalcogenide glass optics by molding for thermal imaging*. Journal of Non-Crystalline Solids, 2003. **326-327**(0): p. 519-523.
17. Lloyd, J.M., *Thermal Imaging Systems*. 1975: Springer.
18. Savage, J.A., *Infrared optical materials and their antireflection coatings*. 1985: Adam Hilger Ltd.
19. Photonics. *Barium Fluoride and Calcium Fluoride Windows for UV, VIS and IR*. (www.photonics.com/Article.aspx?AID=14658).
20. Haig, N.D., C. Lewis and R.H. Runalls, *Assessment of Imaging Systems*. SPIE, 1976.
21. Parker, P.M. and E. Lilly, *The World Market for Germanium and Articles Thereof Including Waste and Scrap: A 2007 Global Trade Perspective*. 2006, ICON Group International, Inc.
22. Nakasuji, T., S. Kodera, S. Hara, H. Matsunaga, N. Ikawa and S. Shimada, *Diamond Turning of Brittle Materials for Optical Components*. CIRP Annals - Manufacturing Technology, 1990. **39**(1): p. 89-92.
23. AMI. *Amorphous Materials Inc.* (www.amorphousmaterials.com).
24. Klocek, P., *Handbook of infrared optical materials*. 1991: CRC Press.
25. Shchurov, A.F., V.A. Perevoshchikov, T.A. Gracheva, N.D. Malygin, D.N. Shevarenkov, E.M. Gavrishchuk, V.B. Ikonnikov and E.V. Yashina, *Structure and Mechanical Properties of Polycrystalline Zinc Sulfide*. Inorganic Materials, 2004. **40**(2): p. 96-101.
26. Gentile, A.L., M. Braustein, D.A. Pinnow, J.A. Harrington, D.M. Henderson, L.M. Holbrock, J. Mayer, R.C. Pastor and R.R. Turk, *Fiber optics, advances in research and development*. 1979: Plenum Press.
27. Nestor, O.H., D.A. Hammond and G. Bastien, *Los Alamos Conference on optics '79*. 1979, SPIE. p. 112-115.

28. Kokorina, V.F., *Glasses for infrared optics*. 1996: CRC Press.
29. Titus, S.S.K., S. Asokan, T.K. Mondal and E.S.R. Gopal, *Effect of selenium on the crystallization behaviour of As-Te glasses*. Solid State Communications, 1994. **89**: p. 23-26.
30. Vitron. *Spezialwerkstoffe GmbH*. (www.vitron.de).
31. Hilton, A.R. and D.J. Hayes, *Interdependence of physical parameters for infrared transmitting glasses*. Journal of Non-Crystalline Solids, 1975. **17**(3): p. 339-48.
32. Hilton, A.R., D.J. Hayes and M.D. Rechtin, *Infrared absorption of some high-purity chalcogenide glasses*. Journal of Non-Crystalline Solids, 1975. **17**(3): p. 319-38.
33. Umicore. *Electro Optics Materials*. (www.eom.umicore.com).
34. Savage, J.A., P.J. Webber and A.M. Pitt, *The potential of Ge-As-Se-Te glasses as 3–5 μm and 8–12 μm infrared optical materials*. Infrared Physics, 1980. **20**(5): p. 313-320.
35. Thornburg, D., *Physical properties of the $\text{As}_2(\text{Se},\text{Te})_3$ glasses*. Journal of Electronic Materials, 1973. **2**(4): p. 495-532.
36. Shiryaev, V.S., C. Boussard-Plédel, P. Houizot, T. Jouan, J.L. Adam and J. Lucas, *Single-mode infrared fibers based on TeAsSe glass system*. Materials Science and Engineering: B, 2006. **127**(2-3): p. 138-143.
37. Lucas, P., D. Le Coq, C. Juncker, J. Collier, D.E. Boesewetter, C. Boussard-Plédel, B. Bureau and M.R. Riley, *Evaluation of Toxic Agent Effects on Lung Cells by Fiber Evanescent Wave Spectroscopy*. Applied Spectroscopy, 2005. **59**(1): p. 1-9.
38. Zhang, X.H., G. Fonteneau and J. Lucas, *The tellurium bromide glasses: New I.R. transmitting materials*. Materials Research Bulletin, 1988. **23**(1): p. 59-64.
39. Lucas, J. and X.H. Zhang, *The tellurium halide glasses*. Journal of Non-Crystalline Solids, 1990. **125**(1-2): p. 1-16.
40. Danto, S., P. Houizot, C. Boussard-Plédel, X.H. Zhang, F. Smektala and J. Lucas, *A Family of Far-Infrared-Transmitting Glasses in the Ga-Ge-Te System for Space Applications*. Advanced Functional Materials, 2006. **16**(14): p. 1847-1852.
41. Wilhelm, A.A., C. Boussard-Plédel, Q. Coulombier, J. Lucas, B. Bureau and P. Lucas, *Development of Far-Infrared-Transmitting Te Based Glasses Suitable for*

- Carbon Dioxide Detection and Space Optics*. Advanced Materials, 2007. **19**(22): p. 3796-3800.
42. Mecholsky, J.J., C.T. Moynihan, P.B. Macedo and G.R. Srinivasan, *Microstructure and properties of an infra-red transmitting chalcogenide glass-ceramic*. Journal of Materials Science, 1976. **11**(10): p. 1952-1960.
 43. Jijian, C., *Microstructure and properties of selenide glasses after controlled crystallization*. Journal of Non-Crystalline Solids, 1983. **56**(1-3): p. 303-308.
 44. Jijian, C., *Phase separation and controlled crystallization of non-oxide glasses*. Journal of Non-Crystalline Solids, 1986. **80**(1-3): p. 52-68.
 45. Jijian, C., *Phase separation and crystallization of chalcogenide glass-forming systems*. Journal of Non-Crystalline Solids, 1993. **161**: p. 304-308.
 46. Zhang, X., H. Ma, J. Lucas, Y. Guimond and S. Kodjikian, *Optical fibers and molded optics in infrared transparent glass-ceramic*. Journal of Non-Crystalline Solids, 2004. **336**(1): p. 49-52.
 47. Zhang, X., M.A. Hongli and J. Lucas, *A new class of infrared transmitting glass-ceramics based on controlled nucleation and growth of alkali halide in a sulphide based glass matrix*. Journal of Non-Crystalline Solids, 2004. **337**(2): p. 130-135.
 48. Calvez, L., P. Lucas, M. Rozé, H.L. Ma, J. Lucas and X.H. Zhang, *Influence of gallium and alkali halide addition on the optical and thermo-mechanical properties of $\text{GeSe}_2\text{-Ga}_2\text{Se}_3$ glass*. Applied Physics A: Materials Science & Processing, 2007. **89**(1): p. 183-188.
 49. Calvez, L., H.L. Ma, J. Lucas, P. Glouannec and X.H. Zhang, *Thermal analysis of RbI crystallization in the $\text{GeSe}_2\text{-Sb}_2\text{Se}_3\text{-RbI}$ system*. Journal of Non-Crystalline Solids, 2007. **353**(52-54): p. 4702-4706.
 50. Calvez, L., H.L. Ma, J. Lucas and X.H. Zhang, *Preparation and properties of glasses and glass ceramics based on $\text{GeSe}_2\text{-Sb}_2\text{Se}_3$ and halides*. Physics and Chemistry of Glasses, 2006. **47**: p. 145.
 51. Calvez, L., H.L. Ma, J. Lucas and X.H. Zhang, *Selenium-Based Glasses and Glass Ceramics Transmitting Light from the Visible to the Far-IR*. Advanced Materials, 2007. **19**(1): p. 129-132.
 52. Calvez, L., H.L. Ma, J. Lucas and X.H. Zhang, *Glasses and glass-ceramics based on $\text{GeSe}_2\text{-Sb}_2\text{Se}_3$ and halides for far infrared transmission*. Journal of Non-Crystalline Solids, 2008. **354**(12-13): p. 1123-1127.

53. Wang, H., X.H. Zhang, G. Yang, Y. Xu, H.L. Ma, J.L. Adam, Z.a. Gu and G. Chen, *Micro-crystallization of the infrared transmitting chalcogenide glass in $\text{GeSe}_2\text{-As}_2\text{Se}_3\text{-PbSe}$ system* Ceramics International, 2009. **35**(1): p. 83-86.
54. Xia, F., X. Zhang, J. Ren, G. Chen, H. Ma and J.L. Adam, *Glass Formation and Crystallization Behavior of a Novel $\text{GeSe}_2\text{-Sb}_2\text{S}_3\text{-PbS}$ Chalcogenide Glass System*. Journal of the American Ceramic Society, 2006. **89**(7): p. 2154-2157.
55. Yang, G., X. Zhang, J. Ren, Y. Yunxia, G. Chen, H. Ma and J.L. Adam, *Glass Formation and Properties of Chalcogenides in a $\text{GeSe}_2\text{-As}_2\text{Se}_3\text{-PbSe}$ System*. Journal of the American Ceramic Society, 2007. **90**(5): p. 1500-1503.
56. Zhao, D., X. Zhang, H. Wang, H. Zeng, H. Ma, J.L. Adam and G. Chen, *Thermal properties of chalcogenide glasses in the $\text{GeSe}_2\text{-As}_2\text{Se}_3\text{-CdSe}$ system*. Journal of Non-Crystalline Solids, 2008. **354**(12-13): p. 1281-1284.
57. Zhao, D., X.H. Zhang, F. Xia, H. Wang, H.L. Ma, J.L. Adam and G. Chen, *Nonisothermal study on crystallization kinetics of $\text{GeSe}_2\text{-As}_2\text{Se}_3\text{-CdSe}$ chalcogenide glasses by differential scanning calorimeter*. Journal of Crystal Growth, 2005. **285**(1-2): p. 228-235.
58. Yang, Z., W. Chen, H. Ma and X. Zhang, *Controlled Crystallization of $\text{GeSe}_2\text{-Ga}_2\text{Se}_3\text{-CsI}$ Chalcohalide Glasses During Molding*. Journal of the American Ceramic Society, 2008. **91**(8): p. 2720-2723.
59. Rozé, M., L. Calvez, J. Rollin, P. Gallais, J. Lonnoy, S. Ollivier, M. Guilloux-Viry and X.-H. Zhang, *Optical properties of free arsenic and broadband infrared chalcogenide glass*. Applied Physics A: Materials Science and Processes, 2010. **98**(1): p. 97-101.
60. Rozé, M., L. Calvez, M. Hubert, P. Toupin, B. Bureau, C. Boussard-Plédel and X.-H. Zhang, *Molded Glass-Ceramics for Infrared Applications*. International Journal of Applied Glass Science, 2011. **2**(2): p. 129-136.
61. Rozé, M., L. Calvez, Y. Ledemi, M. Allix, G. Matzen and X.-H. Zhang, *Optical and Mechanical Properties of Glasses and Glass-Ceramics Based on the Ge-Ga-Se System*. Journal of the American Ceramic Society, 2008. **91**(11): p. 3566-3570.
62. Frumarová, B., M. Frumar and J. Málek, *New halide glasses [the system $\text{CdCl}_2\text{-PbCl}_2\text{-KI-PbO}$]*. Materials Research Bulletin, 1994. **29**(10): p. 1035-1040.
63. Popescu, M., *Non-crystalline chalcogenides*. 2000: Kluwer Academic Publishers.
64. IUPAC, *Compendium of Chemical Terminology, 2nd edition*. 1997.

65. Arora, A., D.B. Marshall, B.R. Lawn and M.V. Swain, *Indentation deformation/fracture of normal and anomalous glasses*. Journal of Non Crystalline Solids, 1979. **31**(3): p. 415-28.
66. Lide, D.R., *CRC handbook of chemistry and physics: a ready-reference book of chemical and physical data*. 2005: CRC Press.
67. Ford, E.B. and J.A. SAverage, *A furnace for the synthesis of chalcogenide glasses*. Journal of Physics E: Scientific Instruments, 1976. **9**(8): p. 622.
68. Rozé, M., *Verres et vitrocéramiques transparents dans l'infrarouge pour application à l'imagerie thermique*. 2009, Université de Rennes 1, France, PhD dissertation (in French).
69. Guillevic, E., *Verres et vitrocéramiques de chalcogénures: Nouveau procédé de synthèse et dopage par les ions lanthanides*. 2009, Université de Rennes 1, PhD Dissertation (in French).
70. Suryanarayana, C., *Mechanical alloying and milling*. Progress in Materials Science, 2001. **46**(1-2): p. 1-184.
71. Benjamin, J.S., *Dispersion strenghtened superalloys by mechanical alloying*. Metallurgical Transactions, 1970. **1**(10): p. 2943-&.
72. Benjamin, J.S. and M.J. Bomford, *Dispersion strengthened aluminum made by mechanical alloying*. Metallurgical Transactions a-Physical Metallurgy and Materials Science, 1977. **8**(8): p. 1301-1305.
73. Benjamin, J.S. and R.D. Schelleng, *Dispersion strengthened aluminum-4 pct magnesium alloy made by mechanical alloying*. Metallurgical Transactions a-Physical Metallurgy and Materials Science, 1981. **12**(10): p. 1827-1832.
74. Bernal-Correa, R., A. Rosales-Rivera, P. Pineda-Gomez and N.A. Salazar, *Structural and magnetic properties of Fe₆₀Al₄₀ alloys prepared by means of a magnetic mill*. Journal of Alloys and Compounds, 2010. **495**(2): p. 491-494.
75. Campos, C.E.M., J.C. de Lima, T.A. Grandi, J.P. Itie, A. Polian and A. Michalowicz, *Pressure-induced phase transition of nanocrystalline ZnSe*. Journal of Physics-Condensed Matter, 2005. **17**(34): p. 5187-5200.
76. Grandi, T.A., J.C. De Lima, C.E.M. Campos, K.D. Machado and G.L.F. Fraga, *Study of amorphous Co₅₆Nb₂₂Sn₂₂ alloy prepared by mechanical alloying*. Journal of Non-Crystalline Solids, 2004. **347**(1-3): p. 262-267.

77. Amarin, H., J. Ricote, J. Holc, M. Kosec and M. Alguero, *Homogeneous templated grain growth of $0.65\text{Pb}(\text{Mg}_{1/3}\text{Nb}_{2/3})\text{O}-3-0.35\text{PbTiO}(3)$ from nanocrystalline powders obtained by mechanochemical activation*. Journal of the European Ceramic Society, 2008. **28**(14): p. 2755-2763.
78. Shaw, B.A., G.D. Davis, T.L. Fritz, B.J. Rees and W.C. Moshier, *The influence of tungsten alloying additions on the passivity of aluminum*. Journal of the Electrochemical Society, 1991. **138**(11): p. 3288-95.
79. Koch, C.C., O.B. Cavin, C.G. McKamey and J.O. Scarbrough, *Preparation of amorphous nickel-niobium ($\text{Ni}_{60}\text{Nb}_{40}$) by mechanical alloying*. Applied Physics Letters, 1983. **43**(11): p. 1017-19.
80. Nagahama, M. and H. Suga, *Molecular alloys formed by solid-state vitrification*. Journal of Molecular Liquids, 2002. **95**(3): p. 261-284.
81. Nagahama, M., H. Suga and O. Andersson, *Formation of molecular alloys by solid-state vitrification*. Thermochemica Acta, 2000. **363**(1-2): p. 165-174.
82. Willart, J.F., N. Descamps, V. Caron, F. Capet, F. Danède and M. Descamps, *Formation of lactose-mannitol molecular alloys by solid state vitrification*. Solid State Communications, 2006. **138**(4): p. 194-199.
83. Dudognon, E., J.F. Willart, V. Caron, F. Capet, T. Larsson and M. Descamps, *Formation of budesonide/ α -lactose glass solutions by ball-milling*. Solid State Communications, 2006. **138**(2): p. 68-71.
84. Campos, C.E.M., L.J.C. De, T.A. Grandi, K.D. Machado and P.S. Pizani, *GaSe formation by mechanical alloying $\text{Ga}_{50}\text{Se}_{50}$ mixture*. Solid State Communications, 2003. **126**(11): p. 611-615.
85. De Souza, S.M., C.E.M. Campos, J.C. De Lima, T.A. Grandi and P.S. Pizani, *Structural, thermal and optical studies of Mechanical alloyed $\text{Ga}_{40}\text{Se}_{60}$ mixture*. Solid State Communications, 2006. **139**(2): p. 70-75.
86. De Souza, S.M., J.C. De Lima, C.E.M. Campos, T.A. Grandi and D.M. Triches, *Ageing-induced structural evolution of mechanically alloyed $\text{Ga}_{40}\text{Se}_{60}$* . Journal of Physics-Condensed Matter, 2008. **20**(34).
87. Machado, K.D., J.C. de Lima, C.E.M. Campos, A.A.M. Gasperini, S.M. de Souza, C.E. Maurmann, T.A. Grandi and P.S. Pizani, *Reverse Monte Carlo simulations and Raman scattering of an amorphous GeSe_4 alloy produced by mechanical alloying*. Solid State Communications, 2005. **133**(6): p. 411-416.

88. Machado, K.D., J.C. de Lima, C.E.M. Campos, T.A. Grandi and P.S. Pizani, *Reverse Monte Carlo simulations, Raman scattering, and thermal studies of an amorphous Ge₃₀Se₇₀ alloy produced by mechanical alloying*. Journal of Chemical Physics, 2004. **120**(1): p. 329-336.
89. Machado, K.D., P. Jovari, J.C. de Lima, C.E.M. Campos and T.A. Grandi, *Extended x-ray absorption fine structure, x-ray diffraction and reverse Monte Carlo studies of an amorphous Ga₅₀Se₅₀ alloy produced by mechanical alloying*. Journal of Physics-Condensed Matter, 2004. **16**(4): p. 581-590.
90. Shirakawa, Y., T. Matsuda, Y. Tani, A. Shimosaka and J. Hidaka, *Amorphization of Ge-GeSe mixtures in mechanical alloying process*. Journal of Non Crystalline Solids, 2001. **293-295**: p. 764-768.
91. Soni, P.R., *Mechanical alloying fundamentals and applications*. 2001, Cambridge: Cambridge International Science Publishing Ltd.
92. Schwarz, R.B. and C.C. Koch, *Formation of amorphous alloys by the mechanical alloying of crystalline powders of pure metals and powders of pure metals and powders of intermetallics*. Applied Physics Letters, 1986. **49**(3): p. 146-8.
93. Caron, V., J.F. Willart, F. Danede and M. Descamps, *The implication of the glass transition in the formation of trehalose/mannitol molecular alloys by ball milling*. Solid State Communications, 2007. **144**(7-8): p. 288-292.
94. Courtney, T.H. and Z. Wang, *Grinding media wear during mechanical alloying of nickel-tungsten alloys in a SPEX mill*. Scripta Metallurgica et Materialia, 1992. **27**(6): p. 777-82.
95. Retsch. *Brochure planetary ball mills*. (<http://www.retsch.com>).
96. Troles, J., *Verres infrarouges à base de chalcogénures: Nouveaux systèmes vitreux, synthèses, caractérisations et propriétés optiques non linéaires pour applications en télécommunications en limitation optique*. 2002, Université de Rennes 1, France, PhD dissertation (in French).
97. Niu, Y.-F., J.-P. Guin, T. Rouxel, A. Abdelouas, J. Troles and F. Smektala, *Aqueous Corrosion of the GeSe₄ Chalcogenide Glass: Surface Properties and Corrosion Mechanism*. Journal of the American Ceramic Society, 2009. **92**(8): p. 1779-1787.
98. Quemard, C., *Propriétés optiques non linéaires de verres de chalcogénures en vue de leur application dans les technologies de communication optique en télécom*. 2000, Université de Rennes 1, France, PhD dissertation (in French).

99. Calvez, L., M. Hubert, G. Delaizir and X.H. Zhang, *Procédé d'obtention d'un matériau vitreux et optiquement transparent dans l'infrarouge et dispositif optique comprenant un tel matériau.*, (2010), French Patent FR 10 60133
100. Wei, X., F.S. Han, X.F. Wang and C.E. Wen, *Fabrication of Al-based bulk metallic glass by mechanical alloying and vacuum hot consolidation.* Journal of Alloys and Compounds, 2010. **501**(1): p. 164-167.
101. De Lima, J.C., D.M. Triches, T.A. Grandi and R.S. de Biasi, *Structural study of $TM_{60}Ti_{40}$ ($TM = Fe, Co, Ni$) amorphous alloys produced by mechanical alloying.* Journal of Non-Crystalline Solids, 2002. **304**(1-3): p. 174-181.
102. Rahaman, M.N., *Ceramic Processing and Sintering.* 1995: CRC Press.
103. Kuczynski, G.C., *Study of the Sintering of Glass.* Journal of Applied Physics, 1949. **20**(12): p. 1160-1163.
104. Ristic, M.M. and S.D. Milosevic, *Frenkel's theory of sintering.* Science of Sintering, 2006. **38**(1): p. 7-11.
105. German, R.M., *Powder Metallurgy Science, Second Edition.* 1994: Metal Powder Industries Federation, Princeton, NJ.
106. Tokita, M., *Mechanism of spark plasma sintering and its application to ceramics.* Nyu Seramikkusu, 1997. **10**(10): p. 43-53.
107. Grasso, S., Y. Sakka and G. Maizza, *Electric current activated/assisted sintering (ECAS): a review of patents 1906–2008.* Science and Technology of Advanced Materials, 2009. **10**(5): p. 053001.
108. Bloxam, A.G., *GB Patent No. 27,002*, (1906),
109. Delaizir, G., Y. Gueguen, M. Hubert, X.H. Zhang, J. Monnier, C. Godart and L. Calvez, *Investigation of the mechanisms involved in the sintering of chalcogenide glasses and glass-ceramics by Pulsed Current Electrical Sintering (PCES)* Journal of the American Ceramic Society, accepted January 2012.
110. Amezawa, K., Y. Nishikawa, Y. Tomii and N. Yamamoto, *Electrical and Mechanical Properties of Sr-Doped $LaPO_4$ Prepared by Spark Plasma Sintering.* Journal of the Electrochemical Society, 2005. **152**(6): p. A1060-A1067.
111. Munir, Z.A., D.V. Quach and M. Ohyanagi, *Electric Current Activation of Sintering: A Review of the Pulsed Electric Current Sintering Process.* Journal of the American Ceramic Society, 2011. **94**(1): p. 1-19.

112. Fuji_Electronic_Industrial_Co._Ltd. *Applications of SPS.* (<http://sps.fdc.co.jp/application/>).
113. Kenfaui, D., G. Bonnefont, D. Chateigner, G. Fantozzi, M. Gomina and J.G. Noudem, *Ca₃Co₄O₉ ceramics consolidated by SPS process: Optimisation of mechanical and thermoelectric properties.* Materials Research Bulletin, 2010. **45**(9): p. 1240-1249.
114. Liu, G., K. Chen, H. Zhou, J. Guo, C. Pereira and J.M.F. Ferreira, *Low-temperature preparation of in situ toughened Yb α -SiAlON ceramics by spark plasma sintering (SPS) with addition of combustion synthesized seed crystals.* Materials Science and Engineering: A, 2005. **402**(1–2): p. 242-249.
115. Teber, A., F. Schoenstein, F. Têtard, M. Abdellaoui and N. Jouini, *Effect of SPS process sintering on the microstructure and mechanical properties of nanocrystalline TiC for tools application.* International Journal of Refractory Metals and Hard Materials, 2012. **30**(1): p. 64-70.
116. Gu, Y.W., K.A. Khor and P. Cheang, *Bone-like apatite layer formation on hydroxyapatite prepared by spark plasma sintering (SPS).* Biomaterials, 2004. **25**(18): p. 4127-4134.
117. Chen, H.-b., K. Tao, B. Yang and J.-s. Zhang, *Nanostructured Al-Zn-Mg-Cu alloy synthesized by cryomilling and spark plasma sintering.* Transactions of Nonferrous Metals Society of China, 2009. **19**(5): p. 1110-1115.
118. Xü, C.Y., S.S. Jia and Z.Y. Cao, *Synthesis of Al-Mn-Ce alloy by the spark plasma sintering.* Materials Characterization, 2005. **54**(4–5): p. 394-398.
119. Wuhan_Sintec_Optronics. *CVD ZnSe.* (<http://www.chinaoptronics.com>).
120. Altechna. *Zinc Selenide Laser Grade* (<http://www.altechna.com>).
121. Abdel Rafea, M., *Preparation and characterization of ZnSe nanoparticles by mechanochemical process.* Journal of Materials Science: Materials in Electronics, 2007. **18**(4): p. 415-420.
122. Baltazar, R.J., J.C. De Lima, C.E.M. Campos and T.A. Grandi, *Temperature effects on mechanically alloyed nanometric ZnSe powder.* Powder Technology, 2009. **189**: p. 4.
123. Machado, K.D., J.C. de Lima, C.E.M. de Campos, T.A. Grandi and A.A.M. Gasperini, *Aging of a nanostructured Zn₅₀Se₅₀ alloy produced by mechanical alloying.* Solid State Communications, 2003. **127**(7): p. 477-481.

124. Xi, B., D. Xu, S. Xiong, C. Wang, X. Feng, H. Zhou and Y. Qian, *Preparation and Characterization of Cubic and Hexagonal Polytypes of ZnSe:Cu²⁺ One-Dimensional Nanostructures*. The Journal of Physical Chemistry C, 2008. **112**(14): p. 5333-5338.
125. Hartmann, H., *On the growth of hexagonal ZnSe single crystals*. Kristall und Technik, 1970. **5**(4): p. 527-534.
126. Groupe_Carbone_Lorraine. Papyex (<http://www.carbonelorraine.com>).
127. Hubert, M., G. Delaizir, J. Monnier, C. Godart, H.-L. Ma, X.-H. Zhang and L. Calvez, *An innovative approach to develop highly performant chalcogenide glasses and glass-ceramics transparent in the infrared range*. Optics Express, 2011. **19**(23): p. 23513-23522.
128. Calvez, L., *Nouveaux verres et vitrocéramiques transparents dans l'infrarouge pour l'imagerie thermique*. 2006, Université de Rennes 1, France, PhD dissertation (in French).
129. Delaizir, G., *Nanoporous glass-ceramics transparent in the infrared range to be used as optical sensor - Mechanical and viscoelastic properties of the TAS (Ta-As-Se) glass* 2007, University of Arizona, PhD dissertation.
130. Delaizir, G., P. Lucas, X. Zhang, H. Ma, B. Bureau and J. Lucas, *Infrared Glass-Ceramics With Fine Porous Surfaces for Optical Sensor Applications*. Journal of the American Ceramic Society, 2007. **90**(7): p. 2073-2077.
131. McMillan, P.W., *Glass-ceramics*. Non-metallic solids. 1979: Academic Press.
132. Höland, W. and G.H. Beall, *Glass-ceramic technology*. 2002: American Ceramic Society.
133. Strnad, Z., *Glass-ceramic materials volume 8: Glass Science and Technology*. 1986: Elsevier.
134. Auzel, F., D. Pecile and D. Morin, *Rare Earth Doped Vitroceramics: New, Efficient, Blue and Green Emitting Materials for Infrared Up-Conversion*. Journal of The Electrochemical Society, 1975. **122**(1): p. 101-107.
135. Edgar, A., S. Schweizer, S. Assmann, J.M. Spaeth, P.J. Newman and D.R. MacFarlane, *Photoluminescence and crystallization in europium-doped fluorobromozirconate glass-ceramics*. Journal of Non-Crystalline Solids, 2001. **284**(1-3): p. 237-242.

136. Turnbull, D. and J.C. Fisher, *Rate of Nucleation in Condensed Systems*. The Journal of Chemical Physics, 1949. **17**(1): p. 71-73.
137. Delaizir, G., M. Dollé, P. Rozier and X.H. Zhang, *Spark Plasma Sintering: An Easy Way to Make Infrared Transparent Glass–Ceramics*. Journal of the American Ceramic Society, 2010. **93**(9): p. 2495-2498.
138. Ma, H.L., L. Calvez, B. Bureau, M. Le Floch, X.H. Zhang and J. Lucas, *Crystallization study of infrared transmitting glass ceramics based on $\text{GeS}_2\text{-Sb}_2\text{S}_3\text{-CsCl}$* . Journal of Physics and Chemistry of Solids, 2007. **68**(5-6): p. 968-971.
139. Pan, R.K., H.Z. Tao, H.C. Zang, T.J. Zhang and X.J. Zhao, *Thermal-induced gradually changes in the optical properties of amorphous GeSe_2 film prepared by PLD*. Physica B: Condensed Matter, 2009. **404**(20): p. 3397-3400.
140. Afifi, M.A., A.E. Bekheet, H.T. El-Shair and I.T. Zedan, *Determination and analysis of optical constants for Ga_2Se_3 films near absorption edge*. Physica B: Condensed Matter, 2003. **325**(0): p. 308-318.
141. Franks, J., K. Rogers and Y. Guimond. *Optical and thermo-mechanical properties of infrared glasses*. 2008: SPIE Volume 6940.
142. Le Coq, D., K. Michel, G. Fonteneau, S. Hocde, C. Boussard-Pledel and J. Lucas, *Infrared chalcogen glasses: chemical polishing and fibre remote spectroscopy*. International Journal of Inorganic Materials, 2001. **3**(3): p. 233-239.
143. Chattopadhyay, S., Y.F. Huang, Y.J. Jen, A. Ganguly, K.H. Chen and L.C. Chen, *Anti-reflecting and photonic nanostructures*. Materials Science and Engineering: R: Reports, 2010. **69**(1-3): p. 1-35.
144. Sanghera, J., C. Florea, L. Busse, B. Shaw, F. Miklos and I. Aggarwal, *Reduced Fresnel losses in chalcogenide fibers by using anti-reflective surface structures on fiber end faces*. Optics Express, 2010. **18**(25): p. 26760-26768.
145. Taga, K., D. Schwarzbach, G. Stinger, M. Grasserbauer and R. Kellner, *Surface analysis and characterization of chemically modified chalcogenide fibers*. Analytical Chemistry, 1993. **65**(17): p. 2288-2293.
146. Taga, K., C. Weigel and R. Kellner, *In situ fourier transform infrared analysis of modified chalcogenide infrared-transparent fibre surfaces*. Vibrational Spectroscopy, 1990. **1**(2): p. 125-133.
147. Minakov, A.G. and T.S. Dubrovskaya, *Some chemical processes in glass polishing*. Glass and Ceramics, 1956. **13**(9): p. 407-409.

148. Bodnar, I., G. Ilchuk, R. Petrus', V. Rud', Y. Rud' and M. Serginov, *Electrical properties of In_2Se_3 single crystals and photosensitivity of $\text{Al}/\text{In}_2\text{Se}_3$ Schottky barriers*. Semiconductors, 2009. **43**(9): p. 1138-1141.
149. Yang, M., C. Hu, J. Shen, S. Lan, P. Huang, G. Chi, K. Chen, L. Chen and T. Lin, *Hot Photoluminescence in $\gamma\text{-In}_2\text{Se}_3$ Nanorods*. Nanoscale Research Letters, 2008. **3**(11): p. 427-430.
150. Bolotin, I.L., D.J. Asunskis, A.M. Jawaideh, Y. Liu, P.T. Snee and L. Hanley, *Effects of Surface Chemistry on Nonlinear Absorption, Scattering, and Refraction of PbSe and PbS Nanocrystals*. The Journal of Physical Chemistry C, 2010. **114**(39): p. 16257-16262.
151. Melekhin, V.G., E.V. Kolobkova, A.A. Lipovskii, V.D. Petrikov, A.M. Malyarevich and V.G. Savitsky, *Fluorophosphate glasses doped with PbSe quantum dots and their nonlinear optical characteristics*. Glass Physics and Chemistry, 2008. **34**(4): p. 351-355.
152. Moreels, I., P. Kockaert, D.R. Van, K. Driesen, J. Loicq, T.D. Van and Z. Hens, *The non-linear refractive index of colloidal PbSe nanocrystals. Spectroscopy and saturation behaviour*. Journal of Luminescence, 2006. **121**(2): p. 369-374.
153. Watekar, P.R., S. Ju, A. Lin, M.J. Kim, B.H. Lee and W.-T. Han, *Linear and nonlinear optical properties of the PbSe quantum dots doped germano-silica glass optical fiber*. Journal of Non-Crystalline Solids, 2010. **356**(44-49): p. 2384-2388.
154. Jiang, X., R.D. Schaller, S.B. Lee, J.M. Pietryga, V.I. Klimov and A.A. Zakhidov, *PbSe nanocrystal/conducting polymer solar cells with an infrared response to 2 micron*. Journal of Materials Research, 2007. **22**(8): p. 2204-2210.
155. -, -, -, F.W. Wise and T. Hanrath, *PbSe Nanocrystal Excitonic Solar Cells*. Nano Letters, 2009. **9**(11): p. 3749-3755.
156. Wang, H., X. Zhang, G. Yang, Y. Xu, H. Ma, J.L. Adam, Z.a. Gu and G. Chen, *Micro-crystallization of the infrared transmitting chalcogenide glass in $\text{GeSe}_2\text{-As}_2\text{Se}_3\text{-PbSe}$ system*. Ceramics International, 2009. **35**(1): p. 83-86.
157. Dubček, P., B. Etlinger, B. Pivac and M. Kranjčec, *Infrared investigation of phonon modes in $(\text{Ga}_x\text{In}_{1-x})_2\text{Se}_3$ solid solution in the $0.10 \leq x \leq 0.40$ concentration range*. Solid State Communications, 1992. **81**(9): p. 735-737.

158. Nedeva, Y., T. Petkovaa, E. Mytilineoub and P. Petkov, *Compositional dependence of the optical properties of the Ge–Se–Ga glasses*. Journal of Optoelectronics and Advanced Materials, 2001. **3**(2): p. p. 433 - 436.
159. Sharma, I., S.K. Tripathi and P.B. Barman, *An optical study of a-Ge₂₀Se_{80-x}In_x thin films in sub-band gap region*. Journal of physics D, Applied physics, 2007. **40**(15): p. pp. 4460-4465.
160. Pandey, V., N. Mehta, S.K. Tripathia and A. Kumar, *Optical band-gap and optical constants in Se₈₅Te_{15-x}Pb_x thin films*. Journal of Optoelectronics and Advanced Materials, 2005. **7**(5): p. p. 2641 - 2646.
161. Vassilev, V., K. Tomova, V. Parvanova and S. Parvanov, *New chalcogenide glasses in the GeSe₂–Sb₂Se₃–PbSe system*. Materials Chemistry and Physics, 2007. **103**(2–3): p. 312-317.
162. Ramesh, K., M. Prashantha, E.S.R. Gopal and N. Koteeswara Reddy, *Thermal anomalies in ternary Ge[42-x]Pb[x]Se[58] glasses near the charge carrier reversal threshold*. Journal of Applied Physics, 2009. **106**.
163. Parvanov, S., V. Vassilev and K. Tomova, *Optical properties of new chalcogenide glasses from the GeSe₂–Sb₂Se₃–PbSe system*. Materials Letters, 2008. **62**(12–13): p. 2021-2024.
164. Lucas, P., M.R. Riley, C. Boussard-Plédel and B. Bureau, *Advances in chalcogenide fiber evanescent wave biochemical sensing*. Analytical Biochemistry, 2006. **351**(1): p. 1-10.
165. Balda, R., S. Garcia-Revilla, J. Fernández, V. Seznec, V. Nazabal, X.H. Zhang, J.L. Adam, M. Allix and G. Matzen, *Upconversion luminescence of transparent Er³⁺-doped chalcogenide glass-ceramics*. Optical Materials, 2009. **31**(5): p. 760-764.
166. Seznec, V., H.L. Ma, X.H. Zhang, V. Nazabal, J.L. Adam, X.S. Qiao and X.P. Fan, *Spectroscopic properties of Er³⁺-doped chalcogenide glass ceramics*. Proceeding SPIE - International Society for Optical Engineering, 2006. **6116**(Optical Components and Materials III): p. 61160B/1-61160B/9.
167. Zakery, A. and S.R. Elliott, *Optical properties and applications of chalcogenide glasses: a review*. Journal of Non-Crystalline Solids, 2003. **330**(1-3): p. 1-12.
168. Tonchev, D.T., C.J. Haugen, R.G. DeCorby, J.N. McMullin and S.O. Kasap, *Thermal and photoluminescence properties of Er³⁺-doped (GaSe)_x(As₂Se₃)_{1-x} glasses*. Journal of Non-Crystalline Solids, 2003. **326-327**: p. 364-368.

169. Solé, J.G., L.E. Bausá and D. Jaque, *An introduction to the optical spectroscopy of inorganic solids*. 2005: J. Wiley.
170. Shaw, L.B., P.A. Thielen, J.S. Sanghera, S.S. Bayya and I.D. Aggarwal, *Rare-earth-doped chalcogenide glass for mid- and long-wave IR fiber lasers*. Proceedings SPIE - International Society for Optical Engineering, 2003. **4974**(Advances in Fiber Lasers): p. 60-64.
171. Park, B.J., H.S. Seo, J.T. Ahn, Y.G. Choi, D.Y. Jeon and W.J. Chung, *Mid-infrared (3.5-5.5 μ m) spectroscopic properties of Pr³⁺-doped Ge-Ga-Sb-Se glasses and optical fibers*. Journal of Luminescence, 2008. **128**(10): p. 1617-1622.
172. Cole, B., L.B. Shaw, P.C. Pureza, R. Mossadegh, J.S. Sanghera and I.D. Aggarwal, *Rare-earth doped selenide glasses and fibers for active applications in the near and mid-IR*. Journal of Non-Crystalline Solids, 1999. **256&257**: p. 253-259.
173. Seznec, V., H.L. Ma, X.H. Zhang, V. Nazabal, J.-L. Adam, X.S. Qiao and X.P. Fan, *Preparation and luminescence of new Nd³⁺ doped chloro-sulfide glass-ceramics*. Optical Materials, 2006. **29**(4): p. 371-376.
174. Georgescu, S., A.M. Voiculescu, S. Salamu, H. Niciu, D. Niciu, M. Popescu, A. Lorinczi, A. Velea and I.D. Simandan, *Synthesis and luminescence properties of Nd-doped chalcogenide glass (Ge₅As₂S₁₃) (NdCl₃)_x (x = 0.3%, 0.5%)*. Chalcogenide Letters, 2010. **7**(11): p. 621-624.
175. Schweitzer, T., B.N. Samson, J.R. Hector, W.S. Brocklesby, D.W. Hewak and D.N. Payne, *Infrared emission and ion-ion interactions in thulium- and terbium-doped gallium lanthanum sulfide glass*. Journal of the Optical Society of America B, 1999. **16**(2): p. 308-316.
176. Zhao, D., G. Yang, Y. Xu, H. Zeng, P. Nemec, M. Frumar and G. Chen, *Luminescence of Dy³⁺-doped Ge_xGa₅Se_(95-x) glasses*. Journal of Non-Crystalline Solids, 2008. **354**(12-13): p. 1294-1297.
177. Tao, G., H. Guo, L. Feng, M. Lu, W. Wei and B. Peng, *Formation and properties of a novel heavy-metal chalcogenide glass doped with a high dysprosium concentration*. Journal of the American Ceramic Society, 2009. **92**(10): p. 2226-2229.
178. Yang, Z., B. Li, F. He, L. Luo and W. Chen, *Concentration dependence of Dy³⁺:1.3 μ m luminescence in Ge-Ga-Sb-Se glasses*. Journal of Non-Crystalline Solids, 2008. **354**(12-13): p. 1198-1200.

179. Tikhomirov, V.K., C. Goerller-Walrand and K. Driesen, *Transparent nano-glass-ceramics for efficient infrared emission*. Journal of Alloys and Compounds, 2008. **451**(1-2): p. 542-544.
180. Moizan, V., V. Nazabal, J. Troles, P. Houizot, J.-L. Adam, J.-L. Doualan, R. Moncorgé, F. Smektala, G. Gadret, S. Pitois and G. Canat, *Er³⁺-doped GeGaSbS glasses for mid-IR fibre laser application: Synthesis and rare earth spectroscopy*. Optical Materials, 2008. **31**(1): p. 39-46.
181. Tang, G., W. Chen, Z. Yang and L. Luo, *Preparation and application of rare earth-doped chalcogenide glass*, (2008),
182. Dai, S.X., B. Peng, P.-j. Zhang, T.F. Xu, W. Xunsi, Q.-H. Nie and X.H. Zhang, *The near- and mid-infrared emission properties of Tm³⁺-doped GeGaS-CuI chalcogenide glasses*. Journal of Non-Crystalline Solids, 2010. **356**(44-49): p. 2424-2428.
183. Dantelle, G., M. Mortier, G. Patriarche and D. Vivien, *Er³⁺-doped PbF₂: Comparison between nanocrystals in glass-ceramics and bulk single crystals*. Journal of Solid State Chemistry, 2006. **179**(7): p. 1995-2003.
184. Wu, M., J.R. Lakowicz and C.D. Geddes, *Enhanced Lanthanide Luminescence Using Silver Nanostructures: Opportunities for a New Class of Probes with Exceptional Spectral Characteristics*. Journal of Fluorescence, 2005. **15**(1): p. 53-59.
185. Jia, Y.Q., *Crystal radii and effective ionic radii of the rare earth ions*. Journal of Solid State Chemistry, 1991. **95**(1): p. 184-187.
186. Gu, M., L. Xiao, X. Liu, R. Zhang, B. Liu and X. Xu, *Highly enhanced luminescence of GdTaO₄:Eu³⁺ phosphors by codoping with Zn²⁺ ions*. Journal of Alloys and Compounds, 2006. **426**(1-2): p. 390-394.
187. Santos, R., L.F. Santos and R.M. Almeida, *Optical and spectroscopic properties of Er-doped niobium germanosilicate glasses and glass ceramics*. Journal of Non-Crystalline Solids, 2010. **356**: p. 2677-2682.